EXPERIMENTAL AND NUMERICAL APPROACHES TO EVALUATE THE CRUSHING BEHAVIOR OF COMBINED GEOMETRY CORE SANDWICH STRUCTURES AGAINST BLAST

A Thesis Submitted to
The Graduate School of Engineering and Sciences of
İzmir Institute of Technology
in Partial Fulfillment of the Requirements for the Degree of

DOCTOR OF PHILOSOPHY

in Mechanical Engineering

by
Ali KARA

July 2015
İZMİR

We approve the thesis of **Ali KARA**

Examining Committee Members:

Assoc. Prof. Dr. Alper TAŞDEMİRCİ
Department of Mechanical Engineering, İzmir Institute of Technology

Prof. Dr. Ramazan KARAKUZU
Department of Mechanical Engineering, Dokuz Eylül University

Assist. Prof. Dr. H. Seçil ARTEM
Department of Mechanical Engineering, İzmir Institute of Technology

Prof. Dr. Hakan ÇETİNEL
Department of Mechanical Engineering, Celal Bayar University

Assoc. Prof. Dr. Buket OKUTAN BABA
Department of Mechanical Engineering, Celal Bayar University

09 July 2015

Assoc. Prof. Dr. Alper TAŞDEMİRCİ
Supervisor, Department of
Mechanical Engineering
İzmir Institute of Technology

Prof. Dr. Mustafa GÜDEN
Co-Supervisor, Department of
Mechanical Engineering
İzmir Institute of Technology

Prof. Dr. Metin TANOĞLU
Head of the Department of
Mechanical Engineering

Prof. Dr. Bilge KARAÇALI
Dean of the Graduate School of
Engineering and Sciences

ACKNOWLEDGEMENTS

Firstly I would like to thank to my supervisor Assoc. Prof. Dr. Alper TAŞDEMİRCİ for accepting me to unique Dynamic Testing and Modeling Laboratory, for his lead the way for me in the high strain rate universe, and for the great contributions, encouragement, and support during my studies even at the times that I feel desperate.

Secondly, I would like to thank to my co-supervisor Prof. Dr. Mustafa GÜDEN for his precious comments and contributions during my studies. I would like to thank also my committee members; Prof. Dr. Ramazan KARAKUZU, Assist. Prof. Dr. Seçil ARTEM, Prof. Dr. Hakan ÇETİNEL, and Assoc. Prof. Dr. Buket OKUTAN BABA for their comments to convert my work into a better dissertation.

I also would like to thank the Scientific and Technological Research Council of Turkey for the grant 112M141 and İzmir Institute of Technology Scientific Research Projects Program for the grant 2011İYTE16.

I owe thanks to my colleagues in DTM; İ. Kutlay ODACI, A. Kıvanç TURAN, Assist. Prof. Dr. Cenk KILIÇASLAN, Selim ŞAHİN, Atacan YÜCESOY, and Fulya AKBULUT for making the work for me like home providing enjoyable and pleasant environment. I also would like to thank my close friends Doğuş ZEREN, Yiğit ATTİLA, Umut SAVACI, Hasan ÇELİK, and Mustafa KARAMAN for their friendship and support. I also appreciate the on and off presence of my best friend Tunç BİLGİNCAN in İYTE, resulted in very productive discussions about life and work.

I owe gratefulness to my family; my father Hasan, my mother Sevil, my mother-in-law İlgül, and my brother Eren. Their presence in my life always relieves me even through the most intricate paths that I have to deal with. They always enlighten my way and be there for me.

Last but not least, my nuclear family deserves the better expression of my gratefulness that to express it the leaves of this thesis are not sufficient. My wife Arzu is the best thing that happened in my life, helps me continuously for five years, and making a building home for us. My beautiful daughter Ada even makes my life better, her smile and joy are real remedy for all of the sorrow in the world. Their endless support and love motivate me continuously.

ABSTRACT

EXPERIMENTAL AND NUMERICAL APPROACHES TO EVALUATE THE CRUSHING BEHAVIOR OF COMBINED GEOMETRY CORE SANDWICH STRUCTURES AGAINST BLAST

In this study, novel sandwich structures containing combined geometry structures as core materials were designed and developed for blast protection applications. The proposed combined geometries consist of a hemispherical geometry attached seamlessly to a cylindrical segment. Deep drawing method was used to obtain four different types of combined geometries having two different radii from blanks with two different initial thicknesses. The mechanical properties of the blank material were obtained by conducting tensile experiments at quasi-static and high strain rate regimes. Thereafter, crushing and energy absorption behavior of core units were determined by tests at quasi-static and low velocity regimes, experimentally. Before crushing simulations, manufacturing method was simulated to have realistic residual stress/strain and thickness variations of numerical specimens. Having accurate deformation history, crushing experiments were simulated and a good agreement was reached proving the realistic modeling of the manufacturing effects. The effect of heat treatment on the crushing behavior of combined geometry shells was also investigated both experimentally and numerically and there was a good agreement noted. After, cross-shaped sandwich structures of one type of combined geometry were prepared. Static, low velocity and high velocity crushing behavior of sandwiches were investigated. Study on sandwich structures also included confined experiments in order to account for the interaction between the core units and between the core units and surrounding environment; such a case might be a bigger sandwich in which adjacent cores could exert forces to each other. Numerical study was validated by comparing experimental and numerical results of three different loading regimes for sandwiches. Having well-verified numerical models, numerical study was extended to investigate strain rate and inertial effects on sandwich structures by simulations at high crushing velocities. With complete knowledge on crushing and energy absorption of single geometries and sandwiches, behavior of sandwiches under blast was investigated by using ConWep function. Various types were proposed for arrangements of sandwiches to have higher energy absorption and lower transmitted forces to the protected structures.

ÖZET

KOMBİNE GEOMETRİ ÇEKİRDEKLİ SANDVİÇ YAPILARIN PATLAMAYA KARŞI EZİLME DAVRANIŞLARININ ÖLÇÜLMESİNDE DENEYSEL VE NÜMERİK YAKLAŞIMLAR

Bu çalışmada, bileşik geometrili yapıları çekirdek malzemesi olarak kullanan özgün sandviç yapılar patlamaya karşı koruma uygulamaları için tasarlanmış ve geliştirilmiştir. Önerilen bileşik geometri silindirik bir kesite dikişsiz olarak ekli bir yarıküresel geometriden oluşmaktadır. Derin çekme yöntemi iki farklı yarıçaplı bileşik geometrileri iki farklı ilk kalınlıktaki iş parçasından üretmek amacıyla kullanılmıştır. Bileşik geometrilerin oluşturulduğu iş parçasının mekanik özellikleri kuasi-statik ve yüksek deformasyon hızlarında çekme testleri ile elde edilmiştir. Ardından birim çekirdeklerin ezilme ve enerji emme davranışları statik ve düşük hız rejimlerindeki deneylerle deneysel olarak belirlenmiştir. Ezilmenin nümerik simülasyonlarından önce, nümerik numune kesiti boyunca gerçeğe uygun kalıcı gerilme/şekil değiştirme ve kalınlık dağılımı elde edebilmek için üretim yöntemi modellenmiştir. Hatasız deformasyon tarihçesinin eldesiyle, ezilme deneyleri modellenmiş ve gerçeğe uygun modellemenin sonucunda iyi bir uyum elde edilmiştir. Kombine geometrilerin ezilme davranışlarına ısıl işlemin etkisi de ayrıca deneysel ve nümerik olarak incelenmiştir. Sonuçlar oldukça uyumludur. Sonra, artı şeklinde sandviç yapılar seçilen bir bileşik geometri kullanılarak oluşturulmuştur. Sandviç yapılar ile ilgili deneysel çalışma birim çekirdek malzemelerinin kendi arasındaki ve birim çekirdek malzemeleri ile çevresi arasındaki etkileşimi de hesaba katmak amacıyla sınırlandırılmış deneyleri de içermektedir; örneğin daha büyük bir sandviç içerisindeki çekirdekler birbirine kuvvet uygulayabilir. Nümerik çalışma üç yükleme rejiminde sandviçler için de deneysel ve nümerik sonuçları karşılaştırarak gerçeklenmiştir. Doğruluğu kanıtlanmış nümerik modellerin eldesi ile nümerik çalışma şekil değiştirme ve atalet etkilerinin incelenmesi amacıyla sandviç yapılar üzerinde gerçekleştirilen yüksek hızlı ezilme simülasyonlarına genişletilmiştir. Hem bileşik geometriler hem de bunların sandviçlerinin ezilme ve enerji emme davranışları ile ilgili tam bilgilere sahip olunduktan sonra, sandviç yapıların patlama altındaki davranışları, ConWep fonksiyonu kullanılarak, nümerik olarak incelenmiştir. Daha yüksek enerji emme ve daha düşük kuvvet iletimi elde etmek amacıyla sandviç yapıların dizilimi için çeşitli konfigürasyonlar önerilmiştir.

I dedicated this thesis to Arzu and Ada

TABLE OF CONTENTS

LIST OF FIGURES x

LIST OF TABLES xvii

CHAPTER 1. INTRODUCTION 1
1.1. Introduction 1
1.2. Aim of the Study 5
1.3. Scope of the Study 6

CHAPTER 2. LITERATURE SURVEY 8
2.1. Energy Absorbing Structures and Materials 8
2.2. Spherical Shells, Circular Tubes, and Combined Geometries 21
2.3. Blast Loading on Sandwich Structures 41

CHAPTER 3. MANUFACTURING AND EXPERIMENTAL AND NUMERICAL DETAILS 55
3.1. Materials and Manufacturing 55
3.1.1. AISI 304L Stainless Steel 55
3.1.2. Manufacturing of Combined Geometry Shells 56
3.1.3. Manufacturing of Sandwich Structures with Combined Geometry Shell Cores 61
3.1.4. Heat Treatment of Combined Geometry Shell Structures 62
3.2. Experimental Details 63
3.2.1. Quasi-Static Experiments 63
3.2.2. Drop Weight Impact Experiments 64
3.2.3. Split Hopkinson Tension Bar Experiments 65
3.2.4. Direct Impact Experiments 68
3.2.5. High Speed Photography 70
3.3. Numerical Details 70
3.3.1. Johnson-Cook Constitutive Equation 70

3.3.2. Numerical Specimen Preparation – Restart Analysis Technique of LS-DYNA 75
3.3.3. Crushing and Blast Simulations 77
3.3.4. Mesh Sensitivity Analysis 79

CHAPTER 4. CRUSHING AND ENERGY ABSORPTION BEHAVIOR OF COMBINED GEOMETRY SHELL STRUCTURES 80
4.1. Quasi-Static Crushing Behavior of Combined Geometry Shells 80
4.2. Low Velocity Crushing Behavior of Combined Geometry Shells 88
4.3. Comparison of Experimental and Numerical Results of Combined Geometry Shell Structures 95
4.3.1. Details of Numerical Simulations of Quasi-Static and Low Velocity Crushing 95
4.3.2. Comparison of Experimental and Numerical Results 96

CHAPTER 5. EFFECT OF HEAT TREATMENT ON CRUSHING AND ENERGY ABSORPTION BEHAVIOR OF COMBINED GEOMETRY SHELL STRUCTURES 101
5.1. Quasi-Static Crushing Behavior of Heat Treated Combined Geometry Shells 102
5.2. Low Velocity Crushing Behavior of Heat Treated Combined Geometry Shells 105
5.3. Comparison of Experimental and Numerical Results 107

CHAPTER 6. CRUSHING AND ENERGY ABSORPTION BEHAVIOR OF SANDWICH STRUCTURES WITH COMBINED GEOMETRY SHELL CORES 114
6.1. Experimental Results 115
6.2. Numerical Results 125

CHAPTER 7. EFFECT OF INERTIA STRAIN RATE AND MULTILAYERING ON CRUSHING AND ENERGY ABSORPTION BEHAVIOR OF SANDWICH STRUCTURES WITH COMBINED GEOMETRY SHELL

CORES 134
7.1. Inertia and Strain Rate Effects on Crushing Behavior of Sandwich Structures 135
7.2. Effect of Multilayering on Crushing Behavior of Sandwich Structures 139

CHAPTER 8. BLAST LOADING ON SANDWICH STRUCTURES WITH COMBINED GEOMETRY SHELL CORES 147
8.1. Blast Simulation Details 148
8.2. Blast Simulation Results and Discussions 153

CHAPTER 9. CONCLUSIONS 162

REFERENCES 166

LIST OF FIGURES

Figure **Page**

Figure 1.1. (a) The Altay, (b) Otokar Arma, (c) BMC Kirpi, and (d) FNSS Akıncı. 2

Figure 1.2. Historical development of lightweight armor. 2

Figure 1.3. A typical sandwich structure. 3

Figure 1.4. de Havilland DH.98 Mosquito multi-role combat aircraft. 3

Figure 1.5. Core materials used in sandwich structures (a) square honeycomb, (b) hexagonal honeycomb, (c) metal foam, (d) triangular and diamond corrugated structures, and (e) balsa wood. 4

Figure 2.1. Deformation modes for square tubes; (a) progressive buckling, (b) transition from progressive buckling to global buckling, and (c) global buckling. 10

Figure 2.2. Paper model representation of collapse modes for long and short square tubes. 10

Figure 2.3. (a) Comparison of static and dynamic force – displacement curve and (b) ratio between static and dynamic mean forces for square tubes. 11

Figure 2.4. Aluminum tube panels proposed for blast loading applications. 12

Figure 2.5. Parameters defining a honeycomb cell. 12

Figure 2.6. In-plane loading of honeycombs (a) stress-displacement and (b) deformation scheme. 14

Figure 2.7. (a) An open cell polyurethane foam, (b) a closed cell polyethylene foam... 15

Figure 2.8. (a) Foam modulus vs. density and (b) collapse stress vs. density for polyurethane foams.. 15

Figure 2.9. Specific absorbed energy of various foams for various plateau stresses. 16

Figure 2.10. Structure of a foam model. 16

Figure 2.11. Computer tomography image of an aluminum foam 17

Figure 2.12. (a) Open cell, (b) closed cell Voronoi foams. 17

Figure 2.13. (a) Corrugated fiberboard, (b) corrugated fiberboard box. 18

Figure 2.14. A second order hierarchical corrugated structure. 19

Figure 2.15. Energy absorption vs. Relative density for corrugated structure 20

Figure 2.16. Low velocity indentation results for full and homogenized models of 21

Figure 2.17. (a) Undeformed shell and (b) deformed shell 22

Figure 2.18. Force - displacement curves: (a) effect of radius to thickness ratio on

deformation under point load, and (b) effect of boss width 22
Figure 2.19. Comparison of mean collapse loads of spherical domes of different R/t values 24
Figure 2.20. (a) Various modes of deformation; local flattening, inward dimpling, and unsymmetric lobe formation, and (b) effect of mode jump in load-deformation behavior..... 25
Figure 2.21. Deformed shapes (a) woven single-ply, (b) woven double-ply 0/0, (c) woven double-ply 0/45, (d) knitted single-ply, (e) knitted double-ply 0/0, and (f) knitted triple-ply 0/0/0. 28
Figure 2.22. Compression of four connected balls in a 1-D array; (a) the normalized load-deformation curve; (b) the final deformation profile in each ball's top and bottom parts. 29
Figure 2.23. (a) Sketch of dynamic test system, and (b) force-deflection curves for a single ball..... 30
Figure 2.24. Collapse modes of circular tubes under axial loading; (a) symmetric mode; (b) diamond mode, and (c) mixed mode..... 31
Figure 2.25. A mode classification chart for annealed aluminum tube 31
Figure 2.26. Load-displacement curve of an aluminum tube. 32
Figure 2.27. Experimental load–displacement curves of double-end constraint tubes .. 34
Figure 2.28. Load and average crushing load–displacement curves of foam-filled single Al tube, empty tube, empty tube+foam and foam: (a) 0.27, (b) 0.35 and (c) 0.43 g/cm^3 Al foam-filled tube. 35
Figure 2.29. Effect crushing speed on Kevlar/Epoxy tubes. 36
Figure 2.30. (a) Deformed nose cone of aircraft, (b) gas tank with combined hemispheres and cylinder, (c) various caliber bullets, and (d) Cirit laser-guided 70 mm rocket system. 38
Figure 2.31. Typical load–compression curves in impact experiments for specimens S6 (α=21°, bottom diameter=165 mm) and S7 (α=23°, bottom diameter=165 mm)..... 39
Figure 2.32. Comparison of experimental and numerical results. 40
Figure 2.33. Experimental set-ups that are used in the blast effect investigations, (a) real scale explosion experiments, (b) ballistic pendulum, (c) shock tube, (d) foam projectile, (e) underwater explosion tests. 42
Figure 2.34. Deformation profiles of sandwich structures under localised loading , (a)

air-core, (b) honeycomb core sandwich structures. 44
Figure 2.35. Experimental conditions and geometry of core structures used. 45
Figure 2.36. (a) Transmitted pressure in sandwich structures, (b) photographs of dynamically tested sandwich panels. 46
Figure 2.37. (a) Solid plate deflection, (b) front face deflection of sandwich plates, and (c) back face deflection of sandwich plates. 47
Figure 2.38. Deformed sandwich plates under impulsive loads; (a) 21.5 kPa.s, (b) 28.4 kPa.s, and (c) 33.7 kPa.s. 48
Figure 2.39. The measured maximum deflection at the mid-span of the (a) H100 PVC foam core, (b) H250 PVC foam core and (c) balsa wood core sandwich beams, as a function of the foam projectile momentum. 49
Figure 2.40. Comparison of the measured maximum mid-span deflections of the back face of sandwich and monolithic beams of equal mass; (a) Set 1, (b) Set 2 and (c) Set 3. 50
Figure 2.41. (a) Core configurations and real specimen, (b) deformation of first configuration, and (c) deformation of second configuration. 51
Figure 2.42. Two different configurations for sacrificial claddings made of thin-walled beverage cans 52
Figure 2.43. Cylindirical metallic hollow sphere specimen. 52
Figure 2.44. Results of modeling studies used to predict inertial effect on deformation of metallic hollow sphere structures. 53
Figure 2.45. Deformation history of sandwich structures. 53
Figure 2.46. (a) Acceleration history, (b) acceleration versus core thickness. 54
Figure 3.1. An example of a combined geometry shell. 56
Figure 3.2. Manufacturing drawing of combined geometry shells; (a) R75T05, (b) R75T1, (c) R125T05, and (d) R125T1. 57
Figure 3.3. Schematic representation of deep drawing method (green part: forming die, blue part: blank holder, red part: mechanical punch, grey part: workpiece) 58
Figure 3.4. Combined geometry shells; (a) bottom view of R75T05 and R75T1, (b) bottom view of R125T05 and R125T1, (c) top view of R75T05 and R75T1, (d) top view of R125T05 and R125T1, (e) cross-section view of R125T1. 59
Figure 3.5. Measured thickness variation contours of combined geometry shells; (a) R125T1, (b) R125T05, (c) R75T1, (d) R75T05 specimens. 60

Figure 3.6. Bonding pattern for manufacturing of sandwich structures; (a) solid model, and (b) manufactured pattern. 61
Figure 3.7. Sandwich specimen. 62
Figure 3.8. Shimadzu AG-X 300 kN universal testing machine. 64
Figure 3.9. Fractovis Plus drop weight tester. 65
Figure 3.10. Split Hopkinson Tension Bar. 66
Figure 3.11. SHTB voltage history of a test conducted on AISI 304L stainless steel.... 67
Figure 3.12. Direct Impact experimental setup..... 69
Figure 3.13. (a) Quasi-static tension specimen, (b) Hopkinson tension specimen. 72
Figure 3.14. Quasi-static true stress – true plastic strain curves. 72
Figure 3.15. High strain rate true stress – true plastic strain curves. 73
Figure 3.16. Curve fitting of test result. 73
Figure 3.17. Strain rate sensitivity of AISI 304L stainless steel..... 74
Figure 3.18. Comparison of experimental results and Johnson-Cook model of AISI 304L stainless steel. 74
Figure 3.19. Comparison of measured and simulated thickness variations of a R125T1 specimen. 76
Figure 4.1. Quasi-static crushing test results of R125T1 specimen..... 81
Figure 4.2. Deformation history results of quasi-static experiments of R125T1 specimens. 82
Figure 4.3. Quasi-static crushing test results of R125T05 specimen..... 83
Figure 4.4. Deformation history results of quasi-static experiments of R125T05 specimen. 84
Figure 4.5. Quasi-static crushing test results of R75T1 specimen..... 85
Figure 4.6. Deformation history results of quasi-static experiments of R75T1 specimen. 86
Figure 4.7. Quasi-static crushing test results of R75T05 specimen..... 87
Figure 4.8. Deformation history results of quasi-static experiments of R75T1 specimen. 87
Figure 4.9. (a) R125T1 specimen drop weight test result, (b) comparison of quasi-static and drop weight test results..... 90
Figure 4.10. (a) R125T1 drop weight test history, (b) a view from the tested specimen. 90
Figure 4.11. (a) R125T05 specimen drop weight test result, (b) comparison of quasi-

static and drop weight test results. 91
Figure 4.12. R125T05 specimen drop weight test history. 92
Figure 4.13. (a) R75T1 specimen drop weight test result, (b) comparison of quasi-static and drop weight test results. 92
Figure 4.14. R75T1 specimen drop weight test history 93
Figure 4.15. (a) R75T05 specimen drop weight test result, (b) comparison of quasi-static and drop weight test results. 94
Figure 4.16. R75T05 specimen drop weight test history. 94
Figure 4.17. Deep-drawing model and crushing simulation model. 96
Figure 4.18. (a) R125T1 quasi-static test and simulation result, (b) R125T1 drop weight test and simulation result. 96
Figure 4.19. R125T1 specimen (a) quasi-static test and simulation and (b) drop weight test and simulation result. 97
Figure 4.20. Parameters for crushing investigation. 98
Figure 5.1. As-received and heat-treated combined geometry shell specimens. 102
Figure 5.2. Quasi-static test results of heat-treated R125T05H specimen. 102
Figure 5.3. Effect of heat treatment on quasi-static crushing behavior of; (a) R125T1, (b) R125T05, (c) R75T1, (d) R75T05 specimens. 103
Figure 5.4. Deformed views of heat treated and as-received specimens; (a) R125T1, (b) R125T05, (c) R75T1, (d) R75T05 specimens. 104
Figure 5.5. Effect of heat treatment on low velocity crushing behavior of; (a) R125T1H, (b) R125T05H, (c) R75T1H, (d) R75T05H specimens. 106
Figure 5.6. Deformed views of heat treated low velocity test specimens; (a) R125T1H, (b) R125T05H, (c) R75T1H, (d) R75T05H specimens. 107
Figure 5.7. Experimental and numerical force-displacement curves of (a) quasi-static R125T05H, (b) quasi-static R75T1H, (c) drop weight R125T1H, and (d) drop weight R75T05H specimens. 109
Figure 5.8. Experimental and numerically deformed pictures of (a) quasi-static R125T05H and (b) drop weight R125T05H specimens. 110
Figure 5.9. Static and dynamic *CFE* for heat-treated specimens. 112
Figure 5.10. Comparison of (a) mean load and (b) *SAE* for heat-treated and as-received specimens. 113
Figure 6.1. (a) Manufacturing pattern on which core structures were placed, (b) R125t05 metal face sandwich structure. 115

Figure 6.2. (a) The force–displacement curves of three unconfined quasi-static crushing tests and (b) deformation pictures of one representative test..... 116
Figure 6.3. (a) Comparison of unconfined and confined quasi-static crushing test results, deformed top views of (b) unconfined, and (c) confined specimen 118
Figure 6.4. (a) Drop-weight crushing result comparatively with unconfined quasi-static crushing test result and (b) deformation scheme. 120
Figure 6.5. (a) Unconfined and confined direct impact crushing test results and (b) deformation scheme of unconfined experiment..... 124
Figure 6.6. Crushing simulation models for (a) unconfined quasi-static and low velocity experiments, and (b) confined quasi-static experiment. 125
Figure 6.7. (a) Sectional view of confined direct impact model and (b) unconfined direct impact model..... 126
Figure 6.8. Comparison of experimental and numerical results (a) quasi-static – unconfined, (b) quasi-static – confined, (c) drop weight. 128
Figure 6.9. Comparison of deformation history of experimental and numerical quasi-static – unconfined crushing results of R125T05 sandwich specimen. 129
Figure 6.10. Comparison of deformation history of drop weight results. 130
Figure 6.11. Comparison of experimental and numerical direct impact results (a) unconfined and (b) confined..... 131
Figure 6.12. Experimental vs. numerical deformed specimens; (a) unconfined – quasi-static, (b) confined – quasi-static, (c) drop weight, (d) unconfined – direct impact, and (e) confined – direct impact. 132
Figure 7.1. (a) Type I structure, (b) Type II structure, (c) force-displacement and (d) energy displacement curves of energy absorbing structures..... 135
Figure 7.2. Effect of strain rate and inertia for 200 m/s simulation..... 137
Figure 7.3. Average increase in mean crush load vs. impact velocity..... 138
Figure 7.4. (a) Sequential, and (b) opposite two layered specimens, and (c) three layered specimen. 139
Figure 7.5. Mean load vs. % displacement curves of single and multilayered sandwiches. 141
Figure 7.6. Misalignment angle. 142
Figure 7.7. *SAE* vs. misalignment angle for different multilayered sandwiches. 143
Figure 7.8. Effect of cross-head speed and angle of misalignment on deformation mode of sequential two layered specimen. 144

Figure 7.9. Effect of cross-head speed and angle of misalignment on deformation mode of opposite two layered specimen. 145
Figure 8.1. Blast wave pressure-time profile. 149
Figure 8.2. Blast wave pressure-time profile obtained from simulations. 151
Figure 8.3. Sandwich configurations; (a) close-packed (CP), (b) cross-sharing packed (CSP), (c) cross-unsharing packed (CUP), and (d) Hybrid cross-sharing packed(H-CSP). 151
Figure 8.4. Transmitted force histories for sandwich specimens; (a) CP, (b) CSP, (c) CUP, and (d) H-CSP. 155
Figure 8.5. Deformed views of middle or near-middle specimens for sandwiches; (a) CP, (b) CSP, (c) CUP (near middle specimen), and (d) H-CSP. 158
Figure 8.6. Deformed views of (a) middle as-received specimen and (b) heat-treated specimen for H-CSP. 159
Figure 8.7. Deformed views of sandwich specimens; (a) CP, (b) CSP, (c) CUP, and (d) H-CSP. 160

LIST OF TABLES

Table **Page**

Table 2.1. Effect of R/t ratio on mean collapse load. 26

Table 2.2. Summary of results of tests..... 45

Table 3.1. Chemical composition of AISI 304L stainless steel..... 55

Table 3.2. Geometrical parameters of combined geometry shells..... 56

Table 3.3. Material properties of SHTB test setup. 66

Table 3.4. Material properties of direct impact test setup. 68

Table 3.5. Johnson-Cook material model parameters of AISI 304L stainless steel. 75

Table 4.1. Absorbed energy by combined geometry shell structures..... 88

Table 4.2. Drop weight test conditions..... 89

Table 4.3. Quasi-static and drop weight experiment results of combined geometry shell structures. 99

Table 5.1. Drop weight test conditions for heat treated specimens. 105

Table 5.2. Johnson–Cook model properties of as-received and heat-treated AISI 304L stainless steel used in numerical models..... 108

Table 5.3. Experimental and numerical crushing results of heat-treated specimens.... 111

Table 6.1. Comparison of quasi-static test results with 5 combined geometry structures. 119

Table 8.1. *LOAD_BLAST_ENHANCED card input variables..... 150

Table 8.2. Properties of four alternative configurations. 152

Table 8.3. Velocity and acceleration results from blast simulations. 153

Table 8.4. Energy and deformation results from blast simulations. 154

CHAPTER 1

INTRODUCTION

1.1. Introduction

As a result of excessive fossil fuel demand by international community, there have always been conflicts in the Middle East region. Due to its geopolitical position, it is not possible not to involve in such conflicts for Turkey. Besides, there are a lot of terrorist organizations operating in Turkey and its neighbors. Considering above facts, Turkey must be able to design and manufacture its national instruments that can be used under the command of the Turkish security forces.

Over the last decade, many projects were initiated both by government and private sector in order to supply for national defense inquiries. Some of these projects can be listed as follows:

- The Altay is a main battle tank designed and developed by Otokar (Figure 1.1.a),
- Otokar Arma is an armored tactical vehicle (Figure 1.1.b),
- BMC Kirpi is a MRAP vehicle (Figure 1.1.c),
- Otokar Tulpar is an infantry fighting vehicle,
- FNSS ACV 15 - 19 (Akıncı) -30 are armored combat vehicles (Figure 1.1.d),
- Nurol Ejder is a 6x6 wheeled armored personnel carrier (APC),
- The Pars is an amphibious ACV.

Regardless the highly technologically powerful design and development ability of Turkish defense industry, there can be further improvements for the initial designs of vehicles of armed forces. One of the main expectations from vehicles of armed forces is to maximize the occupant survivability during attack. In order to achieve this goal, generally vehicles are equipped with a heavy steel armor. In a hot battle situation, survivability of occupants is also dependent on the mobility of the vehicles. Besides, the lighter the vehicle, the more distance can be travelled on duty. A lighter armored carrier

can be used for longer duties without refueling. Therefore, designs of lightweight blast resistant armors in order to use in tanks or armored vehicles of armed forces are very important by considering aforementioned issues.

(a) (b)

(c) (d)

Figure 1.1. (a) The Altay (Source: www.otokar.com.tr), (b) Otokar Arma (Source: www.otokar.com.tr), (c) BMC Kirpi (Source: www.bmc.com.tr), and (d) FNSS Akıncı (Source: www.fnss.com.tr).

Blast resistant structures have many intersections with lightweight armors used in ballistic protection applications. Mobility of an armored vehicle is basically related to the areal density of its armor structure as can be seen in Figure 1.2. (Fink 2000). High mobility requirements of infantry vehicles due to the technological advancements in modern weapons led to the developments of lightweight armors.

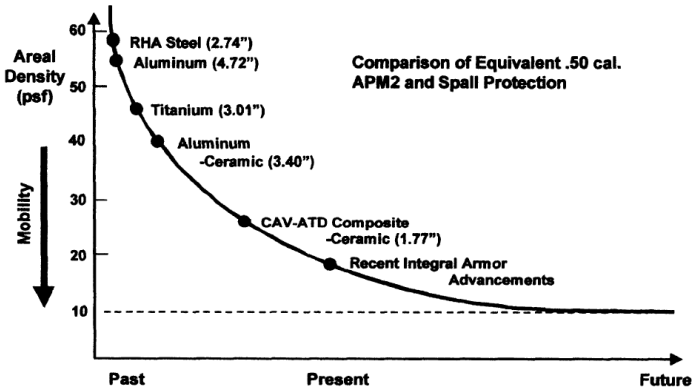

Figure 1.2. Historical development of lightweight armor (Source : Fink 2000).

One of the main components used in lightweight armor design has been proposed as sandwich structures due to their high stiffness-to-weight, high strength-to-weight ratio and high energy absorption capability. A sandwich structure consists of a light weight, thick core sandwiched between thin, stiff face sheets (Figure 1.3.). Having a thicker and lighter core between face sheets, sandwiches have high flexural stiffness and by the use of collapsible structures as core materials, higher energy absorption can be guaranteed by sandwich structures. Easy structural integrity, tailoring/engineering of their mechanical properties and ease of manufacturing/maintenance makes the sandwich structures better candidates in the use of lightweight structures.

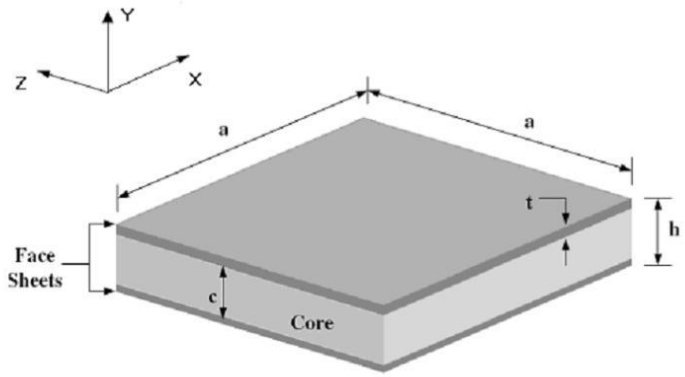

Figure 1.3. A typical sandwich structure
(Source : Odacı 2011).

An early modern example of a sandwich construction can be found in the de Havilland DH.98 Mosquito (The Wooden Wonder) multi-role combat aircraft (Figure 1.3.) used by the Royal Air Force during and after the World War II. The Wooden Wonder was built with balsa-wood core and plywood skins.

Figure 1.4. de Havilland DH.98 Mosquito multi-role combat aircraft
(Source : en.wikipedia.org).

In contemporary applications, many materials have been developed in order to use as core materials of sandwich structures. Square honeycombs ((Dharmasena et al. 2008), (Rathbun et al. 2006), (Xue and Hutchinson 2004)), hexagonal honeycombs ((Zhu, Zhao, et al. 2009), (Zhu et al. 2008), (Chi, Langdon, and Nurick 2010)), metallic foams ((Hanssen, Enstock, and Langseth 2002), (Radford et al. 2006), (Sriram, Vaidya, and Kim 2006)), polymeric foams ((Tekalur, Shukla, and Shivakumar 2008), (Wang, Gardner, and Shukla 2009), (Tagarielli, Deshpande, and Fleck 2007)), balsa wood ((Tagarielli, Deshpande, and Fleck 2007), (Chen et al. 2011)), triangular and diamond corrugated structures ((Rubino, Deshpande, and Fleck 2009), (Radford, Fleck, and Deshpande 2006)), Y frames ((Rubino, Deshpande, and Fleck 2009), (Guruprasad and Mukherjee 2000)), I frames ((Mori et al. 2009)) are widely used examples of core materials.

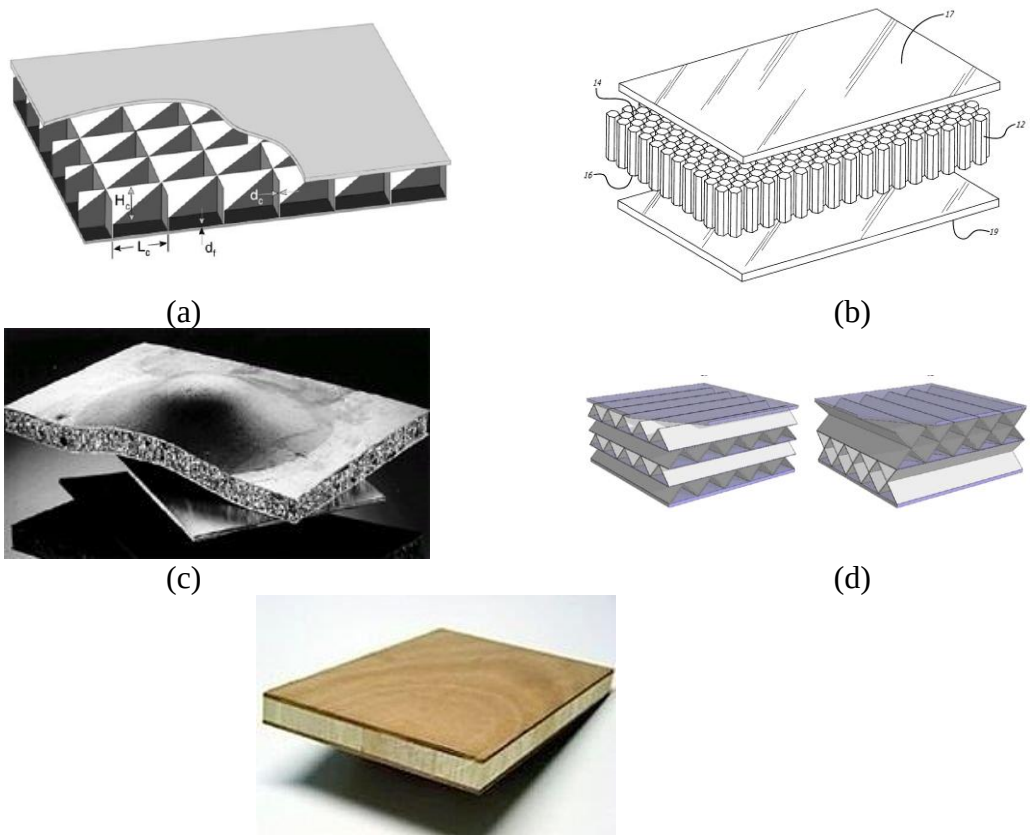

Figure 1.5. Core materials used in sandwich structures (a) square honeycomb (Source : Rathbun et al. 2006), (b) hexagonal honeycomb, (c) metal foam (Source : Banhart 2000), (d) triangular and diamond corrugated structures (Source : Dharmasena et al. 2010), and (e) balsa wood.

Considering the aforementioned requirements of lightweight sandwich structures, newly developed core geometries are continuously being proposed by the scientific and industrial communities. The need of Turkish defense industry for lightweight sandwich structures is obvious. It is important to design, develop, manufacture and even export lightweight sandwich structures with the use of facilities of Turkish industry in order to balance the current account of Turkey. It is obviously possible to design, develop and manufacture national lightweight sandwich structures by also considering the engineering knowledge level of Turkish professionals.

1.2. Aim of the Study

This study focuses on designing, manufacturing and optimization of novel lightweight sandwich structures for the use of blast threat. As a novel design, repeated combined geometries were offered as core structures. To the author's knowledge, such structures have never been used as core structures of sandwich structures. Additionally, the simplistic design of novel combined geometries allowed the use of facilities of Turkish manufacturers instead of importing expensive trademark products of other countries.

The specific objectives of this work are as follows;

- Design and manufacturing of novel combined geometry structures consisting of a hemispherical geometry attached seamlessly to a cylindrical segment.
- Numerical modeling of manufacturing method of combined geometries in order to account for strain hardening and geometrical variations through the section of geometries.
- Determination of static and dynamic crushing and energy absorption behavior of combined geometry core structures experimentally.
- Numerical modeling of static and dynamic crushing behavior of combined geometry core structures.
- Determination of effect of heat-treatment on the static and dynamic crushing behavior of combined geometry core structures experimentally and numerically.

- Design and manufacturing of novel sandwich structures having combined geometries as core structures.
- Experimental determination of unconfined and confined static and dynamic crushing and energy absorption behavior of sandwich structures having combined geometries as core structures.
- Numerical modeling of unconfined and confined static and dynamic crushing and energy absorption behavior of sandwich structures having combined geometries as core structures.
- Numerical determination of effect of blank material's strain rate sensitivity and inertial effects on the crushing behavior of sandwich structures.
- Numerical determination of multilayering on the crushing behavior of sandwich structures.
- Numerical determination of dynamic response of newly developed sandwich structures under blast loading and optimization of protection offering various alternative configurations for repeated core arrangements.

1.3. Scope of the Study

The following chapter provides relevant literature on energy absorbing structures and materials and lightweight sandwich structures especially used in blast loading applications. Results of various experimental and numerical efforts were discussed in order to build a base in understanding the energy absorption of structures.

In Chapter 3, materials and manufacturing methods were introduced. Details of experimental methods used in the study were given. Besides, numerical part of the study was elaborated. Results of specimen preparation simulations were shown.

In Chapter 4, experimental and numerical results of investigation on static and low velocity crushing and energy absorption behavior of single combined geometry shells were given.

In Chapter 5, effect of heat-treatment on crushing and energy absorption behavior of combined geometry shells was investigated.

In Chapter 6, experimental and numerical results on static, low velocity, and dynamic crushing and energy absorption behavior of sandwich structures with

combined geometry shell cores were given. Effect of confinement and interactions between unit shell structures were determined, under different loading regimes.

In Chapter 7, effects of strain rate, inertia, and multilayering were distinguished by using results of fictitious simulations.

In Chapter 8, results of blast simulations were provided. Variations of types of sandwich structures were offered and their performances were discussed under blast type of loading.

Finally in the Chapter 9, conclusions drawn as a result of detailed experimental and numerical efforts of the current study were provided along with the suggested future studies.

CHAPTER 2

LITERATURE SURVEY

For centuries, mankind tried to build defense structures to avoid occupation by invader groups. With the advancements of industrial revolution, and as a result of introduction of mass production in the late 1800s and early 1900s, weapon technologies evolved and consecutively defensive requirements modified from early primitive applications. As a result of invention of computer technologies in the middle of 1900s, researches on both weapon technologies and defensive structures also jumped to a new level. Therefore, a number of studies were dedicated to seek new technologies for defense applications for over decades. Considering the requirements of defensive structures and simplistic design of core structures offered herein, energy absorbing structures deserved to be mentioned as a background in this study. Afterwards, details of relevant literature on sandwich structures subjected to dynamic loading and blast were given and results were discussed thoroughly.

2.1. Energy Absorbing Structures and Materials

Energy absorbing structures and materials must be able to convert initial kinetic energy due to loading exerted by accidents, explosive events etc. to the plastic deformation or any other energy dissipation mechanism irreversibly. The peak reaction force of energy absorbing structures must be set below a limit to avoid damage of adjacent structures or protected cargo and occupants. Lightweight and high energy absorption capability must also be provided in order to be able to achieve minimum additional weight by protecting structures (Lu and Yu 2003). Generally axially crushed thin-walled tubes of various sections were proposed in the literature as energy absorbing structures. As examples, circular tubes (Guillow, Lu, and Grzebieta 2001), square tubes (Langseth and Hopperstad 1996), polygonal tubes (Rossi, Fawaz, and Behdinan 2005), elliptic tubes (Marzbanrad, Mehdikhanlo, and Pour 2009), and multicellular tubes (Kim 2002) can be listed. Tubes of different sections were also prepared having different materials such as; polymers (Langseth and Hopperstad 1996) and composite structures

(Mahdi and Hamouda 2005). Cellular structures such as; honeycombs of various sections (hexagonal (Chawla et al. 2003), circular (Papka and Kyriakides 1999), square (Xue and Hutchinson 2006)), polymeric foams (Tasdemirci, Turan, and Guden 2012) and metallic foams (Hall, Guden, and Yu 2000) are also widely used examples of energy absorbing structures and materials. Obviously different geometrical shapes were also offered in energy absorbing applications such as; different arrangements of metallic hollow spheres (Taşdemirci, Ergönenç, and Güden 2010) and twin-spherical microstructures as in Skydex® (Zhu et al. 2014). Triangular, diamond (Dharmasena et al. 2010), and zig-zag (Kılıçaslan et al. 2014) corrugations were also proposed as energy absorbing structures in the studies. In this section, studies in the literature related in listed structures and materials are given except for circular tubes. Because circular tubes deserve more attention as a part of proposed combined geometries, explanations containing details of literature related to circular tubes postponed to the next section along with the literature on spherical sections and combined geometries.

Square tubes generally subjected to axial loads and when it is the case they exhibits progressive collapse behavior (Lu and Yu 2003). Typical load – displacement curves for square tubes collapsing in different modes can be seen in Figure 2.1. along with views of deformed specimens. As can be seen in Figure 2.1.a, a typical force-displacement curve for a progressively collapsing square tube shows an initial peak force followed by a sharp fall and subsequent fluctuations corresponding to formation of folds. Transition and global buckling modes are undesirable energy absorbing mechanisms because their unstable nature and low energy dissipation.

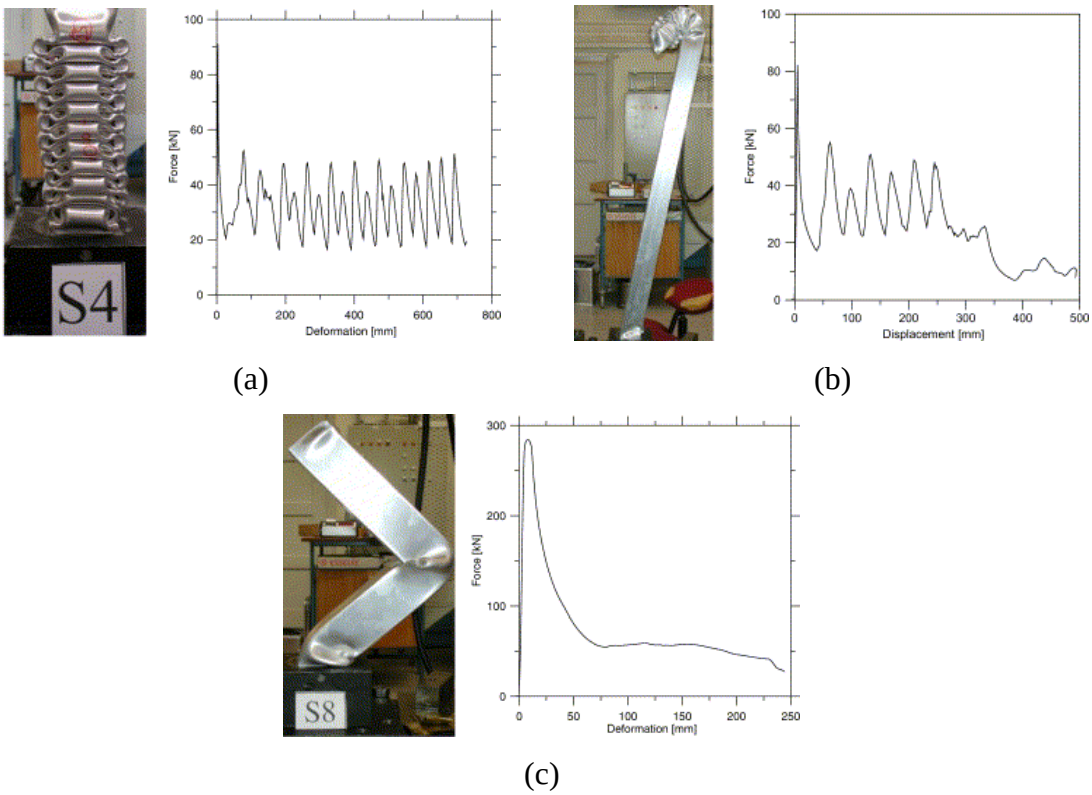

(a) (b)

(c)

Figure 2.1. Deformation modes for square tubes; (a) progressive buckling, (b) transition from progressive buckling to global buckling, and (c) global buckling (Source : Jensen, Langseth, and Hopperstad 2004).

In the literature, axial crushing of square tubes was investigated analytically and collapse modes were demonstrated by using paper models as shown in Figure 2.2 (Meng, Al-Hassani, and Soden 1983). As can be seen in the figure, length-to-perimeter ratio obviously affects the deformation behavior of square tubes.

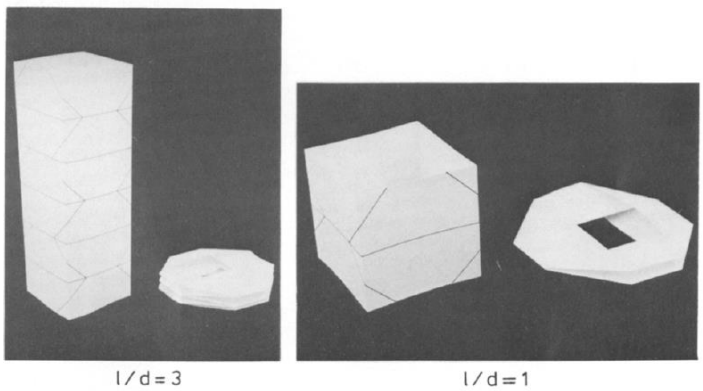

Figure 2.2. Paper model representation of collapse modes for long and short square tubes (Source : Langseth and Hopperstad 1996).

It is proposed by researchers that dynamic mean force is substantially higher than static mean forces obtained from experiments of square tubes considering strain rate and inertial effects when dynamic loading is the case (Langseth and Hopperstad 1996) (Lu and Yu 2003). Especially main difference between static and dynamic force displacement curves were encountered in the initial peak forces. Dynamic initial peak was found substantially higher than the static force due to the initiation of folding process was affected by inertial effects (Langseth and Hopperstad 1996); example can be seen in Figure 2.3. Obviously, with the increase in displacement, difference between dynamic and static mean forces decrease because inertial effects are minor in the consequent progressive fold formation behavior in square tubes (Abramowicz and Jones 1997).

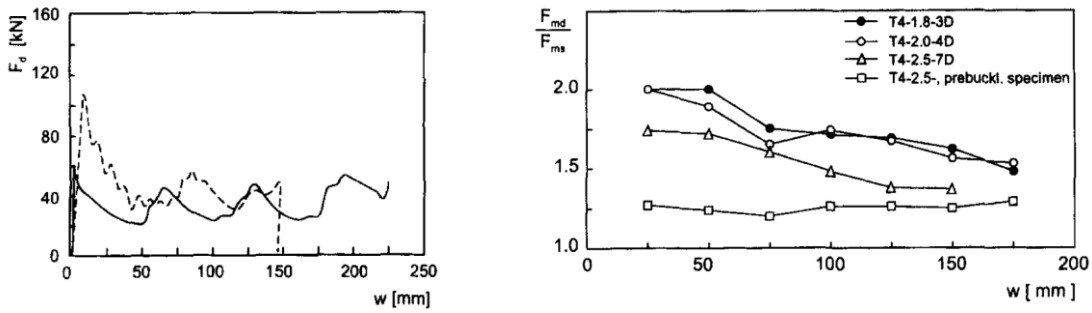

(a) (b)

Figure 2.3. (a) Comparison of static and dynamic force – displacement curve and (b) ratio between static and dynamic mean forces for square tubes (Source : Langseth and Hopperstad 1996).

Considering aforementioned progressively collapsing nature of square tubes, their applications in energy absorption is vast. For instance, their arrangements can be used as core structures in protective cladding applications as seen in Figure 2.4. (Theobald and Nurick 2010). Results showed that, as initial impulse increased crushing distances increased differently for different arrangements relatively to the number of units.

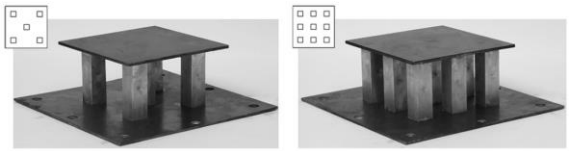

Figure 2.4. Aluminum tube panels proposed for blast loading applications (Source : Theobald and Nurick 2010).

Honeycombs, as mentioned, are vastly used as energy absorbing structures. Honeycombs are one of the most important bio-inspiration examples, designed initially by imitating the miraculous hexagonal structures prepared by bee colonies. Geometrical parameters defining a hexagonal cell were given in Figure 2.5. A hexagonal unit can be defined by cell wall lengths (*l* and *h*), the angle between two cell walls (θ), and the cell wall thickness (*t*). In addition to geometrical parameters, relative density (ρ*) is also an important parameter defined as the ratio of the density of the cellular material to the density of the material that cellular material was made up of.

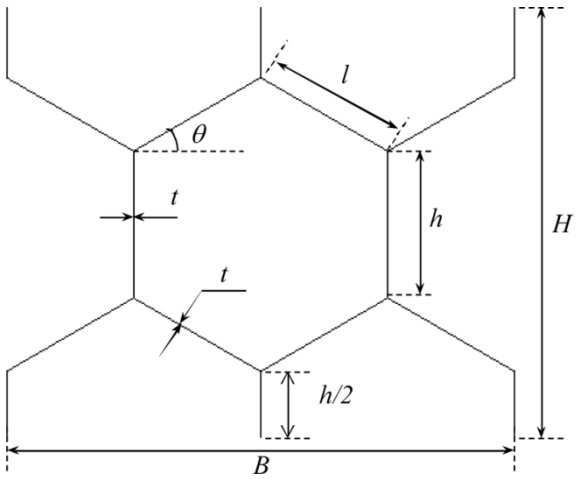

Figure 2.5. Parameters defining a honeycomb cell (Source : Chen and Ushijima 2013).

Simple formulas were proposed in order to relate mean crushing force of hexagonal honeycombs with the geometrical and material parameters of the cell wall material as in following equation (Wierzbicki 1983) where *h* equal to *l*:

$$P_m = 8.61\sigma_0 t^{5/3} h^{1/3} \tag{2.1}$$

where σ_0 is the flow stress of the cell wall material and the investigation assumed a rigid-perfectly plastic material. Relatively simple formula offered yielded

good correlation with the experimental investigations. Study was also extended in order to account for strain hardening effects considering large plastic strains encountered in crushing process (Wierzbicki 1983).

Initial elastic collapse behavior of hexagonal, triangular and square honeycombs was investigated by considering that adjacent cells were constraining each other through the buckling process (Wang 1991). Although the constraining phenomenon in the study was only proposed for initial elastic buckling and small deformations, it is also the case for large deformations of honeycombs. In the literature, it is proposed that, as loading rate increased to dynamic from static, overall deformation and folding mechanism was more irregular than that of static loading case. As a result, dynamic crushing strength of honeycombs were reported 1.33 – 1.74 times higher than static ones (Wu and Jiang 1997). Reported results also showed that larger cell size showed the most significant loading-rate effect. Study also proposed the best honeycomb as having small cell size and core height and made of high strength material; which is reasonable even considering relatively simple formula given in equation 1.1. Multilayered honeycombs were also proposed in order to increase energy absorption ability (Yasui 2000). Uniform or pyramidal type multilayers were investigated in static and dynamic loading conditions. Both static and dynamic collapse behavior of multilayers showed progressive nature, successive peaks were formed as signs of buckling initiation in following layers. Both energy absorption capacity and efficiency was found to be higher for pyramidal type multilayers. It was reported that, for dynamic loading conditions, energy absorption of honeycomb increases with increase in cell wall thickness and decreases with the increase of cell wall length of paper honeycombs (Wang 2009). It was also proposed in the literature that, the strain hardening of honeycombs during the dynamic crushing was highly influenced by the pressure developed by entrapped air in unit cells of honeycombs (Xu et al. 2012). Analytical formulas were also developed in order to account for strain hardening caused by entrapped air.

In-plane buckling and crushing behavior of honeycombs were also investigated in the literature ((Papka and Kyriakides 1999), (Liu and Zhang 2009), (Hu, You, and Yu 2013)). In the in-plane loading, honeycombs do not exhibit higher initial peak loads. The peak load observed after the initial linear-elastic region maintains constant until densification strain was reached as observed in most cellular structures like foams. An example of an equibiaxial load-displacement curve and deformation scheme can be seen in Figure 2.6. In-plane crushing behavior of honeycombs were found to be related to

different factors in different directions (Hu, You, and Yu 2013) considering cell wall angles. It was observed that, the most effective factor on the crushing strength in y-direction is the density of the honeycomb. Effects of defects (imperfections) such as missing or fractured cell walls on the deformation behavior of honeycombs were also investigated ((Zhang et al. 2010), (Wang and McDowell 2003)).

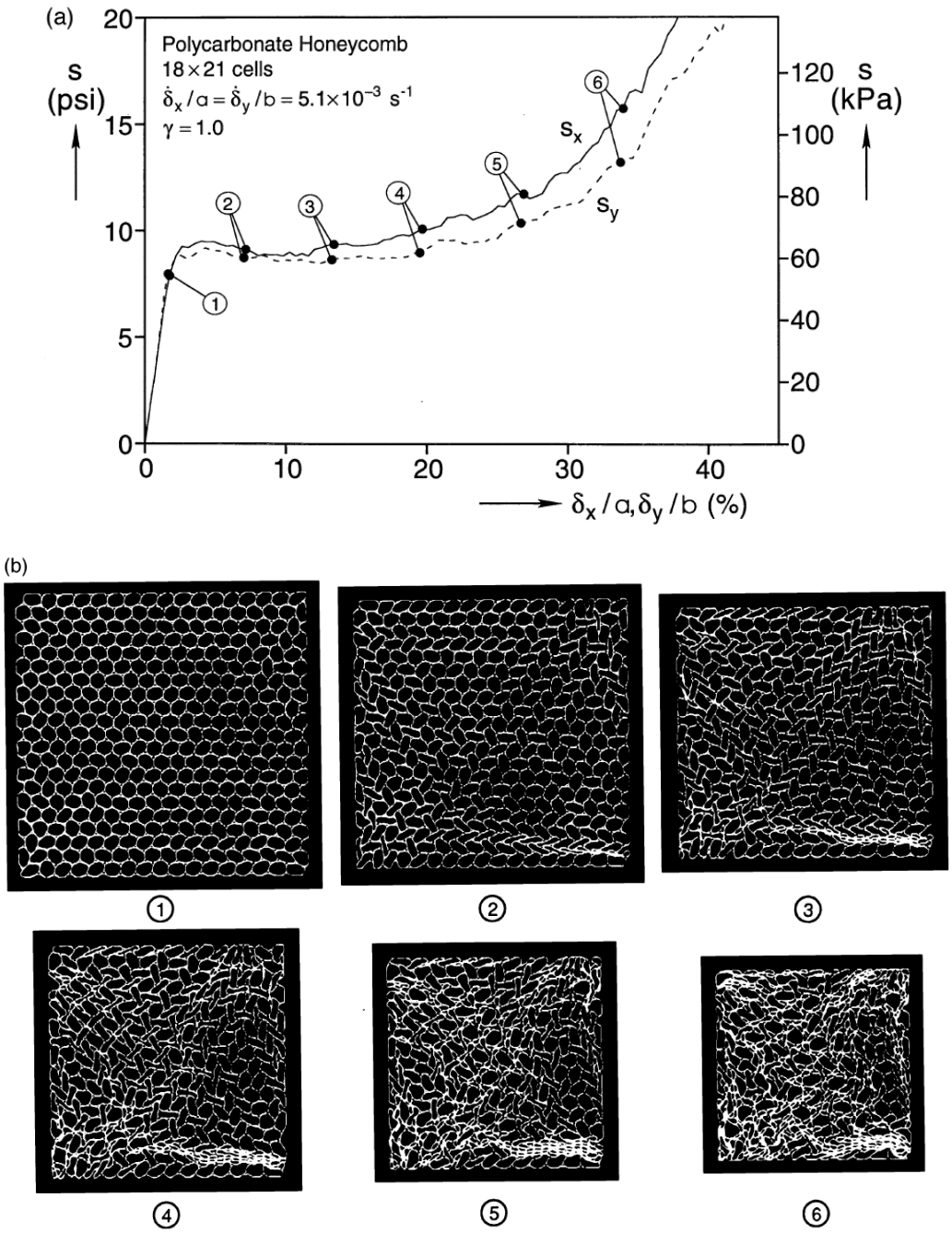

Figure 2.6. In-plane loading of honeycombs (a) stress-displacement and (b) deformation scheme (Source : Papka and Kyriakides 1999).

One of the most widely used cellular structures are foams. Different from two dimensional cell arrangements of honeycombs, foams have three dimensional cells.

Foams can be classified in terms of cell types; open (Gong and Kyriakides 2005) and closed cell (Aktay, Toksoy, and Güden 2006) foams as seen in Figure 2.7. Besides base materials can be metals (Barnes et al. 2014), polymers ((Daniel, Cho, and Werner 2013), (Tasdemirci, Turan, and Guden 2012)) or even glass residue (Attila, Güden, and Taşdemirci 2013) etc.

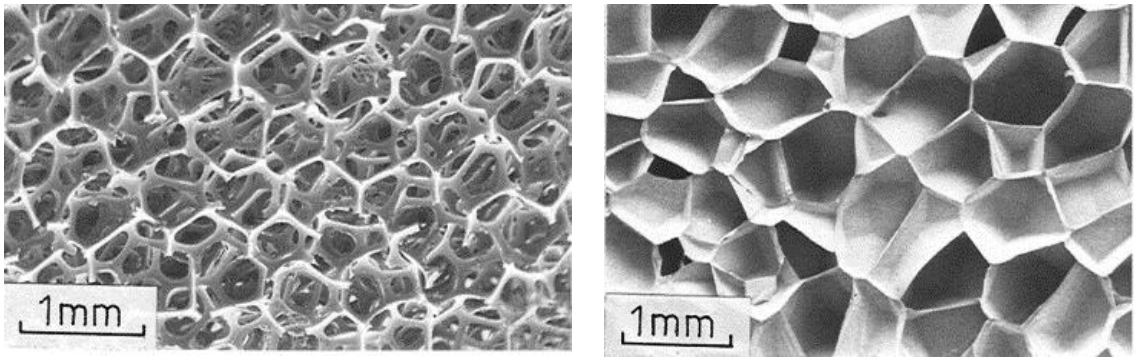

(a) (b)

Figure 2.7. (a) An open cell polyurethane foam, (b) a closed cell polyethylene foam (Source : (Gibson 2005)).

Relative density of foams is also an important parameter defining behavior of structure as in honeycombs. In Figure 2.8, relations between tensile and compressive moduli and collapse stress of polyurethane foams were plotted against density of the foam. It was also proposed that for lower density polyurethane foam studied, an initial peak was followed by a decreased plateau stress resembling a yield-like behavior (Goods, Neuschwanger, and Whinnery 1998).

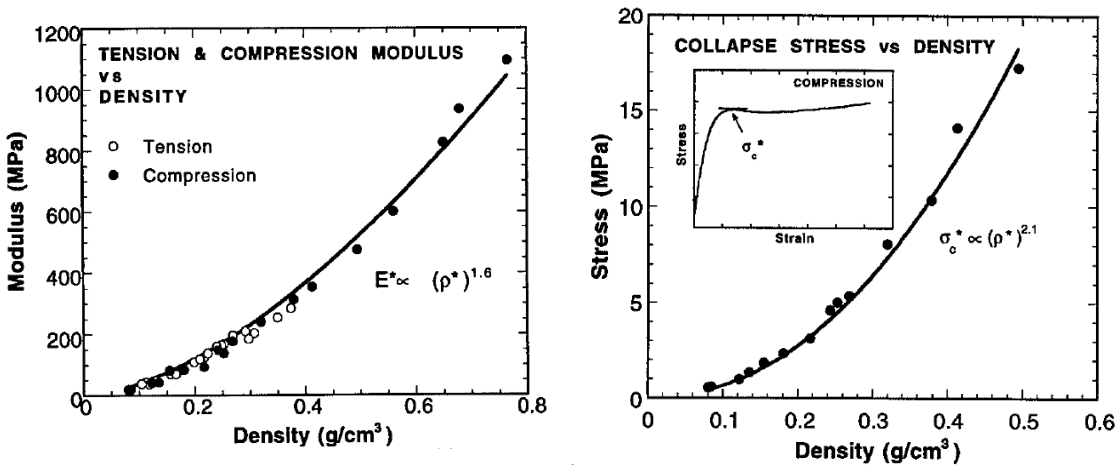

(a) (b)

Figure 2.8. (a) Foam modulus vs. density and (b) collapse stress vs. density

(Source : Goods, Neuschwanger, and Whinnery 1998).

As seen in the Figure 2.9., both specific absorbed energy and plateau stress increases with increasing relative density of metal foams.

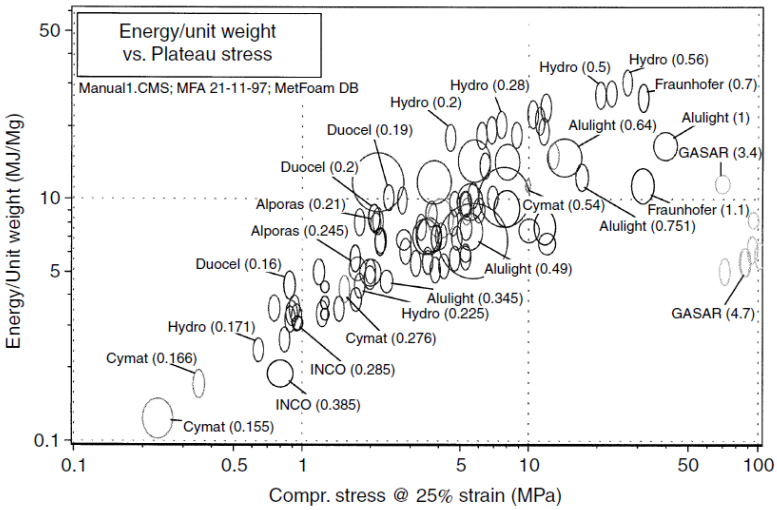

Figure 2.9. Specific absorbed energy of various foams for various plateau stresses (Source : Ashby 2000).

Considering cell wall arrangements of foams, their numerical representation is substantially intricate; micron or even nano-sized cell walls were distributed within the volume and micro scale modeling must be incorporated in order to account for dimensional deformation behavior of foams. Because cells of a foam are arrays having wide spectrum of sizes, in the literature a structure consisting of densely packed cells were proposed to represent foam as shown in Figure 2.10 (Kim et al. 2006). This modeling technique was proposed as an efficient technique to represent the crushing behavior of Al-alloy foams.

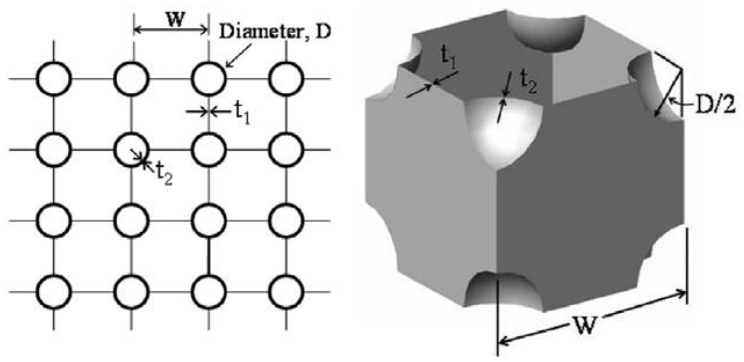

Figure 2.10. Structure of a foam model (Source : Kim et al. 2006).

Randomness of cellular microstructures was also accounted for in the literature (Gaitanaros, Kyriakides, and Kraynik 2012). Microstructure was determined by using X-Ray tomography (Figure 2.11), and random soap froth microstructures generated using Brakke's surface evolver (Brakke 1992).

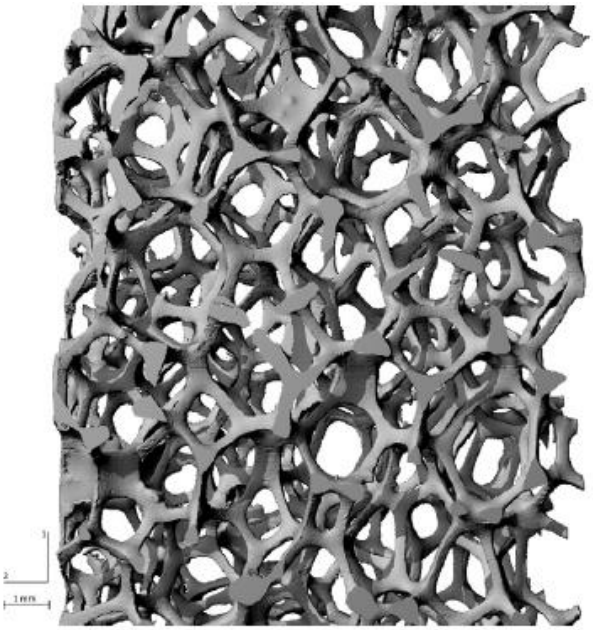

Figure 2.11. Computer tomography image of an aluminum foam
(Source : Gaitanaros, Kyriakides, and Kraynik 2012).

Open cell (Sotomayor and Tippur 2014) and closed cell (Song et al. 2010) foams were also modeled by using Voronoi tessellations as can be seen in Figure 2.12.

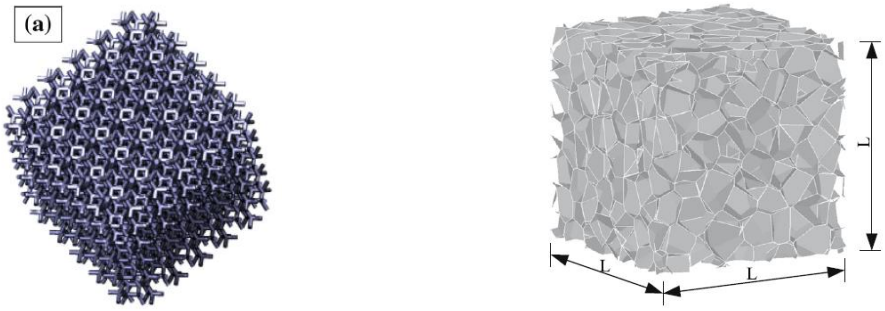

(a) (b)

Figure 2.12. (a) Open cell, (b) closed cell Voronoi foams.

Considering the aforementioned problems in order to numerically model behavior of foams, homogenized models were also used. In this technique, foams were modeled with brick elements, geometrical complexity was not taken into account but their anisotropic behavior can be given as input in the modeling studies. In LS-DYNA for example, *MAT_HONEYCOMB constitutive model can be used to simulate anisotropic behavior of structural foams. Of course, inertial and strain rate effects resulted from geometrical complexity cannot be directly incorporated.

One of the interesting designs used in energy absorption applications is corrugated structures (Wiernicki et al. 1991). Corrugated galvanized iron was invented in 1820s in order to use as a prefabricated lightweight roofing material. Due to their lightweight, sufficient strength, and ease of prefabrication, corrugated fiberboards were used in protective packaging applications widely ((Wang and E 2011), (Naganathan, He, and Kirkpatrick 1999)). A corrugated fiberboard and a box can be seen in Figure 2.13.

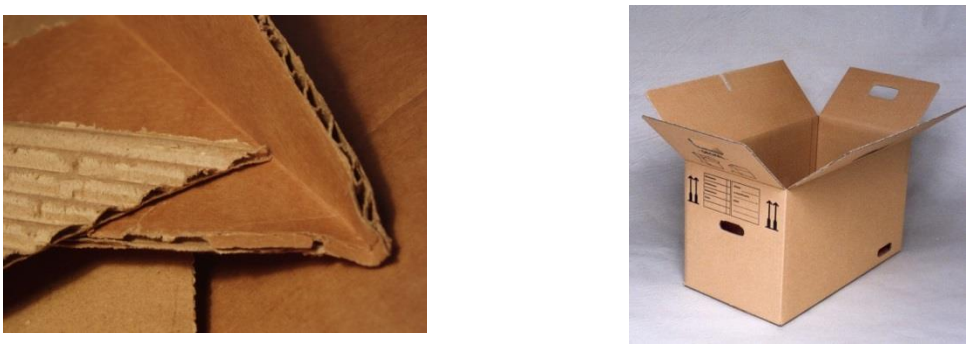

(a) (b)

Figure 2.13. (a) Corrugated fiberboard, (b) corrugated fiberboard box (Source : en.wikipedia.org).

Simple elastic-plastic phenomena to investigate dynamic behavior of metallic corrugated structures were proposed (Wiernicki et al. 1991). Results showed that, ease of integrity and offered lightweight makes the corrugated structures a good choice to use in ship structures in military applications. Corrugated structures were also offered to use for civil transportation applications considering their improved crash performance and lightweight (Torre and Kenny 2000). Optimum corrugations were proposed by utilizing analytical formulations related to buckling and failure behavior of corrugated structures (Liang, Yang, and Wu 2001). Considering great buckling resistance, corrugated structures were offered in longitudinal loading applications also (Valdevit, Hutchinson, and Evans 2004). Metal foam projectile loading method was used to

investigate the shock loading behavior of corrugated structures (Radford, Fleck, and Deshpande 2006). It was shown that corrugated structures exhibited lower midspan deflections than monolithic structures and for lower and intermediate impulses; they performed better than foam or pyramidal structures. Hierarchical corrugations were also implemented in that struts were also corrugated structures as shown in Figure 2.14 (Kooistra, Deshpande, and Wadley 2005). It was suggested that, second order hierarchical corrugated structures outperformed first order corrugated structures.

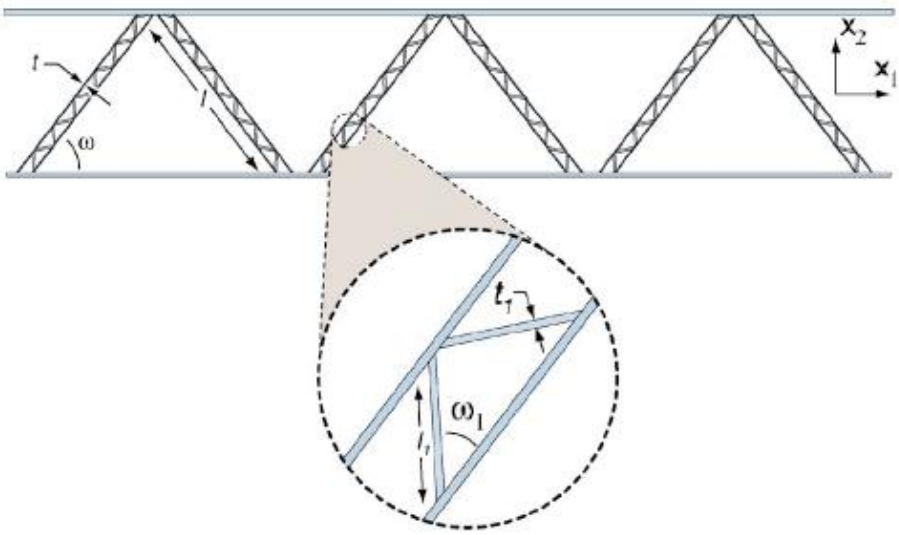

Figure 2.14. A second order hierarchical corrugated structure
(Source : Kooistra, Deshpande, and Wadley 2005).

It was proposed for paperboard corrugated sandwiches, reducing the corrugation size and increasing the thickness of base material resulted in increase of the relative density and improved energy absorption capability as seen in Figure 2.15 (Dongmei 2009).

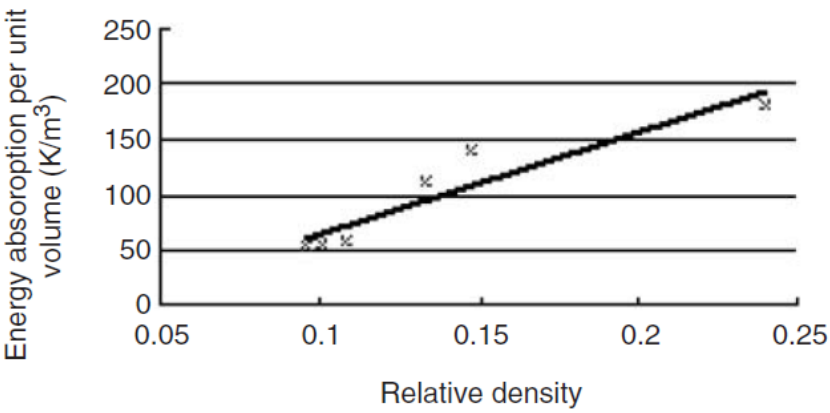

Figure 2.15. Energy absorption vs. Relative density for corrugated structure (Source : Dongmei 2009).

Corrugated all-composite sandwich structures having sandwich struts instead of monolithic ones as in hierarchical corrugations were also used in applications (Kazemahvazi, Tanner, and Zenkert 2009, Kazemahvazi and Zenkert 2009). For different failure modes failure maps were created. In the higher order hierarchical corrugations, different types of core materials were investigated.

Dynamic impact responses of layered trapezoidal zig-zag corrugated cores were investigated (Kılıçaslan et al. 2013). Their results showed that, brazing process used for bonding the layers reduced the yield stresses thereof. Adhesive bonding when layering showed better performance in terms of low velocity penetration applications. Besides, orientation of different layers had effect in terms of lateral load distribution. In another study (Kılıçaslan et al. 2014) static and dynamic crushing behavior of same materials were investigated. Effect of confinement and crushing velocity were shown. It was shown that multi-layering decreased buckling stress and increased the densification strain of corrugated sandwich structures. Homogenized multilayered models were also offered to model corrugated structures and low velocity behavior was predicted with an acceptable error in a reduced computational time (Kılıçaslan 2014). Some of the results can be seen in Figure 2.16.

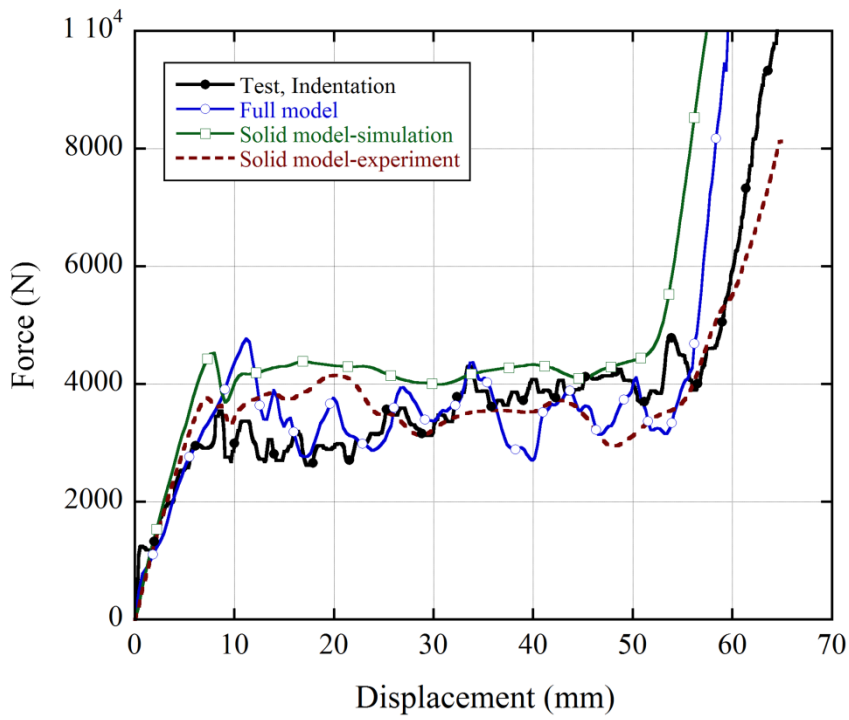

Figure 2.16. Low velocity indentation results for full and homogenized models of corrugated structures (Source : Kılıçaslan 2014).

2.2. Spherical Shells, Circular Tubes, and Combined Geometries

As mentioned previously, spherical shell sections and circular tubes deserve more attention as constituents of proposed core structures. Therefore this section was dedicated to the relevant literature on crushing and energy absorption behavior of spherical shell sections and circular tubes. Even it is very few, literature on combinations of various geometries was given to have a detailed coverage on the crushing and energy absorption phenomena of structures proposed so far in the literature.

One of the early study was conducted on deformation of plastic spherical shells compressed between rigid platens (Figure 2.17.) statically (Updike 1972). In the study, the problem was investigated analytically by treating the material as rigid-perfectly plastic and the results were restricted to small displacements comparable to a few thicknesses. In the investigation, a toroidal portion BCD was determined to move radially outward as deformation progresses, which was called as an inward dimpling.

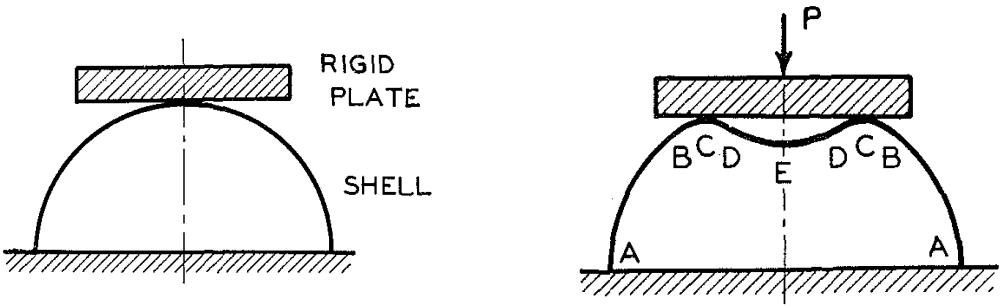

(a) (b)

Figure 2.17. (a) Undeformed shell and (b) deformed shell (Source : Updike 1972).

Analysis of crushing of rotationally symmetric plastic shells were conducted in another study (De Oliveira and Wierzbicki 1982). Closed form solutions were derived for conical and spherical shells compressed between rigid plates, subjected to point and boss loading. The analyses were limited to the solutions for axisymmetric deformations, it is obvious that the analyses are not valid for the further stages of deformations associated with unsymmetrical lobe formation.

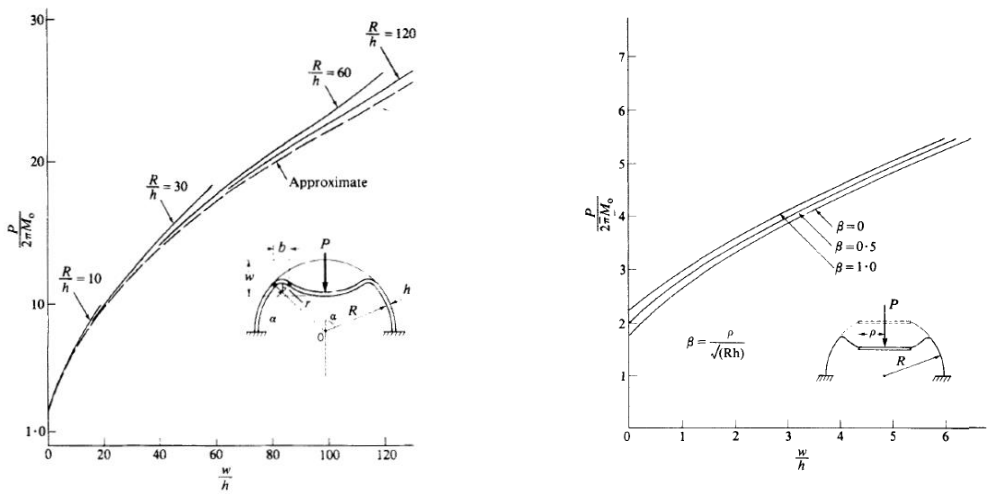

(a) (b)

Figure 2.18. Force - displacement curves: (a) effect of radius to thickness ratio on deformation under point load, and (b) effect of boss width (Source : De Oliveira and Wierzbicki 1982).

As can be seen from Figure 2.18. (a) that, under point loading, as radius to thickness ratio increased maximum load increased. Again, under point loading, the one with lower radius to thickness ratio shows lower deformation under same load

parameter. In Figure 2.18. (b) effect of boss width on deformation can be seen. As boss width increases load parameter increases.

A tentative analysis was employed to predict dynamic collapse behavior of spherical shells with a simplified approach (Kinkead et al. 1994). In the investigation, strain rate effects were included but relatively low velocity was chosen in order to exclude inertial effects. Their analysis was basically assumed two modes of deformation, i.e.; local flattening and inward dimpling. They showed that even a simple power law strain hardening was enough to predict deformation of thick shells, a different strain hardening model must be employed for thin shell sections.

Buckling of imperfect hemispheres subjected to external pressure was investigated experimentally and numerically (Błachut and Galletly 1995). Because of the spinning process used in the manufacturing, thickness of the structures varied between 0.37 and 2.5 mm along the meridional direction. Axisymmetric finite element models were used in the numerical part of the study. Although dimensional imperfection was accounted for in the investigation, because material imperfection was not incorporated, the results of numerical study were not in agreement with experimental results. Dependence of results on material imperfections obtained from numerical studies were also emphasized in a more recent investigation on spherical structures (Thacker, McKeighan, and Pepin 2005). Results revealed that manufacturing process must be taken into account in material model calibration to have a valid numerical analysis.

In an analytical investigation (Wen 1997), deformation behavior of a spherical shell subjected to the impact by a blunt-ended projectile was simplified considering experimental observations to the problem of impact to an equivalent circular plate. Good agreement was reached comparing permanent transverse deflections and dimpling radius computed with the proposed theory and observed in the experiments of shells of different material. The same theory was extended in order to account for perforation of the shells subjected to high velocity loading in a subsequent study (Wen 1998). Ballistic limit of the structure was underestimated by the proposed theory.

Static axial compression of metallic spherical shells between rigid plates was investigated by using the concepts of stationary and rolling plastic hinges analytically and results were validated by experiments (Gupta, Easwara Prasad, and Gupta 1999). A wide range of R/t ratio was chosen in the experimental part of the study. Energy absorbed by the structure was assumed to be dissipated by rolling plastic hinges,

stationary hinges, and meridional strain. Analytical force-deformation history then was calculated by using rolling plastic hinge radius from experimental measurements.

Dynamic axial compression of thin walled aluminum spherical shells were studied by using a gravity drop hammer setup and FORGE2 finite element code (Gupta and Venkatesh 2004). Impact mean collapse load and the radius of rolling plastic hinge values were found to be higher than static values. By using numerical computations, it was found that hydrostatic pressure, nodal velocities, equivalent strain rate etc. to be higher than quasi-static values.

An experimental study conducted on both spherical domes and conical frusta revealed their static and dynamic collapse behavior (Prasad and Gupta 2005). Variation of thickness was indicated as a result of spinning process used in the manufacturing of specimens. Results showed that, a substantial mode change was observed when loading rate increased for spherical structures. It was proposed that specimens failed with concertina or diamond fold mechanism during the impact tests, the axisymmetric inward dimpling part of collapse did not occur, therefore the specimens could be compressed with larger stroke. The effect of geometrical parameter and loading rate on collapse behavior can be understood by investigating mean load during the crushing process. Therefore mean load vs. radius-to-thickness ratio was given in Figure 2.19. As seen from the figure, as radius-to-thickness ratio increased mean load was increased too. Besides dynamic mean load was higher than static mean load for all geometries tested which was also reasonable considering strain rate and inertial effects.

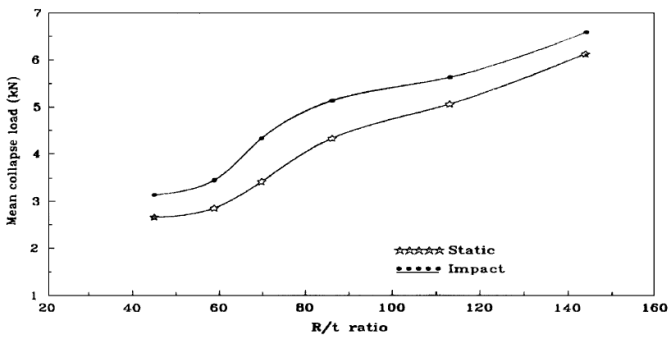

Figure 2.19. Comparison of mean collapse loads of spherical domes of different R/t values (Source : Prasad and Gupta 2005).

A coupled experimental and numerical study was conducted to reveal the collapse behavior of thin spherical shells under low velocity impact regime (Gupta,

Mohamed Sheriff, and Velmurugan 2007). The study included a wide range of radius-to-thickness ratio specimens, i.e. from 28 to 219. The numerical part of the study covered nonlinearities of material and geometry, and by the use of full models, large deformation response was also investigated. Results showed that as radius-to-thickness ratio increased, the range of elastic compression decreased. This is expected because slenderness of structure increased and buckling initiated more easily.

Buckling of thin spherical shells under axial loads were investigated experimentally, analytically, and numerically (Gupta, Mohamed Sheriff, and Velmurugan 2008b). Numerical results were validated with experimental results and plastic hinge radius history was used as input for analytical investigation. Unsymmetrical modes (as in large deformation of structures) of deformation were also accounted for and they divided deformation history into three different modes that can be distinguished in the load – deformation history as decreasing slopes; local flattening, axisymmetric inward dimpling, and unsymmetrical lobe formation (Figure 2.20.). It is obvious that, in combined shell geometries in addition to three deformation mode of spherical part, other modes of deformation of additional cylindrical part are going to be observed. They showed that as *R*/*t* value increases mean buckling load decreases as can be seen from Table 2.1.

(a)

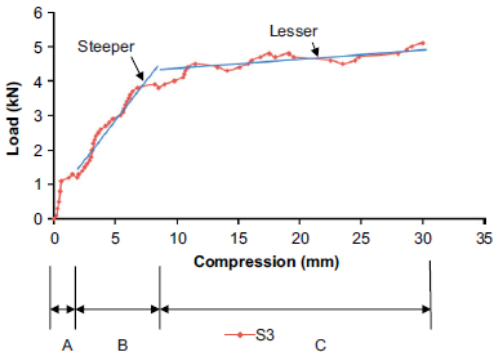

(b)

Figure 2.20. (a) Various modes of deformation; local flattening, inward dimpling, and unsymmetric lobe formation, and (b) effect of mode jump in load deformation behavior (Source : Gupta, Mohamed Sheriff, and Velmurugan 2008b).

Table 2.1. Effect of R/t ratio on mean collapse load
(Source : Gupta, Mohamed Sheriff, and Velmurugan 2008b).

Specimen	R/t	Mean collapse load (kN)			
		Experimental	Analytical	(Updike 1972)	(De Oliveira and Wierzbicki 1982)
H1	64.29	2.8	3.2	1.92	1.9
H2	50	3.2	3.4	2.8	2.78
H3	38.14	3.8	4.2	4.64	4.65
H4	28.13	5.4	6.2	6.76	6.83
H5	156.92	2.6	3.6	3.71	2.54
H6	114.6	2.8	3.4	3.79	3.22
H7	87.18	8.4	8.6	6.28	6.2
H8	218.57	4	5.6	3.04	2.95
H9	170	6	6.4	4.43	4.32
H10	129.66	10.2	12.4	7.33	7.2
S1	145.71	2.8	3.4	2.1	2.07
S2	114.61	3.6	4.8	3.07	3.04
S3	86.44	3.8	5.8	5.08	5.07
S4	218.57	3.8	5.2	2.5	2.45
S5	173.86	4.2	6.4	3.65	3.59
S6	129.16	4.8	7.2	6.05	5.99

In another coupled study, FORGE2D was used to investigate parameters that were not readily available from experiments such as effect of friction of loading plates (Gupta and Gupta 2009). By having radius-to-thickness ratio between 26 and 45, the investigation was limited in the axisymmetric range, therefore in the numerical calculations axisymmetric models were used. It was shown that friction between the top plate and specimen contact did not affect the crushing mechanism, on the other hand friction between bottom plate and specimen contact affected the behavior. It was proposed that as friction increased, energy absorbing capacity also increased. It was also

shown that contribution of elastic deformations on the crushing behavior was insignificant by comparing rigid-viscoplastic and elastic-viscoplastic material models.

Buckling of steel semi-spheres was investigated under various tip loading conditions experimentally and numerically (Shariati and Allahbakhsh 2010). It was shown that; mean collapse load changes with the change of loading tip geometry. By using a rigid plate with a hole in experiment, maximum mean collapse load was obtained and with a spherical sectioned rigid bar minimum mean collapse load was observed.

Parametric numerical studies were conducted also to investigate effects of geometrical and loading parameters on static and dynamic energy absorption behavior of semi-spherical shells (Dadrasi 2011). It was reported that, as wall thickness of structure was increased, number of lobes formed at large deformation was increased. Semi-spherical height did not affected the crushing results significantly. No significant mode change was observed when loading rate was increased for the geometry tested.

Experimental and numerical studies on static deformation behavior of simple and multicell quasi-hemispherical sections were also conducted (Parsapour 2014). It was proposed that as number of cells was increased specific energy absorption increased. It was shown that for the structure investigated crushing force efficiency values were identical and independent from geometrical dimensions.

Stability of elastoplastic spherical shells were also investigated under different boundary conditions and with the inclusion of a central hole (Bazhenov et al. 2014). According to the calculations for the problem, buckling occurs when the stress intensity reaches the yield point. Effects of lateral loading and external pressure were also investigated. In another study, effects of carving a square cutout on the axial deformation behavior of a semispherical shell were investigated (Torabi and Shariati 2014). It was shown that while side length of cutout was constant, as height of the cutout increased mean collapse load decreased negligibly. On the other hand as side length was increased the mean collapse load decreased extremely.

Deformation behavior of spherical thin-walled structures made of composite materials were also investigated in the literature (Gupta and Easwara Prasad 1999). It was shown that main collapse mode of composite hemispheres was due to initiation of crack along circumferential and meridional directions. A steadily increasing load-deformation curve was observed. Some of the specimens having relatively lower thickness showed catastrophic failure due to single meridional fracture, and their energy

absorption capacity was lower. Spherical feature included composite plates were also offered in energy absorption applications (Deb et al. 2012). Results showed that specific absorbed energy of a single hemisphere with a narrow square flange was higher than that of a geometrically identical steel structure. On the other hand, it was stated that the use of aluminum as a base material was more cost effective and energy absorption capability was higher.

It was also shown in the literature that type of reinforcement, stacking sequence, and total thicknesses were effective on deformation behavior of composite hemispherical structures (Cui, Moltschaniwskyj, and Bhattacharyya 2004). Due to orthotropy of materials, deformation pattern was different for different materials. For instance round dimples were formed for all knitted composites; on the other hand, four lobes were formed for woven composites as shown in Figure 2.21. Effect of matrix material on collapse behavior of composite materials was also investigated (Saleh et al. 2004). Energy dissipation mechanisms were explained by different failure progression stages through the course of deformation.

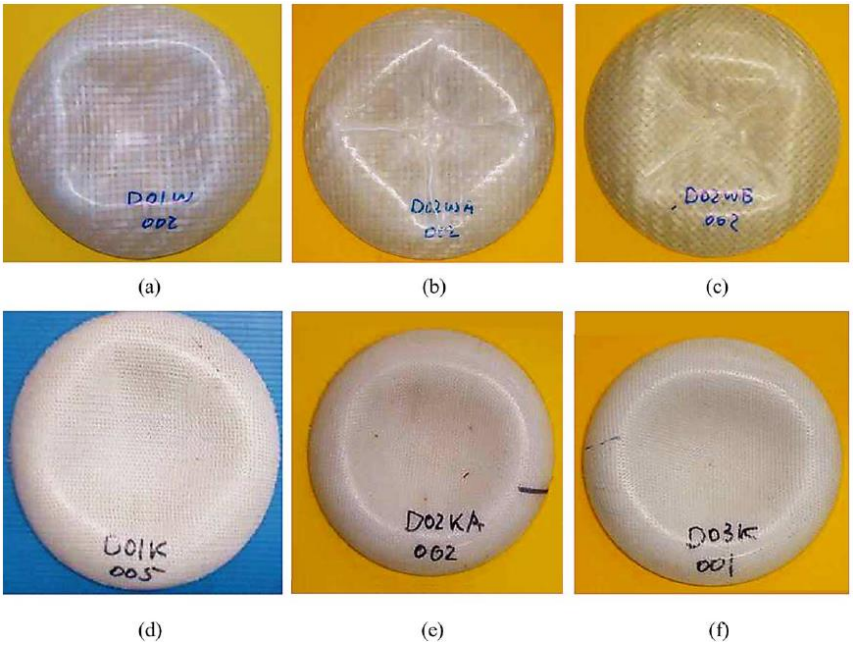

Figure 2.21. Deformed shapes (a) woven single-ply, (b) woven double-ply 0/0, (c) woven double-ply 0/45, (d) knitted single-ply, (e) knitted double-ply 0/0, and (f) knitted triple-ply 0/0/0. (Source : Cui, Moltschaniwskyj, and Bhattacharyya 2004).

Because of wide variety of use areas of spherical sections, their crushing behavior was also investigated under fluid-filled condition also ((Taber 1983), (Yang et

al. 2013)). Results showed that, under fluid-filled condition, applied localized load spread around the section and a uniform loading was achieved. A higher buckling load was observed for fluid-filled structure than empty structure.

Ping pong balls were selected in order to study plastic crushing behavior of thin-walled spheres and sphere arrays (Ruan, Gao, and Yu 2006). Quasi-static experiments were conducted on single spheres, 1-D, and 2-D sphere arrays by using various loading tips such as; point load, rigid ball, rigid plate, rigid cap etc. The effects of connections between balls were also investigated, and it was shown that the deformation will be localized in a ball until the force increases to a certain value. After that the next ball start to deform and this can be seen as local maxima in load deformation curve (Figure 2.22.)

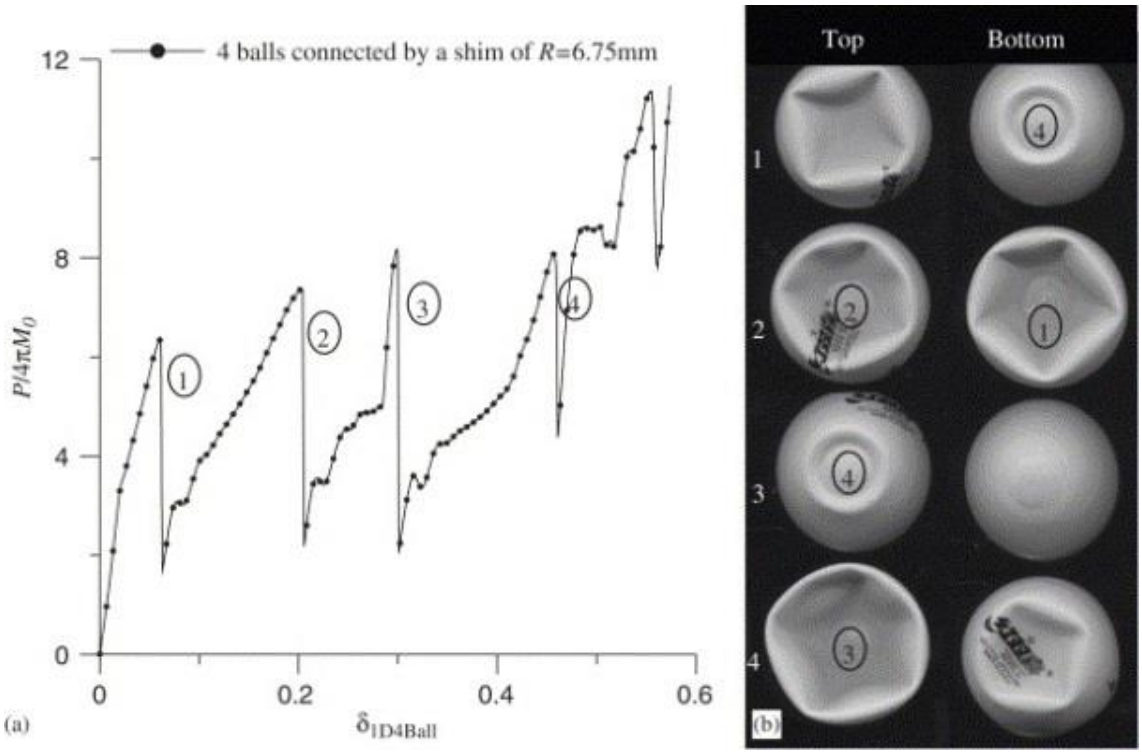

Figure 2.22. Compression of four connected balls in a 1-D array; (a) the normalized load-deformation curve; (b) the final deformation profile in each ball's top and bottom parts (Source : Ruan, Gao, and Yu 2006).

A modified Split Hopkinson Pressure Bar (SHPB) (Figure 2.23. (a)) was employed in order to investigate strain rate and inertia effects on thin walled spheres (Dong, Gao, and Yu 2008). It was shown that the buckling dimpling is sensitive to the loading rate and the dynamic force was significantly lower than quasi-static one after a small elastic deformation as can be seen in Figure 2.23. (b).

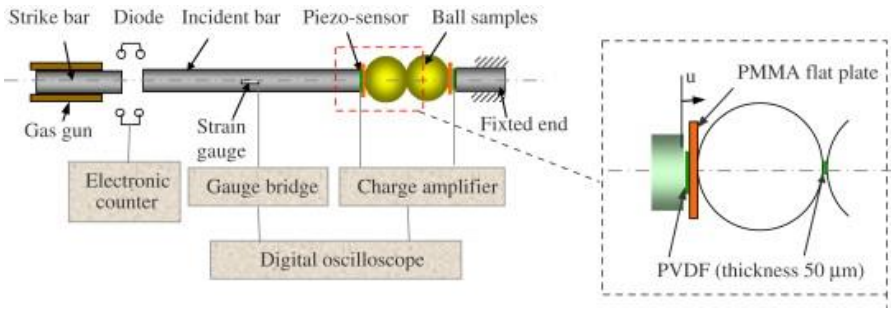

(a)

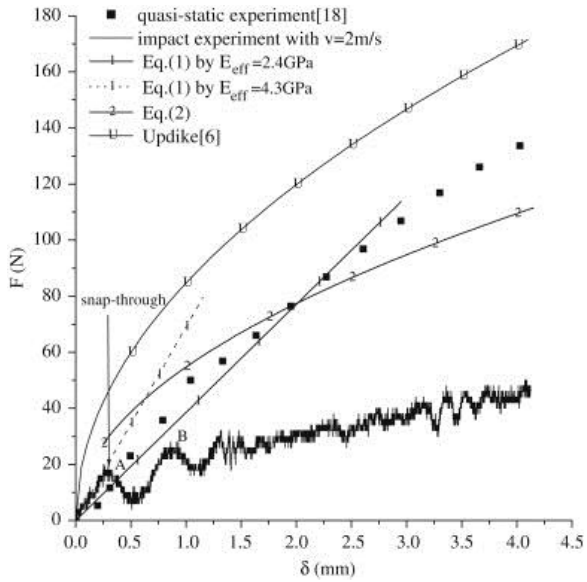

(b)

Figure 2.23. (a) Sketch of dynamic test system, and (b) force-deflection curves for a single ball (Source : Dong, Gao, and Yu 2008).

As an application, hemispherical sections can be used in combination with other structures as in the application of mine rescue chamber (Song, Ge, and Fang 2011). In the investigation, problem was reduced to the dynamic axial compression of a hemispherical structure. It was proposed that the dynamic response of hemispherical rescue chamber was mainly dependent on thickness of the structure.

As one of the constituents of the combined geometry proposed herein, circular tubes also deserve to be mentioned in order to complete the related literature. When a cylindrical tube was subjected to the loading along its longitudinal axis, depending on the geometry and material of the tube, axisymmetric (or concertina), asymmetric (or diamond), and mixed deformation modes may be observed (Lu and Yu 2003), also global (Euler type) buckling may be observed for long, slender tubes. In high velocity and high energy impact events, additional modes of deformation such as mushrooming and thickening can be observed in circular thin-walled tubes (Wang and Lu 2002).

Collapse modes of circular tubes subjected to static or low velocity crushing can be seen in Figure 2.24.

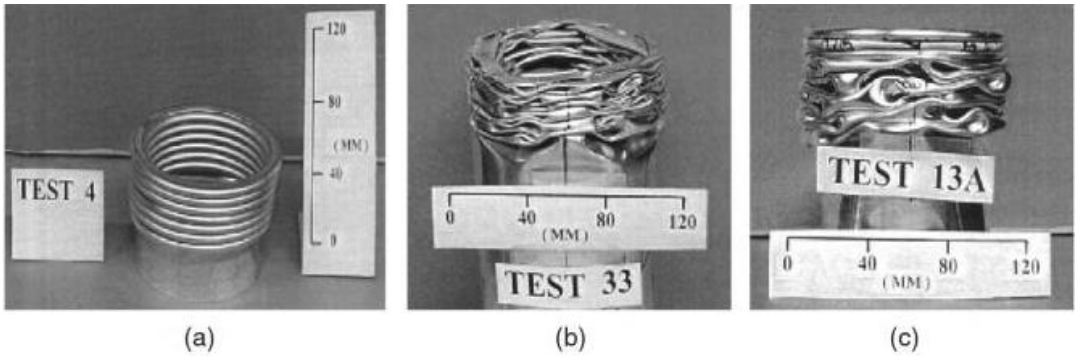

Figure 2.24. Collapse modes of circular tubes under axial loading; (a) symmetric mode; (b) diamond mode, and (c) mixed mode (Source : Lu and Yu 2003).

Based on experimental data for circular tubes of specific material, generally mode classification charts were established to distinguish geometrical limits of different modes of deformation. An example of such a mode classification chart can be seen in Figure 2.25 for an annealed aluminum tube.

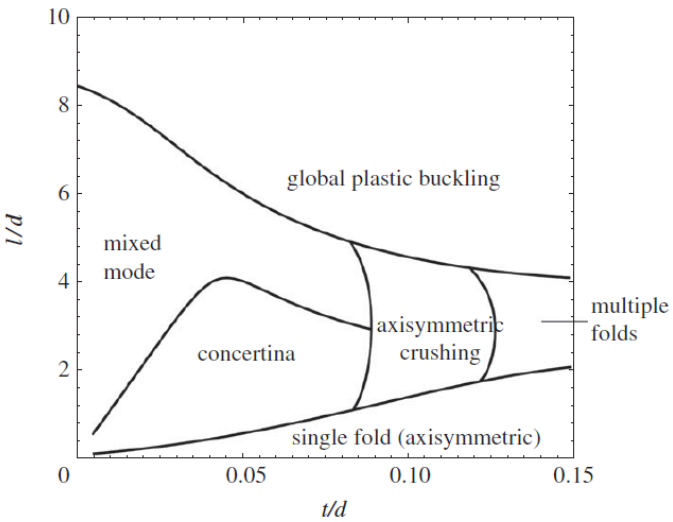

Figure 2.25. A mode classification chart for annealed aluminum tube (Source : Pingle et al. 2011).

In the figure *l* is length, *d* is diameter and *t* is the thickness of the tube. As can be seen from the figure, for low length-to-diameter ratios single fold axisymmetric crushing was guaranteed for all thickness-to-diameter ratios (Abramowicz and Jones 1984). Obviously as in the figure, longer tubes are more prone to global plastic buckling mode. As reported in the literature, the mean collapse load, initial peak load and size of

folds of circular tubes decreased and eccentricity increased with increase in the diameter to thickness ratio (*D*/*t* ratio) for tubes of identical diameter and different thicknesses, and increased with increased in the diameter to thickness ratio (*D*/*t* ratio) for tubes of same thickness and different diameters. The crushing force efficiency increased with the increase in *D*/*t* ratio (Gupta and Venkatesh 2006). A typical example of force-deformation behavior of a circular tube is given in Figure 2.26. As can be seen in the figure, immediately after the crushing initiates, a high peak load was observed representing the formation of the first fold. As deformation continues, fluctuations around a constant average load were observed and all peaks represent the formation of successive folds. At the end of the compression a densification point was followed by load increase due to increase in contact area. Although the deformation started with an axisymmetric fold, deformation proceeded with diamond mode due to the influence of axisymmetric trigger on the first fold (Guden et al. 2007).

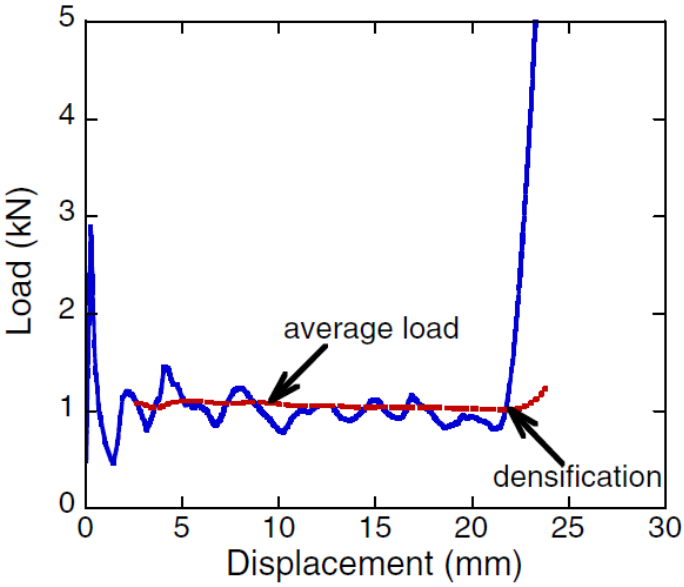

Figure 2.26. Load-displacement curve of an aluminum tube
(Source : Guden et al. 2007).

In one of the earliest investigations on circular tubes, an analytical model was proposed for predicting the average axisymmetric crushing loads of thin walled tubes (Alexander 1960). In the investigation, a simple formula was proposed to relate mean crushing load with geometrical and material parameters. The formula is as follows;

$$P = Ct^{1.5}\sqrt{D} \tag{2.2}$$

where P is the collapse load, t is the thickness, D is the diameter, and C is the material property of the tube. The simple formula was derived by the assumptions of rigid perfectly plastic material and the fold goes completely outwards. Concertina mode deformation behavior of circular tubes was successfully captured with such a simple model. A modification later was proposed in the literature including a correction for the effective crush length (Abramowicz and Jones 1984). In the investigation, theoretical analyses were also accounted for asymmetric modes also. Their results showed better agreement with experimental results in both static and dynamic regime including strain rate sensitive material behavior because the study includes eccentricity in lobe formation. It was suggested that eccentricity of crushing was dependent on diameter-to-thickness ratio of tubes (Gupta and Velmurugan 1997). Later, eccentricity factor as a function of tube geometry and number of lobes formed were also proposed in the literature (Singace 1999).

It was suggested that as diameter-to-thickness ratio increased, ratio of maximum force to mean collapse load increased (Guillow, Lu, and Grzebieta 2001). It was shown in the study that dimensionless average collapse load was proportional to $(D/t)^{0.32}$. The dimensionless relation proposed was suggested to be applicable to both axisymmetric and asymmetric modes of deformation.

An energy absorption effectiveness factor was introduced in the literature in order to be able to compare the performance of tubes of different materials (Hsu and Jones 2004). Their comparison between stainless steel, mild steel, and aluminum alloy tubes shown that, the highest amount of energy was absorbed by stainless steel tubes but their energy absorption effectiveness factor was the lowest. Considering their effectiveness factor, the most efficient tube was made of aluminum alloy. It was also shown that, transition from progressive buckling to global catastrophic buckling was independent from the material and mainly dependent on geometrical dimensions of tubes.

The effects of boundary conditions on deformation behavior of circular tubes were also investigated in the literature ((Singace and El-Sobky 2001), (Tasdemirci 2008)). In the experimental investigation (Singace and El-Sobky 2001), it was shown that partially constrained tubes collapse in either pure concertina or pure diamond mode depending on their geometry. On the other hand, both end constraining resulted in mixed mode of deformation. In the coupled experimental and numerical investigation

on the effect of end constraining on the axial crushing of aluminum tubes (Tasdemirci 2008), it was seen that single-end constraint has no effect on load-deformation behavior, on the other hand, double-end constraining of tube resulted in an increase in initial drop-load values. Results of the study can be seen in Figure 2.27.

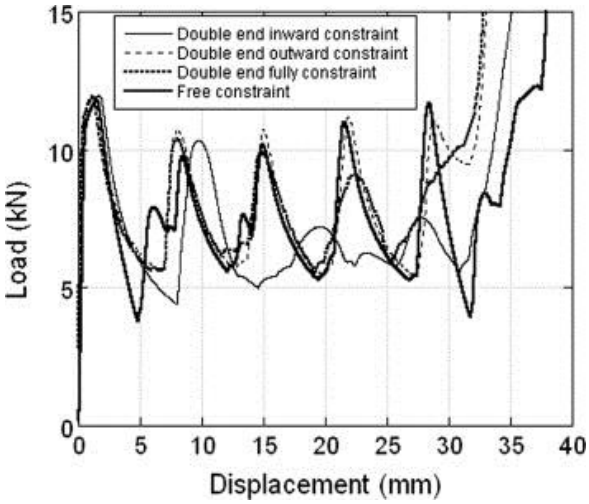

Figure 2.27. Experimental load–displacement curves of double-end constraint tubes (Source : Tasdemirci 2008).

One of the main challenges that researchers tried to overcome in circular tube crushing problems is to lower the initial peak load encountered during the formation of first fold while retaining high specific energy absorption capacity. There are a lot of methods proposed such as foam filling (Güden and Kavi 2006), triggering (Airoldi and Janszen 2005), preparation of cutouts (Song, Chen, and Lu 2013), manufacturing corrugated tubes (Eyvazian et al. 2014), use of buckling initiators (Zhang, Tian, and Yu 2009), and their combinations (Yan, Chouw, and Jayaraman 2014) etc.

Effects of foam filling on the deformation behavior of circular tubes were investigated in the literature ((Hanssen, Langseth, and Hopperstad 2000) ,(Güden and Kavi 2006), (Aktay et al. 2008), (Goel 2015), (Duarte et al. 2015)). Crushing behavior of hollow and aluminum foam filled cylindrical tubes was investigated experimentally (Güden and Kavi 2006). They successfully showed that aluminum foam filling changes the deformation mode from diamond to concertina and as a result increases energy absorption of tubes. Load-displacement curves of empty and different relative density Al foam filled tubes can be seen in Figure 2.28. In situ foam-filled tubes were also offered in order to simplify the manufacturing process (Duarte et al. 2015). Numerical methods were also employed in order to investigate crushing behavior of foam-filled

tubes (Aktay et al. 2008). Honeycomb were also offered as filler for tubes ((Çakıroğlu 2008), (Yin et al. 2011), (Zarei and Kröger 2008)) and it was shown that energy absorption capacity was increased when honeycomb filler was used.

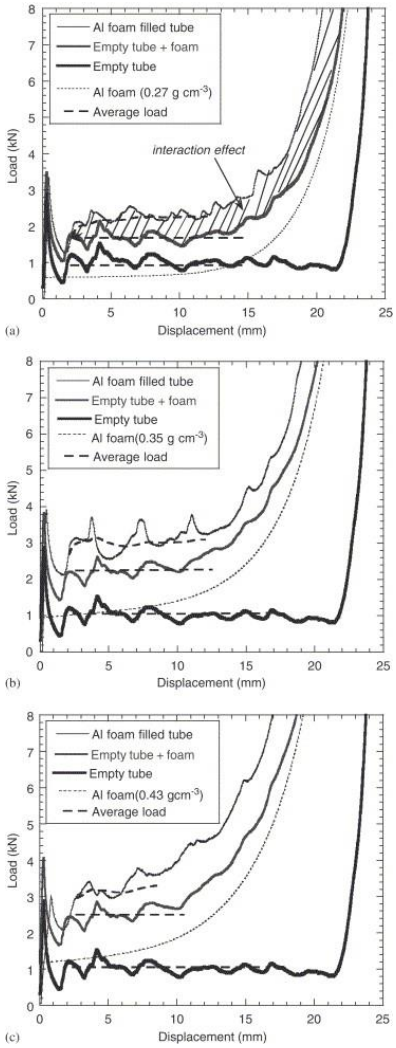

Figure 2.28. Load and average crushing load–displacement curves of foam-filled single Al tube, empty tube, empty tube+foam and foam: (a) 0.27, (b) 0.35 and (c) 0.43 g/cm^3 Al foam-filled tube (Source : Güden and Kavi 2006).

Results of an optimization study showed that, when triggering method was used, maximum force level during a crash event was decreased which was related to occupant injury when tubes were used as crash absorber component (Marzbanrad, Abdollahpoor, and Mashadi 2009).

In a recent study, a rigid steel ring was press-fitted inside of a cylindrical aluminum tube in order to shape the crushing behavior of the structure (Salehghaffari et al. 2010). It was shown that method proposed prevented the occurrence of global

buckling even for long tubes. Besides a moderate increasing and decreasing of load after formation of each plastic fold was observed in the plastic fold formation stage.

Determination of deformation behavior of composite circular tubes were also investigated and in one of the earliest examples of such an investigation a wide variety tubes of composite materials were presented (Thornton 1979). Most of the composite specimens tested disintegrated into small fragments. It was shown that orientation of composite was effective on the deformation mode; a Kevlar tube of $0^o/90^o$ orientation was collapsed by fracture, on the other hand same material with $45^o/45^o$ orientation collapsed by buckling. The effects of crushing speed on energy absorption capability of composite tubes were also investigated in the literature (Farley 1991). In the study, crushing modes of composites were listed as; transverse shearing, brittle fracturing, lamina bending, and local buckling. It was suggested that, enhancement of energy absorption capability was mainly related to the crushing mode which was controlled by ply orientation and strain rate sensitivity of the materials. Effect of crushing speed and ply orientation on specific sustained crushing stress of Kevlar/Epoxy tubes can be seen in Figure 2.29. Coupled experimental and numerical studies were also conducted in order to simulate progressive crushing behavior of composite tubes (Huang and Wang 2009). It was shown that the chamfer successfully controlled the progressive crushing and suggested bevel trigger model was appropriately simulated experiments.

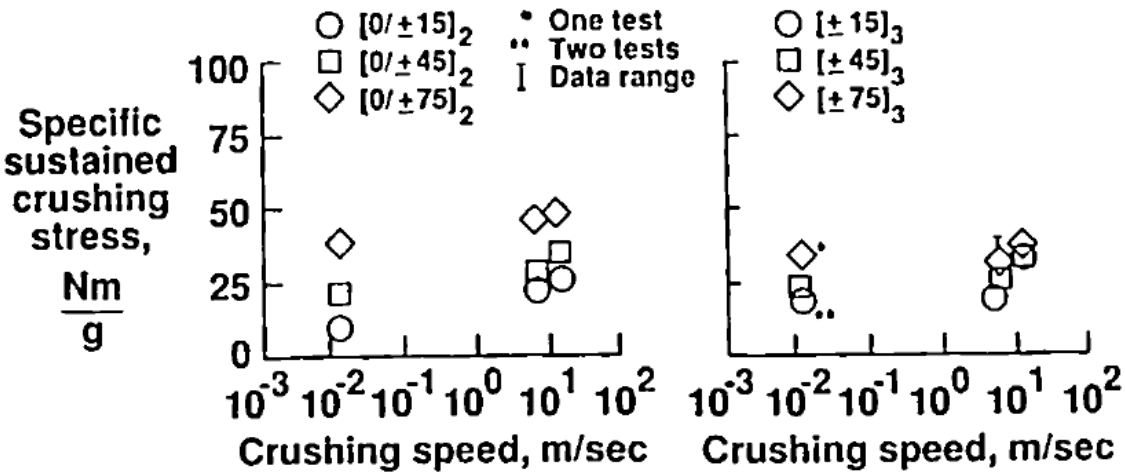

Figure 2.29. Effect crushing speed on Kevlar/Epoxy tubes. (Source : Farley 1991).

Effects of radial corrugations on axial and lateral deformation behavior of composite tubes were investigated (Abdewi et al. 2008). It was observed that, radial

corrugation significantly changed deformation mode and improved energy absorption capacity in the axial crushing. On the other hand, no effect was observed in the lateral crushing.

Multicell cylindrical columns were also offered in energy absorption applications ((Tang, Liu, and Zhang 2013), (Zhang and Zhang 2014), (Goel 2015)). It was suggested that the wall thickness, the number of cells along the circumferential and radial directions have different effects on energy absorption. Even better energy absorption provided by cylindrical multicells than square tubes and their multicells (Tang, Liu, and Zhang 2013). In terms of specific energy absorption, up to %30 increase was achieved with multicell structures (Zhang and Zhang 2014). It was also suggested in the literature that foam filled single tubes absorbed lower energy in dynamic loading, on the other hand bi-tubular and tri-tubular structure showed increase in energy absorption (Goel 2015).

Arrangements of circular tubes were offered to use energy absorbing structure in ship hulls (Jurisich and Achtarides 1996). The invention proposed arrangement of cylindrical tubes between an inner hull and outer hull functioning as structural integration elements and energy absorption elements in crash events. The proposed invention then operated as a sandwich structure preventing damage of occupants and valuable cargo. In order to increase energy absorption efficiency of the sandwich, flutes were also used around some tubes as radial corrugations.

Investigation of oblique crushing behavior of empty, foam-filled single or bi-tubular structures was also carried out (Li, Yu, and Guo 2012). Some new deformation modes were also identified for oblique loading case such as; spiral folding mode, irregular extensional folding mode and irregular axisymmetric or diamond deformation mode. Within the investigated range of obliquity angles studied, the energy absorption capacity increased as the load angle increased.

With the completion and detailed coverage of relevant literature on constituents of proposed geometry, next paragraphs were devoted to similar suggestions containing combinations of different geometries. Combined geometry structures are mainly contains two or more different geometrical identities. Constituents of combined geometry may be manufactured, seamlessly by an appropriate method, by adhesive bonding, and by using appropriate geometrical adaptor. A combined geometry has its advantage by combining the deformation behavior of its constituents and behaves differently from each of its constituents. Comparing with previously reported literature

on energy absorbing structures, research on combined geometries is limited to a few, and almost all accessible studies were summarized in next paragraphs.

Combined geometry shells are widely used in many engineering applications because of their superior energy absorption properties which are mixture of properties of their individual components as mentioned. Some examples include; nose cone of aircrafts, projectiles, fuel and gas tanks, pressure hulls, etc. Combined geometry shells can offer protection of internal structures from external dangers by deforming and a safe storage for pressurized material inside. Determination of crushing patterns and load response of combined shells in various deformation and loading rates with various loading and boundary conditions is very important in order to guarantee energy absorption without damaging protected structures inside.

(a)

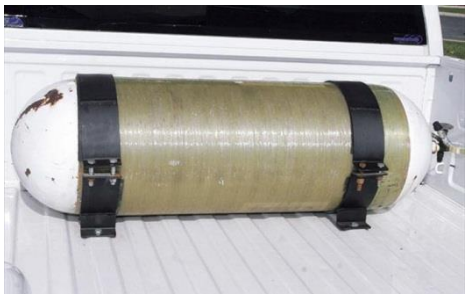

(b)

(c)

(d)

Figure 2.30. (a) Deformed nose cone of aircraft, (b) gas tank with combined hemispheres and cylinder, (c) various caliber bullets, and (d) Cirit laser-guided 70 mm rocket system.

In Figure 2.30 deformed nose of an aircraft, a natural gas tank, various caliber bullets, and Roketsan Cirit laser-guided 70 mm rocket system can be seen. Their geometries contain combinations of hemispheres, conical frusta, and cylinders. As can be seen, nose of the aircraft was deformed probably after a bird impact, absorbed energy, and the plane landed safely.

Analysis of collapse behavior of combined geometry shells under impact loading was conducted (Gupta, Mohamed Sheriff, and Velmurugan 2008a). They compared the experimental results with numerically calculated results using LS-DYNA. Their geometries comprises a spherical part with *R*/*t* values ranging between 27 and 218 attached to a conical frusta having mean diameter-to-thickness ratio between 79 and 190. They showed that, in addition to aforementioned modes of deformation of hemispherical part, deformation progresses with collapse of conical portion. Addition of hemispherical part changed the boundary conditions for conical frusta and thus, collapse pattern was different from simple frusta. In Figure 2.31., effect of thickness and cone angle can be seen.

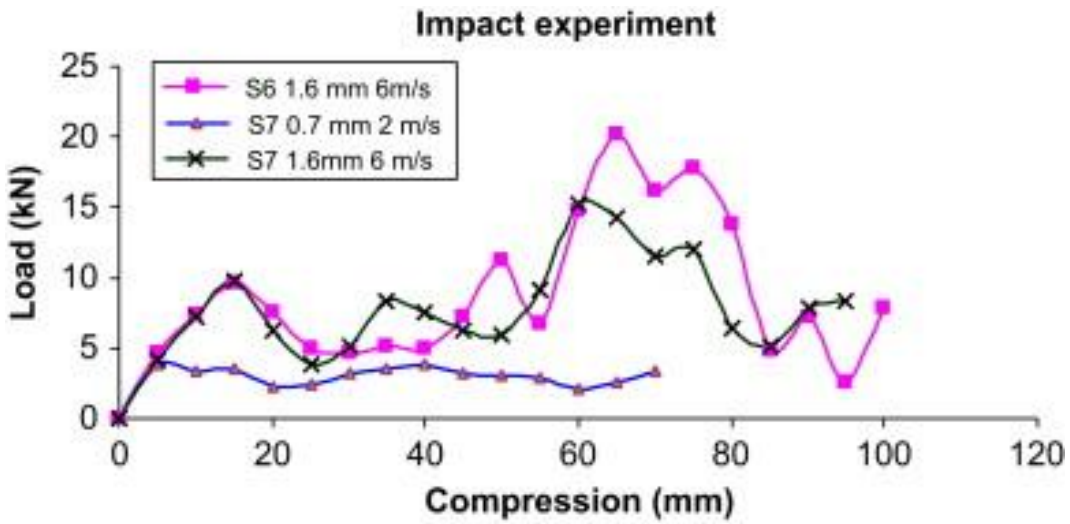

Figure 2.31. Typical load–compression curves in impact experiments for specimens S6 (α=21°, bottom diameter=165 mm) and S7 (α=23°, bottom diameter=165 mm) (Source : Gupta, Mohamed Sheriff, and Velmurugan 2008a).

Two studies reported the collapse of the metallic shells having combined tube-frusta geometry subjected to axial compression between two parallel plates ((Gupta 2011), (Gupta and Gupta 2013)). In studies, axisymmetric computational models were prepared. The mode of collapse was formed by the development of one concertina fold which was followed by a plastic zone. It was shown that the mode of collapse of combined geometry specimens governed by the semi-apical angle of the truncated cone portion. It was reported that for semi-apical angles between 20° and 23°, relatively constant collapse load was obtained (Gupta and Gupta 2013). Experimental and numerical results of deformation can be seen in Figure 2.32.

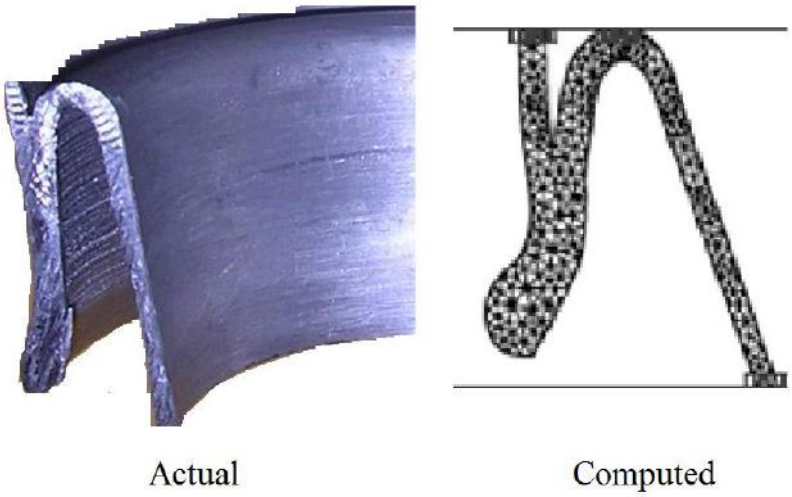

Figure 2.32. Comparison of experimental and numerical results
(Source : (Gupta 2011)).

Ghamarian and Abadi (Ghamarian and Tahaye Abadi 2011) and Ghamarian et al. (Ghamarian, Zarei, and Abadi 2011) investigated the energy absorption characteristics of empty and foam-filled circular and conical end-capped tubes and showed that the absorbed energy increased with increasing impact velocity. It was reported that, by using end-capped cylindrical structures, first peak of force-displacement curve of structures can be controlled and better results can be achieved. Fillet of end-cap region was also effective on the deformation behavior (Ghamarian and Tahaye Abadi 2011). In the literature an enhancement due to foam-filling was also reported resulted from interaction effects (Ghamarian, Zarei, and Abadi 2011). Ghamarian et al. (Ghamarian et al. 2013) in which shallow spheres were used as end-cap in conical tubes. The crush force efficiency and absorbed energy was reported to increase with increasing shallow spherical cap radius. As semi-apical angle decreased, absorbed energy slightly decreased. The number of literature on end-capped structures can be increased; on the other hand, aforementioned ones were enough to relate them with the proposed geometry.

Shojaeefard et al. (Shojaeefard et al. 2014) studied the quasi-static crushing behavior of combined cylindrical and square section tubes and showed that the absorbed energy of the combined tubes was slightly higher than both square and circular tubes of the same length. The combination geometry exhibited a progressively combined behavior i.e.; one force-displacement behavior attached afterwards force-displacement behavior of other portion, somewhat distinctly.

A composite combined energy absorber to use in Formula One racing cars against side impact was proposed having a spherical portion combined with a conical portion (Bisagni et al. 2005). The conical structure was important as it functioned as a major stabilizer during the progressive crushing, while the circular section helped to distribute the stresses uniformly to avoid longitudinal failure. Effect of stiffeners on deformation behavior of composite conical-spherical structures was also investigated in a recent study (Vasanthanathan et al.). It was shown that stiffener use resulted in higher energy absorption along with an increase in collapse load of the composite structure. Besides, composite stiffeners provided superior buckling resistance than aluminum stiffeners.

2.3. Blast Loading on Sandwich Structures

A vast literature has been published on blast resistant structures so far in terms of different aspects. In this section a summary of literature on related work is given. Various test and simulation methods have been used by researchers in this area. Blast resistance characteristics of various materials such as, metals, sandwiches, composites, and polymers have been determined via these test and simulation methods. Analytical methods were also utilized by researchers.

In the literature, researchers used following experimental methods to investigate performance of blast protection structures; real scale explosions (Dharmasena et al. 2008), ballistic pendulum (Nurick et al. 2009), shock tube (Tekalur, Shukla, and Shivakumar 2008), metal foam projectile impact (Rathbun et al. 2006), and underwater explosion (Wadley et al. 2008) etc. In Figure 2.33. these experimental methods can be seen. While experiments, generally a high speed camera was used by researchers and they investigated deformation and damage progression of structures, as well ((Tekalur, Shukla, and Shivakumar 2008), (Zhu, Zhao, et al. 2009), (Zhu, Wang, et al. 2009), (Zhu et al. 2008), (Wang, Gardner, and Shukla 2009), (Jackson and Shukla 2011), (Wang and Shukla 2012) etc.).

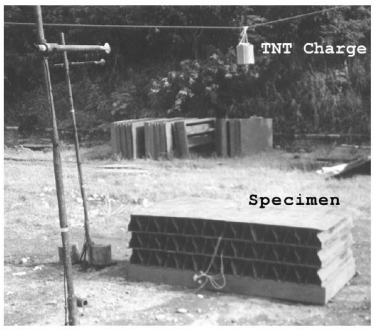

(a)

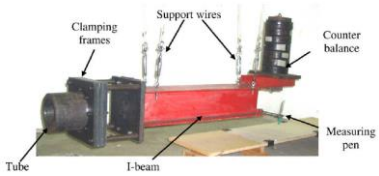

(b)

(c)

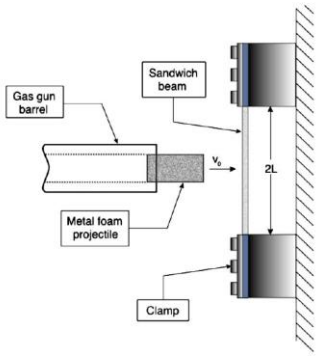

(d)

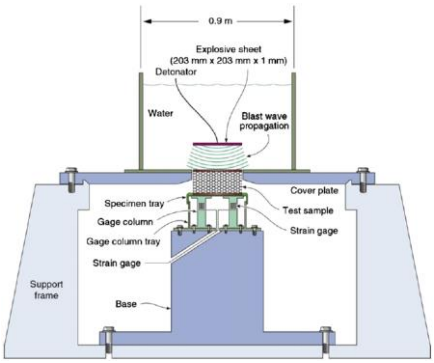

(e)

Figure 2.33. Experimental set-ups that are used in the blast effect investigations, (a) real scale explosion experiments (Source : Dharmasena et al. 2008), (b) ballistic pendulum (Source : Nurick et al. 2009), (c) shock tube (Source : Tekalur, Shukla, and Shivakumar 2008), (d) foam projectile (Source : Rathbun et al. 2006), (e) underwater explosion tests (Source : Wadley et al. 2008).

In some of the studies, numerical simulations were also carried out. In order to model blast effect on structures, researchers used ConWep air blast function given in equation 2.3 ((Dharmasena et al. 2008), (Jackson and Shukla 2011), (Hanssen, Enstock, and Langseth 2002)), arbitrary lagrangian-eulerian (ALE) formulation ((Wadley et al. 2008), (Zhu, Zhao, et al. 2009), (Dharmasena et al. 2009)), or they simply modeled metallic foam impact problem ((Radford et al. 2006), (Rubino, Deshpande, and Fleck

2009)). Some of researchers only conducted modeling studies ((Lee and O'Toole 2004), (Sriram and Vaidya 2004), (Xue and Hutchinson 2004)).

$$P(\tau) = P_r * \cos^2\theta + P_i * (1 + \cos^2\theta - 2 * \cos\theta) \tag{2.3}$$

where, θ is the angle between incident wave and target, P_i is the incident wave; P_r is the reflected wave (Zhu 2007). Equivalent TNT mass and standoff distance are input parameters for ConWep air blast function in commercial hydrocodes such as LS-DYNA and ABAQUS.

Zhu et al. (Zhu, Zhao, et al. 2009) investigated response of cellular core structures under blast loading by experimentally and numerically by ALE. In the investigation, explosive was modeled with brick elements having ALE formulation. In order to deal with the difficulties of the traditional Lagrange method in large deformation problems and the Eulerian approach when working with multi material interaction or moving boundaries, the ALE approach uses meshes that are imbedded in material and deform with the material.

Nurick et al. (Nurick et al. 2009), compared performances of hexagonal honeycomb core and air-core (without a solid core) sandwich structures against high blast pressures. It was shown that honeycomb core sandwich structures were exposed to lower back face deflection for relatively higher impulses. Below 20 Ns, the back plate of the honeycomb sandwich structure deforms more for a given impulse than the air-core sandwich back plate due to load transfer through the honeycomb. Deformation profiles of sandwiches are given in Figure 2.34.

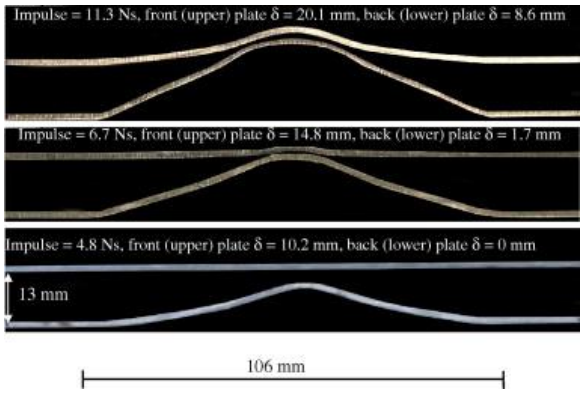

(a)

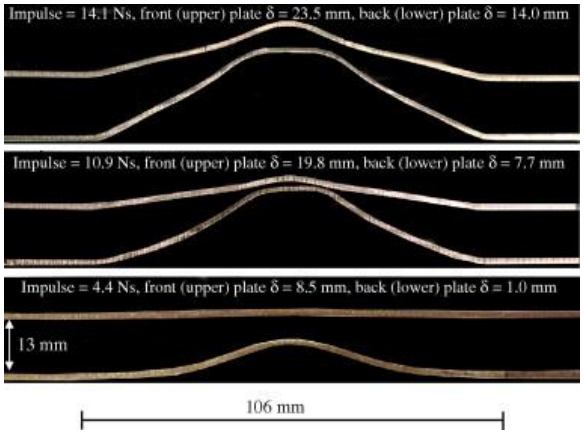

(b)

Figure 2.34. Deformation profiles of sandwich structures under localised loading , (a) air-core, (b) honeycomb core sandwich structures (Source : Nurick et al. 2009).

Rubino et al. (Rubino, Deshpande, and Fleck 2009), used metallic foam projectile testing technique in order to compare blast responses of Y-frame core, triangular corrugated core, and equivalent monolithic structures. It was determined that, against same blast pressure, triangular corrugated core sandwich structures showed superior properties. In Figure 2.35., experimental conditions and geometry of core structures used in the study can be seen. In Table 2.2. summary of the test results can be seen comparatively.

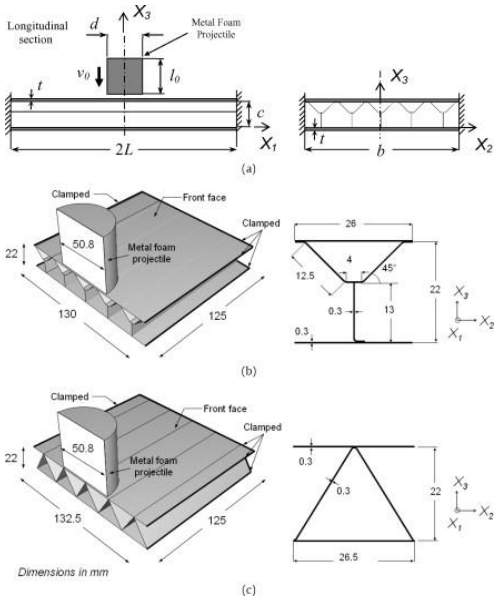

Figure 2.35. Experimental conditions and geometry of core structures used (Source : Rubino, Deshpande, and Fleck 2009).

Table 2.2. Summary of results of tests (Source : Rubino, Deshpande, and Fleck 2009).

Specimen	Projectile		Response
	Impulse (kN s m^{-2})	Initial Velocity (m s^{-1})	Back Face Deflection (mm)
Monolithic	1.6	94	10.5
	3	191	15
	5.1	299	23
	5.5	351	26
	6.2	392	28.8
	6.6	451	33
Y-frame	1.7	99	2
	3.1	198	6
	5.1	301	18
	5.4	351	X
Corrugated	1.7	99	2.5

Dharmasena et al. (Dharmasena et al. 2010), investigated underwater blast resistance of square and triangular honeycomb core sandwich structures compared to pyramidal and triangular corrugated core sandwich structures. It was observed that

among all structures, triangular corrugated and pyramidal core sandwich structures showed higher resistance to underwater blast loads.

In Figure 2.36., transmitted pressure of sandwich structures and photographs of tested sandwich panels can be seen. According to Figure 2.36. (a), the lowest transmitted peak pressures among sandwich structures was observed in triangular corrugated cores (~5 MPa) and the highest one was encountered in triangular honeycomb core sandwich structures (~30 MPa). As can be seen from Figure 2.36 (b), the highest deformation was observed in diamond corrugation and the lowest was in square honeycomb.

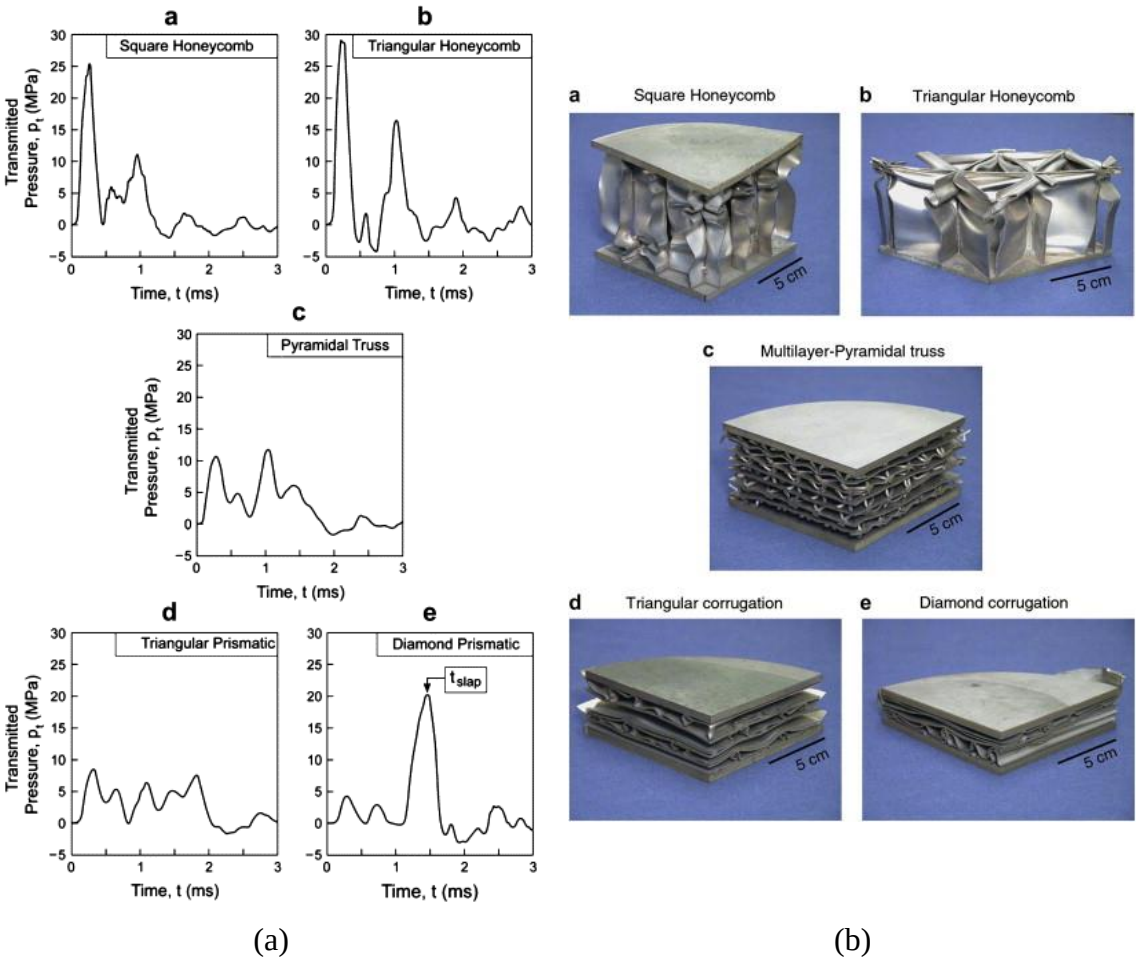

(a) (b)

Figure 2.36. (a) Transmitted pressure in sandwich structures, (b) photographs of dynamically tested sandwich panels (Source : Dharmasena et al. 2010).

Dharmasena et al. (Dharmasena et al. 2008), investigated blast performance of square honeycomb core sandwich structures comparing to equivalent monolithic structure. In experiment, 1-3 kg TNT was exploded in 10 cm distance. It was calculated from test results that, back face deflections of sandwich structures are ~63% lower than

that of monolithic plates for relatively small blast pressures, and difference is ~4% for higher pressures.

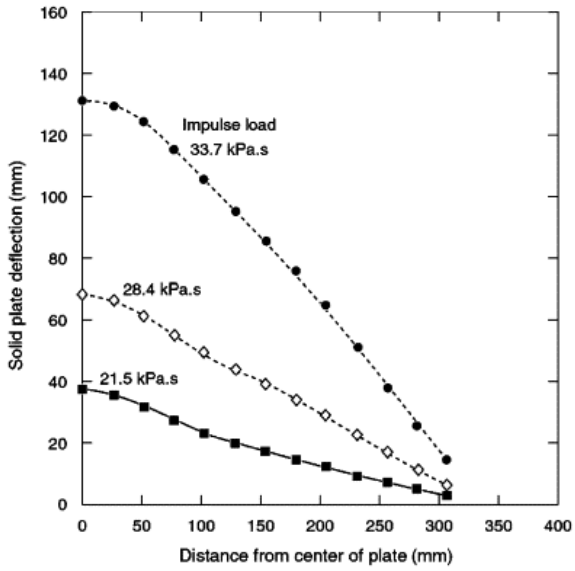

(a)

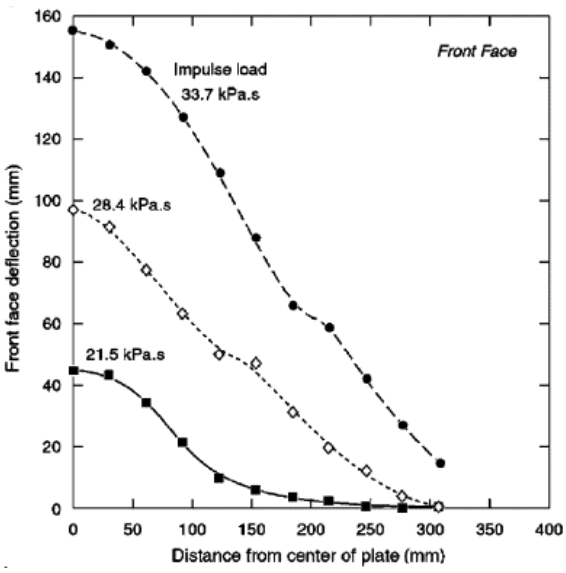

(b)

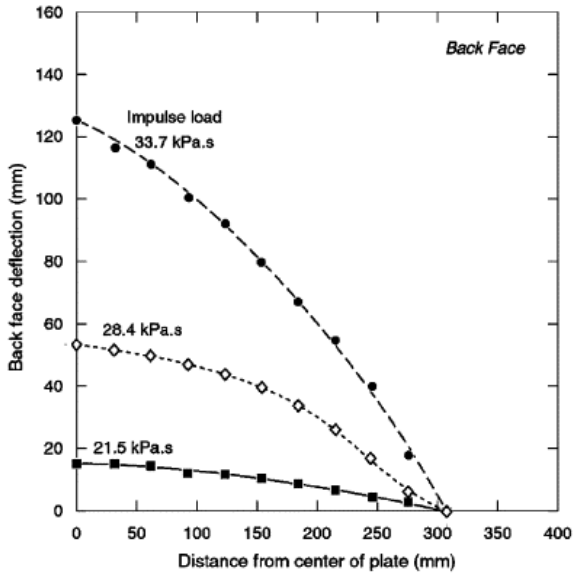

(c)

Figure 2.37. (a) Solid plate deflection, (b) front face deflection of sandwich plates, and (c) back face deflection of sandwich plates (Source : Dharmasena et al. 2008).

In Figure 2.37., deflection profiles of monolithic and sandwich plates can be seen for different impulse loads. In Figure 2.38. deformed sandwich structures can be seen, from top to bottom, impulsive load increases.

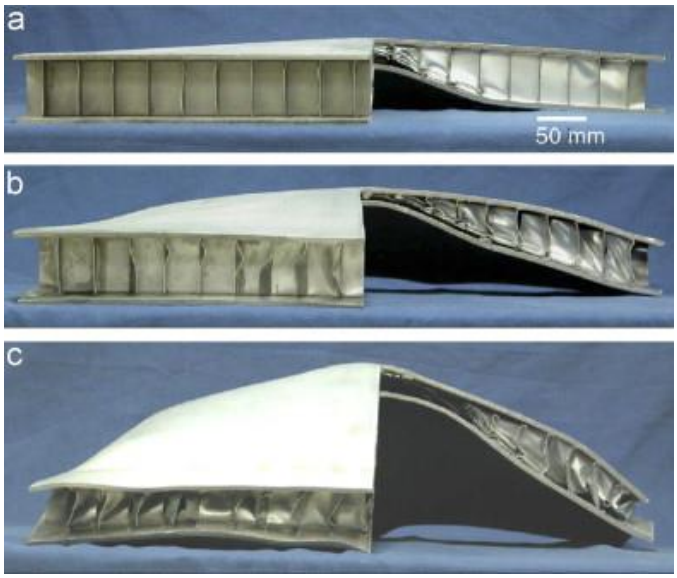

Figure 2.38. Deformed sandwich plates under impulsive loads; (a) 21.5 kPa.s, (b) 28.4 kPa.s, and (c) 33.7 kPa.s (Source : (Dharmasena et al. 2008)).

Tagarielli et al. (Tagarielli, Deshpande, and Fleck 2007), used metal foam projectile testing to compare behavior of polymeric foam and balsa wood foam sandwich structures with equivalent monolithic structures. It was shown that core thickness and mass of structures affect performance of them. It was observed that sandwich beams with the low strength H100 PVC foam core with higher core thickness can outperform sandwich beams with the high strength H250 PVC foam core. The balsa wood core outperforms the PVC cores at low impulses. In Figure 2.39. measured maximum mid-span deflection of three different alternative core sandwich structures can be seen. In the figure a power law fit to the experimental data was also included.

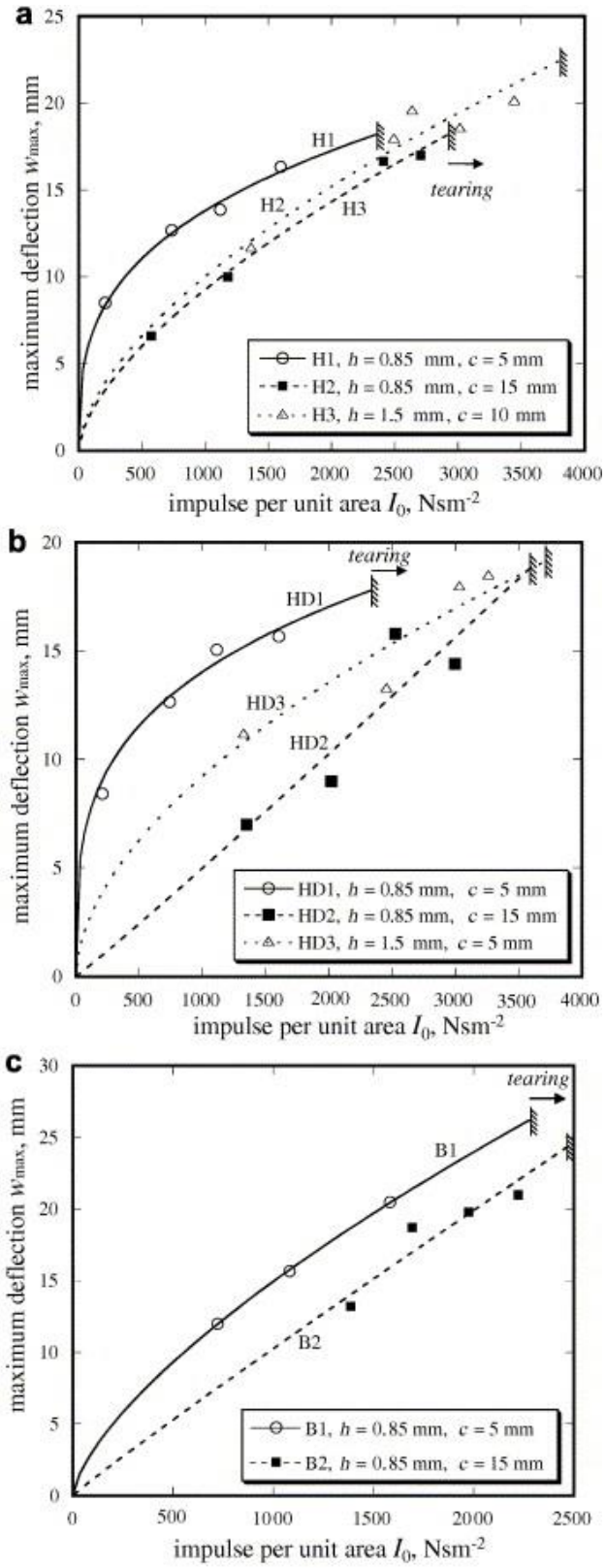

Figure 2.39. The measured maximum deflection at the mid-span of the (a) H100 PVC foam core, (b) H250 PVC foam core and (c) balsa wood core sandwich beams, as a function of the foam projectile momentum (Source : Tagarielli, Deshpande, and Fleck 2007).

In Figure 2.40., a comparison is given for the measured maximum mid-span deflections of the back face of sandwich and monolithic beams of equal mass. In both figures, results are given as a function of projectile momentum.

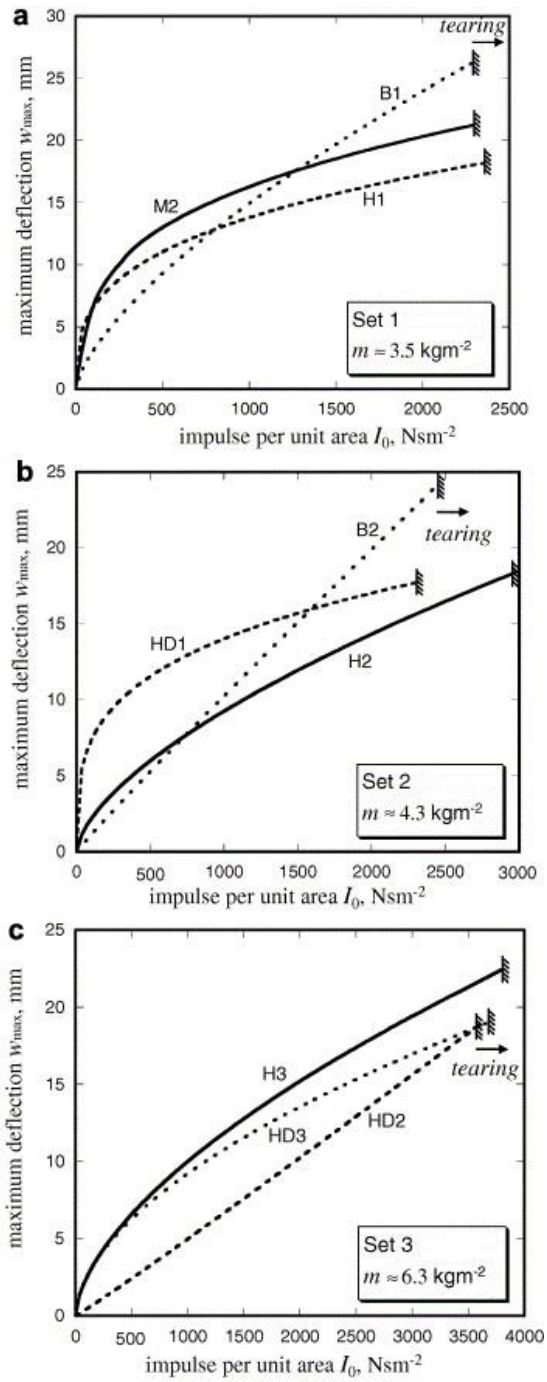

Figure 2.40. Comparison of the measured maximum mid-span deflections of the back face of sandwich and monolithic beams of equal mass; (a) Set 1, (b) Set 2 and (c) Set 3 (Source : Tagarielli, Deshpande, and Fleck 2007).

Wang et al. (Wang, Gardner, and Shukla 2009) developed stepwise graded polymeric foam core sandwich structures to resist blast loads. They used shock tube experimental set-up and polymeric foam cores with three different densities. The effect of grading on absorbed energy level was reported. Low-middle-high (l-m-h) density core sandwich structures showed lower deformation energy than middle-low-high (m-l-h) density core sandwich structures. That was a proof of effect of grading on blast performance of such structures. Front face deflection of l-m-h density core sandwich structure was higher than m-l-h. In Figure 2.41., alternative configurations and deflection histories of them can be seen.

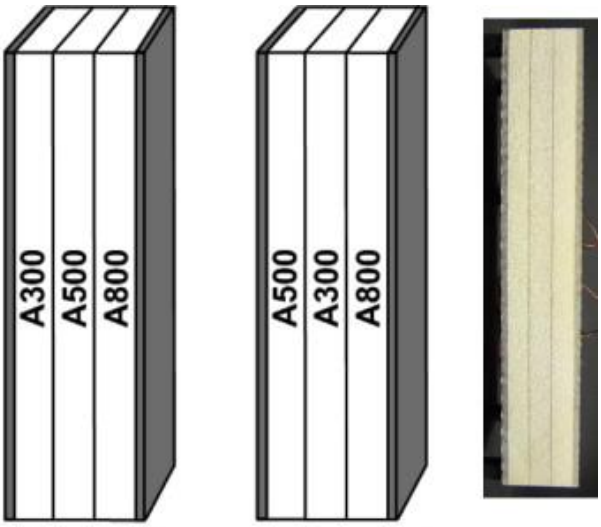

(a)

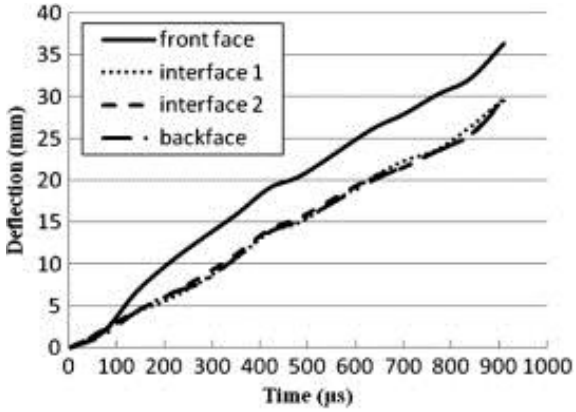

(b)

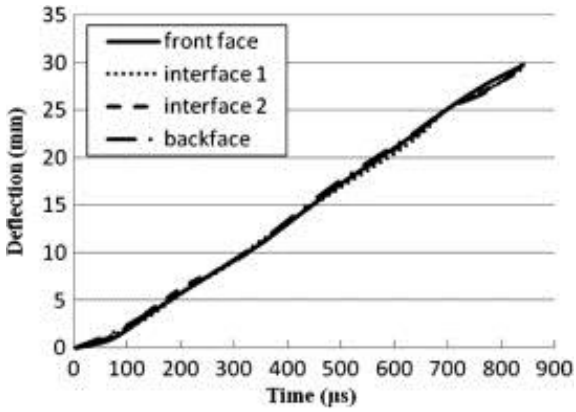

(c)

Figure 2.41. (a) Core configurations and real specimen, (b) deformation of first configuration, and (c) deformation of second configuration (Source : Wang, Gardner, and Shukla 2009).

An interesting application for protection against blast was offered by Palanivelu et al. (Palanivelu, Van Paepegem, Degrieck, Reymen, et al. 2011) in their study. They used beverage cans as sacrificial claddings, with a side advantage of recycling of aluminum cans. Specimens were exposed to blast loads by real scale tests and efficiency of the structures was proved. In Figure 2.42. configurations for the usage of beverage cans as sacrificial cladding can be seen.

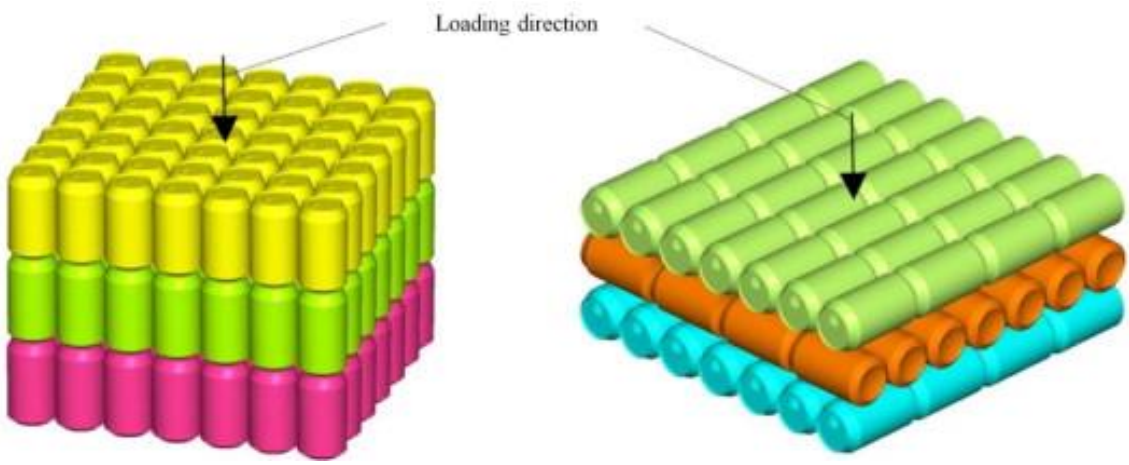

Figure 2.42. Two different configurations for sacrificial claddings made of thin-walled beverage cans (Source : Palanivelu, Van Paepegem, Degrieck, Reymen, et al. 2011).

Metallic hollow spheres also can be used as blast resistant materials. Taşdemirci et al. (Taşdemirci, Ergönenç, and Güden 2010) investigated effects of high strain rate and micro-inertia on deformation behavior of such kind of structures. Figure 2.43 shows views of metallic hollow sphere specimen that used in their study.

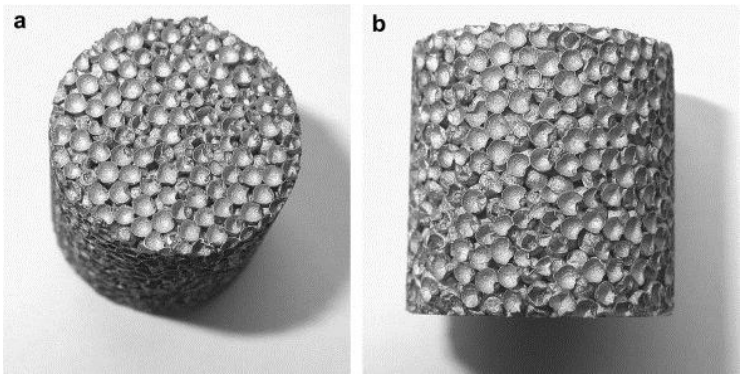

Figure 2.43. Cylindirical metallic hollow sphere specimen (Source : Taşdemirci, Ergönenç, and Güden 2010).

It was shown that, contribution of the inertial effects to the stress enhancement at high strain rate is calculated to be 35% and 26% at strain of 0.4 and 0.6, respectively. The increase in the quasi-static stress values due to micro inertia was also predicted 36% and 27% within the studied strain rate limits at 0.4 and 0.6 strains, respectively (Figure 2.44.).

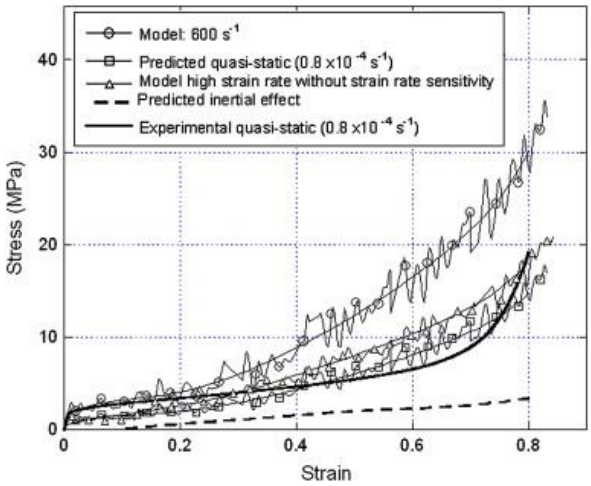

Figure 2.44. Results of modeling studies used to predict inertial effect on deformation of metallic hollow sphere structures (Source : Taşdemirci, Ergönenç, and Güden 2010).

Taşdemirci et al. (Taşdemirci, Güden, and Ergönenç 2010) investigated blast protection performance of aluminum foam core sandwich structures numerically (Figure 2.45). They used ConWep air blast function with 10 kg TNT and 30 cm standoff distance. They also studied effects of face sheets on the blast resistance behavior. They proved that as core material gets thicker, energy absorption of structure improves. On the other hand, permanent global deformation of structure increases with increasing core material thickness.

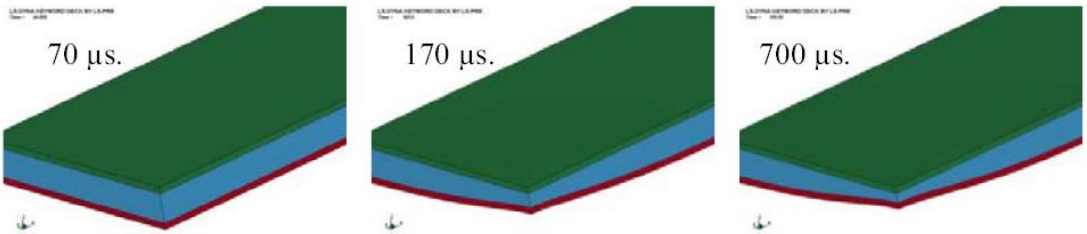

Figure 2.45. Deformation history of sandwich structures.
(Source : Taşdemirci, Güden, and Ergönenç 2010)

In Figure 2.46 acceleration of components of sandwich structures are plotted against time and core thickness. It is obvious from figure that as deformation progress core absorbed most of the blast energy. Moreover, this resulted in lower acceleration in back face sheet than front face sheet.

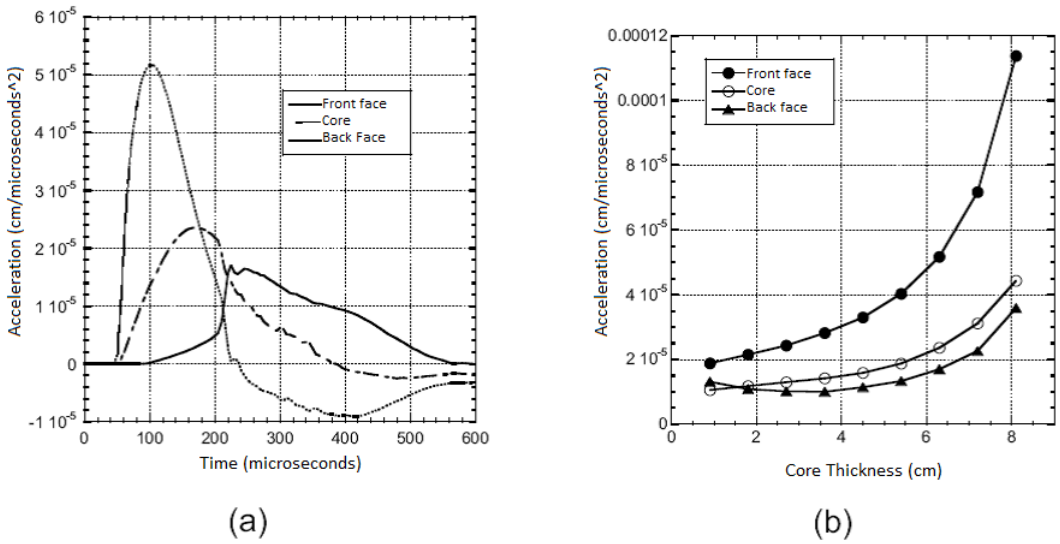

Figure 2.46. (a) Acceleration history, (b) acceleration versus core thickness.
(Source : Taşdemirci, Güden, and Ergönenç 2010)

Amini et al. (Amini, Simon, and Nemat-Nasser 2010) in their study investigated the effect of shock loading on monolithic DH-36 plates and polyurea coated DH-36 plates. In the investigation, shock loading was produced by so-called direct pressure pulse test setup. The setup uses a confined polyurethane elastomer material to exert shock loading on material. In another study (Amini, Simon, and Nemat-Nasser 2010) they modeled the same problem numerically by using LS-DYNA.

CHAPTER 3

MANUFACTURING AND EXPERIMENTAL AND NUMERICAL DETAILS

This chapter provides essential information about material of specimens, manufacturing processes utilized in order to obtain both combined geometries and sandwich structures. The following sections also elaborate the experimental techniques and devices used both for characterization and performance evaluation of specimens. Subsequent sections also introduce the numerical details of the study in terms of specimen preparation, real test, and fictitious simulations.

3.1. Materials and Manufacturing

3.1.1. AISI 304L Stainless Steel

Combined geometries proposed in current study and face sheets of sandwich structures were made of AISI 304L stainless steel sheet material. AISI 304L stainless steel is a steel alloy that contains a high level of chromium in order to provide a quite stain-proof passive/corrosion resistant chromium oxide layer. The chemical composition of the material used in the study was given in Table 3.1. As can be seen from the table, received material contains chromium between 17.5 and 19.5 %weight.

Table 3.1. Chemical composition of AISI 304L stainless steel.

C (%wt)	Cr (%wt)	Ni (%wt)	Mn (%wt)
0.03	17.5-19.5	8.0-10.0	2.0

Material selection in this study was simply based on widely reported strain rate sensitive behavior of AISI 304L stainless steel ((Lee and Lin 2001), (Lee and Lin 2002)), because of strain rate regimes that covered through the study. Formability of AISI 304L stainless steel also facilitated the choice of the manufacturing method of combined geometries proposed in the study (Rezaei Shahreza, Dehghani, and Salimi

2012). Besides, ability and know-how of Turkish manufacturing industry to work with AISI 304L stainless steel were assets while decision-making to select such a material, considering the present assertion of utilization of sources of Turkish industry.

3.1.2. Manufacturing of Combined Geometry Shells

Core geometries used in this study consisted of a hemispherical cap attached seamlessly to a cylindrical portion. An example of a combined geometry shell having a diameter of 40 mm and height of 30 mm and with a complete hemispherical cap can be seen in Figure 3.1. The proposed geometry in this study was chosen in order to combine the deformation and energy absorption behavior of its constituents.

Figure 3.1. An example of a combined geometry shell.

Considering the capacity of experimental devices and manufacturing ease of combined geometries, details of geometrical dimensions of combined geometries were determined and tabulated in Table 3.2. Besides table includes a designation which is related to the geometry of the combined geometry shells. Four different types of combined geometries were designed in order to show the effect of radius and thickness of the structure. Manufacturing drawings of combined geometries were given in Figure 3.2.

Table 3.2. Geometrical parameters of combined geometry shells.

Designation	Outer radius (mm)	Thickness (mm)	Total height (mm)
R75T05	7.5	0.5	13
R75T1	7.5	1.0	13
R125T05	12.5	0.5	23
R125T1	12.5	1.0	23

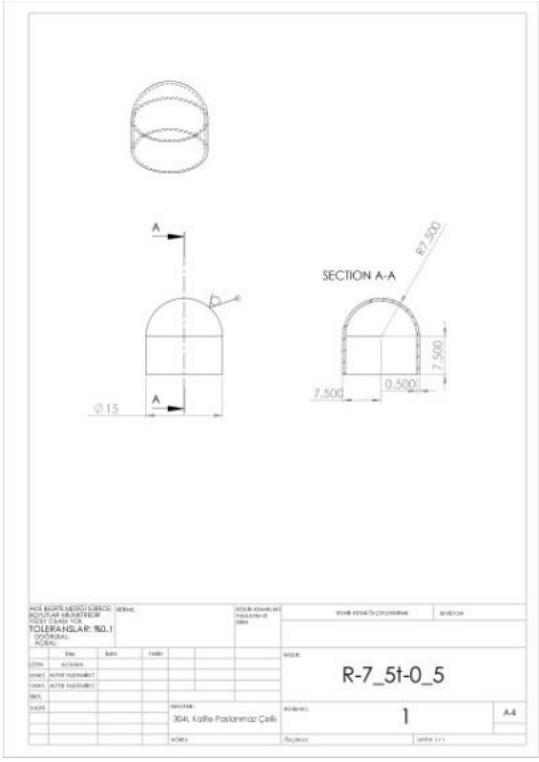

(a)

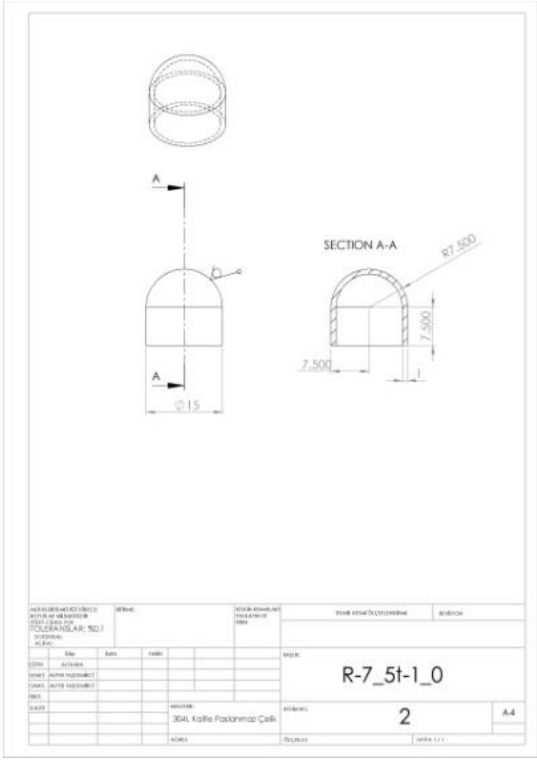

(b)

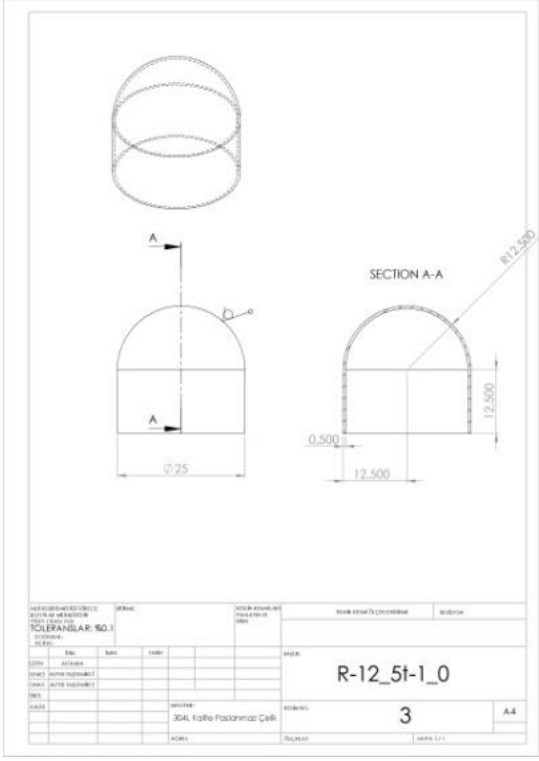

(c)

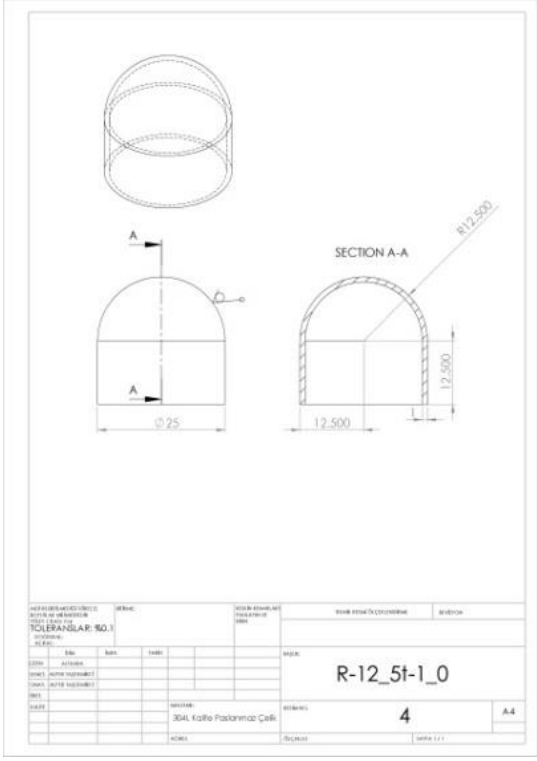

(d)

Figure 3.2. Manufacturing drawing of combined geometry shells; (a) R75T05, (b) R75T1, (c) R125T05, and (d) R125T1.

In order to manufacture such a combined geometry without using welding or adhesive bonding, deep-drawing method was obviously appropriate and chosen. The method is a sheet metal forming process in which a sheet metal workpiece is radially drawn into a forming die by usage of a mechanical punch with the shape of internal geometry of semi-finished or finished product. In the method, workpiece is held with a blank holder applying an appropriate axial force in order to prevent undesirable wrinkling of product. In the process, sometimes multistage manufacturing may be needed in order to have a better thickness variation through the section of the product and to have a better finish.

In the manufacturing of hemispherical core materials, in addition to deep-drawing, a subsequent cutting operation was done in order to remove excessive material in the flange region. Besides, edges of cylindrical portions were sandpapered in order to reduce the imperfection of the edge to some level. In Figure 3.3 deep-drawing method can be seen with finished product.

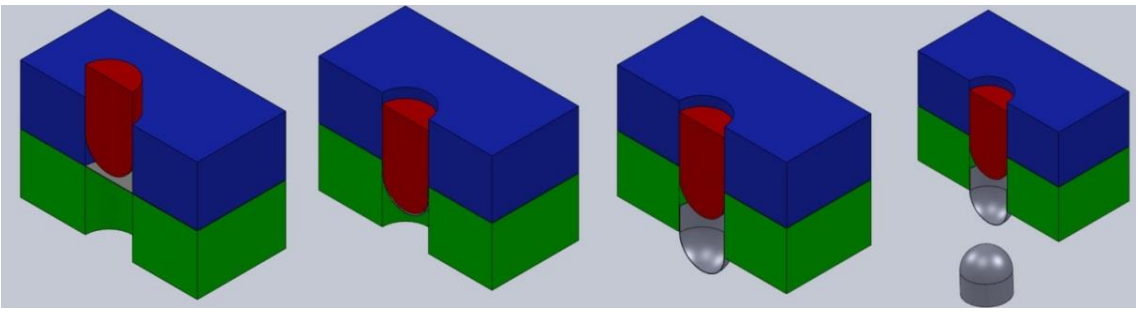

Figure 3.3. Schematic representation of deep drawing method (green part: forming die, blue part: blank holder, red part: mechanical punch, grey part: workpiece).

In Figure 3.4 bottom and top views of combined geometry shell structures manufactured by deep-drawing, cut by a CNC lathe and ground by emery cloth can be seen. Besides, cross-sectional view of R125T1 was given. It is obvious from the cross-sectional view of R125T1 specimen; at the edge a thinning was observed.

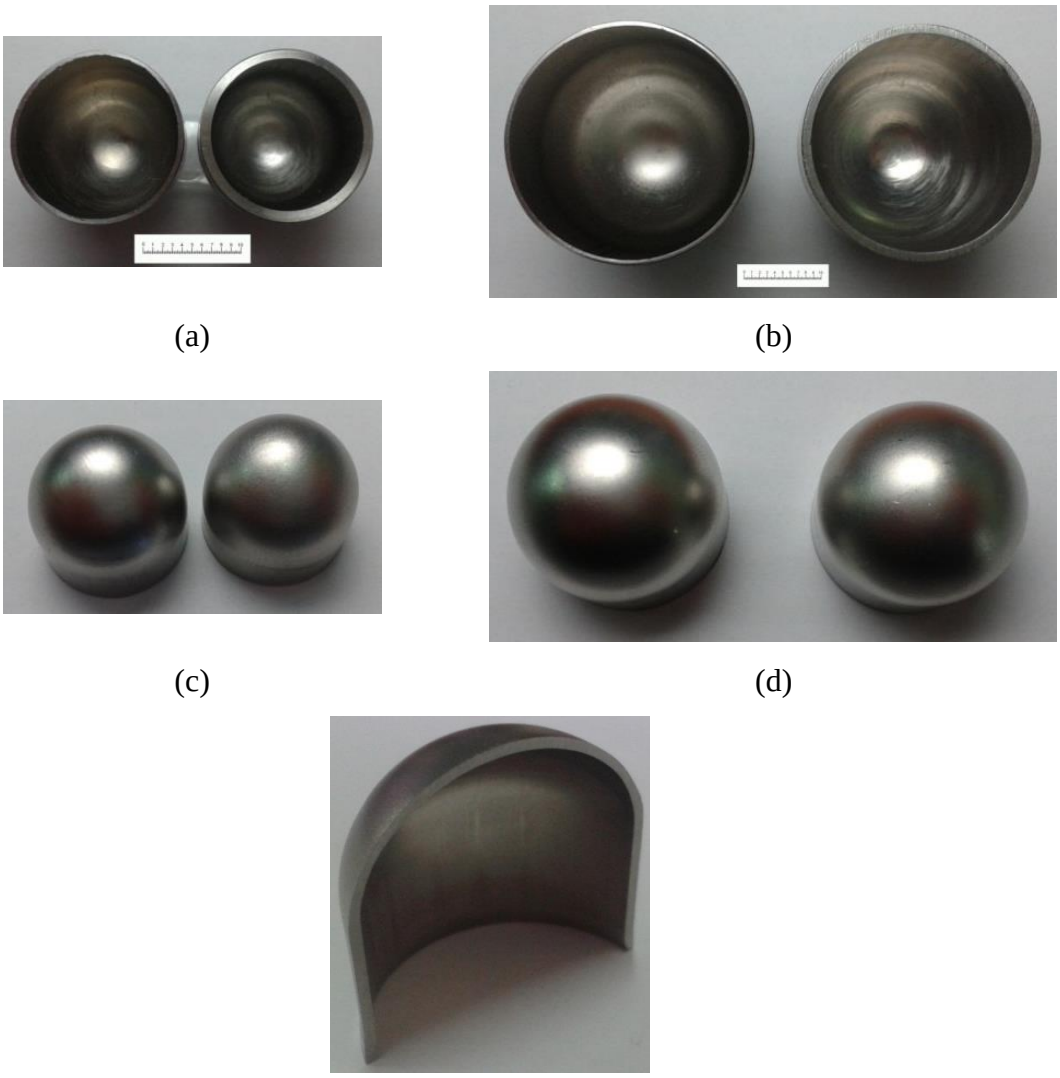

Figure 3.4. Combined geometry shells; (a) bottom view of R75T05 and R75T1, (b) bottom view of R125T05 and R125T1, (c) top view of R75T05 and R75T1, (d) top view of R125T05 and R125T1, (e) cross-section view of R125T1.

Obviously deep-drawing method induced high level of plastic deformation on the blank material while forming it to its desired shape. Therefore, thicknesses of combined geometries varied through the meridional direction, as also obvious in Figure 3.4. (e). This thickness variation was also simply a sign of residual stress through the section of combined geometries. Therefore the knowledge of this geometrical variation is of great importance considering modeling studies carried out in this study and also high level of plastic deformation results in work hardening of blank material and affects the deformation behavior substantially. In order to determine thickness variations, geometrical measurements were carried out on all types of specimens. Results were

obtained as point clouds. A commercial computer aided design software was used to convert point clouds to solid sectioned identities to have a better understanding on the thickness variations. In Figure 3.5 thickness contours acquired by this process can be seen for all of the specimens.

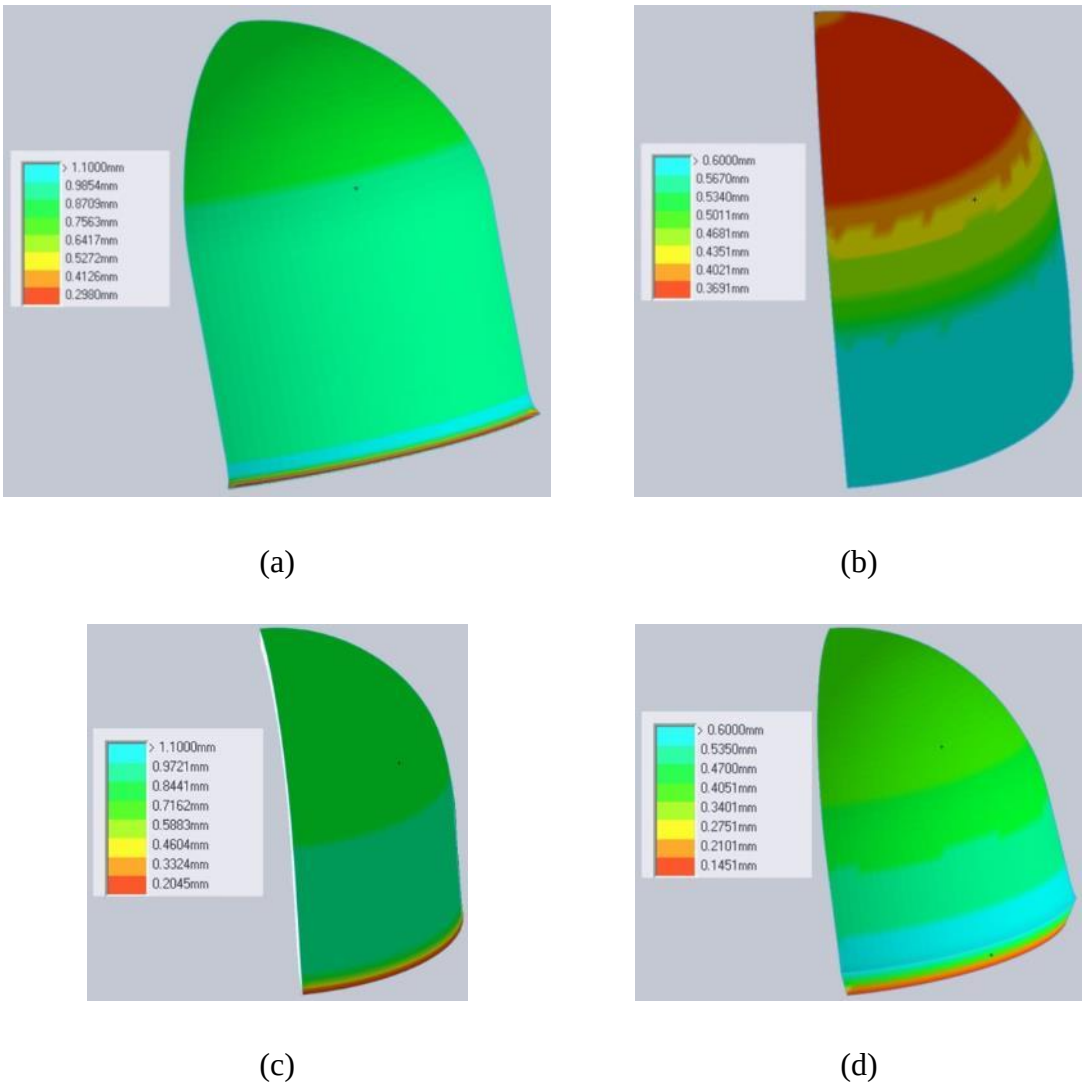

Figure 3.5. Measured thickness variation contours of combined geometry shells; (a) R125T1, (b) R125T05, (c) R75T1, (d) R75T05 specimens.

In Figure 3.5. (a), it can be seen that hemispherical portion has two sections with varying thicknesses for R125T1 specimen. Cylindrical segment thickened near the bottom edge. R125T05 specimen showed more varying thickness segments. Especially through cylindrical segment thickness varied from top to bottom edge. R75T1 specimen has a variation from 0.9 to 0.7 mm thickness. At cylindrical segment, thicker sections were observed. R75T05 specimen has a variation from 0.5 to 0.4 mm and three

segments formed at cylindrical segment. At bottom edges of all specimens, the lowest thicknesses were observed which are due to the specimen preparation steps and does not affect crushing behavior. Considering the results obtained from geometrical measurements, a substantial effect on deformation behavior was expected logically. In the subsequent sections covering numerical simulations, details to handle this geometrical imperfection were given.

3.1.3. Manufacturing of Sandwich Structures with Combined Geometry Shell Cores

Sandwich structures were manufactured by sandwiching core materials between two identical circular face sheets. In the current investigation, 1 mm thick AISI 304L stainless steel sheets were used as face sheets in order to have a good integrity and similar mechanical strength for all parts of the sandwich.

In order to guarantee repeatability of core arrangement for same configuration of sandwich, a pattern was designed and manufactured to use in manufacturing. Solid model and picture of pattern can be seen in Figure 3.6.

(a) (b)

Figure 3.6. Bonding pattern for manufacturing of sandwich structures; (a) solid model, and (b) manufactured pattern.

Sandwich structures were designed to have a cross-shaped packing of individual combined geometry shell structures. In the specimens, five combined geometry shells

were placed into a manufacturing pattern and 1 mm thick AISI 304L stainless steel face sheets were bonded using a cyanoacrylate based adhesive. A point contact between hemispherical top segment and face sheet and a line contact between cylindrical bottom edge and face sheet were obtained. In order to prevent sliding of face sheets before the curing of adhesive and to have standard dimension sandwiches, a ring (same diameter as confinement used in confined tests) was placed around the manufacturing pattern. Besides, the ring also provided a barrier to prevent tilting of individual combined geometry shells. Therefore, sandwich specimens with 75 mm in diameter and 25 mm in length were prepared. A sandwich specimen can be seen in Figure 3.7.

Figure 3.7. Sandwich specimen.

3.1.4. Heat Treatment of Combined Geometry Shell Structures

As a result of plastic deformation, generally a work hardened material is obtained with some embrittlement. Failure/fracture may occur in specimens instead of dissipating energy by plastic deformation, especially at high loading rates as a result of aforementioned embrittlement. Therefore in this study, heat treatment was presented as a stress relieving procedure to have a more ductile material in order to increase absorbed energy without failure/fracture and to change deformation modes. The heat treatment process conducted in this study consisted of two main stages, namely annealing at 1100 ^{o}C and air quenching immediately after the finish of annealing process. The effective heat treatment process duration was determined in this study by repeating the process with three different durations; 0.5, 2.0, and 4.0 and effective heat

treatment duration was determined by comparison of preliminary quasi-static crushing results of specimens (which is presented in corresponding chapter). As a result of comparison 2.0 hours were found to be suitable and all specimens were heat treated for 2.0 hours. This result can be verified considering the results reported for a similar material by Weber et al. (Weber, Martin, and Theisen 2012). Their results showed that with these conditions, an intermediate grain size can be achieved and a tough and ductile material can be obtained.

3.2. Experimental Details

This section presents the experimental techniques used in the current study. The experimental techniques used in the study basically had two main purposes; i.e., characterization and determination of strain rate sensitive behavior of AISI 304L stainless steel and evaluation of performance of combined geometry shells and sandwich structures with combined geometry shell cores subjected to various loading and boundary conditions.

3.2.1. Quasi-Static Experiments

In the current study, a Shimadzu AG-X universal testing machine was used in both quasi-static tension tests of AISI 304L stainless steel and quasi-static performance evaluation tests of combined geometry structures and unconfined and confined sandwich structures with combined geometry shell cores. Tests can be conducted between strain rates of 10^{-4} and 10^{0} s^{-1} by using the testing machine.

Figure 3.8. Shimadzu AG-X 300 kN universal testing machine.

In Figure 3.8 quasi-static testing machine can be seen. The particular quasi-static testing device was equipped with a load cell having a nominal capacity of 300 kN. Testing machine may be used with constant cross-head speeds up to 8 mm/sec. A video extensometer was also coupled with the device in order to remove the elastic deformations of the machine frame which deteriorates the results obtained from the tests. Details of particular tests were given in paragraphs containing results thereof. In confined quasi-static crushing experiments of sandwich structures a steel cylindrical ring with an outer diameter of 120 mm was used.

3.2.2. Drop Weight Impact Experiments

A Fractovis Plus drop weight test device was utilized in the performance evaluation tests of both combined geometries and sandwich structures of the current study in intermediate strain rate levels. The main constituents of the drop weight tester include striker, dropping weights, striker tip, and velocity sensor. The striker was attached to a 90 kN strain-gage sensor connected to data acquisition system and

readings were recorded. The striker velocity was measured by the photocells of the drop-weight tester and the absorbed energy was internally calculated by integrating the force–displacement curves. Tests can be conducted between strain rates of 10^0 and 10^2 s^{-1} by using the testing machine. Details of particular tests were given in paragraphs containing results thereof.

The tests were conducted using a 70 mm diameter flat end striker tip. In the drop weight tester, dropping weights up to 70 kg can be used and 25 m/s maximum initial test velocity can be achieved by the help of attached spring of the system. Figure 3.9 shows the Fractovis Plus drop weight test device.

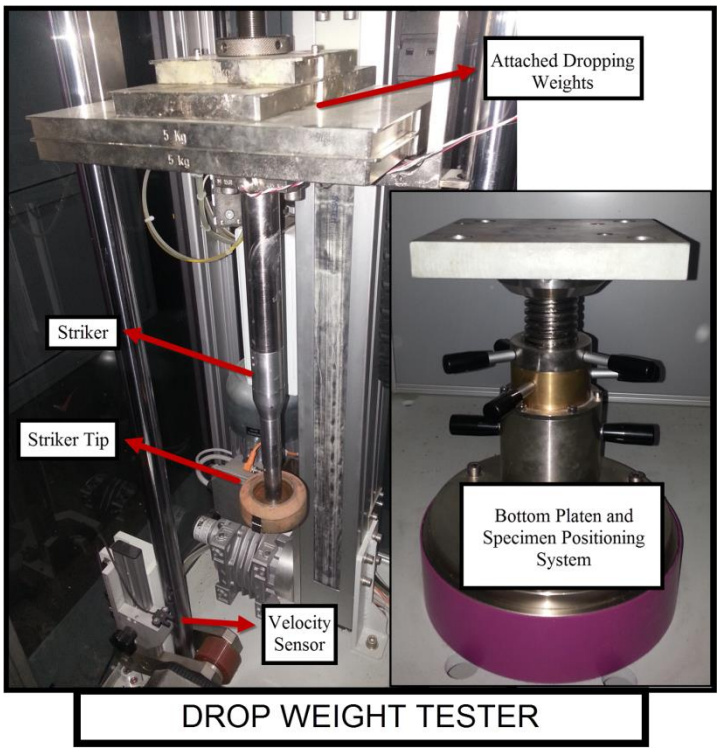

Figure 3.9. Fractovis Plus drop weight tester.

3.2.3. Split Hopkinson Tension Bar Experiments

In the study a Split Hopkinson Tension Bar (SHTB) is used in order to determine strain rate sensitive behavior of AISI 304L stainless steel. SHTB is an experimental setup that generates tensile waves and deforms the specimen under high strain rate loading condition between 10^3 and 10^4 s^{-1}. SHTB contains following parts; all 316L stainless steel incident and transmitter bars, a tubular striker, and a gas gun. Incident and transmitter bars were equipped with strain gages. By using the gas gun, a

variety of initial velocities can be obtained considering the geometry and weight of the striker bar. In Figure 3.10. SHTB system can be seen.

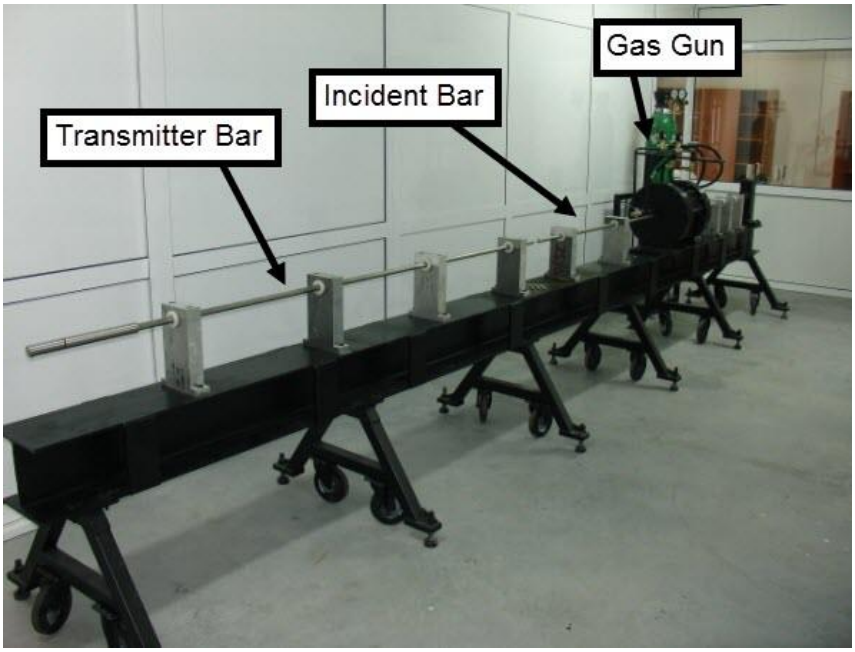

Figure 3.10. Split Hopkinson Tension Bar.

Material properties of Split Hopkinson Tension Bar used in the high strain rate experiments were given in Table 3.3.

Table 3.3. Material properties of SHTB test setup.

Material	Density (kg/m^3)	Modulus of elasticity (GPa)	Poisson's ratio	Yield Strength (MPa)
316L Stainless Steel	8000	193	0.3	300

In Figure 3.11. SHTB voltage history can be seen for a test of 304L stainless steel. As can be seen in the figure, as a result of the hit of the striker bar, an elastic stress wave (incident wave) propagates through the incident bar of the test system. When the wave arrives the incident bar – specimen interface some of them reflects back through the incident bar (reflected wave) and some of them plastically deform the specimen and travels through the transmitter bar (transmitted wave) according to impedance mismatch between specimen and bar materials. As can be seen from the figure that, positive incident wave reflected back as negative wave due to the free surface. By using the

strain gages attached on the bar aforementioned three waves were recorded and used in the calculations.

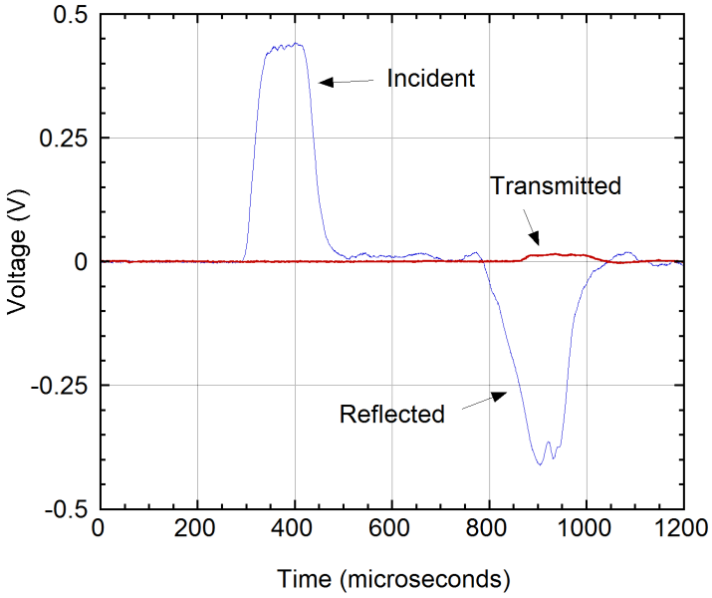

Figure 3.11. SHTB voltage history of a test conducted on AISI 304L stainless steel.

Strain history recorded by a particular strain gage can be calculated by using the formula in equation 3.1.

$$\varepsilon(t) = \frac{4 \times Voltage(t)}{V_{exc} \times GF \times K_{gain}} \tag{3.1}$$

By using the voltage histories recorded by the strain gages mounted on incident and transmitter bars, the strain rate ($\dot{\varepsilon}$), the strain (ε), and the stress (σ) of the tested samples were calculated using the following equations:

$$\dot{\varepsilon}(t) = -\frac{2C_b}{L_s}\varepsilon_r(t) \tag{3.2}$$

$$\varepsilon(t) = -\frac{2C_b}{L_s}\int_0^t \varepsilon_r(t)\,dt \tag{3.3}$$

$$\sigma(t) = \frac{E_b A_b}{A_s}\varepsilon_t(t) \tag{3.4}$$

in which C_b is the elastic wave velocity of the bar, L_s is the sample length and A_s and A_b are the sample and bar cross-sectional area, respectively. ε_i, ε_r, and ε_t are, respectively, the incident, reflected and transmitted strains measured from strain gages on the bar. The above equations are derived based on the assumption that the forces at sample-bar interfaces are equal.

3.2.4. Direct Impact Experiments

Dynamic crushing behavior of confined and unconfined sandwich structures with combined geometry shell cores at strain rates ranging between 10^3 – 10^4 s^{-1} was determined using a 7075-T6 aluminum direct impact experimental setup. This setup consists of a gas gun, a 150 mm long striker bar with a diameter of 75 mm, and a 2000 mm long transmitter bar with a diameter of 70 mm. In confined crushing tests, a confining fixture having an outer diameter of 100 mm was used with a clearance enough to provide radial constraint during impact event. The confinement also used as a dimensional adapter between 75 mm diameter specimen and the 70 mm diameter transmitting bar. In unconfined tests, a specimen holder with a diameter of 100 mm was used only as an adapter between sandwich specimen and transmitting bar. The particular experimental setup can be seen in Figure 3.12. Material properties of bars of direct impact experimental setup are given in Table 3.4.

Table 3.4. Material properties of direct impact test setup.

Material	Density (kg/m^3)	Modulus of elasticity (GPa)	Poisson's ratio
7075-T6	2810	72	0.3

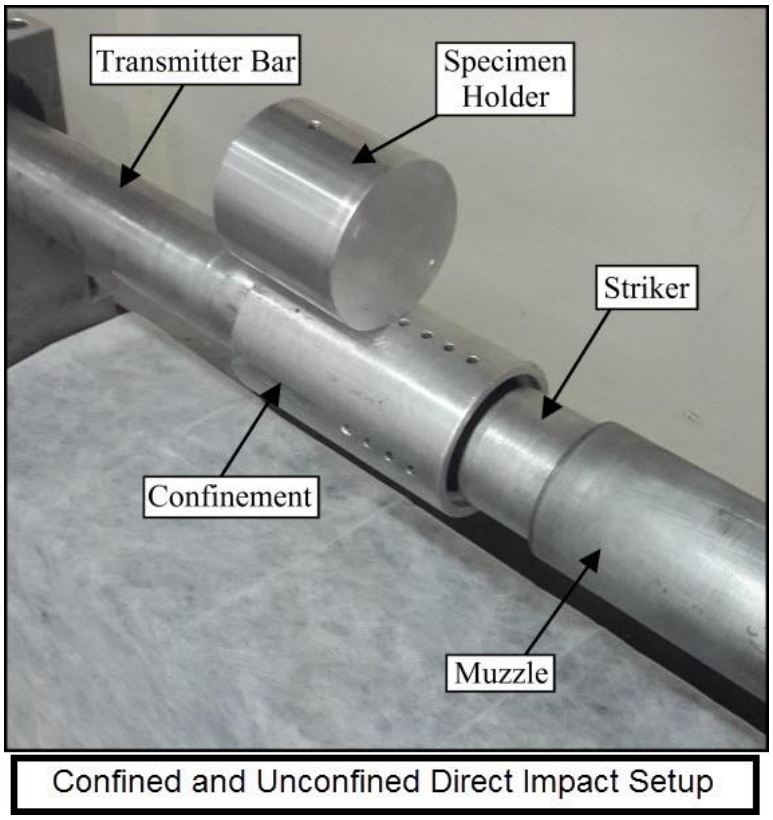

Figure 3.12. Direct Impact experimental setup

In direct impact experiments, striker bar was propelled against a 50 mm thick piston for confined tests and directly onto specimen for unconfined tests. Initial velocity of striker bar was measured using laser velocity sensors attached to the gas gun barrel.

In order to calculate crushing force in dynamic experiments, transmitting bar was equipped with strain gages and strain history (ε_T) was recorded using an oscilloscope. Firstly, voltage history was converted to the bar strain by using the formula given in equation 3.1. Then strain history was used to calculate bar stress (σ_T) and was converted to transmitted force history ($F_{Dynamic}$) which is the dynamic crushing force of sandwich structure. Equations used in the procedure are as follows;

$$\sigma_T = E_{bar}\, \varepsilon_T \tag{3.5}$$

$$F_{Dynamic} = \sigma_T\, A_{bar} \tag{3.6}$$

3.2.5. High Speed Photography

High speed photography was used in this study in order to reveal the crushing behavior of combined geometry shells and their sandwiches in different rates of deformation. Deformation sequences of particular experiments were captured and synchronized with their corresponding force – displacement or force – time histories. Deformation mode change due to effect of strain rate and inertia was captured by using the photographs taken with adequate frame rate considering the rate of the tests. The particular high speed camera used in the study was a Photron FastCam SA 1.1. type device. Obviously in confined experiments recording was not possible, because confinement used was an opaque material. Therefore numerical study was used to reveal deformation sequence in confined tests.

3.3. Numerical Details

This section presents the numerical techniques used in the current study. The numerical techniques used in the study had two main purposes; i.e., validation of the material properties and simulation conditions and determination of crushing behavior under different types of conditions such as blast loading. In the numerical part of the study LS-DYNA (Hallquist 2007) explicit commercial finite element software was used. The numerical part of the study started with the essential introduction of the constitutive model and determination of its parameters for AISI 304L stainless steel material. The second part of the numerical investigation comprises the preparation of numerical specimens. Obviously numerical specimens must inherit plastic deformation history as in real specimens. A special technique was used in order to transfer deformation history to crushing simulations. Then crushing and energy absorption and blast simulations and their corresponding model details were given in this section.

3.3.1. Johnson-Cook Constitutive Equation

A constitutive equation, generally, is a relation which approximates the response of a material under excitation by external forces. The constitutive model considered in this study was based on Johnson–Cook flow stress model. Therefore as a constitutive

equation, Johnson-Cook constitutive equation relates the flow stress of ductile metals subjected to applied strain at varying strain rates and temperatures (Johnson and Cook 1983). Johnson-Cook model uses simple forms of empirical relations of stress with strain, strain rate and temperature in the following form;

$$\sigma_{eq} = \left(A + B{\varepsilon_{eq}}^{n}\right)(1 + Cln\left(\dot{\varepsilon}_{eq}^{*}\right))\ (1 - T^{*m}) \tag{3.7}$$

where, ε_{eq} is the equivalent plastic strain and *A*, *B*, *n*, *C* and *m* are the material constants. The dimensionless plastic strain rate $(\dot{\varepsilon}_{eq}^{*})$ is given by $\dot{\varepsilon}_{eq}^{*} = \frac{\dot{\varepsilon}_{eq}}{\dot{\varepsilon}_0}$, where $\dot{\varepsilon}_0$ is a user defined reference strain rate, and $(\dot{\varepsilon}_{eq})$ is the equivalent plastic strain. The homologous temperature (T^{*}) is defined as $T^{*} = (T - T_r)/(T_m - T_r)$, where T is the absolute temperature, T_r is the room temperature and T_m is the melting temperature.

The failure model considered in this study was based on Johnson–Cook damage model. According to Johnson–Cook damage model, strain at fracture can be written as follows:

$$\varepsilon_f = \left[D_1 + D_2 e^{D_3\sigma^{*}}\right]\left[1 + D_4\, ln\left(\frac{\dot{\varepsilon}}{\dot{\varepsilon_0}}\right)\right](1 + D_5 T^{*}) \tag{3.8}$$

where D_1, D_2, D_3, D_4 and D_5 are damage parameters, $\sigma^{*} = \sigma_m/\sigma_e$ is stress triaxiality ratio. In the current study, the stress state does not change a lot during compression. Thus, the following basic form concentrating only on the strain rate sensitivity was considered. Note that, thermal effects on both material and failure models were neglected.

$$\varepsilon_f = D_1\left[1 + D_4\, ln\left(\frac{\dot{\varepsilon}}{\dot{\varepsilon_0}}\right)\right] \tag{3.9}$$

In order to mechanically characterize and obtain Johnson-Cook material model parameters of AISI 304L stainless steel material of core and face sheet materials quasi-static tension specimens in accord with ASTM: E8M-04 and high strain rate tension specimens were prepared by using wire-cut electrical discharge machining. In Figure 3.13 specimens can be seen. Because sandwich structures are going to be exposed

dynamic mechanical loads in drop weight and blast type loadings, dynamic mechanical characterization must be conducted. It was certain from the literature that 304L stainless steel is strain rate sensitive (Lee and Lin 2001). Therefore, quasi-static tension tests were conducted in three different strain rates (10^{-3}, 10^{-2} ve 10^{-1} s^{-1}) and high strain rate tension tests were conducted in two diferent strain rates (900 ve 1400^{-1} s^{-1}). In the quasi static tests, a video extensometer was used in order to remove elastic strain in the test machine frame as mentioned previously.

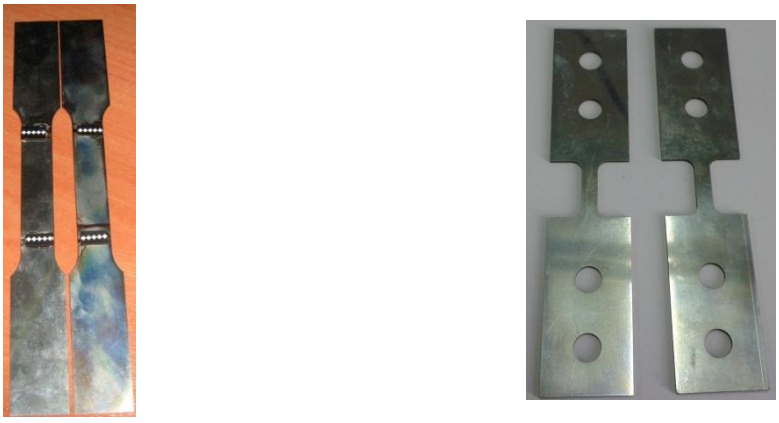

(a) (b)

Figure 3.13. (a) Quasi-static tension specimen, (b) Hopkinson tension specimen.

In Figure 3.14 true stress – true plastic strain curves obtained from quasi static tension tests of three different strain rates can be seen.

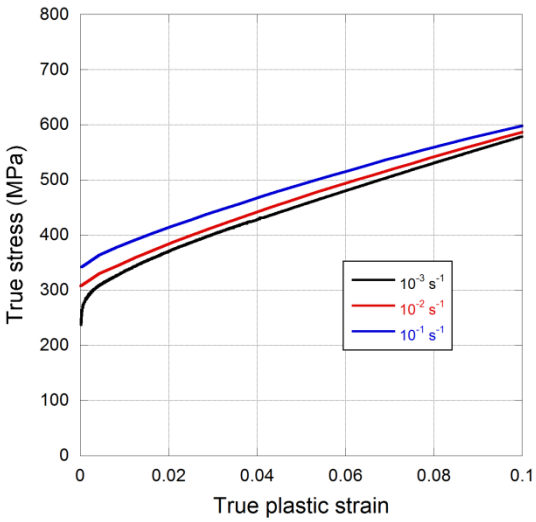

Figure 3.14. Quasi-static true stress – true plastic strain curves.

In Figure 3.15, results obtained from SHTB tests of AISI 304L stainless steel can be seen.

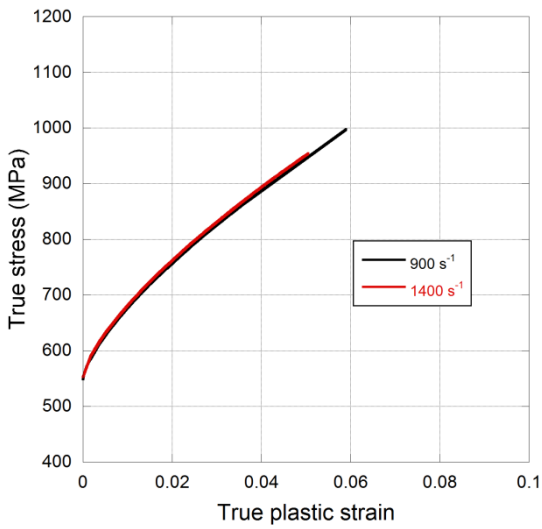

Figure 3.15. High strain rate true stress – true plastic strain curves.

It is obvious from Figures 3.14 and 3.15 that material showed strain rate sensitivity and this phenomenon must be accounted for numerical modeling studies. Test results were fitted by using first bracket of equation 3.7 and *A*, *B*, and *n* material parameters were determined. Result can be seen in Figure 3.16, obviously the coefficient of determination shows that the regression is successful.

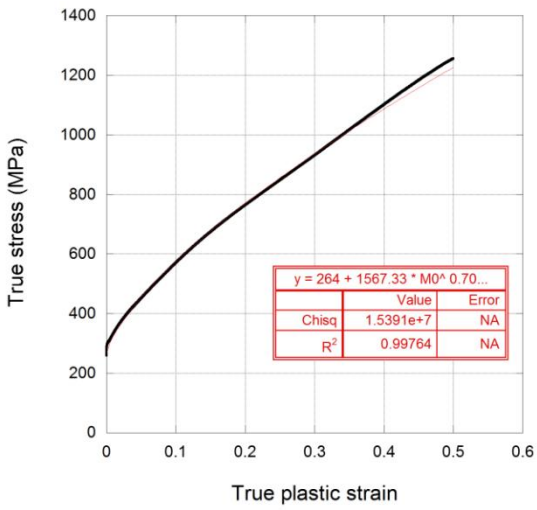

Figure 3.16. Curve fitting of test result.

As can be seen in equation 3.7 that strain rate sensitivity can be represented as a linear strain rate function. By using the results obtained from curve fit for strain hardening term given in Figure 3.16 and results of tests conducted in different strain rates, strain rate sensitivity fit was prepared and given in Figure 3.17.

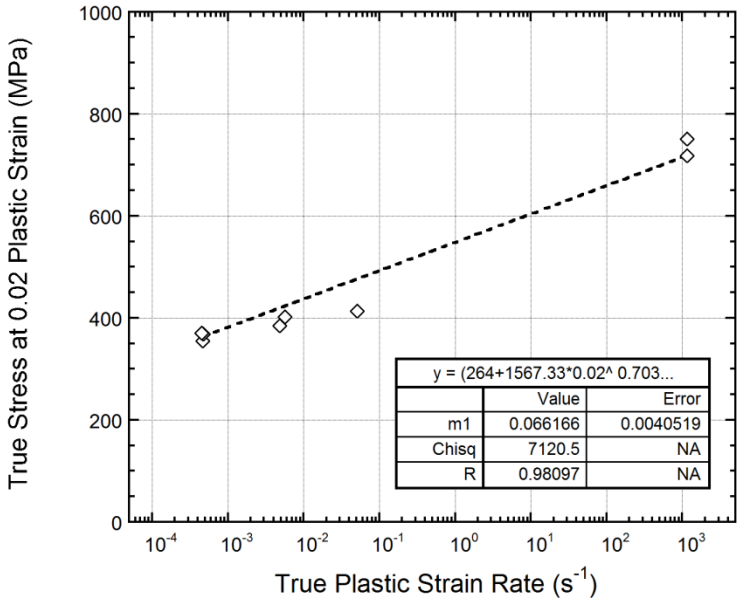

Figure 3.17. Strain rate sensitivity of AISI 304L stainless steel.

Experimental and Johnson-Cook model results for AISI 304L stainless steel can be seen in Figure 3.18.

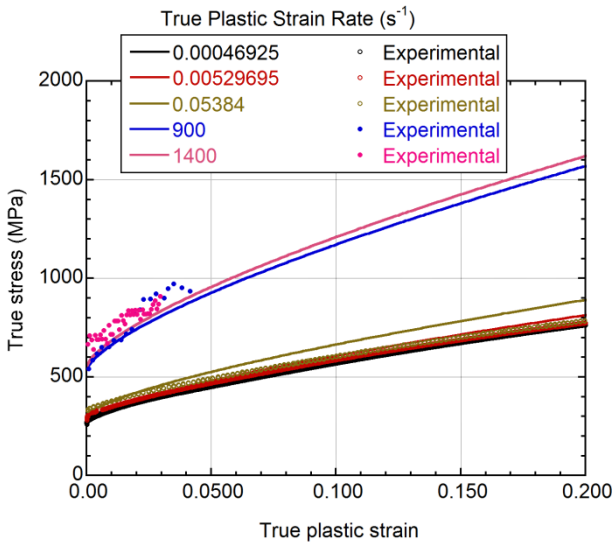

Figure 3.18. Comparison of experimental results and Johnson-Cook model of AISI 304L stainless steel.

As obvious from equation 3.9 that, failure model used herein yields simply a strain rate dependent effective failure strain. Considering this and aforementioned calculations, as a result of characterization tests, Johnson-Cook model parameters were obtained for AISI 304L stainless steel and given in Table 3.5.

Table 3.5. Johnson-Cook material model parameters of AISI 304L stainless steel.

ρ (kg/m^3)	G (GPa)	E (GPa)	υ	A (MPa)	B (MPa)	n	C
7830	80	193	0.305	264	1567.33	0.703	0.067
$D1$	$D2$	$D3$	$D4$	T_R (^{o}K)	T_m (^{o}K)	m	
0.53467	0	0	-0.01913	296	1698	1.0	

3.3.2. Numerical Specimen Preparation – Restart Analysis Technique of LS-DYNA

As already emphasized in the section on manufacturing of combined geometry shells, deep-drawing method used in the manufacturing induced high level of plastic deformation. As a result of plastic deformation in the workpiece, work hardening occurred, and a varying thickness profile was obtained, as reported in the same section in Figure 3.5. Therefore, numerical specimens must inherit plastic deformation history and thickness variation and the knowledge must be transferred to subsequent simulations of any type. Consequently, simulations with nominal thickness and without strain hardened material model cause incorrect results. Two approaches can be used in order to eliminate these limitations; a) an average strain can be assigned for all of the specimen or its different segments, b) deep drawing can be modeled and the same geometry and material properties can be found in order to use in subsequent simulations. The former cannot represent material property and thickness variations through the specimen section and crushing behavior cannot be simulated properly. The latter takes into account thickness changes, residual stress, and plastic strains. Therefore, a proper simulation can be prepared.

In such metal forming simulations, Restart Analysis Technique of LS-DYNA is used vastly. Firstly simulation of deep drawing process can be prepared. The code

creates a file that is the output of first simulation and it can be used as an input for subsequent simulation. This file is called “dynain” and the method that LS-DYNA creates that file is “dynain file method” ((LSTC 2007), (Maker)). That file can be used as input for springback simulations. After springback simulation, another dynain file is created which is the input for subsequent crushing simulation. This dynain file contains all necessary information about residual stress and new thicknesses for each element.

The manufacturing model consisted of punch, blank holder, forming die and blank. The blank was modeled using Belytschko-Tsay shell elements with seven integration points through the thickness. The optimum number of elements was determined by conducting a mesh sensitivity analysis. The analysis showed that an element size of 0.5 mm converged to the solutions within a reasonable time. Simulations must be carried out with mass scaling method in order to guarantee quasi-static strain rate levels. Details of mass scaling methodology were given in the following section. In Figure 3.19 resulting thickness variation for a R125T1 specimen can be seen comparatively.

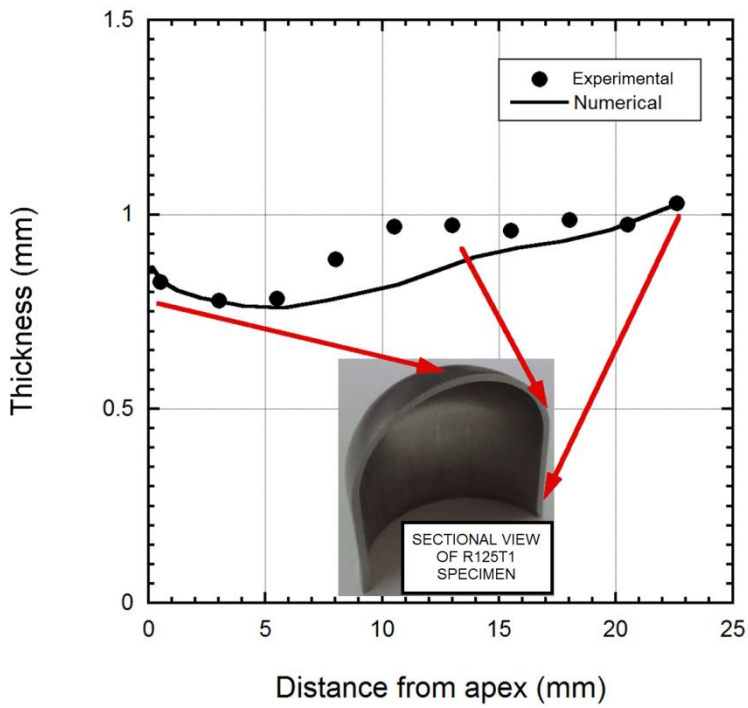

Figure 3.19. Comparison of measured and simulated thickness variations of a R125T1 specimen.

For further details of numerical specimen preparation and manufacturing simulations and for thickness variations of other types of specimens one must refer to

related project (Taşdemirci et al. 2014) supported by TÜBİTAK. By using the prepared specimens containing deformation history, crushing simulations results both for individual combined geometries and their sandwiches were obtained. Furthermore, in order to model the effect of heat-treatment on the deformation behavior of combined geometries, residual strain and stress history was omitted and excluded from the calculations and only thickness variations were taken into account for simulations of heat-treated specimens.

3.3.3. Crushing and Blast Simulations

In this section general details and common points were given for the simulation part of the study. Additional or case specific details of numerical simulations were given in their corresponding chapters or sections such as; initial and boundary conditions, element formulations, contact algorithms and blast conditions etc.

As already mentioned, combined geometry shells were prepared numerically by simulating manufacturing process. In simulations Belytschko-Tsay shell element formulation was used. Full (no symmetry definition) models for all simulations were prepared in order to account for non-symmetric modes of deformations observed in experimental study.

All of the simulations were run in LS-DYNA explicit finite element code. Then, in order to simulate quasi-static condition in such an explicit solver additional care must be taken. In order to use LS-DYNA for quasi-static simulations, mass scaling methodology was followed (Santosa et al. 2000). Mass scaling methodology was simply an approximation of real problem in simulation environment. It is as follows, a quasi-static loading means that there are no strain rate and inertial effects on the material when the load applied even when subjected to high velocity loading in simulations. Strain rate aspect can be achieved in the simulations by switching off the strain rate sensitivity behavior of the material of the specimen. In order to take care of inertia aspect one must scale down (or up) the density and then it is possible to scale up the velocity (or loading rate) of the simulation in order to obtain reasonably small time steps and speed up the solution. Then with the mass-scaling, the ratio of kinetic energy to total internal energy must be less than 4% over the period of quasi-static simulations, ensuring quasi-static strain rates.

There is no need for additional care on dynamic simulations to run in LS-DYNA such as; low velocity crushing, direct impact crushing, and their simulation details were given corresponding parts of the study. As comparing the results of simulations with experimental results, validity of numerical results was proven. Corresponding validation and performance metrics were introduced for the applications such as; mean load, absorbed energy, specific energy absorption etc. and used in validation assessment along with the comparison with force-displacement results and deformation sequences obtained by high speed photography.

Once numerical model was well verified then the numerical study was extended in order to reveal the effect of inertia and base material's strain rate sensitivity on the deformation and energy absorption behavior of sandwich structures at different loading rates. Additional numerical simulations were prepared with different constant impact velocities and models were re-run where the base material was assumed to be rate insensitive.

Constant deformation velocity simulations were used in order to investigate the effect of multilayering on crushing response. In potential engineering applications of the currently studied sandwich structures as blast protection, many repeating unit cells will be stacked along the thickness and in-plane directions. Thus, the investigation of the effect of axial rotation and/or angular misalignment of these repeating cells will become important. In this study this effect was also numerically investigated.

Then, the numerical study was extended in order to investigate dynamic response of sandwich structures consisting of combined geometry shell cores under blast loading. An explosion is a rapid release of energy in extreme manner caused formation of a blast wave which is the most harmful component of an explosion. CONWEP functions (Randers-Pehrson and Bannister 1997) were used in this study to model the pressure load on the front face sheet of the combined geometry core sandwiches. In the current investigation, a 5 kg of equivalent mass of TNT was defined with the standoff distance of 600 mm. As a comparable measure, Composition B type explosive has a TNT equivalency of 1.33 and is used in anti-tank landmines.

3.3.4. Mesh Sensitivity Analysis

Generally, sensitivity analysis is used to determine the uncertainty of mathematical or numerical models as a result of uncertainty in its inputs. In terms of finite element analysis, this uncertainty can be due to material properties (which already were validated) or simply because of reverting mesh dependent results. In order to evaluate mesh sensitivity of numerical simulations, the method includes preparing finer mesh models (lowering element dimensions) and comparison of the results depending on the number or dimension of elements. On the other hand, results by Papadopoulos and Iglesis (Papadopoulos and Iglesis 2007) suggested that, relatively coarse meshes must be used for the buckling analysis of imperfect structures as in the case of this study (thickness, material variation and geometrical imperfections). Even with the finer mesh results can diverge. Preliminary simulation results also confirmed that coarse mesh is working better with imperfect structures. Therefore mesh sensitivity analysis was not carried out in this study.

CHAPTER 4

CRUSHING AND ENERGY ABSORPTION BEHAVIOR OF COMBINED GEOMETRY SHELL STRUCTURES

In this chapter, results of quasi-static and low velocity crushing experiments of four types of combined geometry shell structures were given. Deformation behavior of combined geometry structures were investigated by using experimental force-displacement curves along with corresponding deformation sequences obtained from photography results. Relevant metrics to investigate and to compare the performance of energy absorbers were introduced as measures for behavior of combined geometry structures. At the end of the chapter, comparison of numerical results with experimental results was given for selected cases to show the efficiency and accuracy of the numerical simulation study. For complete numerical results one must refer to related project (Taşdemirci et al. 2014) supported by TÜBİTAK as already mentioned.

4.1. Quasi-Static Crushing Behavior of Combined Geometry Shells

As a first step of investigation of crushing behavior of combined geometry shell structures, quasi-static crushing tests were conducted on R125T1 specimens. Quasi-static crushing test results for both 10^{-3} s^{-1} and 10^{-1} s^{-1} nominal strain rates were given in Figure 4.1. As can be seen from the figure that force-displacement curves show similar characteristics, however slight variations are noted. Therefore, it is obvious that quasi static compression behavior is strain rate insensitive within quasi-static regime. Consequently, no additional tests were conducted on other types of specimen for different strain rates in quasi-static regime.

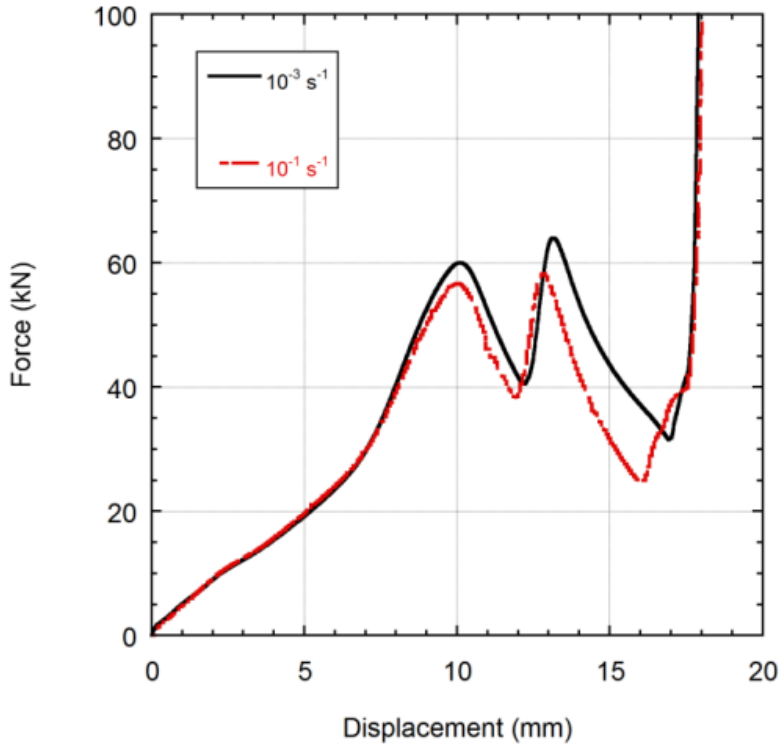

Figure 4.1. Quasi-static crushing test results of R125T1 specimen.

As can be seen in Figure 4.2. deformation starts at the hemispherical end of the specimen and up until a displacement value of 10 mm deformation is contained within the hemispherical portion. As the deformation proceeds buckling of cylindrical segment starts at around 12 mm. While the hemispherical cap deforms, a maximum crushing force of 60 kN was observed. After the peak load, buckling load was overcome and force decreases. There is a secondary peak force observed when the cylindrical segment buckles. After an 18 mm of displacement, densification (compression) starts. Energy absorbed during the deformation of hemispherical cap was calculated as 235 J. As deformation continues, cylindrical segment buckles along with deformation of hemispherical part. Absorbed energy during this stage was calculated as 358 J. According to these results, before the structure densifies, 40% of total energy was absorbed due to the buckling of hemispherical portion and 60% by the deformation of hemispherical part along with buckling of cylindrical segment.

Figure 4.2 shows the deformation history from the experiment. As can be seen from the figure, immediately after the beginning of deformation, upper segment of specimen contacting with upper compression plate flattens. After 3 mm of displacement, axisymmetric inward dimpling mode starts to dominate the deformation

as primary mode and lasts until the start of buckling of cylindrical segment. At 10.2 mm of displacement, buckling of cylindrical segment starts and continues to 13.0 mm.

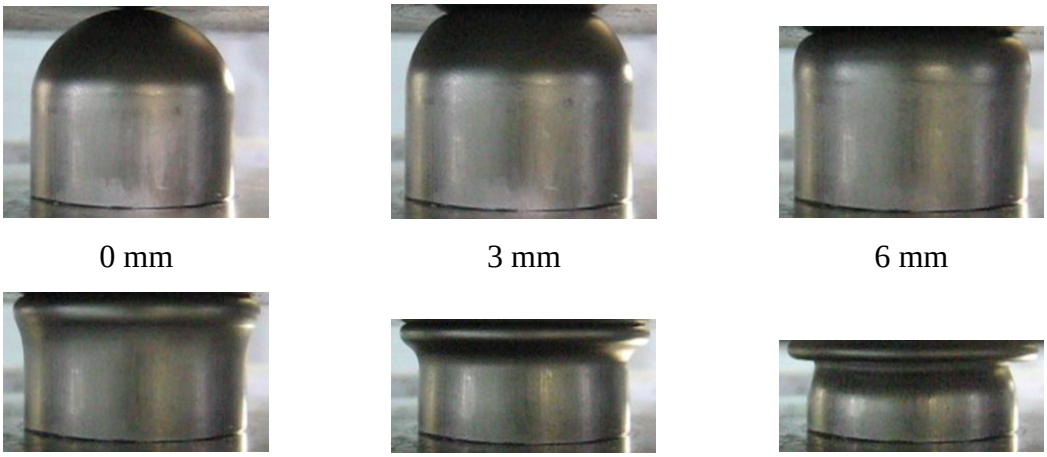

Figure 4.2. Deformation history results of quasi-static experiments of R125T1 specimens.

Combined geometry shell structures having a radius of 12.5 mm and a thickness of 0.5 mm (R125T05) were tested at 10^{-3} s^{-1} loading rate (of equivalent cylinder). Test result was given in Figure 4.3. Deformation of hemispherical portion lasts until 10 mm of deformation and at that point crushing of cylindrical segment starts. According to experimental results, energy absorbed by hemispherical portion was calculated as 74 J. As experiment proceeds, cylindrical segment starts to buckle along with the deformation of hemispherical portion. At this stage of deformation, absorbed energy was calculated as 129 J. Accordingly, before the structure densifies, 36% of total energy was absorbed due to the buckling of hemispherical portion and 64% by the deformation of hemispherical part along with buckling of cylindrical segment.

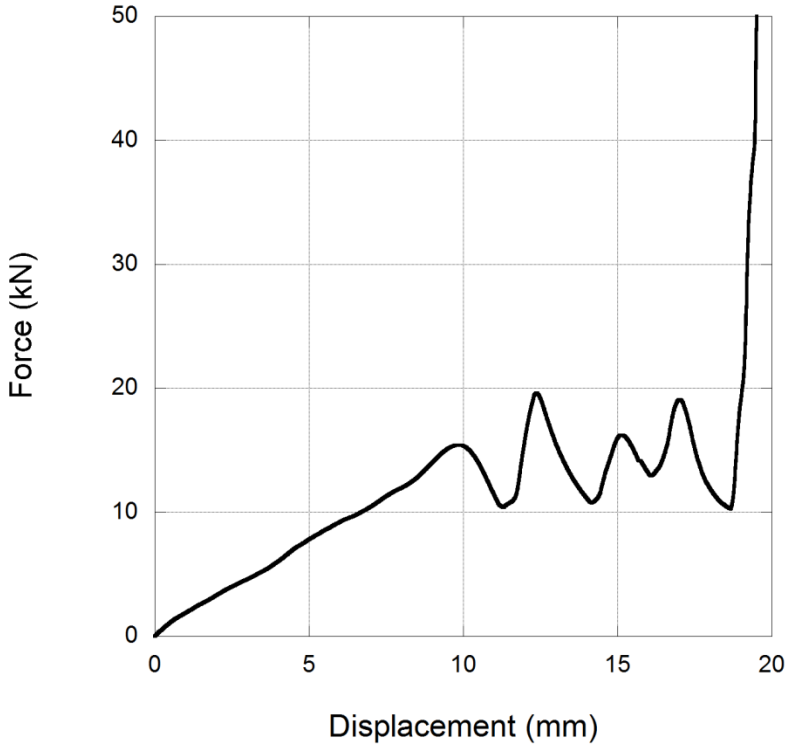

Figure 4.3. Quasi-static crushing test results of R125T05 specimen.

In Figure 4.4, deformation history can be seen from quasi-static crushing test of hemispherical core structure having a radius of 12.5 mm and a thickness of 0.5 mm. As can be seen from the figure, 5 mm deformation image shows axisymmetric inward dimpling mode. As deformation continues to 10 mm, axisymmetric inward dimpling mode continues, rolling plastic hinge radius increases, and buckling of hemispherical portion starts to become clearer. After that stage, crushing of cylindrical portion begins. Image from 15 mm deformation shows two lobes of buckling of cylindrical portion, clearly. As deformation progresses, buckling of cylindrical portion proceeds and a local peak observed as bottom part folds outwardly. At the end of the test, previously overturned apex turns upside down back and all folds densifies. It is obvious that both hemispherical and cylindrical portion shows symmetric deformation behavior.

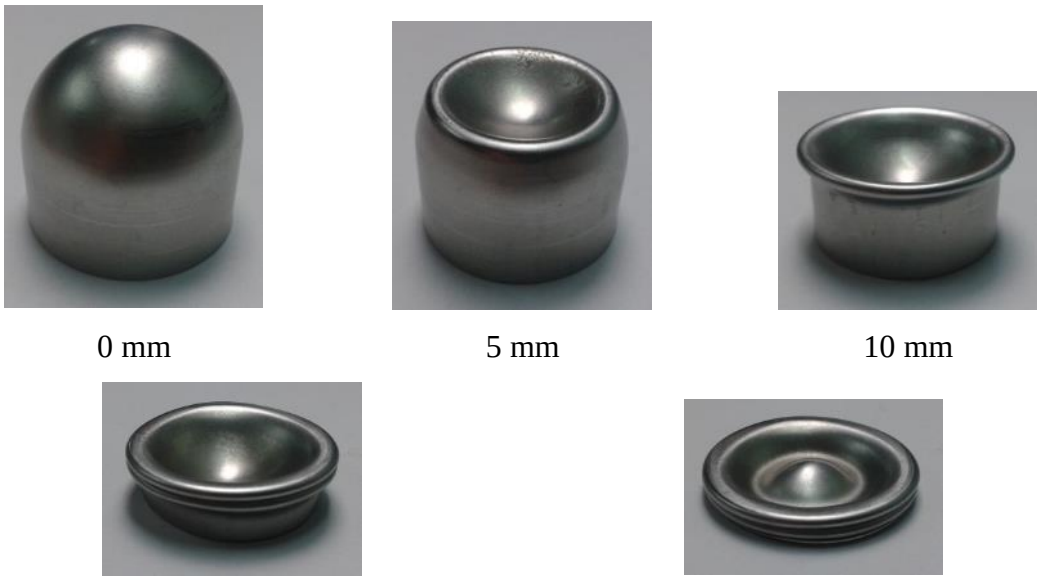

Figure 4.4. Deformation history results of quasi-static experiments of R125T05 specimen.

In the next part, quasi-static crushing behavior of combined geometry shell materials having a radius of 7.5 mm and a thickness of 1.0 mm were investigated (Figure 4.5). As can be seen from the figure, until 7 mm of deformation curve shows a bilinear behavior. At this point, a local peak is observed and load continues to increase to a global peak at 8.5 mm of deformation (except for densification). After 9.5 mm of deformation whole structure starts to densify. As can be seen from the Figure 4.6, bilinear part corresponding 7 mm of deformation is related to deformation of hemispherical portion. Absorbed energy by the deformation of hemispherical portion was calculated as 122 J. Absorbed energy by the deformation of cylindrical portion was calculated as 157 J. Accordingly, before the structure densifies, 44% of total energy was absorbed due to the buckling of hemispherical portion and 56% by the deformation of hemispherical part along with buckling of cylindrical segment.

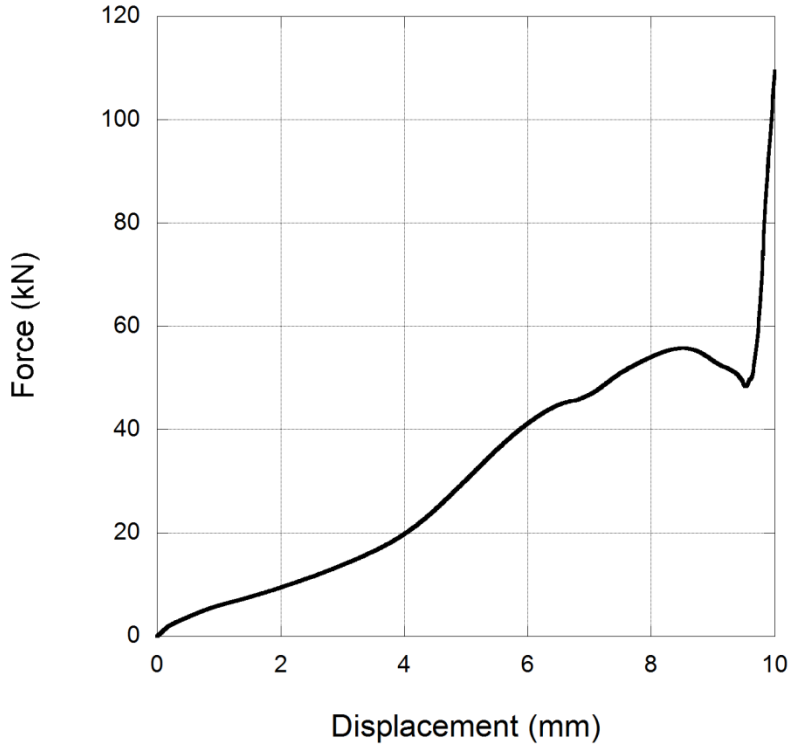

Figure 4.5. Quasi-static crushing test results of R75T1 specimen.

In Figure 4.6 deformed images from quasi-static crushing test of hemispherical specimen having a radius of 7.5 mm and a thickness of 1.0 mm can be seen. As can be seen from the figure, 4 mm deformed structure shows the typical form of axisymmetric inward dimpling mode. After 7 mm of deformation, buckling of hemispherical portion ends and cylindrical portion starts to deform. Fold of buckling of cylindrical portion can be seen clearly from image of 9 mm of deformation. As test continues, whole structure densifies before apex turns upside down back. Both hemispherical and cylindrical portions deformed in a symmetric mode.

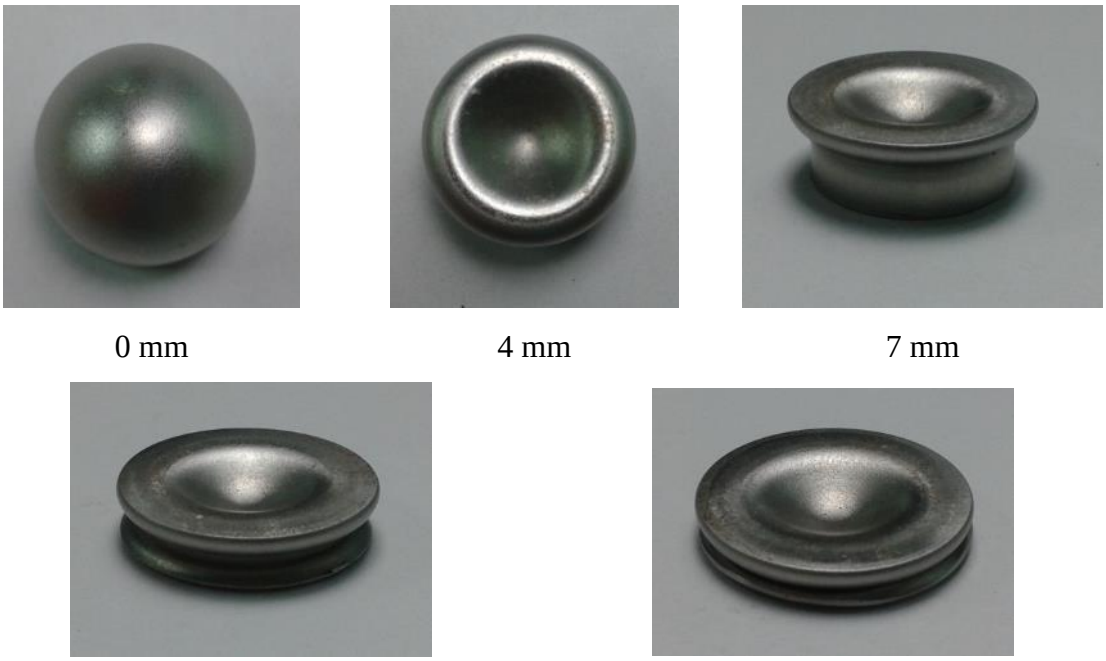

Figure 4.6. Deformation history results of quasi-static experiments of R75T1 specimen.

Investigation of quasi-static crushing behavior of combined geometry shell structures was finished with tests of specimens having a radius of 7.5 mm and a thickness of 0.5 mm. In Figure 4.7 test result can be seen. The force-displacement curve shows a bilinear behavior until 6 mm of deformation. At this point force reaches to a local peak value which corresponds to the deformation of hemispherical portion. A second local peak value was observed at 7.5 mm of deformation. Absorbed energy by the crushing of hemispherical portion was calculated as 38 J and absorbed energy by the buckling of cylindrical portion was calculated as 47 J. As a result, 45% of absorbed energy was absorbed by hemispherical portion and the rest was due to the deformation of cylindrical portion.

In Figure 4.8, deformation history of R75T05 specimen can be seen. Axisymmetric inward dimpling mode can be seen from the image of 4 mm deformation. After 6 mm of deformation, buckling of hemispherical portion ended and deformation of cylindrical portion started. From image of 9 mm deformation, an asymmetric lobe formed due to buckling of cylindrical portion can be seen. This asymmetric lobe can be seen as a second peak in Figure 4.7. As test proceeds, overturned apex turns upside down back and whole structure densifies together. As can be seen from the images of 9 and 10 mm deformation, both hemispherical and cylindrical portions deforms asymmetrically.

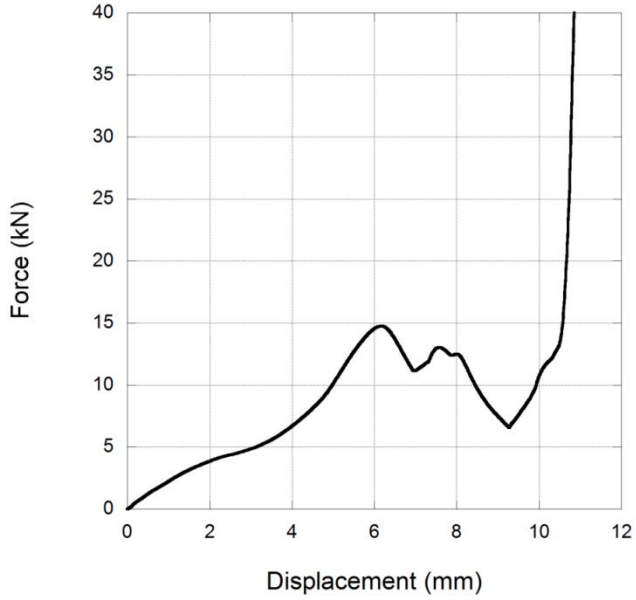

Figure 4.7. Quasi-static crushing test results of R75T05 specimen.

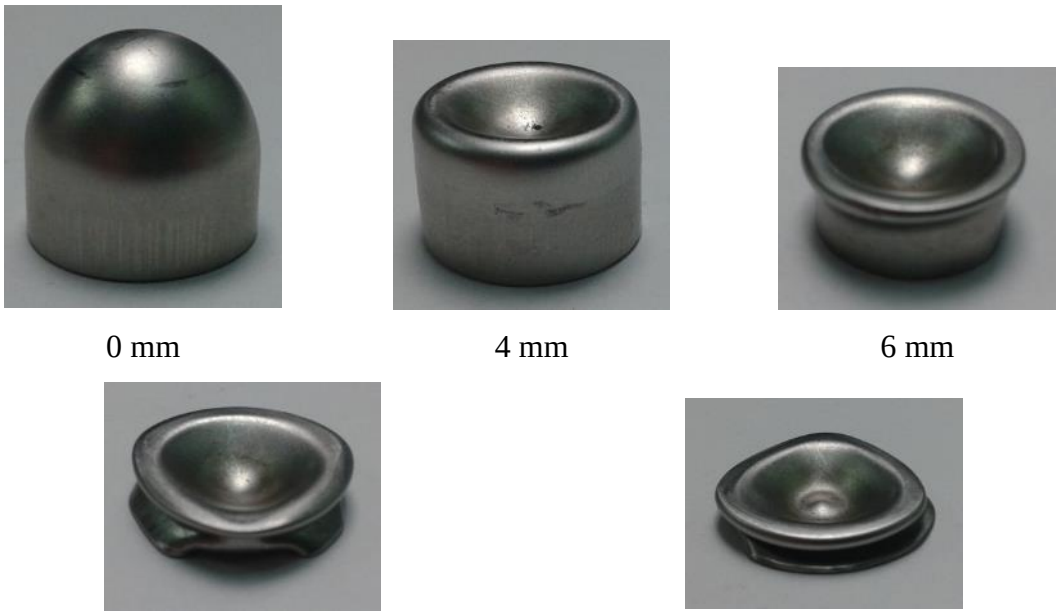

Figure 4.8. Deformation history results of quasi-static experiments of R75T1 specimen.

In Table 4.1 absorbed energy by combined geometry shell structures in quasi-static crushing tests are given. As can be deduced from the table that, on the average, 40% of total absorbed energies is due to the deformation of hemispherical part and the rest 60% is due to buckling of cylindrical portion (partially along with the deformation of hemispherical part). When total specific absorbed energies are compared, the highest

energy was absorbed by the specimen having a radius of 7.5 mm and a thickness of 1.0 mm, and the lowest energy was absorbed by the specimen having a radius of 12.5 mm and a thickness of 0.5 mm. As can be seen, in specimens having a radius of 12.5 mm, as thickness increases, amount of energy absorbed by hemispherical portion increased and specimens having a 7.5 mm radius showed exactly the opposite behavior. When specimens of same thickness were compared, as radius increases, percent amount of energy absorbed by hemispherical portion decreases.

Table 4.1. Absorbed energy by combined geometry shell structures.

Specimen	**Absorbed energy by hemisphere (%)**	**Absorbed energy by cylinder (%)**	**Total specific absorbed energy (kJ/kg)**
R125T1	40	60	49
R125T05	36	64	34
R75T1	44	56	93
R75T05	45	55	43

4.2. Low Velocity Crushing Behavior of Combined Geometry Shells

In order to investigate crushing behavior of combined geometry shell structures within all available strain rate regimes, study continued with the tests under low velocity crushing test conditions. Results of low velocity crushing tests are given in this section. Tests were conducted by using a Fractovis Plus drop weight tester. The apparatus can reach to velocities up to 25 m/s by the help of springs and up to 70 kg of dropping weights can be attached to the system. By using various piezoelectric crystal and strain gage sensor equipped strikers, up to 90 kN of maximum load can be measured. In this study, a striker equipped with a strain gage sensor and a 70 mm diameter cylindrical crosshead was used.

Recording of tests is very important in order to be able to investigate deformation progression throughout the test. Therefore, the Photron FastCam high speed camera was used to record the tests. For all of the tests, frame rate was chosen as 10000 fps.

Dropping weights and dropping velocities depend upon the specimen dimensions. For the specimens having common length same dropping velocity was used for both thicknesses and by using the absorbed energy values calculated from quasi-static tests dropping weight values were calculated. Test conditions are given in Table 4.2.

Table 4.2. Drop weight test conditions.

Specimen	**Dropping weight (kg)**	**Velocity (m/s)**
R125T1	14.4	9.1
R125T05	7.4	9.1
R75T1	23.4	5.1
R75T05	10.4	5.1

In Figure 4.9(a) drop weight test result of R125T1 specimen can be seen. In Figure 4.9(b), comparison of quasi-static and drop weight test results of the same specimen can be seen. When static and dynamic deformation curves are examined, both show a bilinear first region and after 10 mm of deformation a local maximum was reached. For both tests, the local peak value was observed as nearly 60 kN. Similar to quasi-static crushing test result, with the buckling of cylindirical portion, another local maximum was observed in the curve higher than the former. Different from the quasi-static test, in the dynamic test, a lower crushing displacement was observed. This difference arises because failure occurs before the end of buckling of cylindirical portion. Details of test can be seen in Figure 4.10.

In Figure 4.10 (a) deformation history from drop weight test of R125T1 specimen can be seen. View from 6 mm of deformation shows the typical initial form of axisymmetric inward dimpling mode. Along with the increase of plastic hinge radius, this mode lasts until 13 mm of deformation. At this deformation value, crushing of hemispherical portion ends and buckling of cylindirical part starts. However, as can be seen from the view of 15 mm of deformation and Figure 4.10 (b), fold formed by the deformation of hemispherical portion fractured and seperated from the structure. This can be seen in the force-displacement curve with an increase of the force value. As a result of fracture, structure lost the load bearing capacity due to the increase in strain rate.

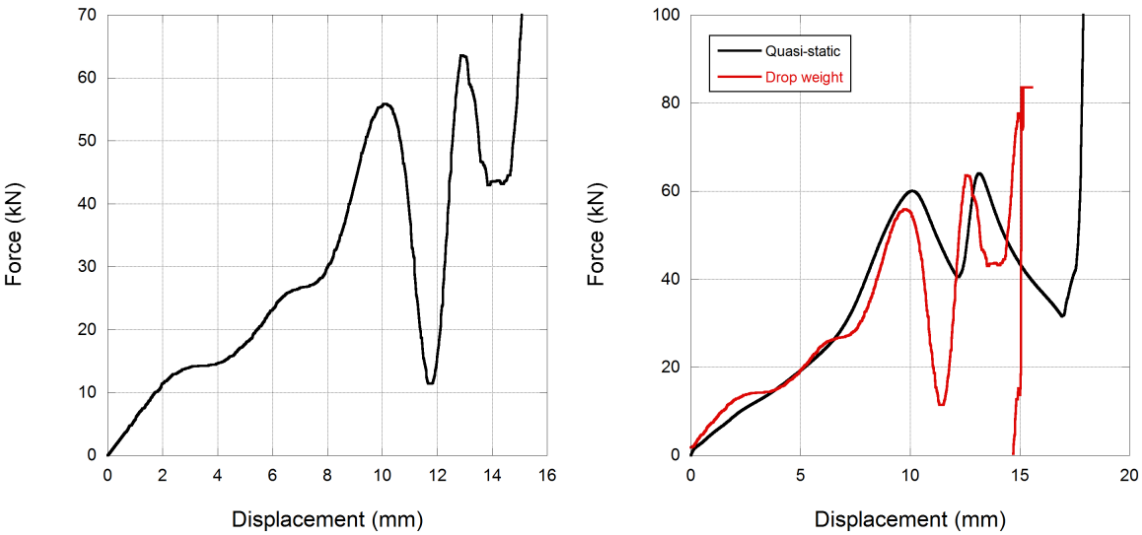

(a) (b)

Figure 4.9. (a) R125T1 specimen drop weight test result, (b) comparison of quasi-static and drop weight test results

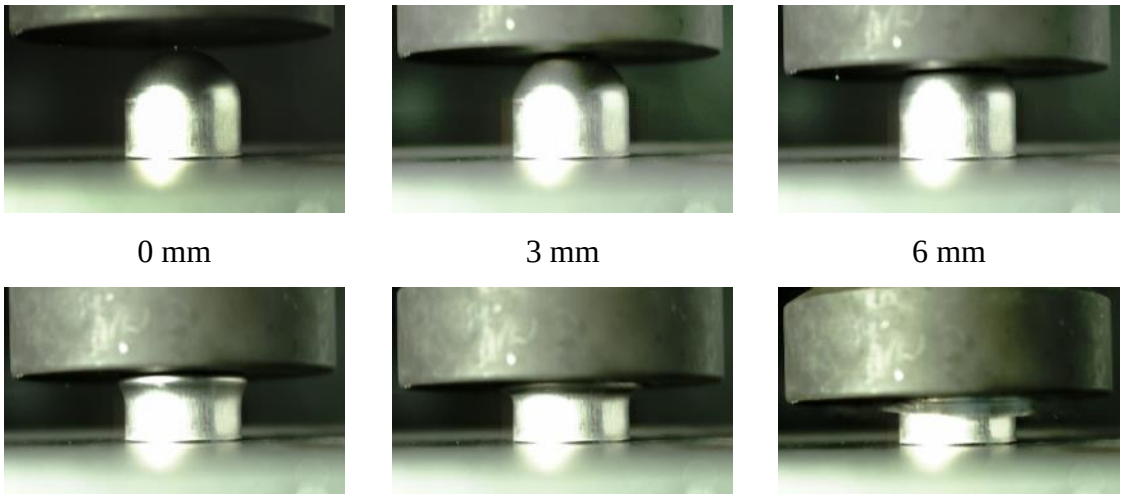

0 mm 3 mm 6 mm

10 mm 13 mm 15 mm

(a)

(b)

Figure 4.10. (a) R125T1 drop weight test history, (b) a view from the tested specimen.

In Figure 4.11, results of drop weight tests conducted on R125T05 specimen can be seen comparatively with quasi-static test results. Comparing static and dynamic deformation curves, similar to previous alternative, a local peak was observed at around 10 mm of deformation. Different from the static curve, dynamic curve shows a nonlinear behavior until the first peak. The same number of peaks were observed as in static test results; however, displacement values that peaks were observed were different. Densification deformation was also shifted as can be seen in Figure 4.11(b).

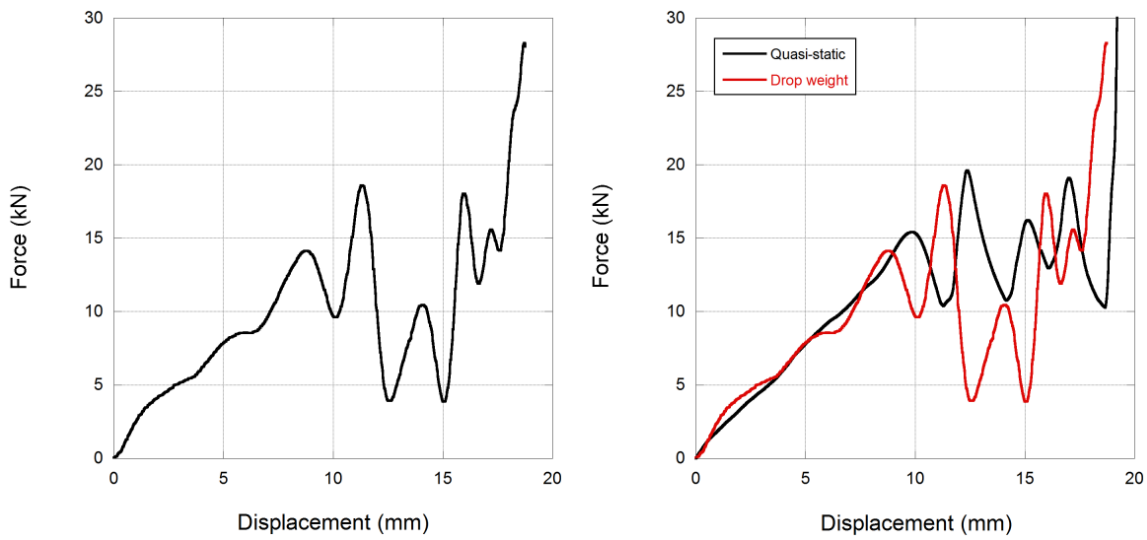

(a) (b)

Figure 4.11. (a) R125T05 specimen drop weight test result, (b) comparison of quasi-static and drop weight test results.

In Figure 4.12, deformation history of R125T05 specimen can be seen. Crushing of specimen starts with the axisymmetric inward dimpling mode and this mode lasts until 15 mm of deformation. Different from the static deformation progression, cylindirical segment shows an asymmetric buckling mode with three lobes. This explains the difference between force-displacement curves. Due to the strain rate sensitive nature of material, in higher strain rate, asymmetric buckling mode was observed different from the quasi-static strain rate. Besides attained inertia by the structure was contributed to the different deformation mode formation.

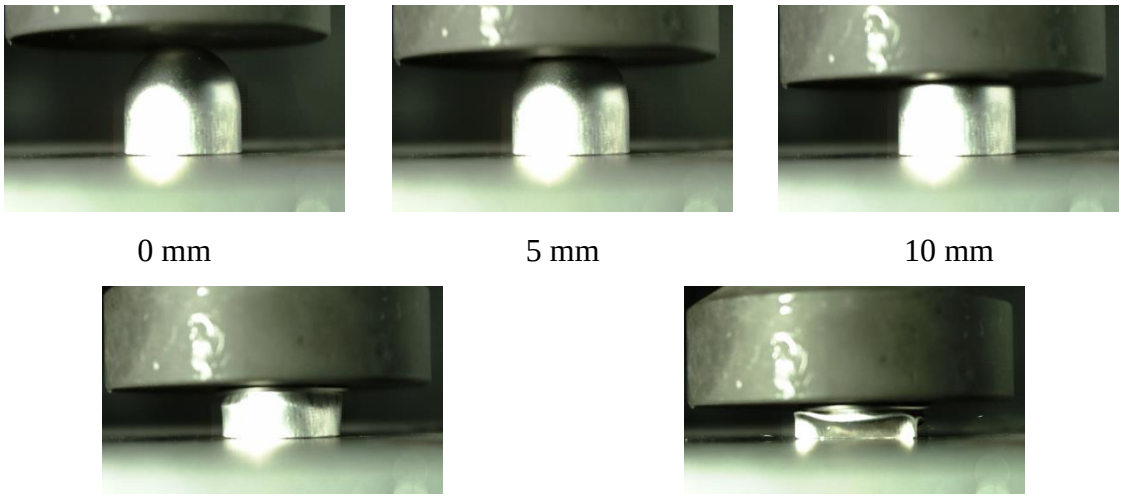

0 mm 5 mm 10 mm

15 mm 19 mm

Figure 4.12. R125T05 specimen drop weight test history.

In Figure 4.13, results of drop weight tests conducted on R75T1 specimen can be seen comparatively with quasi-static test results. As opposed to the one peak behavior observed in quasi-static test, in drop weight test, more than one local peaks were observed. Besides, experiment ended with the fracture of the specimen. It is obvious that this is due to the strain rate sensitive nature of specimen.

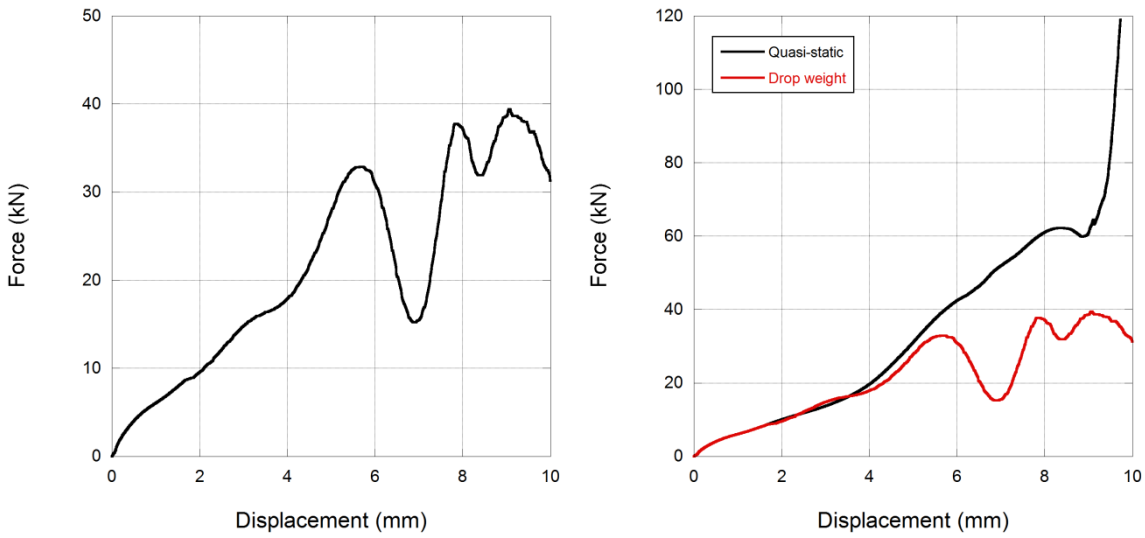

(a) (b)

Figure 4.13. (a) R75T1 specimen drop weight test result, (b) comparison of quasi-static and drop weight test results.

In Figure 4.14, deformation history of R75T1 specimens can be seen. Similar to other specimens, axisymmetric inward dimpling mode can be observed for this

specimen also. As can be seen in 9 mm deformation view, deformation of hemispherical part ends and cylindirical portion starts to deform. Besides, as can be seen in 10 mm deformation view, as test proceeds, hemispherical part seperates from structure as a ring. This results in the difference between static and dynamic curves.

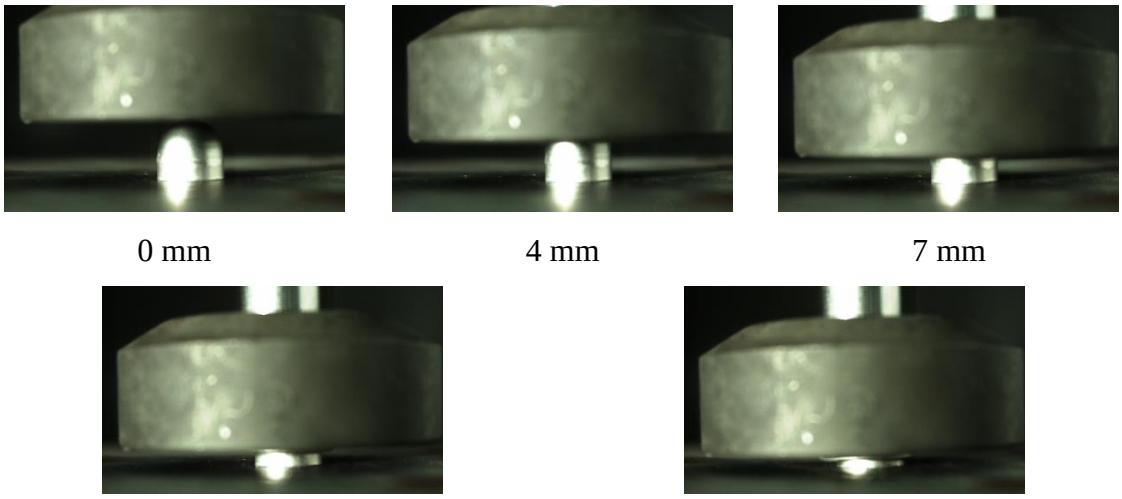

0 mm 4 mm 7 mm

9 mm 10 mm

Figure 4.14. R75T1 specimen drop weight test history

In Figure 4.15, results of drop weight test conducted on R75T05 specimen can be seen. As can be understood by comparing static and dynamic curves, both exhibits similar deformation mode. Different from the static curve, dynamic curve shows a nonlinear behavior until the first peak. After nearly 6 mm of deformation, a local peak was observed with nearly 15 kN of force. A higher load drop was observed and a second peak was nearly found at same force level. Both second peak and densification deformation values were shifted nearly 1.5 mm.

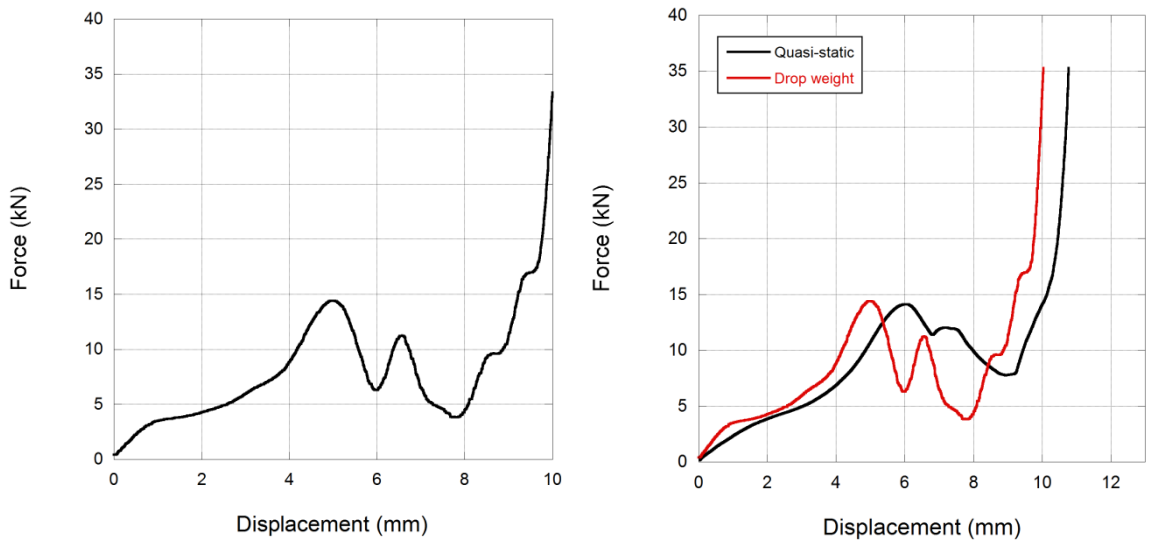

(a) (b)

Figure 4.15. (a) R75T05 specimen drop weight test result, (b) comparison of quasi-static and drop weight test results.

In Figure 4.16, deformation progression of R75T05 specimen can be seen. As can be seen in figure, deformation of hemispherical portion lasts until 6 mm of deformation. Subsequently, deformation of cylindirical portion starts. As in quasi-static test, cylindirical portion crushes with asymmetric mode. Three lobes were observed. Apart from the slight difference observed in deformation values, a similar result to quasi-static one was found.

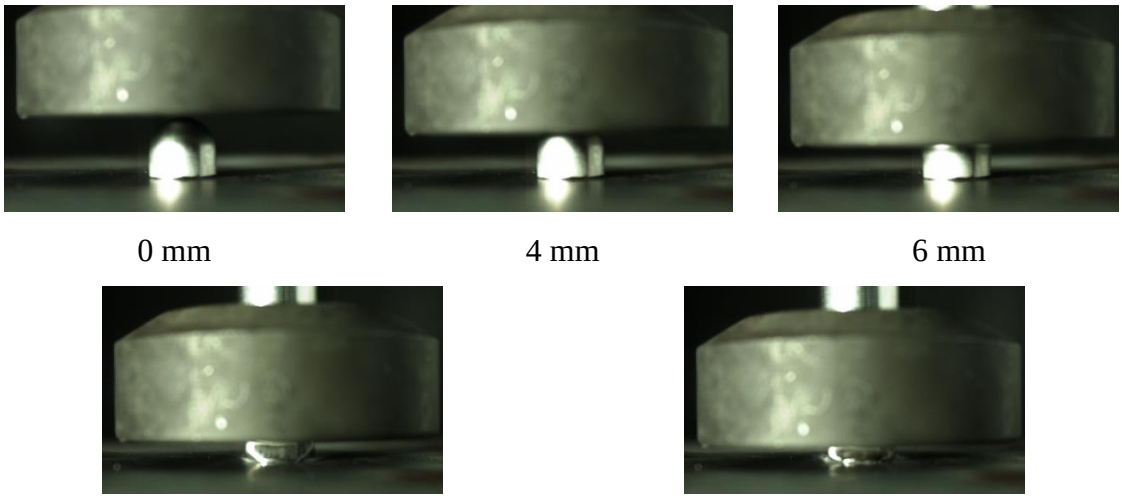

0 mm 4 mm 6 mm

9 mm 10 mm

Figure 4.16. R75T05 specimen drop weight test history.

4.3. Comparison of Experimental and Numerical Results of Combined Geometry Shell Structures

In this section numerical results for both quasi-static and low velocity crushing of combined geometry shell structures were given. The first part contains necessary details directly concerning the simulations of crushing of combined geometry shells. In the second part comparison of experimental and numerical results was given.

4.3.1. Details of Numerical Simulations of Quasi-Static and Low Velocity Crushing

Material model for AISI 304L stainless steel was already given in Table 3.5. As explained before, numerical specimens used in the crushing simulations was numerically manufactured by “Restart Analysis Technique” of LS-DYNA and “dynain” file method was used.

In the quasi-static crushing simulations mass scaling was applied to keep the simulation times within reasonable limits. The mass scaling method, as already explained in detail, can be expressed as; the density of material was scaled down by a factor of 1000 and this allowed increasing the loading rate of simulation by a factor of 100 and the solution time was remained in acceptable limits. The ratio of the kinetic energy (KE) to the total internal energy was found to be less than 4% over the period of the crushing, ensuring the quasi-static strain rates. For crushing simulations, model included three parts: upper moving compression plate, combined geometry shell specimen manufactured in former deep drawing simulation, and stationary bottom supporting plate. The plates were modeled using eight-node constant stress solid elements. Plates were assumed to be rigid and modeled by using rigid material model of LS-DYNA. Combined geometry shell specimen was modeled by using Belytschko-Tsay shell elements with seven integration points through the thickness. Two different types of contact definitions were used in the numerical simulations. For the specimen, an automatic single surface contact was adopted to account for the contact between folds during deformation, while an automatic surface to surface contact was applied between the specimen and rigid plates. A static friction coefficient of 0.3 and a dynamic

friction coefficient of 0.2 between all surfaces in-contact were assumed in the simulations. In Figure 4.17 simulation model steps can be seen.

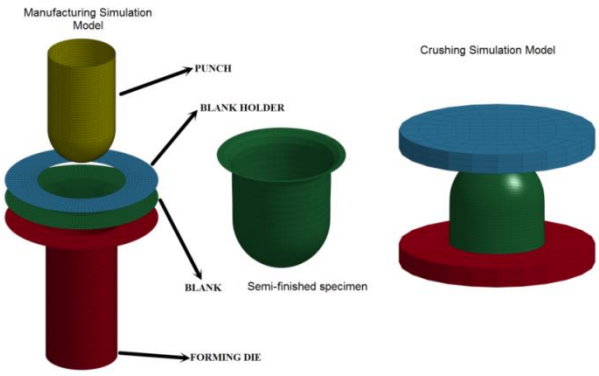

Figure 4.17. Deep-drawing model and crushing simulation model.

4.3.2. Comparison of Experimental and Numerical Results

In this section, previously reported experimental results are analyzed comparatively with quasi-static and low velocity crush simulation results. As mentioned before, numerical specimens were prepared by using so-called "Restart Analysis Technique" of LS-DYNA. Subsequently, this numerical specimens were used in crush simulations. Graphical results for some selected tests and simulations are given in Figure 4.18.

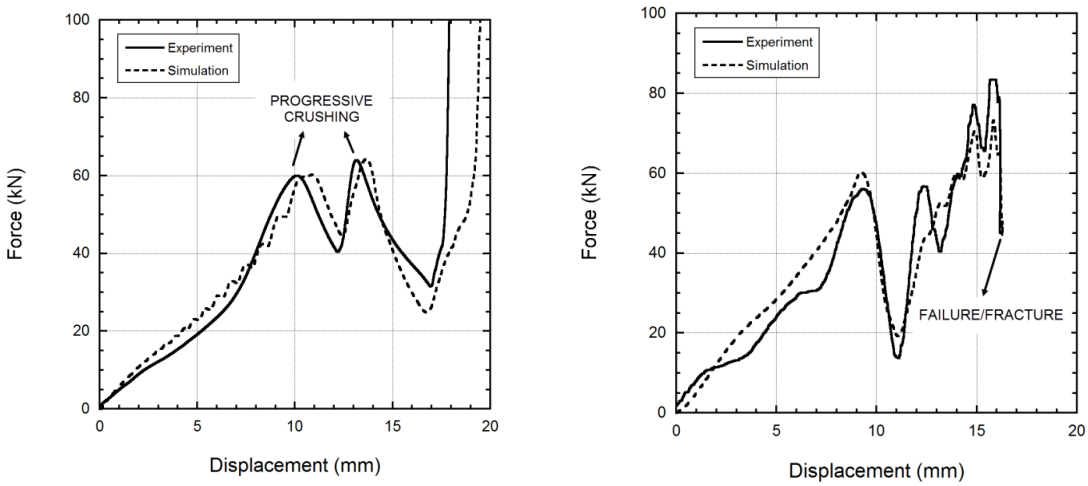

(a) (b)

Figure 4.18. (a) R125T1 quasi-static test and simulation result, (b) R125T1 drop weight test and simulation result.

In Figure 4.18 (a) and (b) show the comparison of simulation results of quasi-static and drop weight tests of R125T1 specimen. Numerical simulations achieved a good agreement with experimental results in terms of deformation modes and force-displacement characteristics. Besides, as can be seen in Figure 4.18 (b) damage observed in drop weight test of R125T1 specimen was simulated properly.

In Figure 4.19, quasi-static and drop weight experiment and simulation results comparisons were given in terms of deformation progression. As can be seen in Figure 4.19 (a), there is no sign of damage (tearing, fracture) seen in quasi-static test, and deformation mode was properly modeled in numerical simulation.

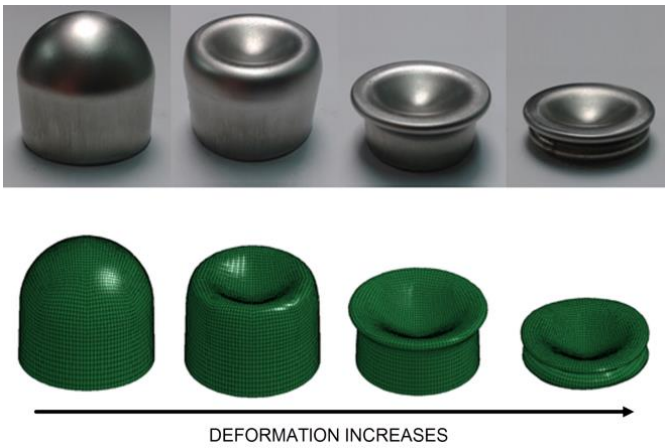

(a)

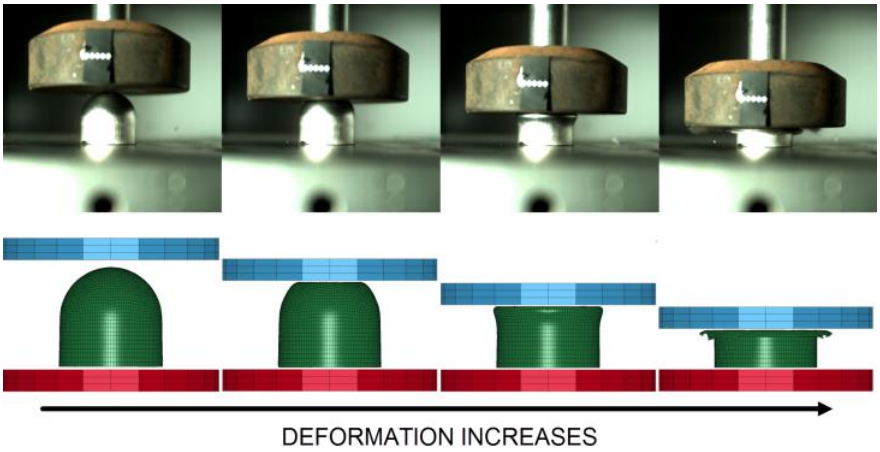

(b)

Figure 4.19. R125T1 specimen (a) quasi-static test and simulation and (b) drop weight test and simulation result.

Differently from quasi-static experiment result, R125T1 specimen was damaged in drop weight test and numerical model achieved to model damage progression also

(Figure 4.19 (b)). As deformation starts, inward dimpling starts to form and apex turns upside down progressively. As deformation progresses, deformation rate increases (geometrical effect; from point contact to line contact) and damage occurs. As previously reported, as strain rate increases, failure strain decreases.

For an energy absorbing material or structure, results of quasi-static and low velocity crushing experiments must be analyzed in terms of different aspects. Important parameters such as peak load, mean load, absorbed and specific absorbed energy values were calculated and results were compared for combined geometry shell structures. Experimental results were tabulated in Table 4.3 and related parameters were given schematically in Figure 4.20.

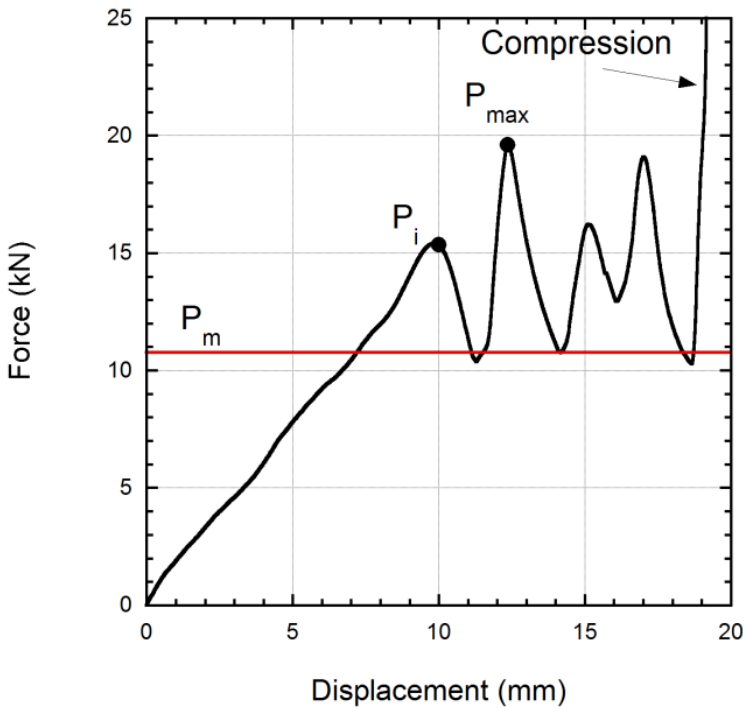

Figure 4.20. Parameters for crushing investigation.

Table 4.3. Quasi-static and drop weight experiment results of combined geometry shell structures.

Specimen	**Speed (m/s)**	**Dropping weight (kg)**	P_i **(kN)**	P_{max} **(kN)**	P_m **(kN)**	**Energy (J)**	***SAE*** **(kJ/kg)**	**Comp. (mm)**
R75T05	13.01e-06	-	14.8	14.8	7.9	79.3	39.6	10.0
R75T05	5.1	10.4	14.9	16.2	8.5	96.5	48.2	11.3
R75T1	13.06e-06	-	62.7	62.7	33.2	323.6	107.9	9.7
R75T1	5.1	23.4	34.8	48.8	27.0	289.3	96.4	10.7
R125T05	23.06e-06	-	15.5	19.6	10.7	203.8	33.9	19.0
R125T05	9.1	7.4	15.4	23.0	9.2	189.7	31.6	20.5
R125T1	22.62e-06	-	59.8	64.0	33.8	600.0	50.0	17.7
R125T1	9.1	14.4	56.1	77.0	33.5	525.1	43.7	15.7

In Table 4.3 quasi-static and drop weight experiment results were tabulated. In the table P_i is the first peak of force – displacement curve corresponding to the deformation of hemispherical portion, P_{max} is the absolute maximum peak of force – displacement curve except for densification (for some of the specimens this value is equal to P_i), P_m is the mean force, and *SAE* is specific absorbed energy. Some of them can be seen in Figure 4.20.

Maximum P_i was observed in the experiment of R75T1 specimen, whereas minimum P_i was observed in the experiment of R75T05 specimen. The highest P_{max} was obtained from the experiment of R125T1 specimen and the lowest value was found for the experiment of R75T05 specimen.

Maximum load transmitted to the protected structure (P_{max}) by structures absorbing energy by crushing mechanism, must be minimized. On the other hand, in order to increase energy absorption capacity, mean force value must be maximized. In the literature, a parameter called crushing force efficiency (*CFE*) was defined in order to evaluate this phenomena. In an ideal energy absorber or for foam-like materials, *CFE* is aimed to be equal to unity. Results given in Table can be used to evaluate *CFE* of the structures.

According to results given in Table 4.3, *CFE* values vary between 0.4 and 0.55 for all of the cases. The maximum *CFE* was calculated for drop weight test of R75T1 specimens and the lowest *CFE* was calculated for drop weight test of R125T05

specimen. As can be deduced from results that, for all of the specimens and for static speeds, as thickness increases *CFE* decreases. For dynamic test results, this is vice versa. For the specimens having the same thickness, in static loading *CFE* increases with increasing radius. On the other hand *CFE* decreases with increasing radius in dynamic loading. Besides, for R125 specimens as test speed increases CFE decreases and this is different for R75 specimens.

By investigating P_i, P_m and P_{max} values, the segment that maximum load was observed can be detected. This information can be useful for optimization studies such as where buckling initiators can be placed etc.

Besides the previously mentioned parameters, it is important to calculate specific energy absorption in order to choose geometrically optimized structures. In this manner, *SAE* values can be used to identify the effectiveness of structures. As given in the Table 4.3., the highest *SAE* value was calculated for quasi-static test of R75T1 specimen. The lowest *SAE* value, on the other hand, was calculated for drop weight test of R125T1 specimen. As thickness increases *SAE* increases for all of the specimens at all of test speeds. For the specimens having the same radius, as thickness increases, P_m and *SAE* values increase. On the other hand, for the specimens having the same thickness, as radius increases *SAE* values decrease and P_m values increase.

Besides given explanations for results in the table, results can be compared considering deformation mode change or damage occurence caused by an increase in deformation velocity. For instance for R75T1 specimen, P_{max} was observed as 62.7 kN in static test and this value is 34.8 kN for dynamic test result. This phenomena is a result of failure in the R75T1 specimen when loading rate increased which is mentioned before.

As can be deduced from experimental results, except for R75T05 and R75T1 specimens, P_{max} and P_i values are different from each other and maximum load was obtained at the deformation of cylindrical portion.

For a more detailed analysis and comparison of experimental and numerical results one must refer to related project (Taşdemirci et al. 2014) supported by TÜBİTAK as already mentioned.

CHAPTER 5

EFFECT OF HEAT TREATMENT ON CRUSHING AND ENERGY ABSORPTION BEHAVIOR OF COMBINED GEOMETRY SHELL STRUCTURES

The aim of the current part of the study is to determine the effect of heat treatment on the energy absorption characteristics and crushing behavior of the combined geometry shells (hemispherical cap and cylindrical segment) at quasi-static and dynamic strain rate regimes. The previous chapter reported the results for as-received combined geometry shells. Previous results revealed that failure/fracture of some specimens occurred instead of dissipating energy by plastic deformation. Therefore in this chapter, heat treatment was presented as a stress relieving procedure to have a more ductile material in order to increase absorbed energy without failure/fracture and change deformation modes.

The heat treatment process conducted in this study consisted of two main stages, namely annealing at 1100 ^{o}C and air quenching immediately after the finish of annealing process. The effective heat treatment process was determined in this study by repeating the process with three different durations; 0.5, 2.0, and 4.0 hours and effective heat treatment duration was determined by comparison of preliminary quasi-static crushing results of specimens. As a result of comparison 2.0 hours were found to be suitable and all specimens were heat treated for 2.0 hours. This result can also be verified considering the results reported for a similar material by Weber et al. (Weber, Martin, and Theisen 2012). Their results showed that with aforementioned treatment conditions, an intermediate grain size can be achieved and a tough and ductile material can be obtained. The pictures of prepared as-received and heat-treated combined shells are shown in Figure 5.1.

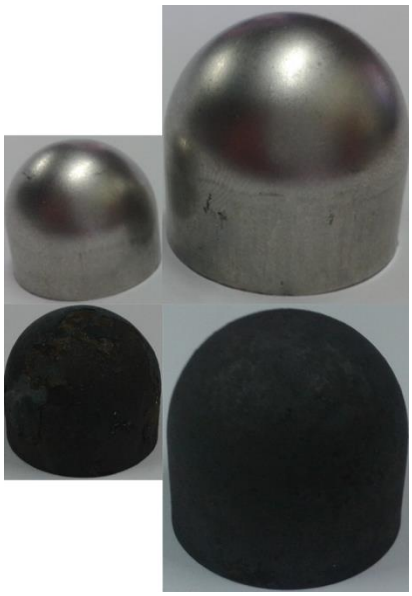

Figure 5.1. As-received and heat-treated combined geometry shell specimens.

5.1. Quasi-Static Crushing Behavior of Heat Treated Combined Geometry Shells

As already mentioned, in order to determine effective heat-treatment duration, R125T05H specimens were heat-treated and quasi-static compression tests were conducted. Results can be seen in Figure 5.2.

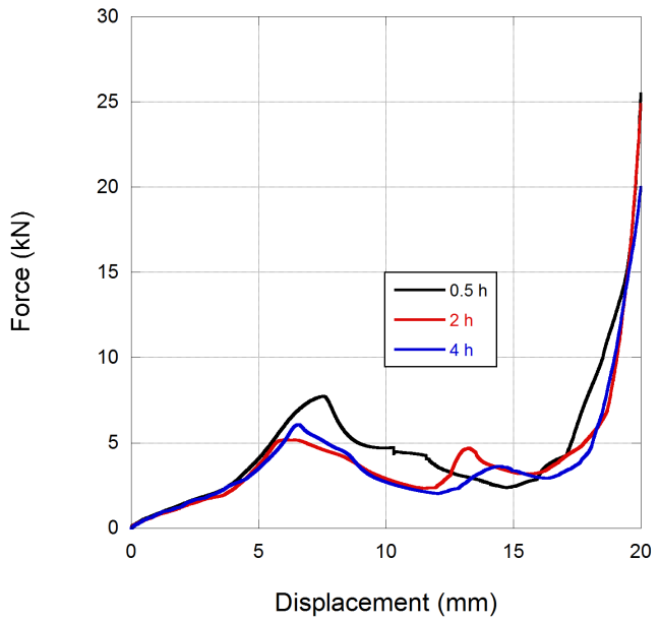

Figure 5.2. Quasi-static test results of heat-treated R125T05H specimen.

As can be seen from the figure, at 1100 ^{o}C, duration of heat treatment process changes the crushing response of the structure. As obvious, 2h and 4h heat treated specimens show nearly the same behavior except for the small differences. Therefore, in the study, heat treatment of all structures conducted at 1100 ^{o}C for 2 hours.

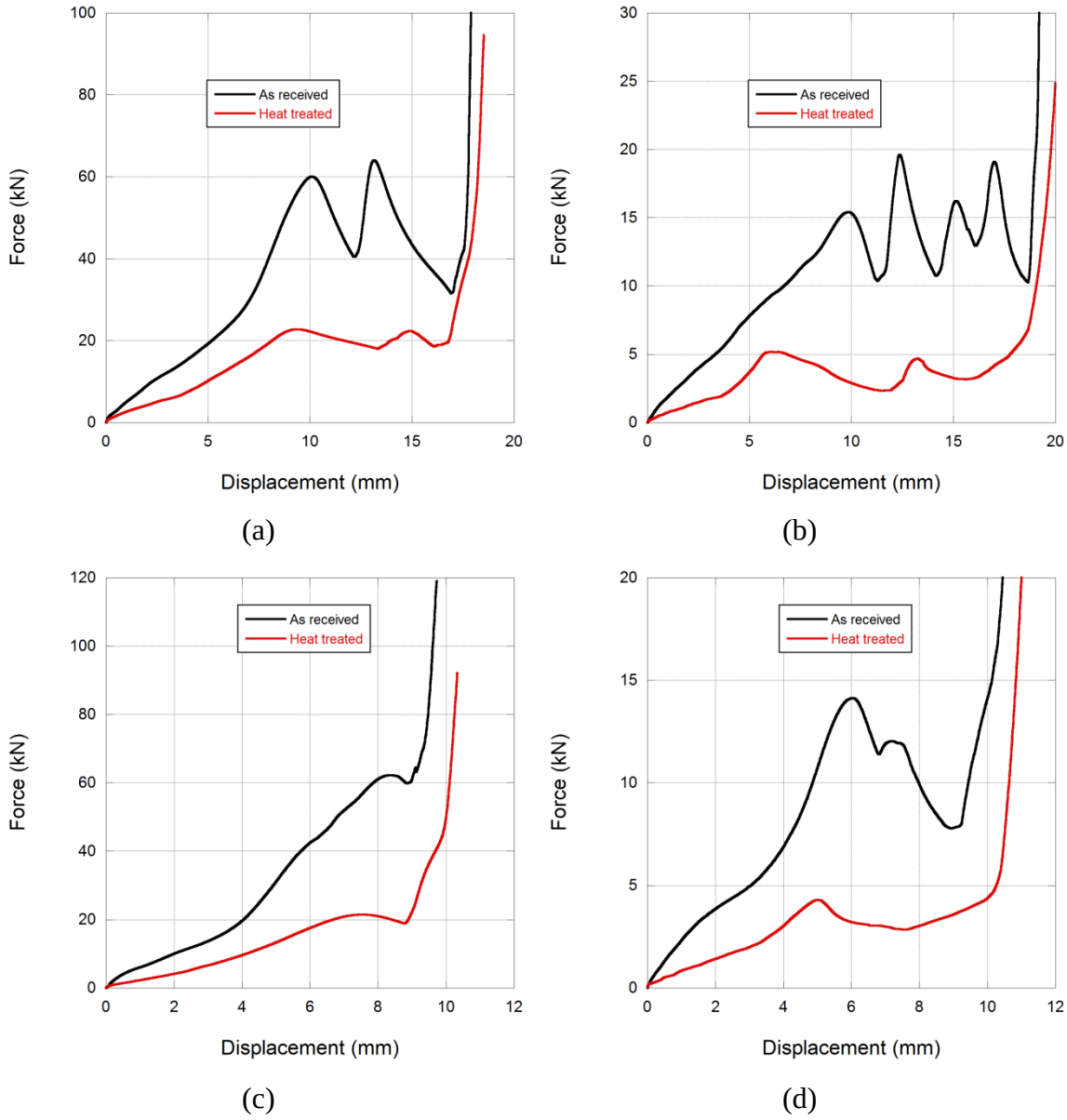

Figure 5.3. Effect of heat treatment on quasi-static crushing behavior of; (a) R125T1, (b) R125T05, (c) R75T1, (d) R75T05 specimens.

In Figure 5.3 results of quasi-static crushing tests of heat treated specimens can be seen comparatively with previously reported results of as-received specimens. As can be seen from the figure, effects of heat treatment are different for different specimens. When Figure 5.3 (a) investigated, heat treated R125T1H specimen shows

same deformation mode as as-received specimen except for the reduced local peak values. Deformation values at local peaks were shifted. First part of the curve corresponding to deformation of hemispherical part was observed to be bilinear as in as-received specimen. Second peak corresponding to buckling of cylindrical part was also observed for heat treated specimen.

Figure 5.3 (b) shows the effect of heat treatment on quasi-static crushing behavior of R125T05H specimen. Different from the linear first part corresponding to deformation of as-received specimen, heat treated specimen shows bilinear behavior. Local peaks were reduced and deformation values were shifted. Instead of three local peaks corresponding to buckling of cylindrical part in as-received specimen, only one local peak was observed and this means that, heat treatment caused a mode transformation in this strain rate regime. Densification value was also shifted.

As can be seen from Figure 5.3 (c), R75T1H specimen showed same deformation behavior except for the little shift observed at local peak value. Local peak corresponding to the deformation of hemisphere was observed nearly one third of peak of as-received material. Differently, R75T05H specimen (Figure 5.3 (d)) shows different deformation behavior from as-received specimen. Second local peak vanished and deformation value at first peak and densification was shifted.

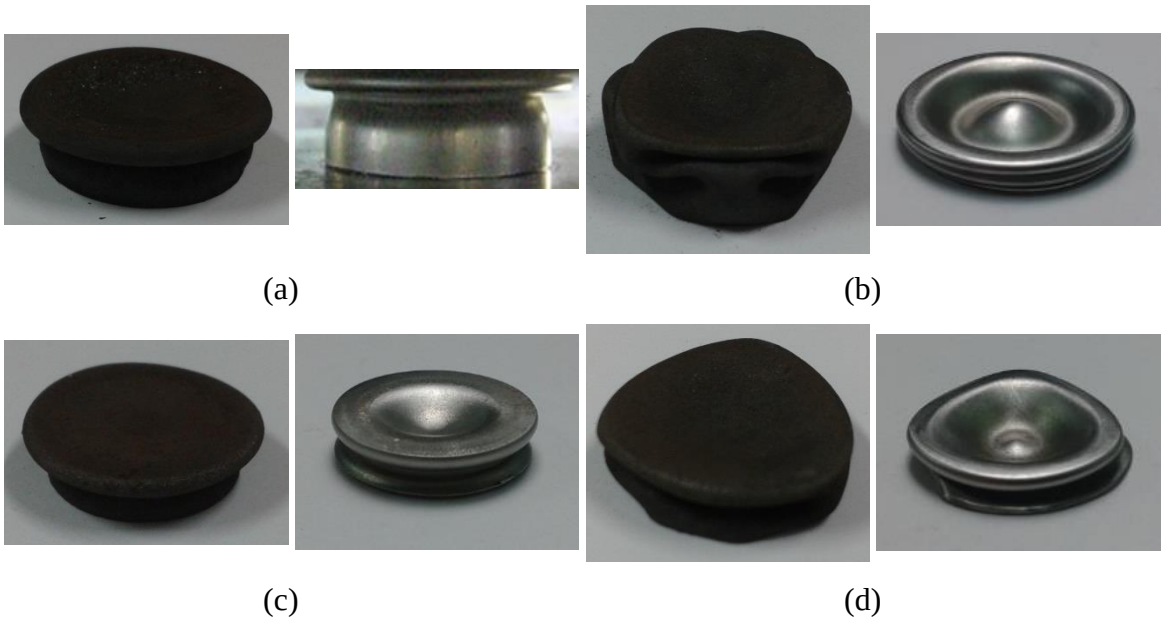

Figure 5.4. Deformed views of heat treated and as-received specimens; (a) R125T1, (b) R125T05, (c) R75T1, (d) R75T05 specimens.

Deformed views of heat treated and as-received specimens can be seen in Figure 5.4, comparatively. As a conclusion from the comparison between quasi-static crushing results of as-received and heat treated specimens, specimens having 1 mm thickness showed no deformation mode transformation, on the other hand, 0.5 mm thick specimens showed mode transformation with heat treatment. Peak load reductions were observed as a result of relief from strain hardening caused by manufacturing method.

5.2. Low Velocity Crushing Behavior of Heat Treated Combined Geometry Shells

In this section, effect of heat treatment on low velocity crushing behavior of combined geometry shells is investigated. It was previously mentioned that effective heat treatment duration at 1100 ^{o}C was chosen as two hours. Therefore, specimens used in low velocity crushing tests were also heat treated for two hours. Drop weight test conditions of heat treated specimens can be seen in Table 5.1.

Table 5.1. Drop weight test conditions for heat treated specimens.

Specimen	**Radius (mm)**	**Thickness (mm)**	**Dropping weight (kg)**	**Velocity (m/sn)**
R125T1H	12.5	1.0	29.4	4.5
R125T05H	12.5	0.5	6.4	4.5
R75T1H	7.5	1.0	33.4	5.1
R75T05H	7.5	0.5	9.4	5.1

In Figure 5.5, low velocity crushing test results of heat treated specimens can be seen comparatively with quasi-static crushing test results. As can be seen, except for the R75T1H specimen, first peak corresponding to the deformation of hemispherical portion was observed higher than the quasi-static first peak. In none of the tests, specimen densified. Except for R75T1H specimen, specimens showed nearly the same deformation behavior as quasi-static specimens.

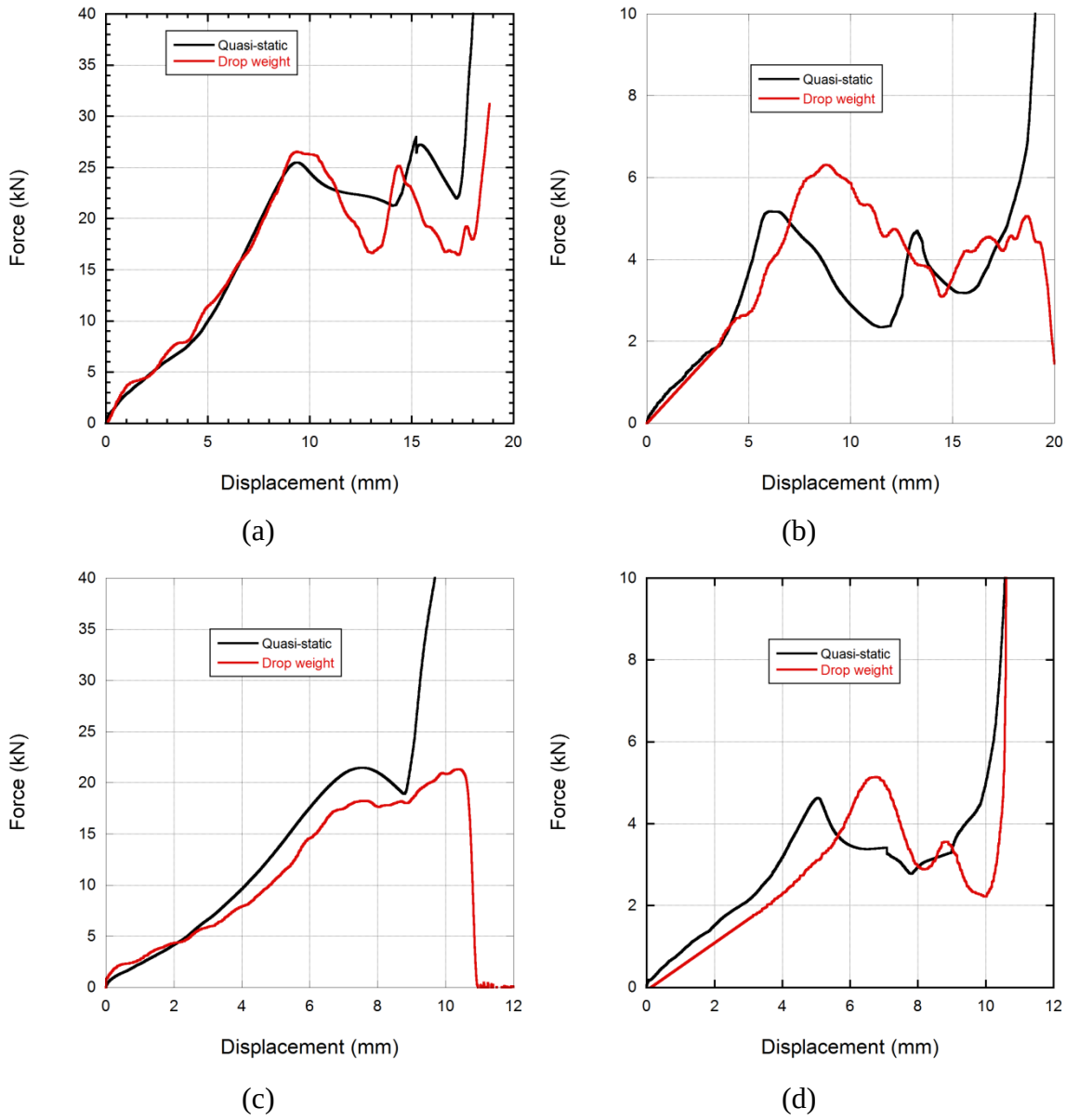

Figure 5.5. Effect of heat treatment on low velocity crushing behavior of; (a) R125T1H, (b) R125T05H, (c) R75T1H, (d) R75T05H specimens.

In Figure 5.6, deformed views of heat treated low velocity test specimens can be seen. As can be seen in Figure 5.6. (a), R125T1H specimen deformed in symmetric mode different from the other types. When R75T1H specimen was investigated (Figure 5.6. (c)), premature failure on cylindrical portion was observed and it is before the end of deformation of hemispherical part. That is the main reason of lower first peak observation in Figure 5.5 (c). As seen, none of the specimens reached the densification point.

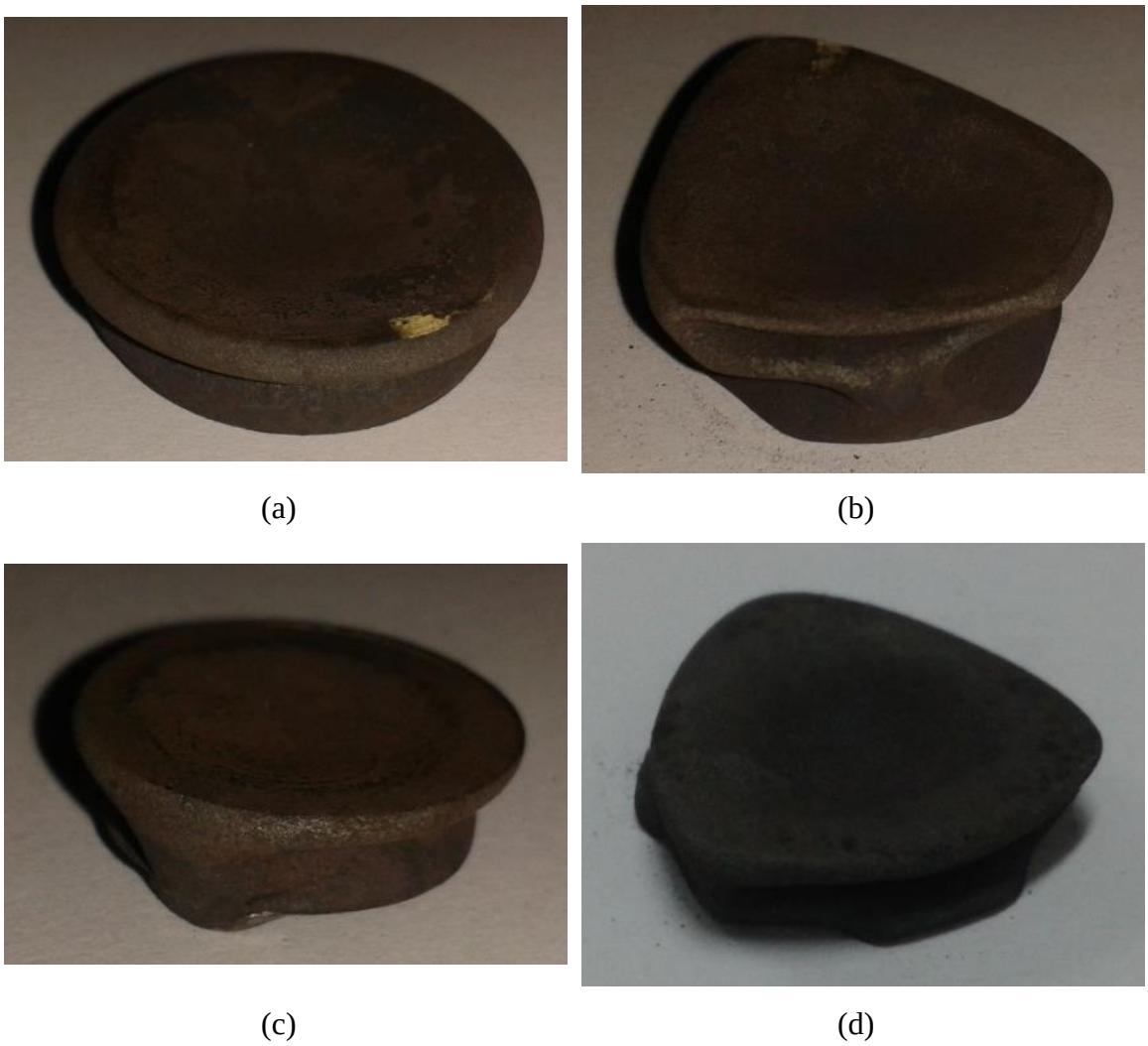

Figure 5.6. Deformed views of heat treated low velocity test specimens; (a) R125T1H, (b) R125T05H, (c) R75T1H, (d) R75T05H specimens.

5.3. Comparison of Experimental and Numerical Results

In this section, previously reported experimental results are analyzed comparatively with quasi-static and low velocity crushing simulation results of heat-treated specimens. Besides results were also compared with the results of as-received specimens. As mentioned before, numerical specimens were prepared by using so-called “Restart Analysis Technique” of LS-DYNA. In order to model the effect of heat-treatment on the deformation behavior of combined geometries, residual strain and stress history was omitted and excluded from the calculations and only thickness variations were taken into account for simulations of heat-treated specimens. Subsequently, this numerical specimens were used in crushing simulations. Quasi-static tensile tests were also conducted on heat-treated tension coupons to check the variation

of material properties after heat-treatment. A negligible difference was observed but parameters obtained from heat-treated specimens were used and given in Table 5.2 along with the parameters obtained from as-received samples.

Table 5.2. Johnson–Cook model properties of as-received and heat-treated AISI 304L stainless steel used in numerical models.

ρ (kg/m^3)	G (GPa)	E (GPa)	υ	A (MPa)	B (MPa)	n	C
7830	80	193	0.305	264	1567.33	0.703	0.067

$D1$	$D4$	A_{HT} (MPa)	B_{HT} (MPa)	n_{HT}
0.53467	-0.01913	232	1272.6	0.8288

The experimental and numerical load-deformation curves of different specimens at quasi-static and dynamic strain rates were shown in Figure 5.7. Similar to as-received specimens, load-displacement response followed the progressive buckling behavior, except for R75T1 specimens. Firstly flattening of apex occurred which was followed by axisymmetric buckling of spherical region, subsequently asymmetric hinges was formed in hemispherical region, then buckling of cylindrical portion initiated and deformation finished with compaction of all folds formed. Comparing the peak values of quasi-static tests of R125T05 and R125T05H specimens, a substantial decrease is obvious as a result of heat treatment. On the other hand, in the drop weight experiment of R125T1 a fracture ended the buckling of specimen due to the excessive plastic strain resulted from manufacturing as reported previously. Heat treatment caused some amount of relief on the effects of manufacturing and for R125T1H specimen fracture did not occur and a long stroke was achieved successfully. Quasi-static R125T05H and R75T1H simulation results showed additional peak forces different from experiments even though the results were in an acceptable error level. Peak loads were overestimated for R125T05H quasi-static specimen and this is the case for mean crush load also. In the simulation of drop weight test of R125T1H specimen, deformation mode was represented well; on the other hand numerical peak loads are a little underestimated. For the simulation of drop weight test of R75T05H specimen, peak forces for crushing of constituents calculated higher and deformation values at peak forces was a little underestimated. Dadrasi

(Dadrasi 2011) associated the difference between experimental results and numerical estimations with the presence of imperfection in the specimens.

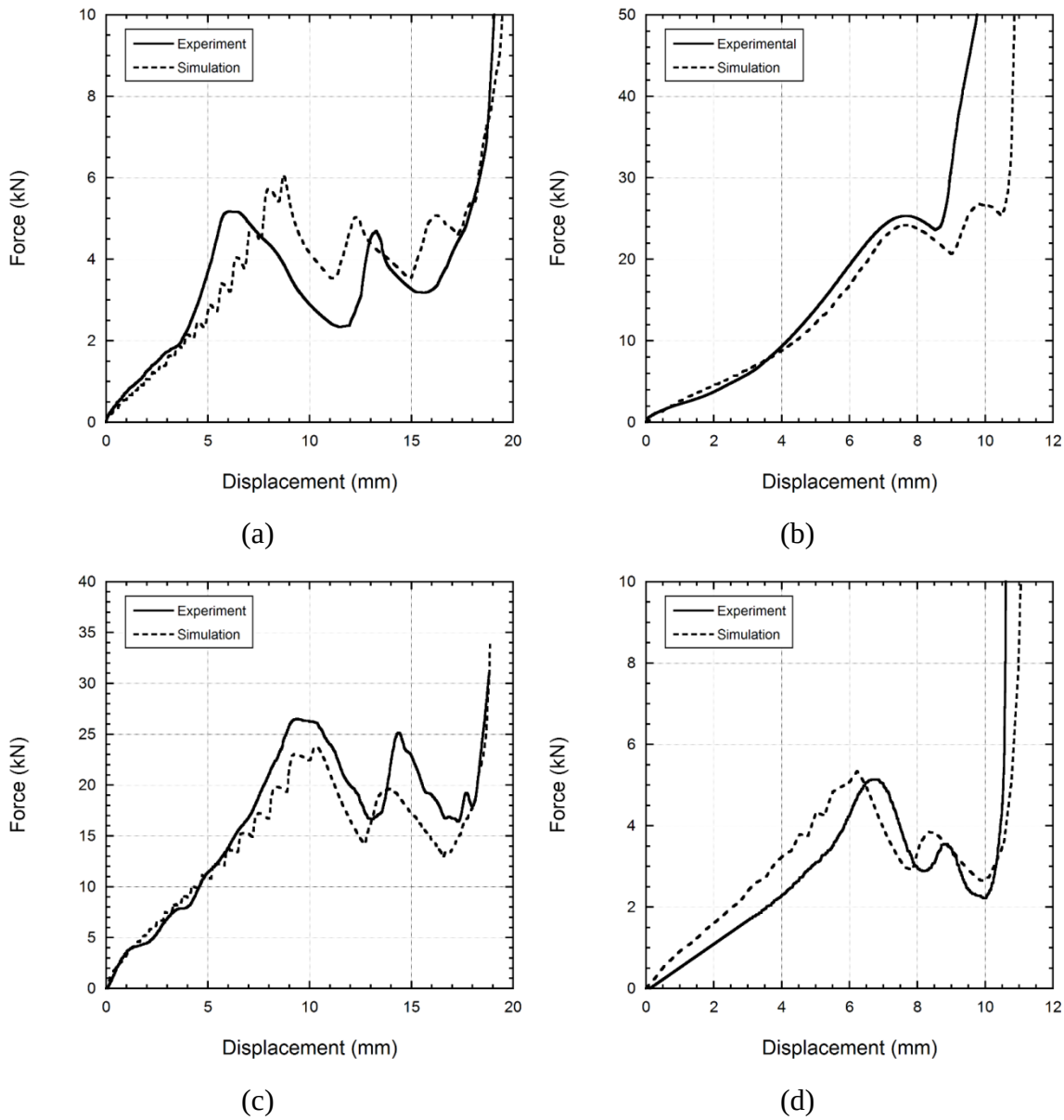

Figure 5.7. Experimental and numerical force-displacement curves of (a) quasi-static R125T05H, (b) quasi-static R75T1H, (c) drop weight R125T1H, and (d) drop weight R75T05H specimens.

In Figure 5.8., deformation sequence for quasi-static and drop weight tests of R125T05H are given. Both static and dynamic numerical models represented the crushing behavior of heat-treated combined geometries with a good agreement.

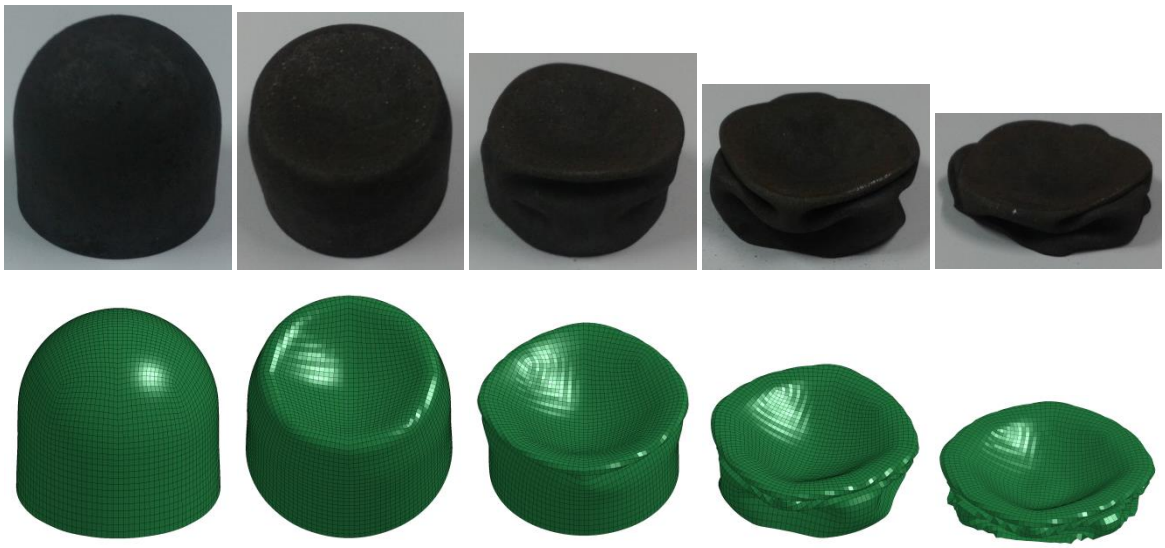

0 5 10 15 19

(a)

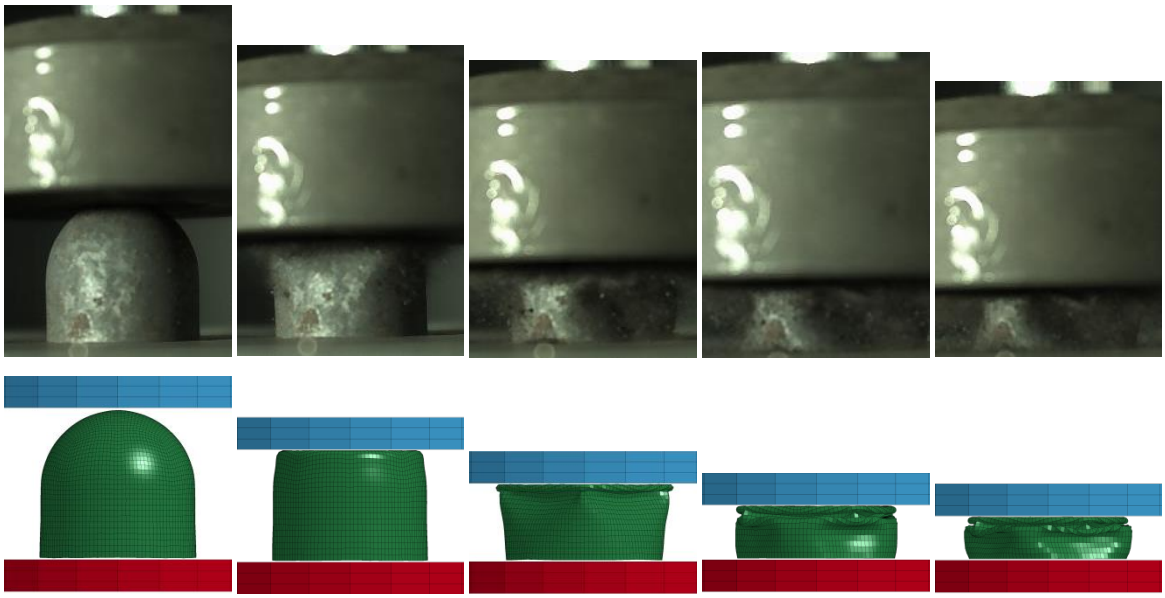

0 6.3 11.6 15.2 16.9

(b)

Figure 5.8. Experimental and numerically deformed pictures of (a) quasi-static R125T05H and (b) drop weight R125T05H specimens.

In Table 5.3, experimental and numerical results of quasi-static and dynamic crushing of heat-treated combined geometry shells were given comparatively. Maximum initial peak value was observed in the drop weight test of R125T1H specimen as 26.54 kN which is 14 % greater than that of quasi-static test (22.8 kN). This initial peak was also the global maximum load and observed at the buckling of hemispherical portion. After that a load-drop was observed and subsequent portion in

the force-displacement curve was the buckling of cylindrical portion. The highest P_{max} was observed for drop weight test of R75T1H specimen and also it has the highest absorbed energy value. The close agreement between experimental and numerical results can also be seen in Table 5.3.

Table 5.3. Experimental and numerical crushing results of heat-treated specimens.

Specimen	**Drop Mass (kg)**	**Result**	P_i **(kN)**	P_{max} **(kN)**	P_m **(kN)**	**Energy (J)**	***SAE* (kJ/kg)**	**Compression (mm)**
R75T05H	-	Exp.	4.7	4.7	2.695	27.3	13.65	10.13
		Num.	4.35	4.35	2.803	28.31	14.155	10.1
R75T05H	10.4	Exp.	5.22	5.22	2.6	33.35	16.675	12.8
		Num.	5.3	5.3	3.16	32.1	16.05	10.1
R75T1H	-	Exp.	25.2	25.2	15.58	119	40	7.6
		Num.	24.3	26.6	14.201	153.74	51.25	10.8
R75T1H	23.4	Exp.	24	33.6	15.75	173.82	57.94	11.03
		Num.	20.63	20.63	18.73	209.86	69.95	11.2
R125T05H	-	Exp.	5.2	5.2	3.3	61	10.16	18.5
		Num.	6.0	6.0	3.395	65.53	10.92	19.3
R125T05H	7.4	Exp.	6.4	6.4	4.1	69.06	11.51	16.8
		Num.	6.47	6.47	4.115	66.65	11.11	16.2
R125T1H	-	Exp.	22.8	22.8	15.6	258.8	21.6	16.6
		Num.	22.77	22.77	14.8	282.46	23.54	19.08
R125T1H	14.4	Exp.	26.54	26.54	20.56	348.93	29.077	16.9
		Num.	23.86	23.86	16.19	275.41	22.95	17.01

Among all the specimens tested in the current study, the highest P_i value was found in drop weight test of R125T1H (quasi-static test for R75T1 for as-received alternatives), whereas the lowest P_i values in quasi-static test of R75T05H (quasi-static test of R75T05 for as-received alternatives) specimen. The highest P_{max} value was attained in drop weight test of R75T1H (drop weight test of R125T1 for as-received alternatives), whereas the lowest P_{max} value in quasi-static test of R75T05H (quasi-static test of R75T05 for as-received alternatives) specimen. In order for the higher energy absorption and protection efficiency, maximum load transmitted to the structure (P_{max}) should be minimized and to increase energy absorption capacity, the mean load value should be maximized. For this purpose, crushing force efficiency (C*FE*) parameter was calculated.

The calculated *CFE* values of the quasi-statically and dynamically tested heat-treated shells are summarized in Figure 5.9. As shown in figure, CFE values vary

between 0.46 and 0.77; dynamic R125T1H specimen shows the maximum, while dynamic R75T1H specimen shows the minimum *CFE* values. Results suggest that for smaller radius specimens, as loading rate increases *CFE* decreases. For big specimens, as loading rate increases *CFE* increases too. This behavior is completely the reverse for as-received R75T1, R125T05, and R125T05 specimens. For the specimens having the same thickness, as radius increases CFE increases for both loading rates investigated. This was different for dynamically loaded as-received specimens and which is possibly the result of plastic strain due to manufacturing effect in as-received specimens.

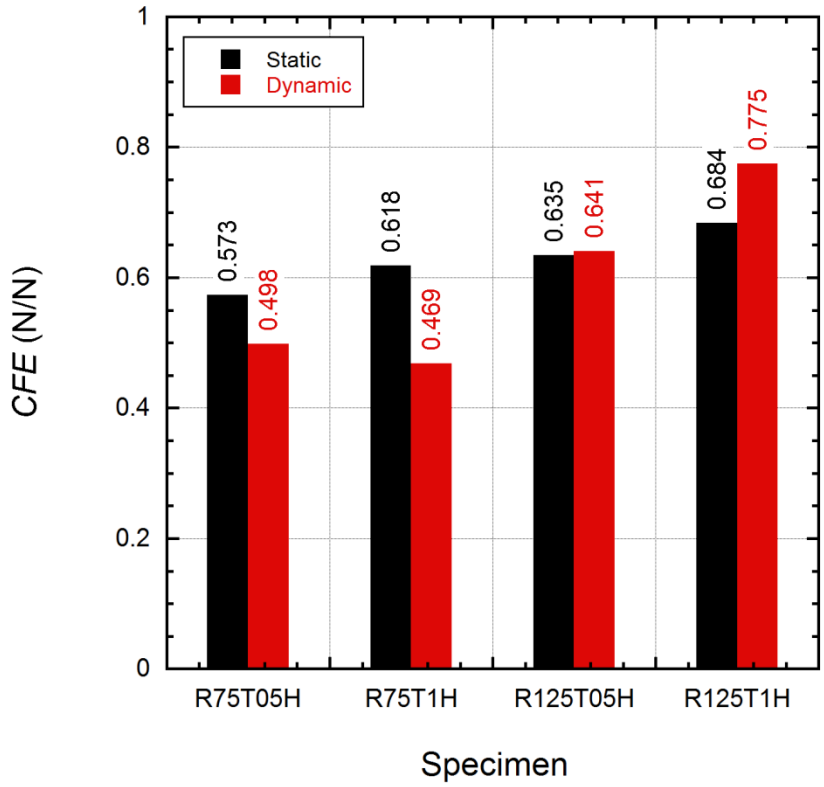

Figure 5.9. Static and dynamic *CFE* for heat-treated specimens.

In Figure 5.10 comparisons for mean crush load and *SAE* values for heat-treated and as-received specimens can be seen. As seen from the Figure 5.10 a and b heat-treatment resulted in decrease of mean crush loads and consecutively lower *SAE* values were calculated for heat-treated specimens even they have longer crushing stroke. As radius and thickness increases for heat-treated specimens a higher mean crush load was observed for dynamically loaded specimens than statically loaded ones. For the specimens having the same thickness, as radius increases mean crush load increases but *SAE* decreases which was also the same as as-received specimens. For the specimens of

same radius, thickness increase resulted in increase of both mean crush load and *SAE* values. For all of the specimens, as loading-rate increases *SAE* values increase. Interestingly this was again vice versa for as-received R75T1, R125T05, and R125T1 specimens as in the case for *CFE*.

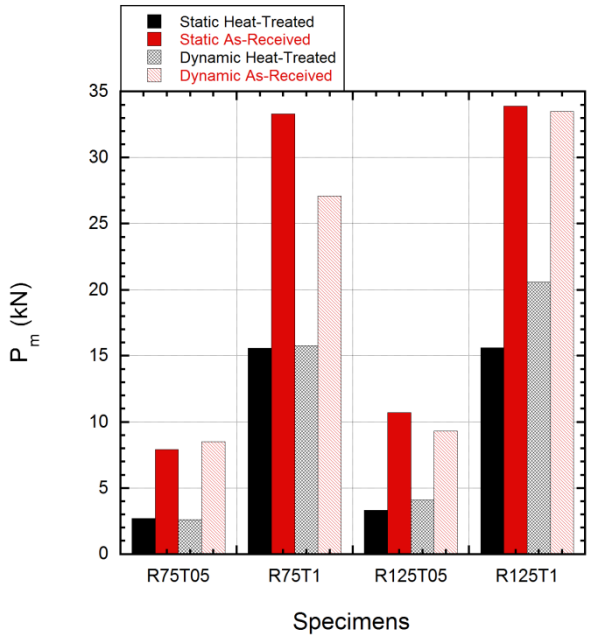

(a)

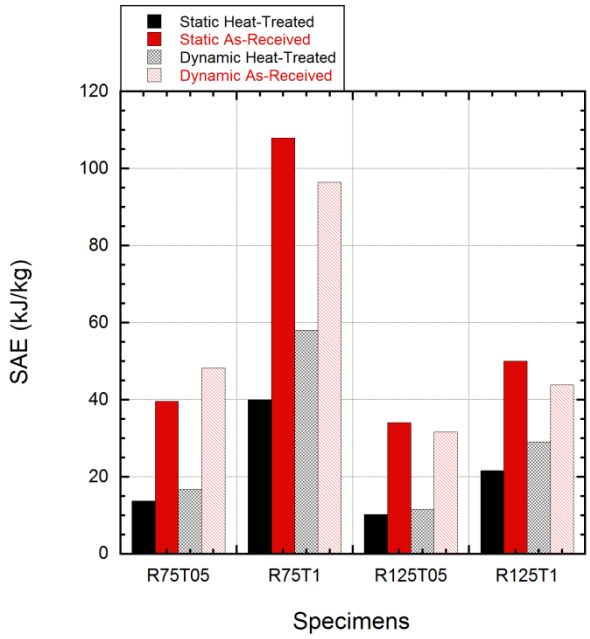

(b)

Figure 5.10. Comparison of (a) mean load and (b) *SAE* for heat-treated and as-received specimens.

CHAPTER 6

CRUSHING AND ENERGY ABSORPTION BEHAVIOR OF SANDWICH STRUCTURES WITH COMBINED GEOMETRY SHELL CORES

In this chapter, dynamic crushing and energy absorption characteristics of sandwich structure with combined geometry shell cores was investigated both experimentally and numerically. As core material, as received R125T05 combined geometry shell structure as energy absorbing structure was chosen in order to provide a macro foam effect as in the study by Palanivelu et al. (Palanivelu, Van Paepegem, Degrieck, Reymen, et al. 2011). Views from their study can be seen in Figure 2.42. They proposed that their material can be adopted in different configurations and exhibit as macro foam depending upon the loading conditions.

The static and dynamic deformation characteristics of the core material only were previously reported in corresponding chapters. In the current chapter, sandwich structures containing the above mentioned core material were prepared and tested at quasi-static, intermediate and high strain rate regimes in order to see the effect of strain rate on the crushing behavior. Confined compression tests at quasi-static and high strain rates were also conducted to understand the effect of confinement. Since the structure will be used consisting repeating number of investigated sandwich specimen and the real response of the whole structure will be in between the two cases, i.e. unconfined and confined. Numerical study was also conducted for the purposes; to better understand the deformation behavior, to investigate the variation of some parameters which cannot be experimentally determined such as stress and strain components along the section of the specimen, (3) to conduct parametrical studies once the models were well verified. The thorough coupled experimental and numerical study was used to understand deformation modes and to evaluate dynamic crushing and energy absorption behavior of sandwich structures.

6.1. Experimental Results

As mentioned, as received R125T05 combined geometry shell unit core structure was used to fabricate a sandwich structure with a cross-shaped core configuration. In the specimens, five combined geometry shells were placed into a manufacturing pattern and 1 mm thick AISI 304L stainless steel face sheets were bonded using a cyanoacrylate adhesive (Figure 6.1).

(a) (b)

Figure 6.1. (a) Manufacturing pattern on which core structures were placed, (b) R125t05 metal face sandwich structure.

Both unconfined and confined quasi-static compression tests were conducted using a Shimadzu AG-X universal testing machine (Figure 3.8) with a 300 kN load cell. Specimens were compressed at a constant cross-head speed of 2 mm/min corresponding to an initial nominal strain rate of 1.33×10^{-3} s^{-1}. A video extensometer was used to monitor motion of upper moving cross-head of the machine. Deformation scheme of unconfined quasi-static crushing experiments were recorded using a Photron FastCam high speed camera at a frame rate of 50 fps. In confined quasi-static crushing experiments a steel cylindrical ring with an outer diameter of 120 mm was used.

The force-displacement curves of three different unconfined quasi-static crushing tests and the deformation pictures of one representative test are shown in Figure 6.2 a and b, respectively. The letters given in the inset of Figure 6.2 a and b correspond to the deformation sequences. A progressive collapse characteristic which can also be verified by the help of damage sequence recordings is observed. As expected from a progressively collapsing structure, a 75 kN peak marked with (c), was

as a result of buckling of hemispherical portion, followed by a second peak of 80 kN (marked with (e)) showing the buckling of cylindrical portion. Each peak corresponding to the buckling of core structure constituents (all of them together) was followed by load decrease due to buckling load overcome where the lateral motion of formed buckling hinges with lower loads occurred. It is observed that the central combined geometry shell is radially constrained by the circumferentially placed neighboring shells and therefore its lateral motion is partly prevented by them (Figure 6.3 b). As deformation continued and the contact area (contact area between the core units and faces) increased (friction increased between core units and face sheets) compaction occurred following the second peak corresponding to the buckling of cylindrical part.

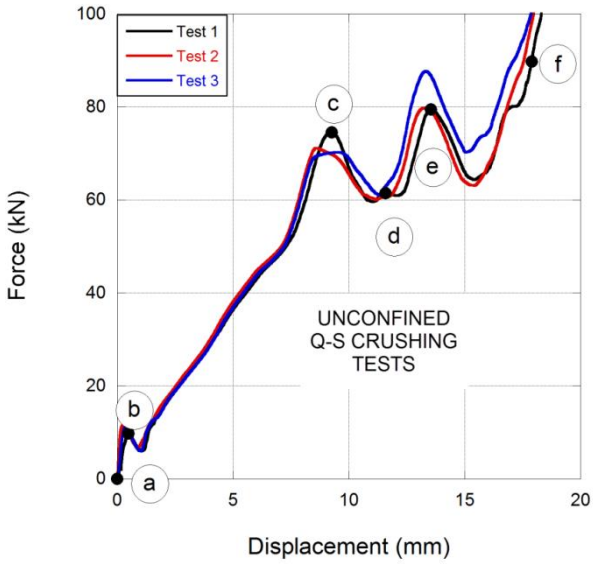

(a)

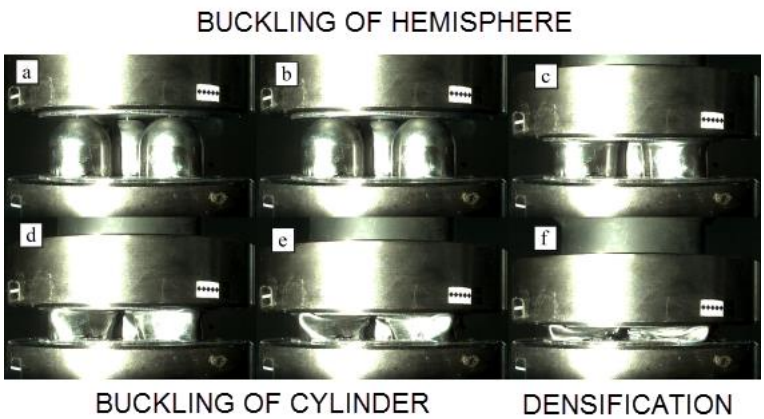

(b)

Figure 6.2. (a) The force–displacement curves of three unconfined quasi-static crushing tests and (b) deformation pictures of one representative test.

A Comparison of unconfined and confined quasi-static compression tests is given in Figure 6.3 with the top views of tested specimens. A similar progressive crushing behavior was also observed for confined quasi-static crushing test. On the other hand, greater loads at lower deformation levels were obtained for both constituents of core structures. The effect of confinement was shown with the dashed area between the force-displacement curves. In the confined test, after some deformation, rolling hinge of hemispherical portion of outer core structures started to touch with the confinement wall and their lateral motion was prevented. Therefore, greater buckling load must be exerted to overcome the support provided by the confinement. Same is valid for the cylindrical portion. Kılıçaslan et al. (Kılıçaslan et al. 2014) obtained similar results for a confined corrugated core sandwich; which was also a progressively crushing structure. In their study, as a result of confining, buckling and post buckling stresses increased.

Effect of confinement can be seen in the deformed views of specimens given in Figure 6.3 b and c. With the lack of radial boundary in an unconfined test, circumferential core units tends to deform in a triangular unsymmetrical form and deformed in a more symmetric fashion in confined test with the additional flattening of side walls of circumferential core units as a result of frictional effects between core units and the confinement wall.

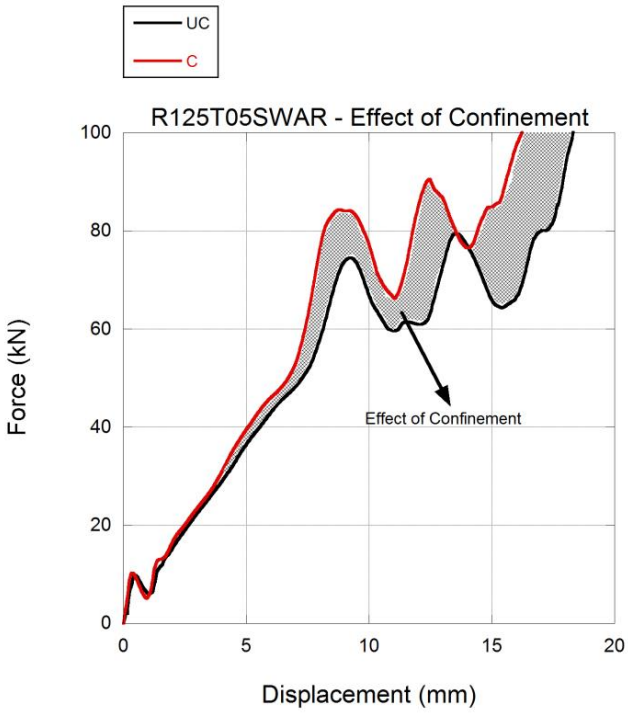

(a)

(b) (c)

Figure 6.3. (a) Comparison of unconfined and confined quasi-static crushing test results, deformed top views of (b) unconfined, and (c) confined specimen

Previously, in Table 4.3, experimental results of R125T05 core material were given. In Table 6.1, comparison of both free and confined quasi-static test results with that of five unit core materials (it is assumed that they were not in contact with each other) can be seen. In this analysis, deformation of face sheets of sandwich structures was ignored.

Table 6.1. Comparison of quasi-static test results with 5 combined geometry structures.

Specimen	**Test Speed**	P_i **(kN)**	P_{max} **(kN)**	P_m **(kN)**	**Energy (J)**	***SAE*** **(kJ/kg)**
5 individual R125T05 core material	Quasi-static	77.5	98.085	53.8	1015	34
R125T05 Sandwich – unconfined	Quasi-static	75	80	52.49	961.57	32.05
R125T05 Sandwich - confined	Quasi-static	84	90	57.09	927.2	30.9

In Table 6.1, it can be seen that, the lowest initial maximum load was obtained in the unconfined test condition. A similar behaviour was also observed for global maximum load, also. As a result of lack of restraint in the radial direction, circumferential core materials were free to move radially and this is the cause of decrease in initial and maximum load values. Even the same was valid for mean load values, absorbed energy and *SAE* values were in the same level. However, for the confined case a decrease in absorbed energy and *SAE* values was obvious even though initial and maximum load values were higher than the other cases. This was the result of confinement effect; geometrically confinement restraints the circumferential core materials and friction on the confinement walls result in a lower absorbed energy value with a lower densification value. But again the *SAE* values are in the same level in all of the cases.

Unconfined low velocity crushing experiments were carried out using a Fractovis Plus drop weight tester (Figure 3.9). The main constituents of the drop weight tester include striker, dropping weights, striker tip, and velocity sensor. The striker was attached to a 90 kN strain-gage sensor connected to data acquisition system and readings were recorded. The striker velocity was measured by the photocells of the drop-weight tester and the tests were conducted using a 70 mm diameter flat end striker tip. The absorbed energy was calculated by integrating the force-displacement curves. Specimens were tested with an initial striker velocity of 10 m/s (which was achieved by the additional stored energy provided by attached springs in the test system) corresponding to an initial nominal strain rate of 400 s^{-1}. A 20 kg of dropping weight was selected after the calculations for sufficient energy level from the quasi-static crushing tests as a measure. High speed camera was also used to record crushing at a frame rate of 10000 fps.

In drop-weight test of sandwich specimen, an initial maximum load of 75 kN at 10.4 mm of deformation and a second peak load of 80 kN due to buckling of cylindrical portion were observed, Figure 6.4. Progressive collapse behavior is still obvious as seen in both force-displacement curve and deformation views. Except for the little shift in the displacement values, result was identical with that of quasi-static test. This was mainly due to the low strain rate and inertial effects at relatively low velocities attained during drop weight experiments, which was in accordance with the behavior observed when the single combined geometry shells tested only. Deformation of the structure started with typical dimpling mode, which is unsymmetrical due to the interaction between the contacting core units. This mode finished with the occurrence of hinges and due to the lack of radial confinement core units were squeezed out.

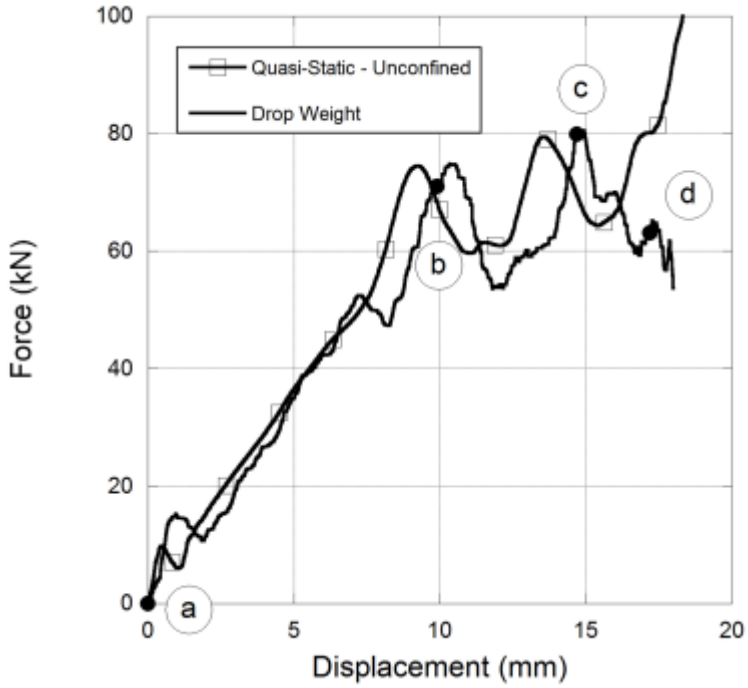

(a)

Figure 6.4. (a) Drop-weight crushing result comparatively with unconfined quasi-static crushing test result and (b) deformation scheme.

(Cont. on next page)

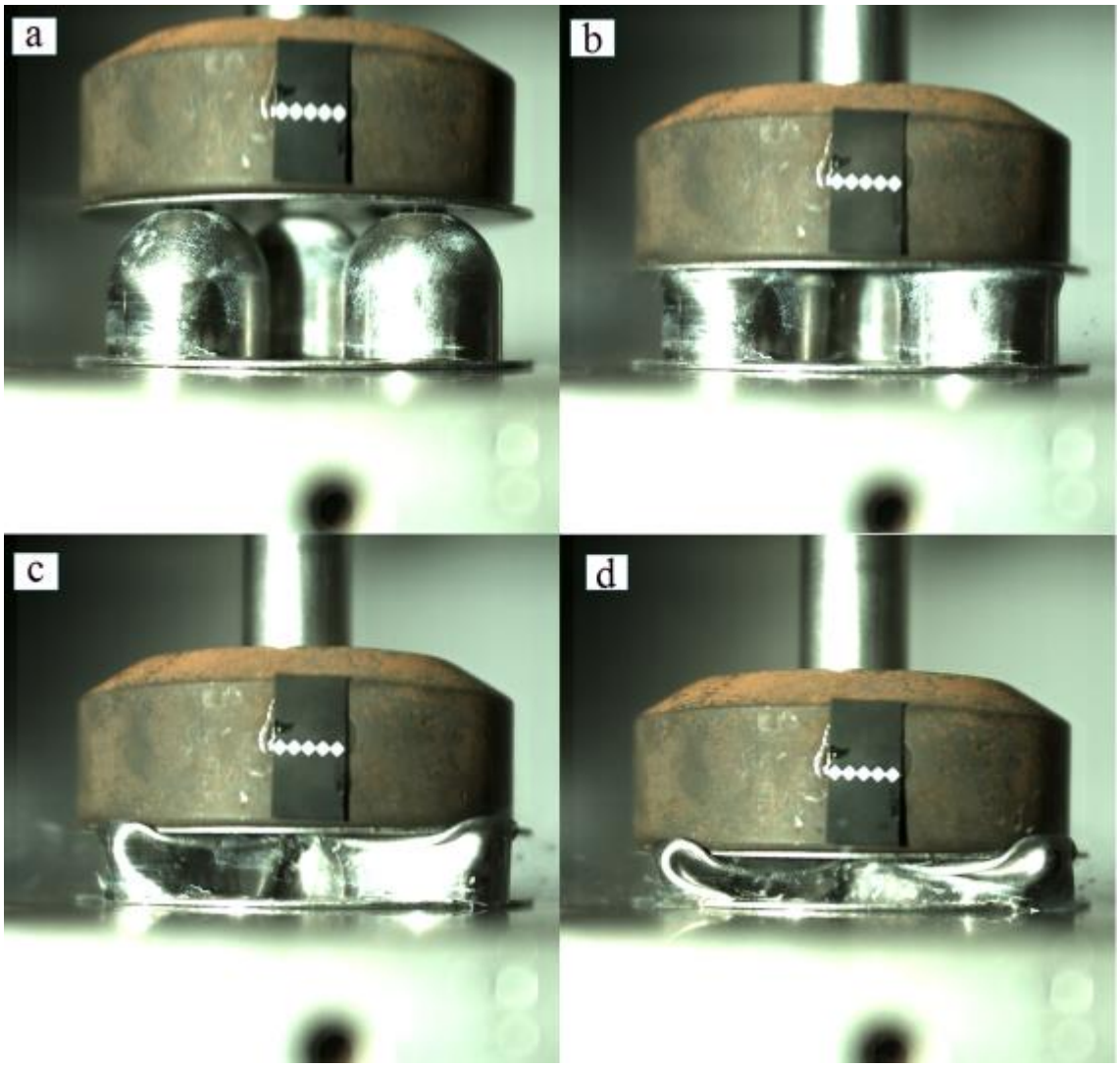

(b)

Figure 6.4. (cont.)

After finishing the investigation on quasi-static and low velocity crushing behaviour of sandwich structures, unconfined and confined direct impact experiments were conducted.

In the blast resistant structures, protective layers are usually designed as an add-on layer attached to body of protected structure (generally vehicles). As a sacrificial layer, sandwich structure deforms to absorb energy when blast load applied. Therefore dynamic crushing behavior must be investigated to reveal the crushing properties under dynamic loading conditions.

Dynamic crushing behavior of confined and unconfined sandwich structures with combined geometry shell cores at strain rates ranging between 10^3 – 10^4 s^{-1} was determined using a 7075-T6 aluminum direct impact experimental setup (Figure 3.12).

As already mentioned, this setup consists of a gas gun, a 150 mm long striker bar with a diameter of 75 mm, and a 2000 mm long transmitter bar with a diameter of 70 mm. In confined crushing tests, a confining fixture having an outer diameter of 100 mm was used with a clearance sufficiently providing radial constraint during the experiment. The confinement also worked as a geometrical adaptor between 75 mm diameter specimen and the 70 mm diameter transmitter bar. In unconfined crushing tests, a specimen holder with a diameter of 100 mm was used only as an adaptor between specimen and transmitter bar.

In direct impact experiments, striker bar was propelled against a 50 mm thick piston for confined tests and directly onto specimen for unconfined tests. Initial velocity of striker bar was measured using laser velocity sensors attached to the gas gun barrel. In all tests an average initial velocity of 40 m/s was provided corresponding to an initial nominal strain rate of 1600 s^{-1}.

In order to calculate crushing force in dynamic experiments, transmitter bar was equipped with strain gages and strain (ε_T) was recorded using an oscilloscope. Then strain history was used to calculate bar stress (σ_T) and was converted to transmitted force history ($F_{Dynamic}$) which is the dynamic crushing force of sandwich structure. Equations used in the procedure are repeated for consistency as follows;

$$\sigma_T = E_{bar}\, \varepsilon_T \tag{6.1}$$

$$F_{Dynamic} = \sigma_T\, A_{bar} \tag{6.2}$$

High speed camera was also used to record crushing scheme in dynamic unconfined experiments with a frame rate of 18000 fps. In confined experiments deformation scheme was revealed by numerical simulations.

In Figure 6.5 a force histories of unconfined and confined direct impact experiments are given comparatively. Deformation sequence can also be seen for unconfined test in Figure 6.5 b. As can be seen from Figure 6.5 a, both unconfined and confined direct impact test results showed similar behavior except for the force values recorded during confined tests were higher than those of unconfined due to the effects of interaction between core materials and confinement. For both of the tests average forces were higher than those of quasi-static and low velocity tests. Kılıçaslan et al.

(Kılıçaslan et al. 2014) also observed an increase in peak stresses for a corrugated core sandwich structure and related these to inertial effect as a result of high impact velocity. Although this is also the same for the case studied, change of deformation mode with increasing impact velocity can obviously be deduced by comparing Figure 6.5 b with Figure 6.2 b. In the unconfined direct impact experiment, outer core units tended to displace in the radial direction during deformation. In the confined direct impact test, this radial displacement is prevented and that is the cause of increase in the crushing load, as can be seen in Figure 6.5 a. A portion of the increase might also be resulted from the friction between the core units and the inner walls of confinement.

In the unconfined direct impcat test, a 80 kN initial maximum load was observed at 50 microseconds. A 90 kN mean load was calculated. After initial peak load, crushing continued with a fixed load for 400 microseconds. Because of lack of confinement, outer hemispherical core structures deformed and displaced radially also. Deformation progression in the test can be seen in Figure 6.5 b.

In the confined direct impact test, at 50 microseconds, an initial peak load of 100 kN was observed. As experiment continues, a load decrease of 20 kN was observed and at 300 microseconds, global maximum load of 150 kN was observed. As test progresses, load decreases and loading ended. Core materials collapsed with a greater load as a result of support of a stationary boundary condition of back face. A 100 kN of mean load was calculated because of the effect of increasing deformation rate and inertial effects, which was around 80 kN in quasi-static crushing tests. When deformed specimen was inspected, it is seen that front face sheet shows a little deformation due to poor support as a result of point contact with hemispherical part of core structures. Outer core structures could not displace in radial direction because of confinement. Instead, they deformed front face sheet a little and move through the edges of face sheet relatively. Middle core structure deformed and confined by outer core structures.

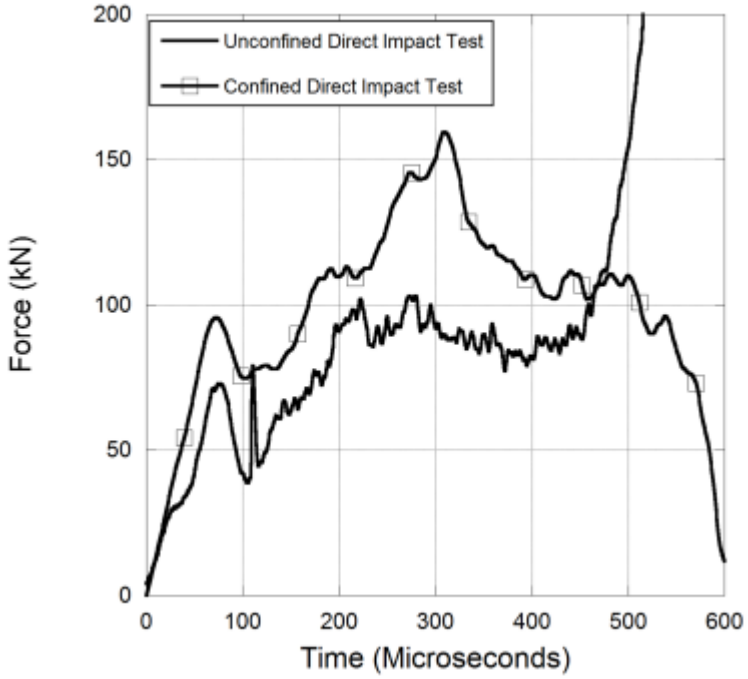

(a)

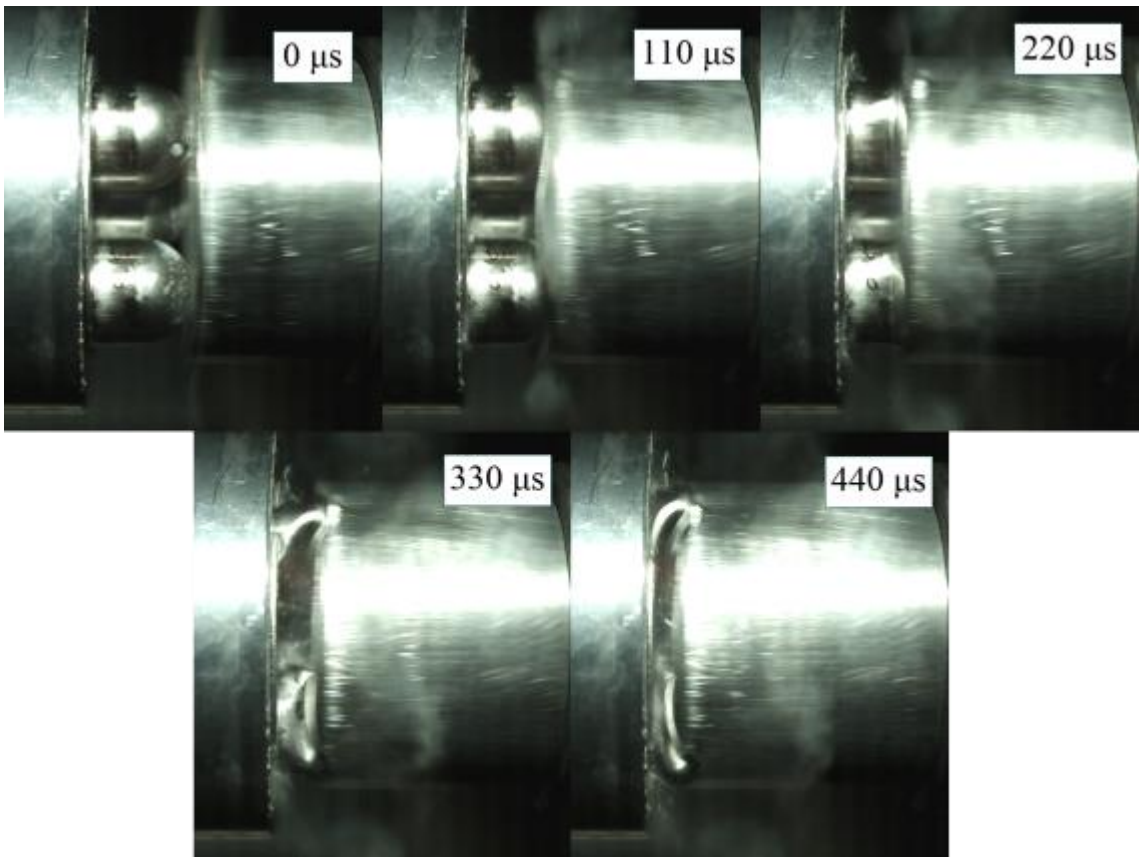

(b)

Figure 6.5. (a) Unconfined and confined direct impact crushing test results and (b) deformation scheme of unconfined experiment.

As can be seen in Figure 6.5 b, deformation initiates on hemispherical portion of core structures and between 110 and 220 microseconds cylindrical part starts to buckle. Actually, force-time curve verifies this phenomena also. As a result of poor constraint in radial direction, outer core structures displaced radially while deforming. Due to this phenomena, a nearly constant load history was seen after an initial peak force. As can be seen, deformation was symmetrical and at 440 microseconds compaction-densification started.

6.2. Numerical Results

After finishing quasi-static, low velocity, and dynamic crushing experiments on R125T05 sandwich structures, numerical simulations of tests were carried out. In Figure 4.17 (b) crushing simulation model for a single combined geometry was given and models for crushing simulations of sandwich structure can be seen in Figure 6.6. Same model was used for both quasi-static and low velocity crushing experiments of sandwich specimens with larger cross-heads. In the quasi-static crushing simulations mass-scaling method was used. In the method, density of materials was scaled down by a factor, namely; 1000 and loading rate was scale up by a factor of 100. In order to guarantee static strain rates, kinetic energy must be lower than the 4% of total energy.

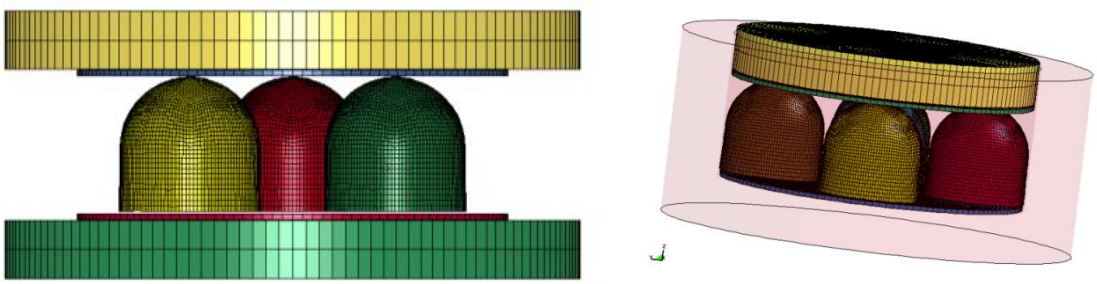

(a) (b)

Figure 6.6. Crushing simulation models for (a) unconfined quasi-static and low velocity experiments, and (b) confined quasi-static experiment.

The quasi-static and drop-weight test numerical models consisted of a moving rigid upper plate, specimen and stationary rigid lower plate. In the confined quasi-static crushing simulations, a rigid confinement ring was also modeled with the appropriate clearance as in the experiments. The lower plate was fully constrained in all directions.

In the drop weight simulations, the top rigid plate moved along axis with a downward velocity and node based mass lumping methodology was followed in order to match the total weight of dropping weights and cross-head. For both quasi-static and drop-weight test simulations, two different types of contact were used. For the combined geometry shell cores and face sheets, an automatic single surface contact was used to account for the contact between folds during the deformation, and contact between core materials and face sheets. While an automatic surface to surface contact was applied between the face sheets and rigid top/bottom plates.

Finite element models used in the direct impact test simulations can be seen in Figure 6.7 a and b. In the simulations surface to surface contact algorithms were used in order to define contact between the parts of experimental set-up. Contacts between the specimens themselves and parts of experimental set-up were modeled with automatic surface to surface contact algorithm. An initial velocity was assigned to the striker bar. In order to compare numerical and experimental results, elements coinciding with the position of strain gages in experiments were determined, stress history was recorded and crushing forces were calculated. Material model constants of parts were previously given in Table 3.4.

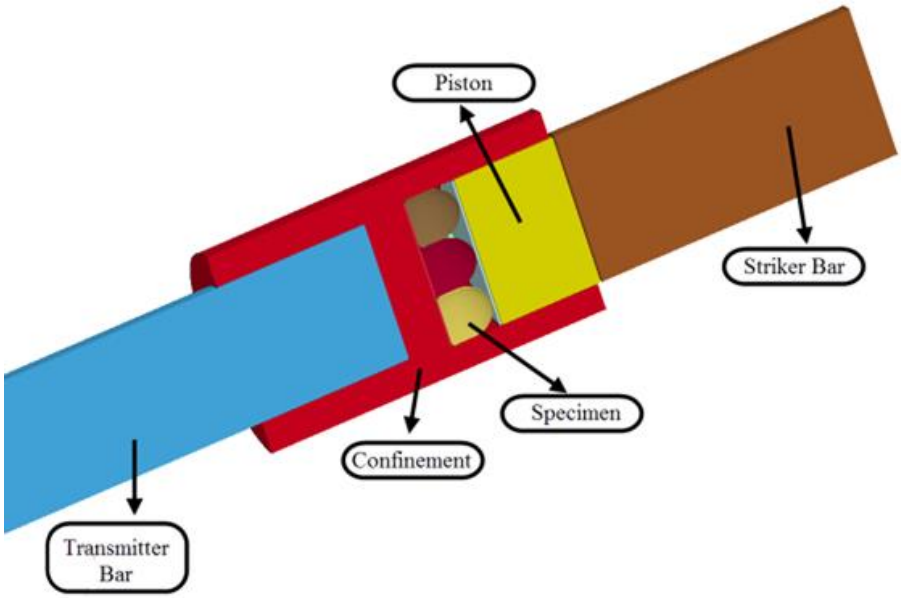

(a)

Figure 6.7. (a) Sectional view of confined direct impact model and (b) unconfined direct impact model

(Cont. on next page)

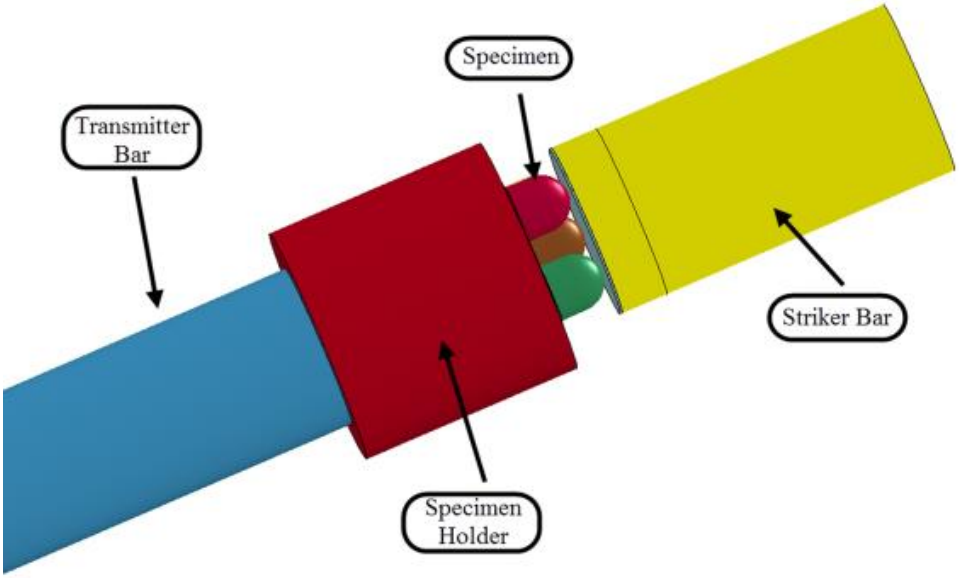

(b)

Figure 6.7. (cont.)

In the numerical simulations, core materials were modeled using Belytschko-Tsay shell elements with five integration points through the thickness. Cross-heads, striker and transmitter bars, and specimen holders were modeled using eight-node constant stress solid elements. A static friction coefficient of 0.3 and a dynamic friction coefficient of 0.2 between all surfaces contacting were assumed in the study. In the numerical model, the air pressure presumably arisen from compression of the enclosed air is assumed to have insignificant effect on the force values as with metallic closed cell foams. Hence, the air was not modeled explicitly.

In Figure 6.8 unconfined and confined behaviour of R125T05 sandwich in quasi-static and drop weight loading rates was given. It is obvious that numerical models achieved to capture the necessary characteristics observed in experiments. Agreement between experimental and numerical results in different loading rates gives the opportunity that numerical models can be used in different simulations even experiments cannot be conducted; such as, blast, high velocity impact etc.

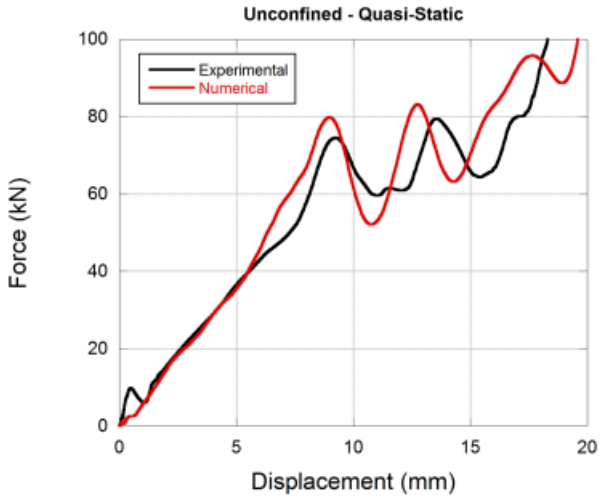

(a)

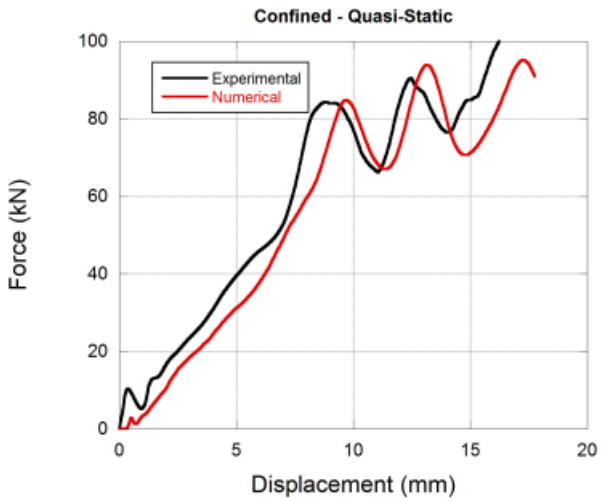

(b)

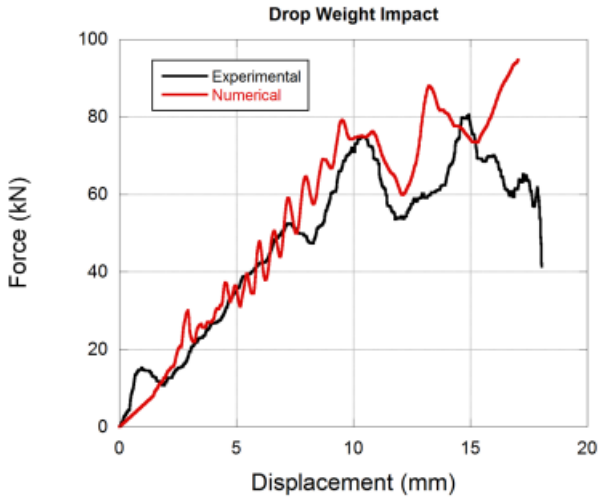

(c)

Figure 6.8. Comparison of experimental and numerical results (a) quasi-static – unconfined, (b) quasi-static – confined, (c) drop weight.

In Figure 6.9, experimental and numerical comparison of deformation history of quasi-static – unconfined crushing results of R125T05 sandwich specimen is given. As can be seen, view at 0.48 mm of deformation corresponds to the seperation of apex of hemispheres from upper face sheet. At 17.9 mm of deformation structure starts to densify. As can be seen in Figure 6.9, circumferential hemispherical core materials tend to move radially and fold outwardly as deformation progresses. This can be explained that tendency of structure to deform in the simplest way. Inward dimpling mode that observed previously in hemispherical core units was observed in sandwich structures but as a constraining effect of middle core unit, it is observed in an asymmetric fashion. In Figure 6.12, crushed specimen can be seen comparatively.

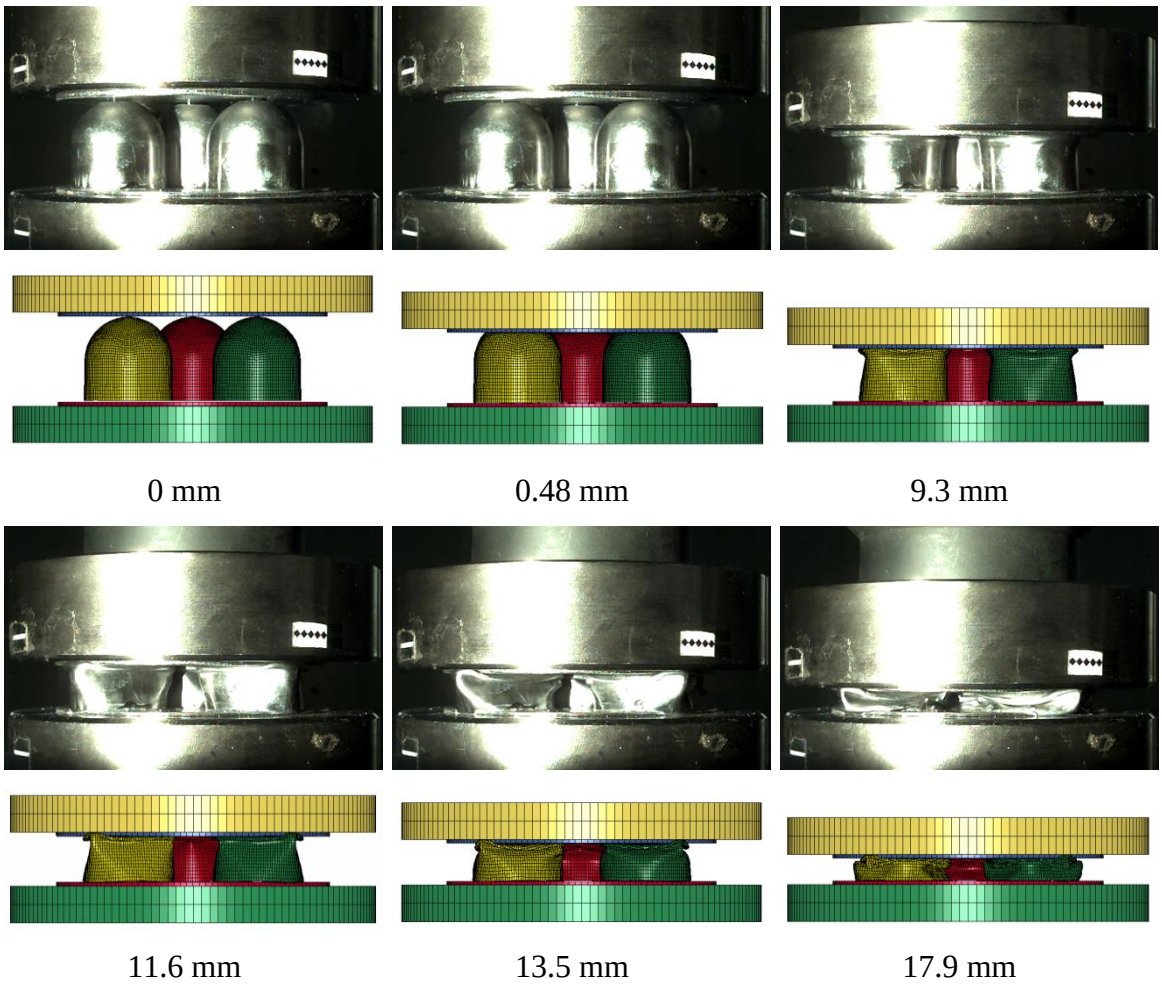

Figure 6.9. Comparison of deformation history of experimental and numerical quasi-static – unconfined crushing results of R125T05 sandwich specimen.

In Figure 6.10, comparison of deformation history experimental and numerical drop weight crushing results of R125T05 sandwich specimen can be seen. As in the

quasi – static unconfined test result, circumferential hemispherical core materials tend to move radially and deform outwardly. Deformation at 9.9 mm coincides with the end of deformation of hemispherical portion. After, cylindrical portion starts to deform and folds tends to expand outwardly.

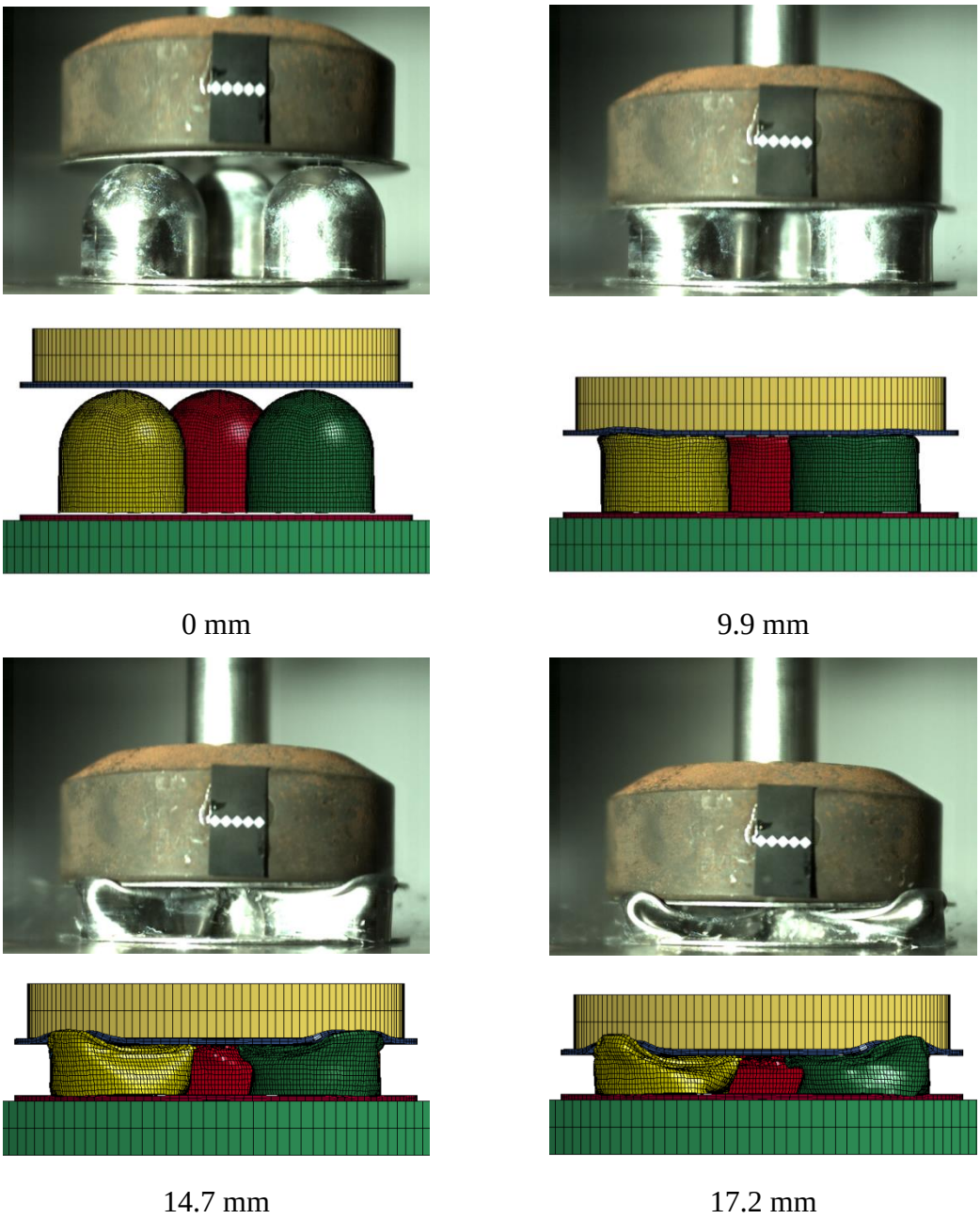

Figure 6.10. Comparison of deformation history of drop weight results.

In Figure 6.11 comparison of experimental and numerical force – time histories for direct impact results can be seen. Both numerical simulations achieved to catch necessary characteristics obtained in the experiments. Because of radial constraining of

confinement, radial deformation of circumferential hemispherical core units were prevented. Middle core unit was confined by circumferential core units at contact lines and as a results middle core deformed symetrically.

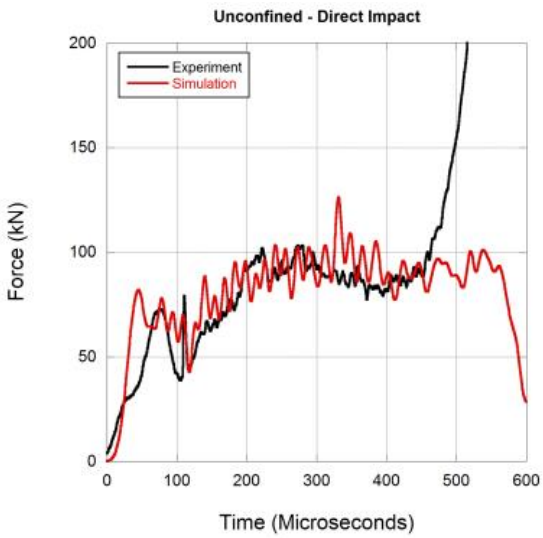

(a)

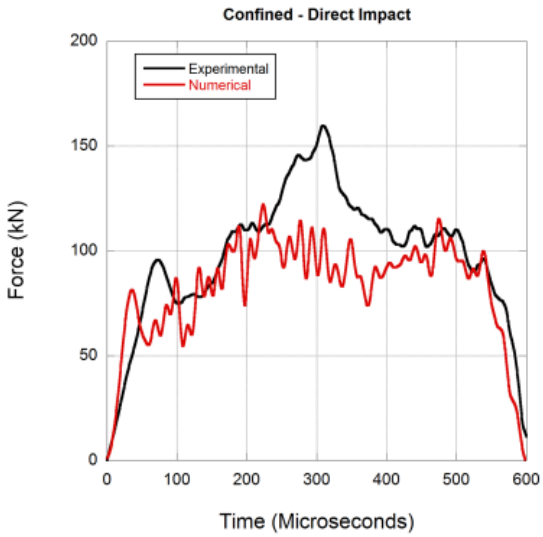

(b)

Figure 6.11. Comparison of experimental and numerical direct impact results (a) unconfined and (b) confined.

All in all, experimental and numerical force-displacement curves obtained from quasi-static, low velocity and dynamic crushing tests are in good agreement. In unconfined quasi-static simulation, peaks corresponding to the buckling of constituents are slightly overestimated. Similar findings are also observed for confined quasi-static and drop weight crushing behavior. These slight variations might arise as a result of

imperfections such as tilting of unit cores while bonding. Similar imperfection effects were previously observed for another energy absorber (Lee et al. 2006), for a honeycomb structure (Wilbert et al. 2011) and for a cylindrical section (Al Galib and Limam 2004). Furthermore, the alignment of the sample and cross-head/striker in the model was assumed to be perfect, while in the experiments the misalignment of the sample and cross-head/striker surfaces may result in the deviation in the higher displacement values. During the initial stages of the deformation, mainly the hemispherical sections of the combined geometries deformed. Then cylindrical segment started to crush and folds were formed. At the later stages of the experiment, for the case of unconfined configuration, outer core units started to move in the radial direction. This displacement was not fully symmetric because of the alignment issues. Therefore, the numerical disagreement started to increase at the later stages of test.

The validity of numerical simulations can also be confirmed inspecting deformed shapes of sandwiches obtained from experiments and simulations (Figure 6.12). In both experimental and numerical simulations of confined tests as a result of local flattening of walls of combined geometry shell a trapezoidal cross-sectioned form is observed, while in unconfined tests the cross-sectional form of deformation changes to a triangular shape. As shown in Figure 6.12 e, the mode of deformation does not change significantly as the deformation rate increases.

(a)

Figure 6.12. Experimental vs. numerical deformed specimens; (a) unconfined – quasi-static, (b) confined – quasi-static, (c) drop weight, (d) unconfined – direct impact, and (e) confined – direct impact.

(Cont. on next page)

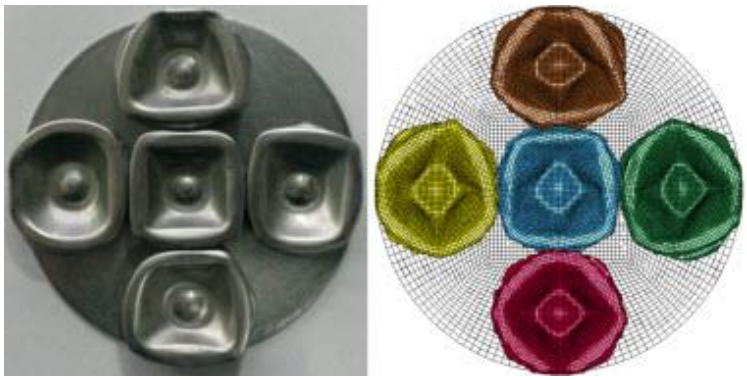

(b)

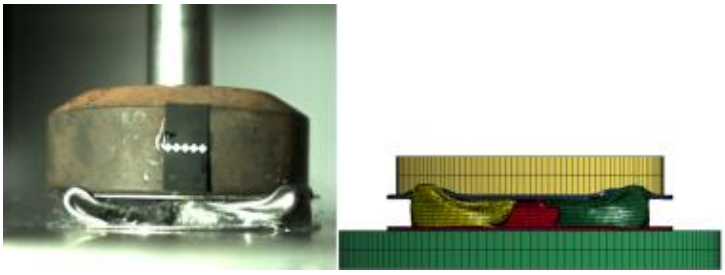

(c)

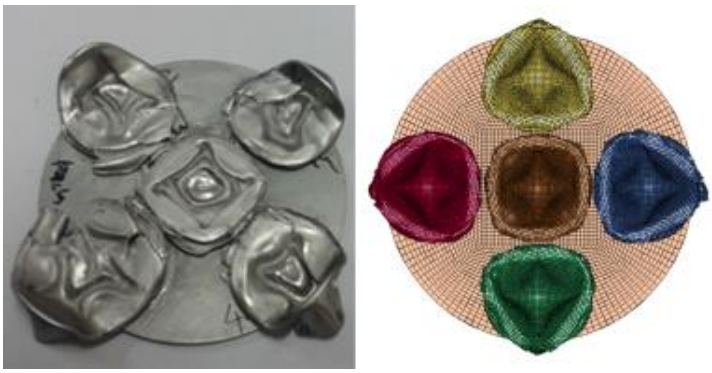

(d)

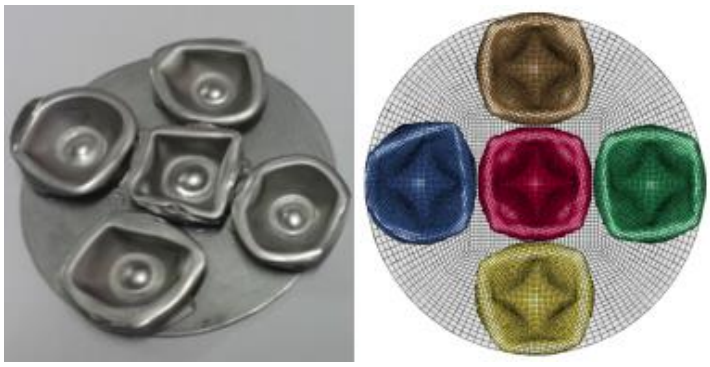

(e)

Figure 6.12. (cont.)

CHAPTER 7

EFFECT OF INERTIA STRAIN RATE AND MULTILAYERING ON CRUSHING AND ENERGY ABSORPTION BEHAVIOR OF SANDWICH STRUCTURES WITH COMBINED GEOMETRY SHELL CORES

Having completely verified numerical models for combined geometry shell structures and after obtaining successful numerical representation of quasi-static and dynamic crushing behavior of sandwiches with combined geometry shell cores at all investigated strain rate regimes, the numerical part of the study was broadened in order to examine the effect of inertia and strain rate sensitivity of stainless steel on the crushing and energy absorption of sandwich structures at different loading rates. Additional numerical simulations were run with different constant impact velocities and fictitious additional models were used with the assumption of base material to be strain rate insensitive. Conducting the analysis, effect of confinement was also distinguished, as mentioned, it is obviously provenly important because the manufactured sandwich structure can be used as a blast mitigation device and its boundary condition will lay in between unconfined and confined cases.

In order to investigate the effect of multilayering on crushing response of sandwich structures with combined geometry shell cores, constant deformation velocity simulations at dynamic loading regime were used. Two different configurations of two-layered specimens; i.e. sequential and opposite specimens were prepared. In engineering applications of the proposed sandwich structures as blast mitigation structure, a lot of repeated unit core structures will be arranged along axial and layer directions. Therefore, the investigation of the effect of axial rotation and/or angular misalignment of these repeated units will be very important. In this study this effect was also numerically investigated. A sequential three layer specimen was also prepared to see the effect of layering and numerically deformed under similar conditions. Deformation

behavior of proposed sandwiches was also investigated under different dynamic loading conditions numerically.

7.1. Inertia and Strain Rate Effects on Crushing Behavior of Sandwich Structures

Dynamic crushing behavior of thin-walled structures is obviously affected by loading conditions. As previous results of this study suggested, an increase in loading rate resulted in increase in mean crush loads and also correspondingly absorbed energy levels for most of the alternative geometries proposed. This phenomenon is caused by two factors, namely “strain rate factor” and “inertia factor”. The former is a property of the material that the structure manufactured from, causes increase in yield and flow stresses, and therefore higher load/energy is needed to deform such a structure when loading/strain rate increased to dynamic level. The latter is the factor that plays role when rapid acceleration is apparent such as in low velocity or dynamic events.

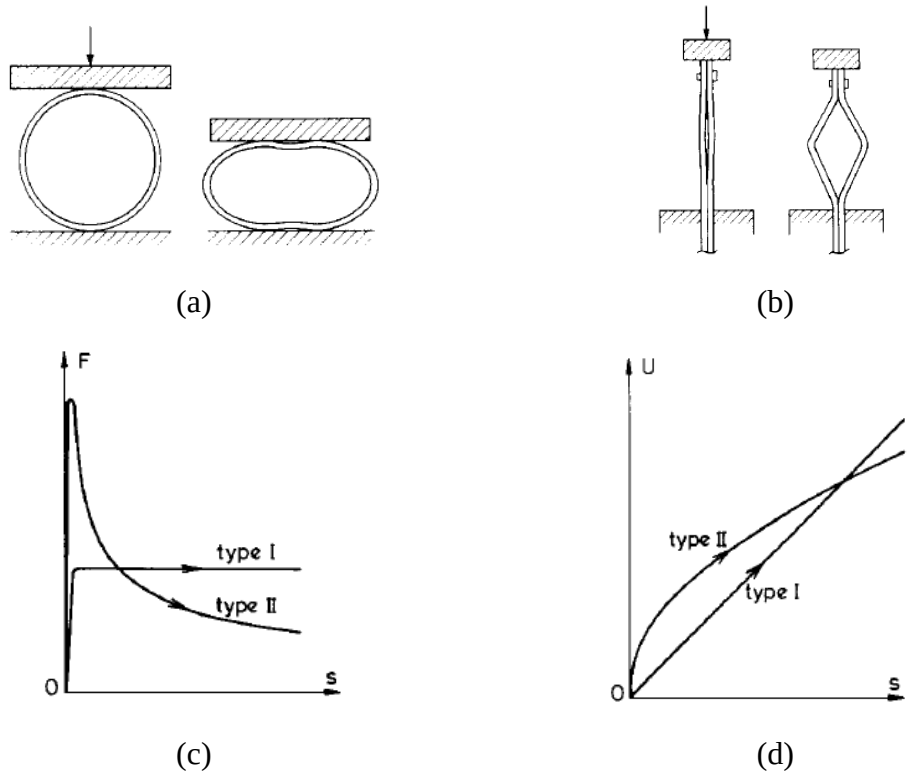

Figure 7.1. (a) Type I structure, (b) Type II structure, (c) force-displacement and (d) energy displacement curves of energy absorbing structures (Source : Calladine and English 1984).

There are two types of energy absorbing structures identified by their different shapes of load-displacement curves (Calladine and English 1984, Zhang and Yu 1989, Tam and Calladine 1991). A flat-topped load displacement curve was classified as a Type I structure (Figure 7.1 a), while a dramatically decreasing curve is an obvious sign of a Type II structure (Figure 7.1 b). It is clear so far that Type II structures are more sensitive in terms of both inertia and strain rate than Type I structures (Calladine and English 1984). The energy absorption efficiency of Type II structures was shown to be enhanced by the structure's material strain rate sensitivity (Tam and Calladine 1991).

In a recent study (Tasdemirci et al. 2015), it was suggested that, the investigated combined geometry structure is a combination of a Type I structure (hemispherical portion) and a Type II structure (cylindrical portion). Therefore, the strain rate and inertia effects are expected to be different from the constituents and combination of them. Therefore such an investigation is also important to distinguish the effects in collapse behavior of sandwich structures also to account for interaction effects.

Single layer sandwich models used in the study were already given in Figure 6.6 a for unconfined case and confined simulation model can be seen in Figure 6.6 b. Material model parameters can be found in Table 3.5.

Different from combined geometry shell structures, an interaction between the unit core materials in a sandwich structure is obviously apparent. Therefore, in order to understand the effects of strain rate and inertia while incorporating the interaction between core materials in a sandwich structure was investigated in the current part of the study. For this purpose, numerical simulations were prepared for both unconfined and confined conditions (Figure 6.6 b). In order to distinguish the effects of strain rate and inertia, simulations were prepared by assigning constant crosshead velocities ranging between 50 to 200 m/s with both strain rate insensitive and sensitive material models.

In Figure 7.2, numerical results from strain rate insensitive and sensitive models at 200 m/s constant crosshead velocity can be seen comparatively with the quasi-static simulation results in terms of mean crush load vs. displacement. As can be seen, dashed area between strain rate insensitive model and quasi-static model represents the increase as a result of effect of inertia at the selected loading rate. By attaining base material with a fictitious strain rate insensitive material model strain rate dependency effects were subtracted and inertial effects were calculated. Additional effect of strain rate can be found by the difference between strain rate sensitive and insensitive models, because

both results contains inertial effects and when the results were subtracted inertial effects were removed and strain rate effects were obtained, as seen in Figure 7.2.

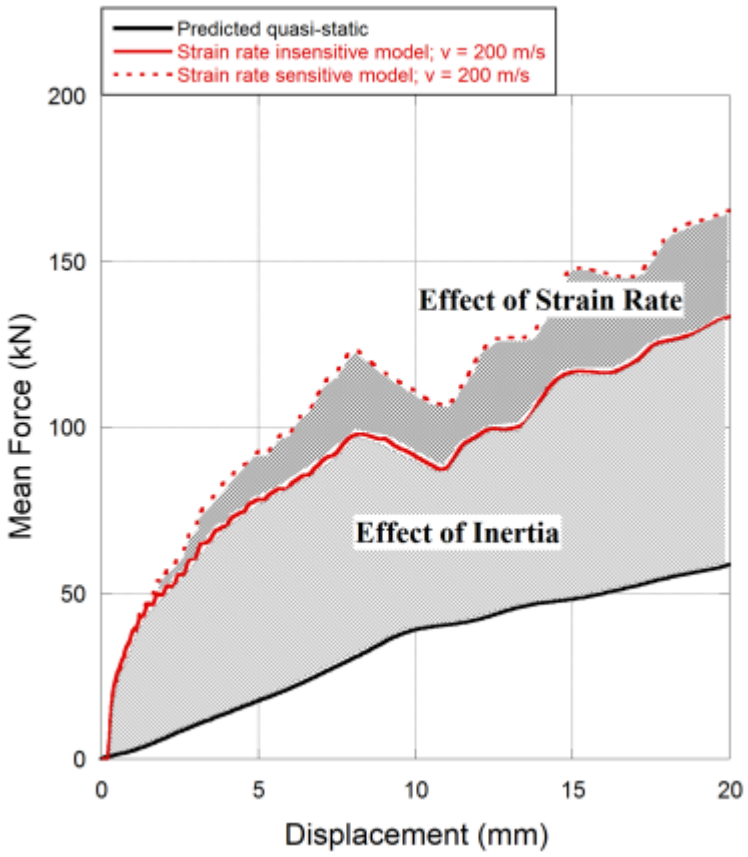

Figure 7.2. Effect of strain rate and inertia for 200 m/s simulation.

In order to determine the effect of impact velocity on inertia and strain rate sensitivities, numerical simulations were conducted at various impact velocities, average increase in mean crush loads are calculated and plotted against impact velocity (Figure 7.3).

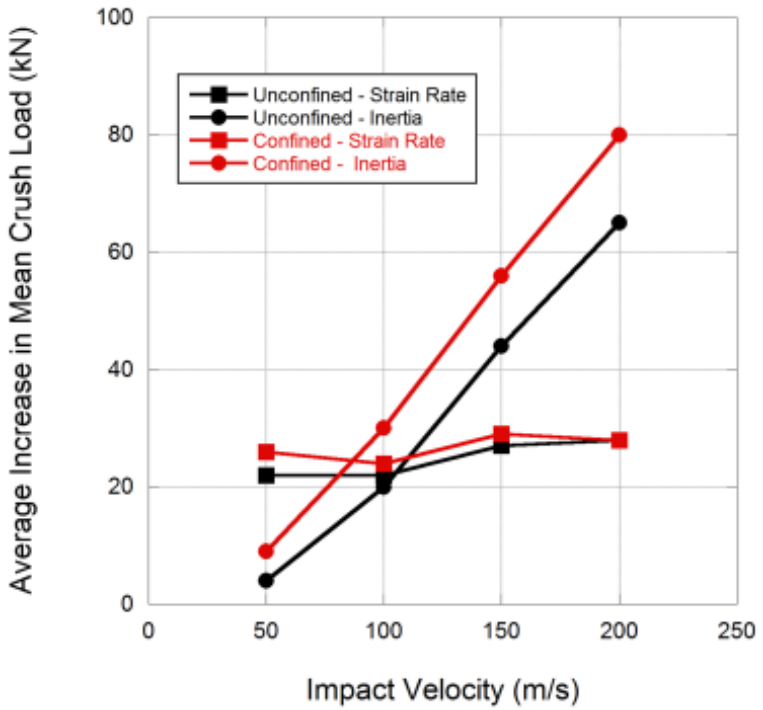

Figure 7.3. Average increase in mean crush load vs. impact velocity.

As can be seen in Figure 7.3, for both unconfined and confined configurations, the effect of inertia is more apparent comparatively with that of strain rate specifically at higher impact velocities. Even, the increase due to strain rate is not dependent on impact velocity, which is in consistence with the previous study on the behavior of unit core material (Tasdemirci et al. 2015). Increase due to strain rate and inertial effect is found to be higher for confined case than that of unconfined condition.

As can be seen, curves of both unconfined and confined inertial effects are nearly parallel revealing that their effects are comparable but with some amount of constant difference due to the constant effect of confinement at all used velocities. This difference might be as a result of the effect of radial boundary condition due to the confinement and also the friction between the singe combined geometries and the wall of confinement. At higher velocities, the effect of strain rate becomes almost independent of confinement condition.

7.2. Effect of Multilayering on Crushing Behavior of Sandwich Structures

Multilayering of lightweight core sandwich structures is a very useful application in terms of increasing absorbed energy with a reasonably low increase in total weight of the structure. Multilayering results in higher energy absorption along with the increase in deformation due to increase in area under force-displacement curves. Besides, interaction between upper and lower layers can cause deformation mode transformation and therefore greater mean crush loads and absorbed energy. Multilayered configurations were investigated by using simulations with 50 m/s constant impact velocities. Three configurations (Figure 7.4) were compared with single layer configuration (Figure 6.6 a). AISI 304L stainless steel interlayer sheets modeled with Johnson-Cook material model were also used to separate neighboring layers and top face sheets were not model in order to prevent high load observed during the first momentum transfer due to high impact velocity.

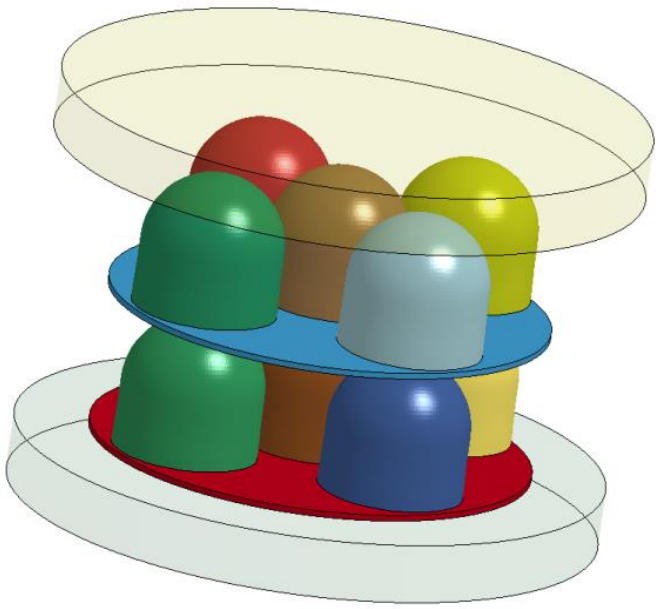

(a)

Figure 7.4. (a) Sequential, and (b) opposite two layered specimens, and (c) three layered specimen.

(Cont. on next page)

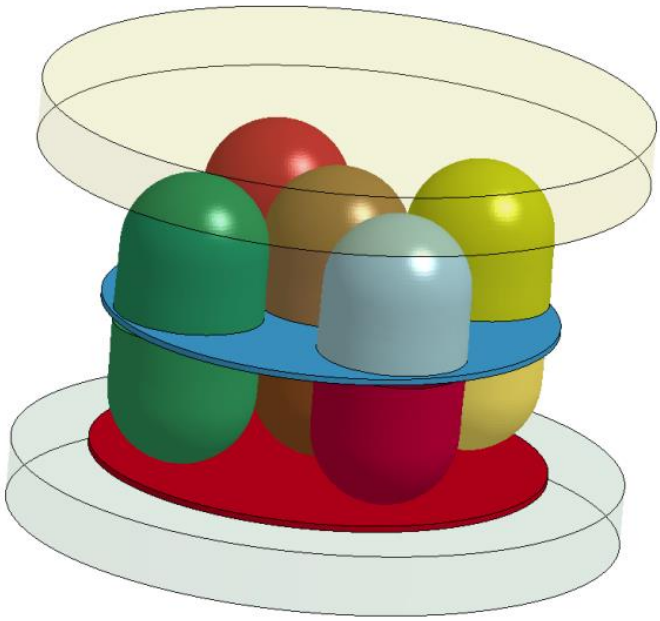

(b)

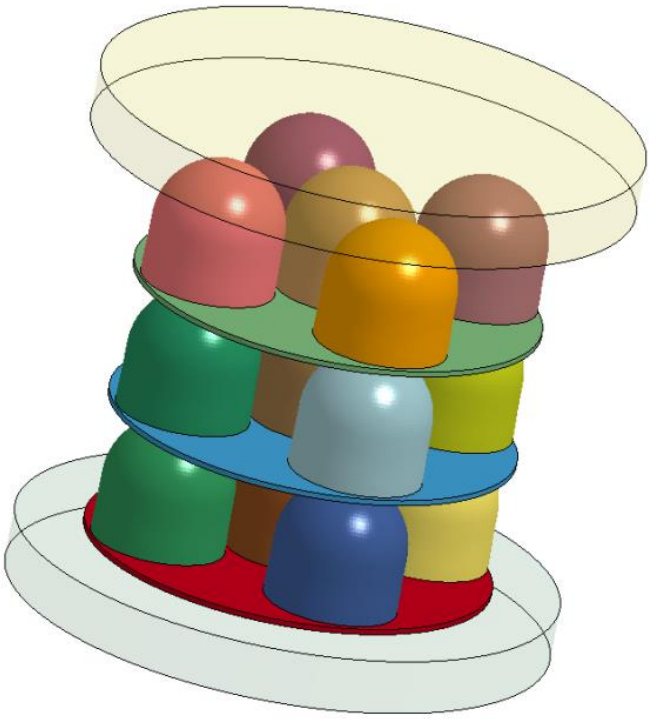

(c)

Figure 7.4. (cont.)

In Figure 7.5 mean load vs % displacement curves can be seen for single and multilayered sandwich structures. % displacement was calculated by dividing deformation to the initial thickness of individual sandwiches. As can be seen from the figure, similar results are obtained for all types of multilayered specimens up to ~10 %

displacement. The lowest mean crush load was calculated for single layer sandwich and the highest for sequential two layer sandwich. Interaction between neighboring layers was observed after 10 % of displacement.

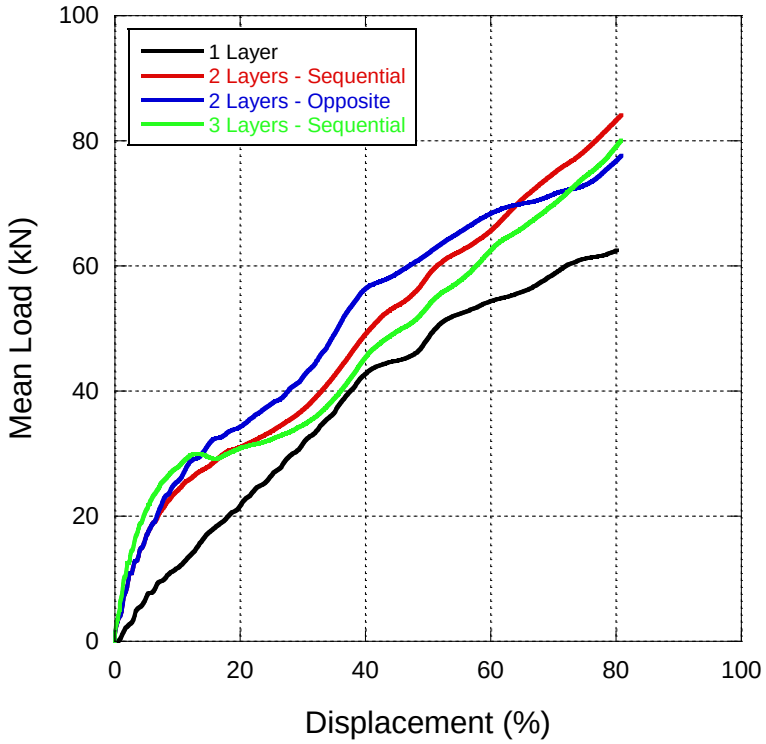

Figure 7.5. Mean load vs. % displacement curves of single and multilayered sandwiches.

In the current study, a possible defect or a desired feature called axial rotation / misalignment of neighboring layers relative to each other in two layered configurations is also examined, Figure 7.6. For lower axial rotations, this may show a possible production failure or for higher misalignment angles this could be an engineered desired property if energy absorption could be increased by the deformation transformation. Besides if a multilayered plate was manufactured in order to use against blast loading, misalignment can vary through in-plane directions. Therefore in this study, effect of misalignment was investigated with misalignment angles between 0° and 45°. It is obvious that the rest is going to be the same due to the symmetry of the circular sandwich configuration.

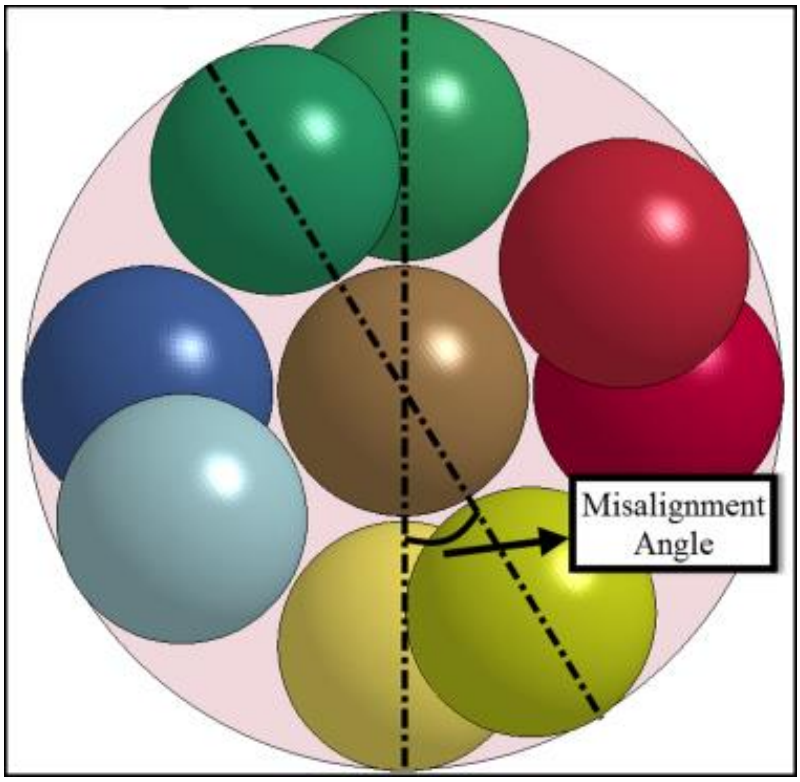

Figure 7.6. Misalignment angle.

In Figure 7.7, SAE vs. misalignment angle is given. As can be seen in figure, all multilayered configurations absorb higher amount of energy than single layer with a reasonable increase in the weight of the sandwich. For both two layered configurations, *SAE* values are greater than single layered configuration. Sequential arrangements have greater *SAE* than opposite arrangements. This is the result of deformation sequence change due to the relative position differences of constituents in different arrangements. It is also interesting to note that rotation/misalignment between neighboring layers affects the results adversely except for 5° rotation for opposite arrangements. As misalignment angle increases, support by lower layer to the upper layer decreases. Therefore, upper layer bends interlayer sheet as deformation progresses and a relatively asymmetric global deformation mode is obtained, which gives a decreased absorbed energy. Another interesting result observed by multilayering is that *SAE* values of sequential two layered sandwiches are higher than three layered sandwich structures until nearly 20° of misalignment. *SAE* values calculated for opposite two layered sandwiches are also in the same level with three layered configurations. Therefore, an optimum configuration could be selected as sequential two layered sandwich with a maximum misalignment angle of 20°.

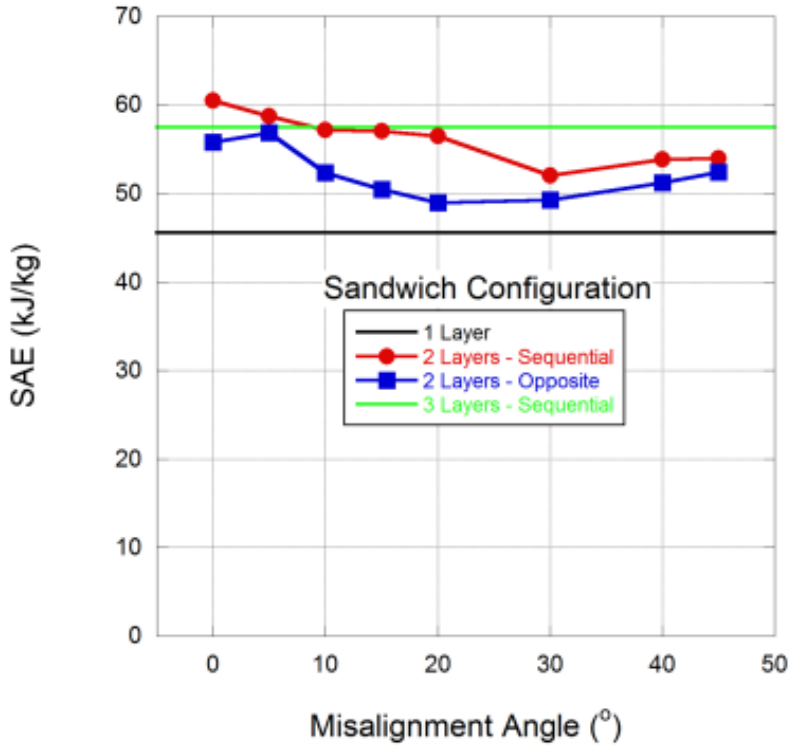

Figure 7.7. *SAE* vs. misalignment angle for different multilayered sandwiches.

In order to have a closer look into the effect of misalignment and crosshead velocity in the deformation of multilayered specimens, simulations for two layered specimens were prepared also with 200 m/s crosshead speed. Results for sequential and opposite specimens can be seen in Figure 7.8 and Figure 7.9. Results are given for 20 and 40 mm displacement values and 0° and 40° misalignment angles for both configurations.

		50 m/s	
		Angle of Misalignment (^{o})	
		0	40
Displacement (mm)	20		
	40		

		200 m/s	
		Angle of Misalignment (^{o})	
		0	40
Displacement (mm)	20	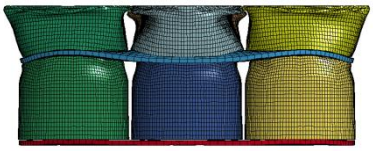	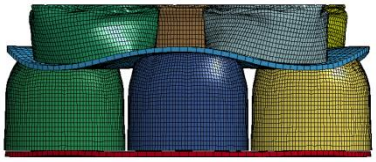
	40		

Figure 7.8. Effect of cross-head speed and angle of misalignment on deformation mode of sequential two layered specimen.

		50 m/s	
		Angle of Misalignment (^{o})	
		0	40
Displacement (mm)	20		
	40		

		200 m/s	
		Angle of Misalignment (^{o})	
		0	40
Displacement (mm)	20		
	40	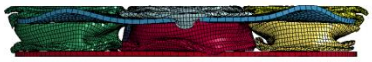	

Figure 7.9. Effect of cross-head speed and angle of misalignment on deformation mode of opposite two layered specimen.

In Figure 7.8 effects of cross-head speed and misalignment angle on deformation mode of sequential two layered specimen can be seen. As seen in the figure, effect of misalignment is apparent for both 50 m/s and 200 m/s velocities. Especially for higher velocity, misalignment angle is responsible for mode change with change in fold thicknesses and with change in boundary conditions for interlayer

resulting in different inertial loads on interlayer. For lower velocity, upper and lower layers has nearly the same amount of deformation. On the other hand, for higher velocity, upper layer crushed more than lower layer for both displacement values.

In Figure 7.9 effects of cross-head speed and misalignment angle on deformation mode of opposite two layered specimen can be seen. Again, effect of misalignment is apparent for both 50 m/s and 200 m/s velocities. Especially for higher velocity, misalignment angle is responsible for mode change. It is interesting to note that, for lower velocity with 0 and 40 degrees and for higher velocity with 40° showed a similar tilting for lower layer – which is acceptable considering loading starts from cylindrical portion for lower layer.

When two configurations were compared, lower velocity deformed shapes are very similar at 20 mm of deformation. Obviously, considering inertial effects, this is not the case for higher velocity. For the configurations investigated, the plates separating the core layers were slightly bent during the course of deformation and it was found that the ratio of energy absorbed by interlayer plate to the total energy absorbed was remained as 3 % and lower.

CHAPTER 8

BLAST LOADING ON SANDWICH STRUCTURES WITH COMBINED GEOMETRY SHELL CORES

Sandwich structures have been the primary design for blast loading applications for decades. Different types of sandwiches distinguished by their core materials and geometry have been designed and developed so far such as metallic foams (Li, Huang, et al. 2014, Liu et al. 2014), metallic honeycombs (Zhu et al. 2008, Nurick et al. 2009, Chi, Langdon, and Nurick 2010), and corrugated structures (Li, Wang, et al. 2014, Yazici et al. 2014). Alberdi et al. (Alberdi, Przywara, and Khandelwal 2013) conducted finite element studies in order to investigate performance of sandwiches against blast loading by using CONWEP functions (Randers-Pehrson and Bannister 1997) present in LS-DYNA (LSTC 2007). According to results of Alberdi et al. (Alberdi, Przywara, and Khandelwal 2013) folded core geometries have better blast mitigation performance than honeycomb geometries considering their lower back face deformations, lower transmitted loads to the back face, and higher energy absorption.

In two works by Palanivelu et al. use of recycled beverage cans for low velocity impact (Palanivelu, Van Paepegem, Degrieck, De Pauw, et al. 2011) and use of their configurations in order to have a macro foam as sacrificial protection structure (Palanivelu, Van Paepegem, Degrieck, Reymen, et al. 2011) were suggested against blast loading. They also proposed that their material can be adopted in different configurations of macro foam depending upon the loading and boundary conditions.

The aim of the current part of the study is to investigate the performance of sandwich structures with combined geometry shell cores when blast loading was applied. LS-DYNA was used to design of computational experiments in simulation environment. As in the previous works, configurations of individual combined geometries were proposed in order to obtain high energy absorption with so-called macro foam effects. Different arrangements of core structures were proposed in order to optimize blast energy absorption by sandwich protective structure.

8.1. Blast Simulation Details

Once numerical models were verified and deformation behavior of both combined geometries and their sandwiches were investigated then the numerical tools can be used in order to investigate dynamic response of sandwich structures consisting of combined geometry shell cores under blast loading. An explosion is a fast release of energy in extreme manner caused formation of a blast wave which is the most harmful component of an explosion. Magnitude of blast load generally represented in terms of scaled distance Z (Smith and Hetherington 1994) and which can be written in the following form:

$$Z = R/W^{1/3} \tag{8.1}$$

where R is the distance from the explosive and W is the weight of charge in terms of TNT equivalent. For a given scaled distance, the pressure resulting from a blast wave is modeled using the Friedlander equation as follows (Smith and Hetherington 1994):

$$P(t) = P_s^+(1 - \frac{t}{t^+})e^{-b\frac{t}{t^+}} \tag{8.2}$$

where P_s^+ is the peak incident pressure, t^+ is the positive phase duration, b is the decay parameter, t_A is the time of arrival. The pressure resulting from a blast wave for a scaled distance can be seen in Figure 8.1.

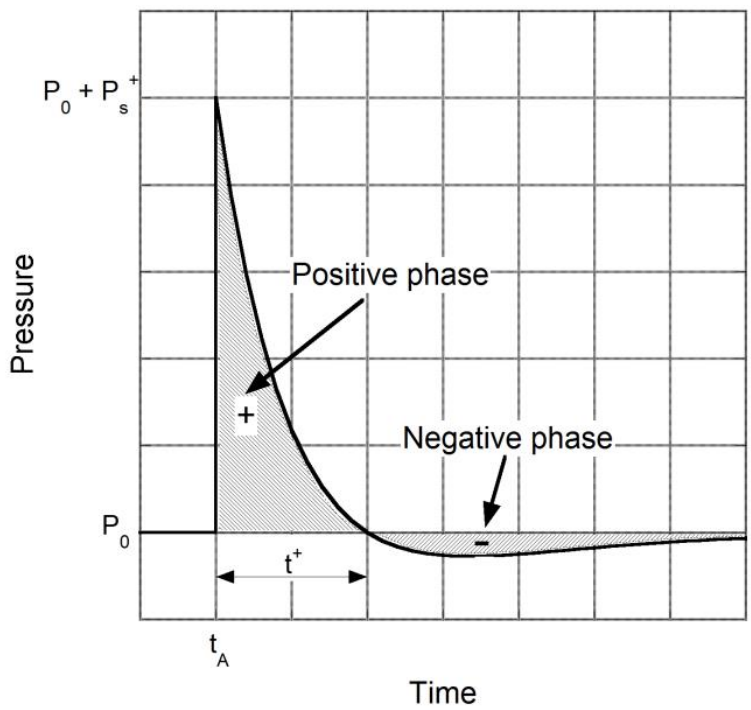

Figure 8.1. Blast wave pressure-time profile.

In LS-DYNA, air blast loading on structures can be modeled by using CONWEP functions (Randers-Pehrson and Bannister 1997) and are used in this study to model the pressure load on the front face sheet of the combined geometry core sandwiches. CONWEP function can be written as follows;

$$P(\tau) = P_r * cos^2\theta + P_i * (1 + cos^2\theta - 2 * cos\theta) \tag{8.3}$$

where θ is angle of incidence, P_i incident pressure and P_r reflected pressure (Zhu and Lu 2007).

In order for the application of pressure loads from the detonation of conventional explosives an air blast function was defined in LS-DYNA by using *LOAD_BLAST_ENHANCED card which also includes enhancements for treating ground-reflected waves, moving warheads and multiple blast sources different from *LOAD_BLAST card of LS-DYNA. *LOAD_BLAST_SEGMENT CARD must also be defined in order to determine the segment that blast pressure is applied. Input variables of *LOAD_BLAST_ENHANCED card is given in Table 8.1.

Table 8.1. *LOAD_BLAST_ENHANCED card input variables.

M	Equivalent mass of TNT
XBO	x-coordinate of charge center
YBO	y-coordinate of charge center
ZBO	z-coordinate of charge center
TBO	Time of detonation
UNIT	Unit conversion flag; EQ.6: kilogram, millimeter, millisecond, GPa
BLAST	Type of blast source; • hemispherical surface burst – charge is located on or very near the ground surface • spherical air burst • air burst – moving non-spherical warhead • air burst with ground reflection – initial shock wave impinges on the ground surface and is reinforced by the reflected wave to produce a Mach front
NEGPHS	Treatment of negative phase. • EQ.0: negative phase dictated by the Friedlander equation. • EQ.1: negative phase ignored as in ConWep.

In the current investigation, a 5 kg of equivalent mass of TNT was defined with the standoff distance of 600 mm. As a comparable measure, Composition B type explosive has a TNT equivalency of 1.33 and used in anti-tank landmines. Type of blast source is chosen as spherical air burst, and negative phase ignored as in CONWEP. Detonation starts immediately at the beginning of simulations and t_a - time of arrival was calculated internally by LS-DYNA as 150 μs. These inputs yield a total peak pressure of 62 MPa and pressure history obtained from simulations can be seen in Figure 8.2.

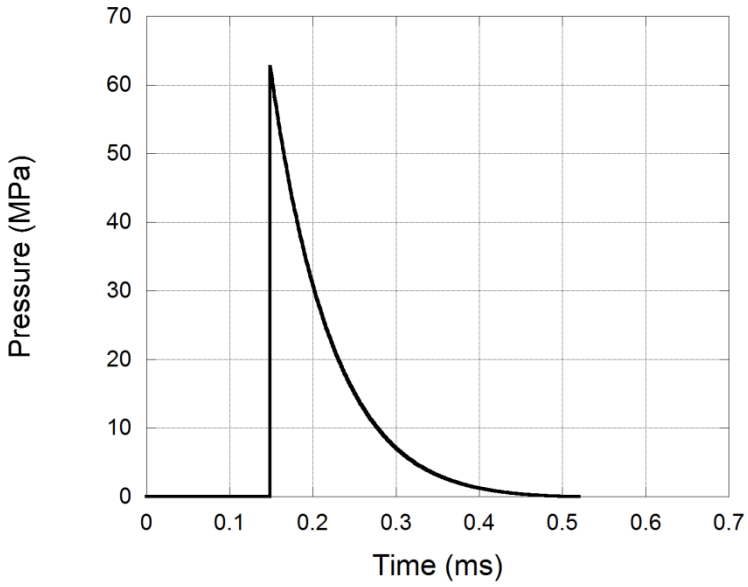

Figure 8.2. Blast wave pressure-time profile obtained from simulations.

In order to evaluate the performance of newly designed sandwich structures under blast loading, a 6 mm thick AISI 304L stainless steel witness plate with 300x300 mm in-plane dimensions was used. Firstly, simulation was run with only aforementioned plate, and then proposed sandwiches were used as cladding. Results were compared in terms of different responses.

(a) (b)

Figure 8.3. Sandwich configurations; (a) close-packed (CP), (b) cross-sharing packed (CSP), (c) cross-unsharing packed (CUP), and (d) Hybrid cross-sharing packed (H-CSP).

(Cont. on next page)

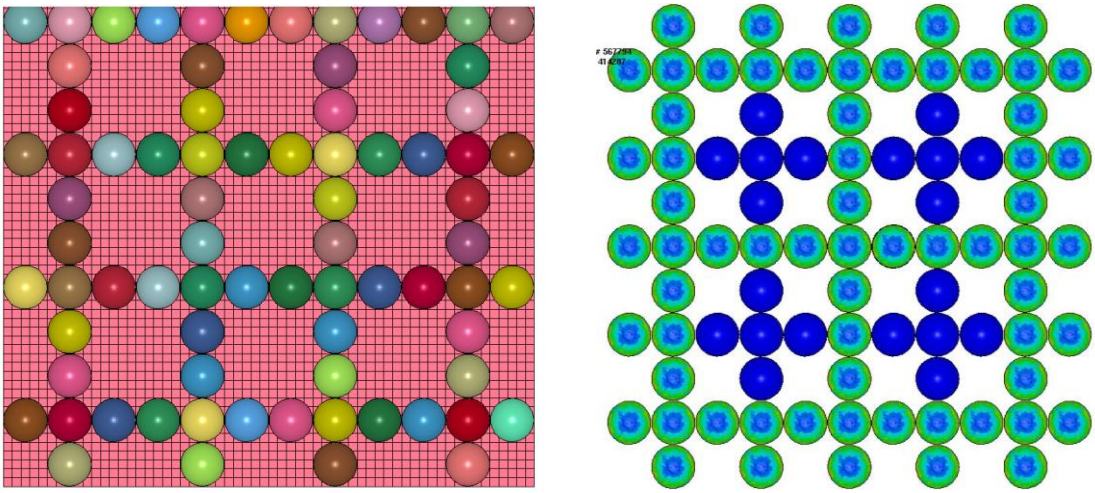

(c) (d)

Figure 8.3. (cont.)

In Figure 8.3 sandwich configurations proposed in the study is given. Close-packed (CP) structure completely fills the area on face sheet and alternatives were designed considering cross-type configuration (Figure 6.6 a) as a repetition unit. Cross-sharing Packed (CSP) and Hybrid Cross-Sharing Packed (H-CSP) configurations share outer core units and form crosses. On the other hand Cross-Unsharing Packed (CUP) type configuration does not share and formed by attaching individual crosses. H-CSP is given with the contours of initial Z-stress in Figure 8.3 d. Initial strain and initial stress values obtained from manufacturing simulations were omitted for blue core units (they have no initial Z-stress) and heat-treated specimens were obtained in this way. Therefore, here hybrid means the usage of as-received and heat-treated specimens together in a sandwich.

Table 8.2. Properties of four alternative configurations.

Configuration	**Number of Unit Core Structures**	**Mass of Sandwich Structure (kg)**
CP	144	2.2
CSP	85	1.88
CUP	80	1.85
H-CSP	85	1.88

Masses and core contents of alternative configurations are given in Table 8.2. CP type configuration has the highest number of unit core structures and therefore has the highest mass. In contrast CUP type sandwich configuration has the highest amount of unsupported space and has the lowest mass among alternatives.

8.2. Blast Simulation Results and Discussions

In this section, results of blast simulations were given. In Table 8.3, velocity and acceleration results for without and alternative sandwich configurations were given in order to have an idea about the applied blast loading and mitigation performance of sandwich structures. Peak front face acceleration can be assumed as a measure of amount of incident loading and as can be seen in table, for all of sandwich configurations incident loading is similar. If peak front face velocities are compared from the table, except for CP configuration all front face velocities are alike. Front face velocity can be assumed as a measure for loading rate in the simulations. Accordingly, a lower loading rate was obtained for CP type sandwiches due to the closer packing of unit core structures and therefore deformation of front face was prevented by high number of unit cores. All peak witness plate velocities are smaller than without simulation. Except for CP configuration, peak witness plate accelerations are lower than that of without configuration. The lowest peak witness plate acceleration was obtained in the case of H-CSP, even it has the same geometry as CSP, and change in material properties resulted in lower acceleration of witness plates.

Table 8.3. Velocity and acceleration results from blast simulations.

	Peak Front Face Velocity (m/s)	Peak Witness Plate Velocity (m/s)	Peak Front Face Acceleration ($x10^6$ m/s^2)	Peak Witness Plate Acceleration ($x10^6$ m/s^2)
Without	N/A	35.7	N/A	0.67
CP	156.4	29.1	5.24	0.75
CSP	193.9	29.08	5.32	0.55
CUP	204.8	33.6	5.35	0.48
H-CSP	202.8	28.3	5.33	0.45

Energy and deformation results obtained from blast simulations were tabulated in Table 8.4. As can be seen, with the addition of cladding, amount of deformation of witness plate reduced, correspondingly deformation energies of witness plates were lower for all alternative sandwich cladding configurations. CP configuration transmitted a lot more force than the other configurations but with a lower loading rate considering results given in Table 8.3, therefore deformation of witness plate was less than the other alternatives even it has a less total internal energy for sandwich.

Table 8.4. Energy and deformation results from blast simulations.

	Peak Middle Displacement of Witness Plate (mm)	Deformation Energy of Witness Plate (kJ)	Total Internal Energy of Sandwich Structure (kJ)	SAE of Sandwich Structure (kJ/kg)	Peak Transmitted Force ($x10^3$ kN)
Without	22.0833	7.746	N/A	N/A	N/A
CP	19.188	6.071	32.99	14.98	8.17
CSP	19.744	6.606	38.26	20.37	5.92
CUP	19.721	6.627	40.36	21.82	4.39
H-CSP	19.190	6.089	38.54	20.52	5.53

Results of Table 8.4 showed also that the most effective sandwich configuration was H-CSP sandwich considering *SAE* and peak middle displacement of witness plate together. The highest total internal energy was calculated for the case of CUP configuration even it has the lowest number of unit core structures (Table 8.2.). The lowest peak transmitted force was observed for CUP configuration but loading rate was the highest among the alternatives considering Table 8.3 and deformation value of witness plate was calculated higher.

Results of blast simulations can be compared with the results from previous chapters on crushing behavior of sandwich structures. In Table 6.1, unconfined and confined quasi-static test results were given for a circular sandwich. As can be seen from the table, test results yield a 32.05 kJ/kg for a unconfined and 30.9 kJ/kg *SAE* for a confined sandwich structure. Also note that, for such a crushing test, whole sandwich

crushing occurs different from blast applications reported in this part of the study. Besides, as can be seen from the comparison of results with five individual core units, higher the interaction between core units lower the effectiveness of sandwich due to the prevention of core structures from deformation. With the highest *SAE* calculated for CUP type configuration (note that blast simulations are different from crushing between rigid plates) quasi-static test results gave a good approximation in the design of blast resistant sandwiches. Results given in Table 8.4 also confirmed the phenomenon knowing CUP type configuration has the lowest interaction between unit combined geometries.

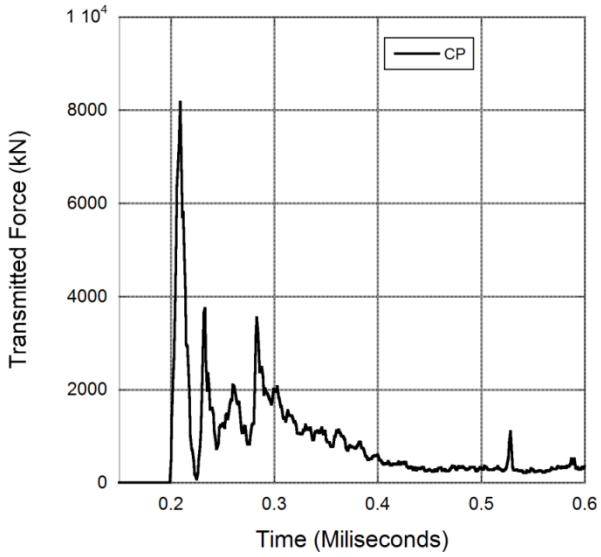

(a)

Figure 8.4. Transmitted force histories for sandwich specimens; (a) CP, (b) CSP, (c) CUP, and (d) H-CSP.

(Cont. on next page)

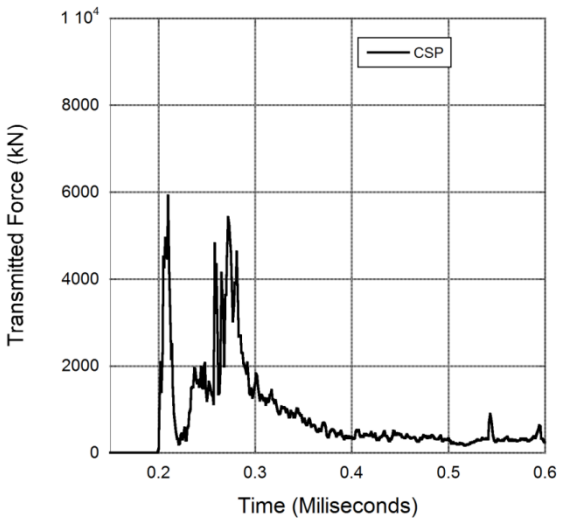

(b)

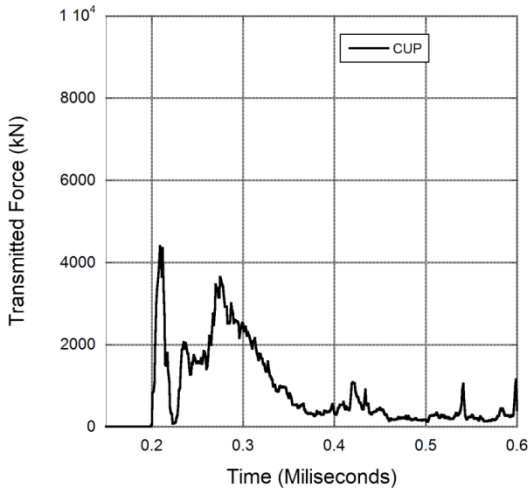

(c)

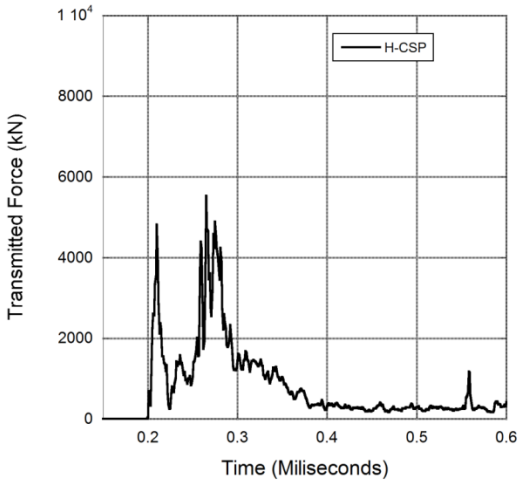

(d)

Figure 8.4. (cont.)

In Figure 8.4, transmitted force histories obtained from simulations can be seen. As results given in Table 8.4 also suggested, the highest peak transmitted force value was observed for CP type sandwich structure. The lowest peak transmitted force was calculated for CUP type sandwich configuration. For all types, a second peak formation is obvious. For the case of CUP sandwich, both first and second peak values were lower than other sandwich structures.

Figure 8.5 shows the deformed views of unit core structures placed in the middle of the sandwiches except for the CUP. For CUP configuration, deformed view is given for the nearest neighbor. It is obvious from the figure, for CP and CSP sandwich configurations, first peak formation occurs with similar deformation except for deformed shape of fractured upside down cap and plastic hinge radius of CSP is a little higher than CP as seen. H-CSP specimen on the other hand showed completely different deformation behavior. At first peak formation time, plastic hinge has not formed yet. Besides, cylindrical portion also started to deform along with hemispherical portion. Unit core structure near the middle of CUP specimen showed a little asymmetrical behavior during first peak formation and at second peak this asymmetry increased. As can be seen for all unit core structures, at second peak formation, fractured hemispherical caps of unit cores crashes onto back face sheet and forms second peak observed in transmitted force histories. The highest deformation was observed for CUP sandwich during second peak formation and considering results of Table 8.4 this is reasonable.

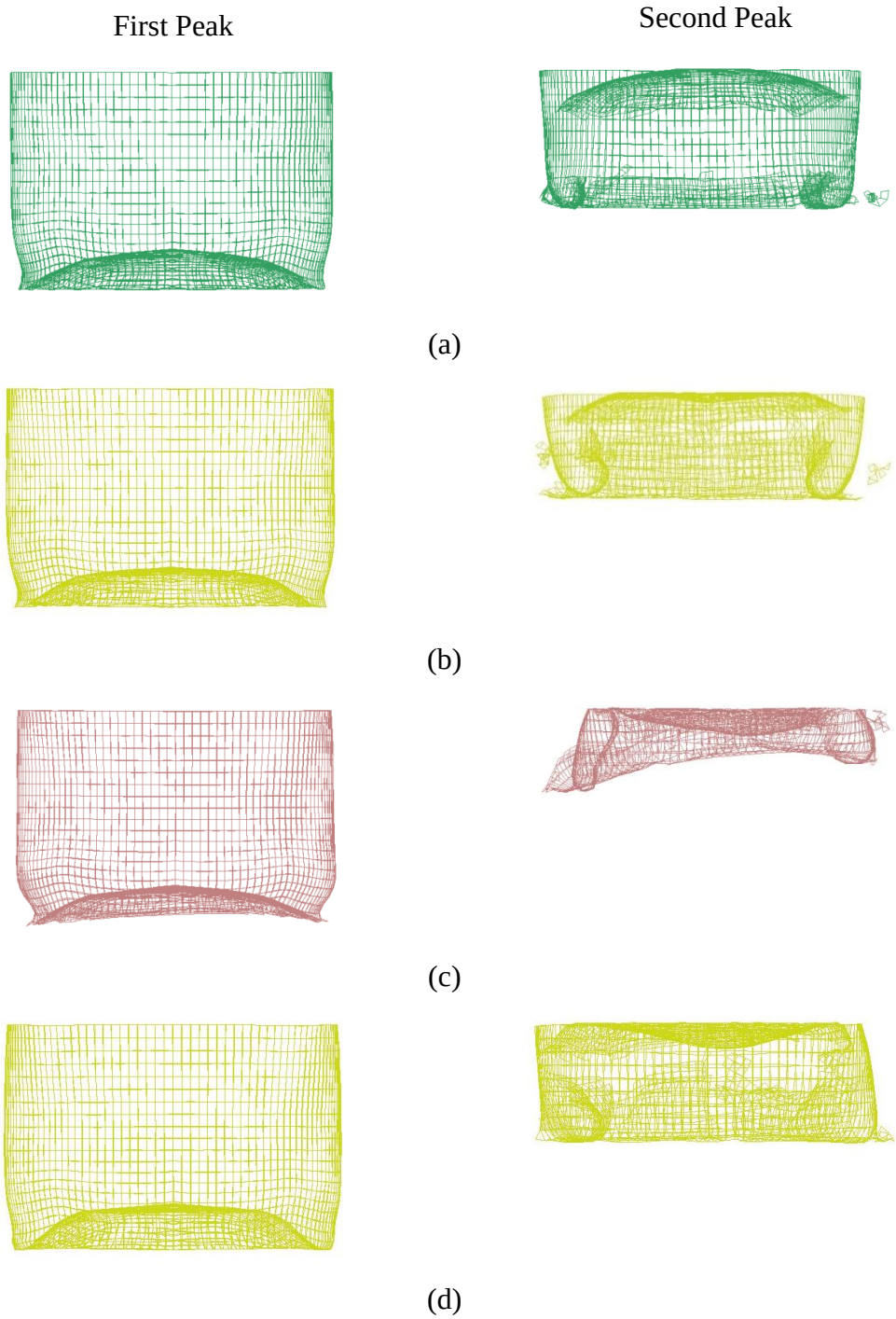

Figure 8.5. Deformed views of middle or near-middle specimens for sandwiches; (a) CP, (b) CSP, (c) CUP (near middle specimen), and (d) H-CSP.

In Figure 8.6, deformed views of unit core structures in H-CSP configurations can be seen in order to compare deformation of as-received and heat-treated specimens. Because heat-treated specimen is located farther comparing to as-received specimen, at first peak formation, its deformation was lesser. On the other hand, it was vice versa at second peak formation. Heat treated specimen completely collapsed, failed elements

were also removed from the simulations. It is obvious that, heat-treated specimen transmitted load in compression mode more than buckling-crushing mode.

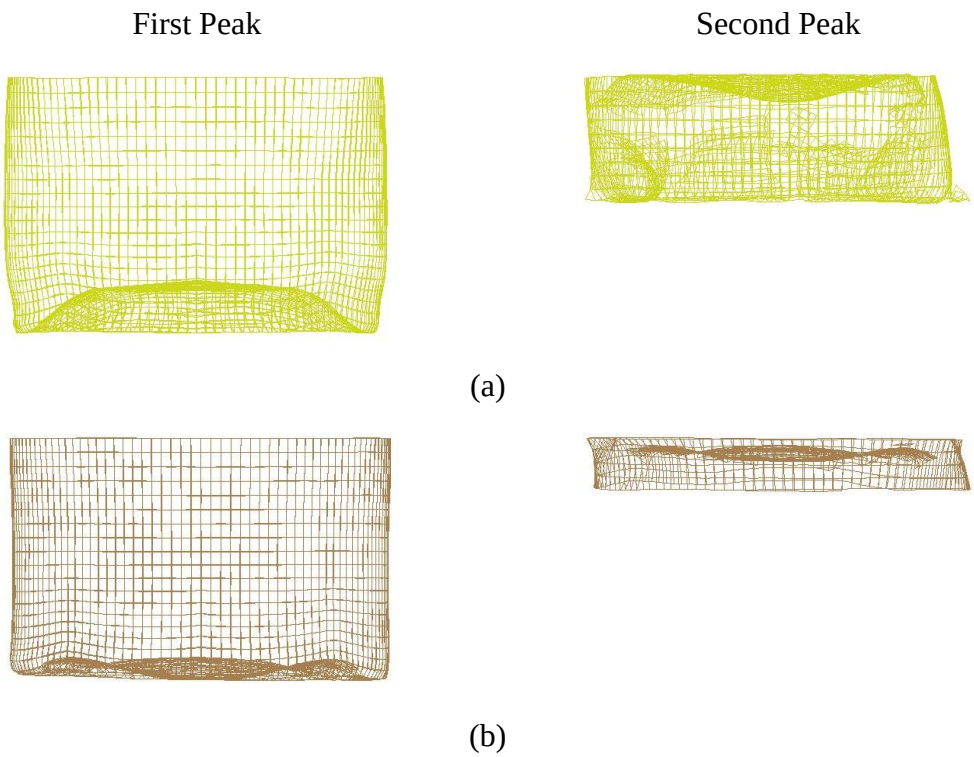

Figure 8.6. Deformed views of (a) middle as-received specimen and (b) heat-treated specimen for H-CSP.

In Figure 8.7 deformed views of sandwich specimens can be seen. As can be seen, the lowest deformation was observed for CP configuration and after hemispherical part deforms and fails cylindrical part starts to transmit force to witness plate. As can be seen in the deformed view of H-CSP sandwich, heat-treated unit core structures nearly completely failed at the end of the simulation. CUP type sandwich showed a deformation profile similar to single cross sandwich unit as shown in corresponding chapter. Among the alternatives, CP configuration still has more deformation capacity and therefore for higher charge amount; CP type configuration is more useful than others. The rest of the sandwiches nearly completely crushed and they do not have more load carrying capability as seen. Conclusively, alternatives other than CP are possible candidates to use against a threat level investigated in this study or less thereof.

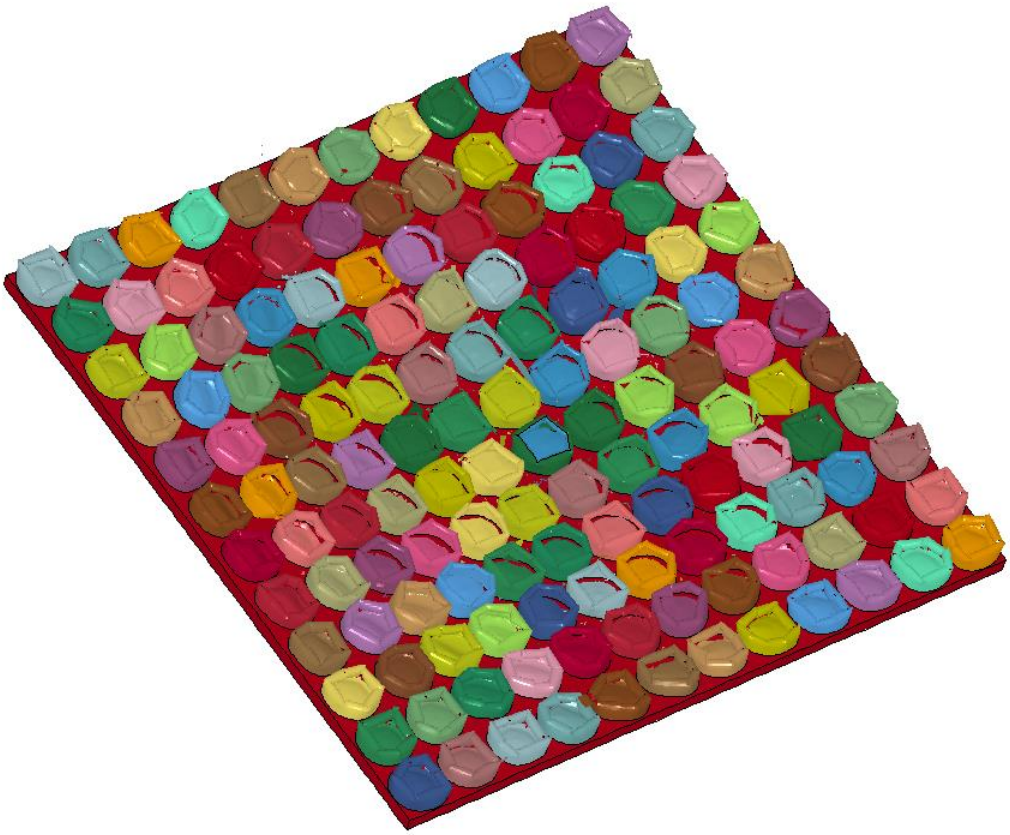

(a)

(b)

Figure 8.7. Deformed views of sandwich specimens; (a) CP, (b) CSP, (c) CUP, and (d) H-CSP.

(Cont. on next page)

(c)

(d)

Figure 8.7. (cont.)

CHAPTER 9

CONCLUSIONS

In this study, novel sandwich structures having combined geometry shell structures as core materials were designed and developed for blast mitigation purposes. The proposed combined geometry shells consist of a hemispherical geometry attached seamlessly to a cylindrical segment. As a core structure, the proposed geometry combines the advantages of a Type I and a Type II energy absorbing structure. The study consists of crushing and energy absorption investigation of both unit combined geometries and their sandwiches with coupled experimental and numerical analyses. Effect of heat-treatment was also investigated experimentally and numerically. Numerical models also inherited the deformation history due to the manufacturing method – deep drawing. Well-validated numerical models then used to conduct parametric analyses to cover the effects of strain rate and inertia on deformation behavior of sandwich structures at high velocities. Besides, blast simulations were conducted in order to investigate the blast mitigation properties of proposed sandwich structures. Based on the detailed experimental and numerical observations following conclusions can be drawn:

- For the as-received specimens with same radius, with higher thickness, P_m and *SAE* values increase too. Reversely, for the specimens with identical thicknesses, radius increase resulted in lower *SAE* values and higher P_m values.
- It is obvious from investigations that for as-received specimens, the energy absorption by the hemispherical section at high strain rate was found to be higher than quasi-static strain rate. This was obviously due to the inertial effects.
- Heat treatment resulted in relief of stress caused by manufacturing process, thus lowering the P_i and P_{max} values in experimental results when compared to as-received materials.
- Numerical models of both quasi-static and low velocity crushing tests showed good correlation with experimental results in terms of force-displacement curves and deformation behavior. Differences in peak loads of some numerical cases were believed to be caused by imperfections in specimens as stated previously in literature.

- Results indicated that for heat-treated specimens increase in loading rate results in decrease in *CFE* value of smaller radius specimens and increase in *CFE* value of bigger radius specimens. When thickness was kept constant, value of *CFE* increased as radius increased for both loading rates.
- Heat treatment of specimens resulted in a negative effect on *SAE* values due to decrease in P_m of structure. When thickness was kept constant and as radius increased, increase in P_m but decrease in *SAE* was observed. It was also concluded that *SAE* was directly proportional with loading rate for all types of specimens.
- For sandwich structures, peaks observed in crushing experimental results corresponds to buckling of constituents of core structures and were followed by load drops because of overcoming of buckling load and those indicated lateral motion of plastic hinges with lower loads.
- The unit core structures in the middle of the sandwich specimens were confined by circumferential core structures and therefore their lateral motion was partly prevented.
- Higher buckling loads at lower deformation were obtained for both components of core structures in confined quasi-static crushing due to additional lateral support and friction due to contact with confinement wall.
- In drop weight results of sandwich structures, except for the shift in the deformation value, force – displacement curve was nearly the same with unconfined quasi-static crushing curve. Deformation of the structure initiated with a typical inward dimpling formation which is asymmetric due to the interaction between adjacent core units.
- For both unconfined and confined cases direct impact test results showed similar behavior except for that in confined test identical initial striker velocity was not able to achieve to deform sandwich until its compaction and an unloading/rebound part was observed.
- Average forces obtained in direct impact experiments were higher than that of quasi-static and low velocity experiments due to inertia as a result of higher impact velocity.
- Numerical simulations were achieved to represent the crushing behavior of sandwich structures with a little difference which is due to amplification of effect of

small difference between thickness variations of tested and modeled specimens; therefore material properties due to strain hardening effect.

- For both unconfined and confined cases, inertial effects were more prominent in comparison with the effect of strain rate especially at higher impact velocities. Increase due to strain rate effect was not dependent on impact velocity. Inertial effects in confined and unconfined configurations were parallel with a common offset due to the effect of confinement at all velocities. At high impact velocities effect of strain rate became almost independent from confinement effect.
- The lowest mean force was calculated for single layer sandwich and the highest was obtained for sequential two layered sandwich.
- All multilayered configurations absorbed more energy than single layer sandwich configuration. Almost all of the sequential configurations have higher *SAE* values than opposite configurations for any misalignment angle.
- Rotation / misalignment between adjacent layers affected results negatively except for 5° rotation for opposite multilayered configurations. As a result of increase in misalignment angle, support by lower layer to the upper layer weakened, absorbed energy decreased. The best sandwich, comparing with other investigated ones, can be chosen as sequential two layered sandwich with a maximum misalignment angle of 20°.
- In order to evaluate the blast mitigation performances of sandwiches having combined geometry shell cores, four types of core configurations were proposed and shown that all was successful to reduce peak displacement values and peak deformation energies of witness plates.
- It was shown that, the higher the interaction between core units, the lower the effectiveness of sandwich due to the prevention of core structures from deformation. It means that more closely packed sandwiches were not as effective as the less closely packed ones in terms of *SAE* comparisons.
- For all sandwich configurations, in force – time histories a second peak force was observed due to the contact of fractured parts of core structures to the back face.
- Among the alternatives, CP configuration still has more deformation capacity and therefore for higher charge amount; CP type configuration was more useful than others. The rest of the sandwiches nearly completely crushed and they do not have more load carrying capability as seen. Conclusively, alternatives other than CP are possible candidates to use against a threat level investigated in this study or less thereof.

For future works, the following can be proposed:

- Investigation on sandwich structures having other types of combined geometry shells can be conducted experimentally and numerically. Results may show the effect of geometry and heat-treatment and confinement effects can be included in sandwich configurations. Even hybrid sandwiches having both as-received and heat-treated core units can be tested and simulated.
- Field blast tests can be conducted in order to better evaluate the performance of sandwich structures.
- Different blast threat levels can be applied on sandwich structures numerically by using validated numerical models.
- Optimization studies can be conducted by using "Design of Computational Experiments – (DOCE)".

REFERENCES

Abdewi, Elfetori F., Shamsuddeen Sulaiman, A. M. S. Hamouda, and E. Mahdi. 2008. "Quasi-static axial and lateral crushing of radial corrugated composite tubes." *Thin-Walled Structures* no. 46 (3):320-332. doi: http://dx.doi.org/10.1016/j.tws.2007.07.018.

Abramowicz, W., and N. Jones. 1997. "Transition from initial global bending to progressive buckling of tubes loaded statically and dynamically." *International Journal of Impact Engineering* no. 19 (5–6):415-437. doi: http://dx.doi.org/10.1016/S0734-743X(96)00052-8.

Abramowicz, Wlodzimierz, and Norman Jones. 1984. "Dynamic axial crushing of circular tubes." *International Journal of Impact Engineering* no. 2 (3):263-281. doi: http://dx.doi.org/10.1016/0734-743X(84)90010-1.

Airoldi, Alessandro, and Gerardus Janszen. 2005. "A design solution for a crashworthy landing gear with a new triggering mechanism for the plastic collapse of metallic tubes." *Aerospace Science and Technology* no. 9 (5):445-455. doi: http://dx.doi.org/10.1016/j.ast.2005.04.001.

Aktay, L., A. F. Johnson, A. K. Toksoy, B. H. Kröplin, and M. Güden. 2008. "Modeling the progressive axial crushing of foam-filled aluminum tubes using smooth particle hydrodynamics and coupled finite element model/smooth particle hydrodynamics." *Materials & Design* no. 29 (3):569-575. doi: http://dx.doi.org/10.1016/j.matdes.2007.03.010.

Aktay, L., A. K. Toksoy, and M. Güden. 2006. "Quasi-static axial crushing of extruded polystyrene foam-filled thin-walled aluminum tubes: Experimental and numerical analysis." *Materials & Design* no. 27 (7):556-565. doi: http://dx.doi.org/10.1016/j.matdes.2004.12.019.

Al Galib, D., and A. Limam. 2004. "Experimental and numerical investigation of static and dynamic axial crushing of circular aluminum tubes." *Thin-Walled Structures* no. 42 (8):1103-1137. doi: http://dx.doi.org/10.1016/j.tws.2004.03.001.

Alberdi, Ryan, John Przywara, and Kapil Khandelwal. 2013. "Performance evaluation of sandwich panel systems for blast mitigation." *Engineering Structures* no. 56 (0):2119-2130. doi: http://dx.doi.org/10.1016/j.engstruct.2013.08.021.

Alexander, J. M. 1960. "An Approximate Analysis of the Collapse of Thin Cylindrical Shells Under Axial Loading." *The Quarterly Journal of Mechanics and Applied Mathematics* no. 13 (1):10-15. doi: 10.1093/qjmam/13.1.10.

Amini, M. R., J. Simon, and S. Nemat-Nasser. 2010. "Numerical modeling of effect of polyurea on response of steel plates to impulsive loads in direct pressure-pulse experiments." *Mechanics of Materials* no. 42 (6):615-627. doi: http://dx.doi.org/10.1016/j.mechmat.2009.09.009.

Ashby, Michael F. 2000. *Metal foams: a design guide*: Butterworth-Heinemann.

Attila, Yiğit, Mustafa Güden, and Alper Taşdemirci. 2013. "Foam glass processing using a polishing glass powder residue." *Ceramics International* no. 39 (5):5869-5877. doi: http://dx.doi.org/10.1016/j.ceramint.2012.12.104.

Banhart, J. 2000. "Manufacturing routes for metallic foams." *JOM* no. 52:22-27.

Barnes, A. T., K. Ravi-Chandar, S. Kyriakides, and S. Gaitanaros. 2014. "Dynamic crushing of aluminum foams: Part I – Experiments." *International Journal of Solids and Structures* no. 51 (9):1631-1645. doi: http://dx.doi.org/10.1016/j.ijsolstr.2013.11.019.

Bazhenov, V. G., E. G. Gonik, A. I. Kibets, and D. V. Shoshin. 2014. "Stability and limit states of elastoplastic spherical shells under static and dynamic loading." *Journal of Applied Mechanics and Technical Physics* no. 55 (1):8-15. doi: 10.1134/S0021894414010027.

Bisagni, Chiara, Giuseppe Di Pietro, Lara Fraschini, and Davide Terletti. 2005. "Progressive crushing of fiber-reinforced composite structural components of a Formula One racing car." *Composite Structures* no. 68 (4):491-503. doi: http://dx.doi.org/10.1016/j.compstruct.2004.04.015.

Błachut, J, and GD Galletly. 1995. "Buckling strength of imperfect steel hemispheres." *Thin-walled structures* no. 23 (1):1-20.

Brakke, Kenneth A. 1992. "The surface evolver." *Experimental mathematics* no. 1 (2):141-165.

Calladine, C. R., and R. W. English. 1984. "Strain-rate and inertia effects in the collapse of two types of energy-absorbing structure." *International Journal of Mechanical Sciences* no. 26 (11–12):689-701. doi: http://dx.doi.org/10.1016/0020-7403(84)90021-3.

Chawla, A., S. Mukherjee, D. Kumar, T. Nakatani, and M. Ueno. 2003. "Prediction of crushing behaviour of honeycomb structures." *International Journal of Crashworthiness* no. 8 (3):229-235. doi: 10.1533/ijcr.2003.0227.

Chen, Antony, Hyonny Kim, Robert J. Asaro, and Jiddu Bezares. 2011. "Non-explosive simulated blast loading of balsa core sandwich composite beams." *Composite Structures* no. 93 (11):2768-2784. doi: http://dx.doi.org/10.1016/j.compstruct.2011.05.027.

Chen, Dai-Heng, and Kuniharu Ushijima. 2013. "Deformation of Honeycomb with Finite Boundary Subjected to Uniaxial Compression." *Metals* no. 3 (4):343-360.

Chi, Y., G. S. Langdon, and G. N. Nurick. 2010. "The influence of core height and face plate thickness on the response of honeycomb sandwich panels subjected to blast loading." *Materials & Design* no. 31 (4):1887-1899. doi: http://dx.doi.org/10.1016/j.matdes.2009.10.058.

Cui, Z., G. Moltschaniwskyj, and D. Bhattacharyya. 2004. "Buckling and large deformation behaviour of composite domes compressed between rigid platens." *Composite Structures* no. 66 (1–4):591-599. doi: http://dx.doi.org/10.1016/j.compstruct.2004.05.007.

Çakıroğlu, Cem. 2008. *QUASI-STATIC CRUSHING BEHAVIOR OF NOMEX® HONEYCOMB FILLED THIN-WALLED ALUMINUM TUBES*, İzmir Institute of Technology.

Dadrasi, Ali. 2011. "Energy absorption of semi-spherical shells under axial loading." *Australian journal of basic and applied sciences* no. 5 (11):2052-2058.

Daniel, Isaac M., Jeong-Min Cho, and Brian T. Werner. 2013. "Characterization and modeling of stain-rate-dependent behavior of polymeric foams." *Composites Part A: Applied Science and Manufacturing* no. 45 (0):70-78. doi: http://dx.doi.org/10.1016/j.compositesa.2012.10.003.

De Oliveira, J G, and T Wierzbicki. 1982. "Crushing analysis of rotationally symmetric plastic shells." *The Journal of Strain Analysis for Engineering Design* no. 17 (4):229-236. doi: 10.1243/03093247v174229.

Deb, Anindya, P. Lakshmanan, Clive Chirwa, and Sravanthi Nowpada. 2012. "Energy absorption behaviours of CSM-based GFRC plates with hemispherical features." *International Journal of Crashworthiness* no. 17 (3):283-294. doi: 10.1080/13588265.2011.650533.

Dharmasena, K. P., D. T. Queheillalt, H. N. G. Wadley, P. Dudt, Y. Chen, D. Knight, A. G. Evans, and V. S. Deshpande. 2010. "Dynamic compression of metallic sandwich structures during planar impulsive loading in water." *European Journal of Mechanics - A/Solids* no. 29 (1):56-67. doi: http://dx.doi.org/10.1016/j.euromechsol.2009.05.003.

Dharmasena, Kumar P., Haydn N. G. Wadley, Zhenyu Xue, and John W. Hutchinson. 2008. "Mechanical response of metallic honeycomb sandwich panel structures to high-intensity dynamic loading." *International Journal of Impact Engineering* no. 35 (9):1063-1074. doi: http://dx.doi.org/10.1016/j.ijimpeng.2007.06.008.

Dharmasena, Kumar, Doug Queheillalt, Haydn Wadley, Yungchia Chen, Philip Dudt, David Knight, Zhensong Wei, and Anthony Evans. 2009. "Dynamic response of a multilayer prismatic structure to impulsive loads incident from water." *International Journal of Impact Engineering* no. 36 (4):632-643. doi: http://dx.doi.org/10.1016/j.ijimpeng.2008.06.002.

Dong, X. L., Z. Y. Gao, and T. X. Yu. 2008. "Dynamic crushing of thin-walled spheres: An experimental study." *International Journal of Impact Engineering* no. 35 (8):717-726. doi: http://dx.doi.org/10.1016/j.ijimpeng.2007.11.004.

Dongmei, Wang. 2009. "Cushioning properties of multi-layer corrugated sandwich structures." *Journal of Sandwich Structures and Materials* no. 11 (1):57-66.

Duarte, Isabel, Matej Vesenjak, Lovre Krstulović-Opara, and Zoran Ren. 2015. "Static and dynamic axial crush performance of in-situ foam-filled tubes." *Composite Structures* no. 124 (0):128-139. doi: http://dx.doi.org/10.1016/j.compstruct.2015.01.014.

Eyvazian, Arameh, Meisam K. Habibi, Abdel Magid Hamouda, and Reza Hedayati. 2014. "Axial crushing behavior and energy absorption efficiency of corrugated tubes." *Materials & Design* no. 54 (0):1028-1038. doi: http://dx.doi.org/10.1016/j.matdes.2013.09.031.

Farley, Gary L. 1991. "The Effects of Crushing Speed on the Energy-Absorption Capability of Composite Tubes." *Journal of Composite Materials* no. 25 (10):1314-1329. doi: 10.1177/002199839102501004.

Fink, Bruce K. 2000. "Performance Metrics for Composite Integral Armor." *Journal of Thermoplastic Composite Materials* no. 13 (5):417-431. doi: 10.1106/fr0l-t33w-jpd0-vfh3.

Gaitanaros, Stavros, Stelios Kyriakides, and Andrew M. Kraynik. 2012. "On the crushing response of random open-cell foams." *International Journal of Solids and Structures* no. 49 (19–20):2733-2743. doi: http://dx.doi.org/10.1016/j.ijsolstr.2012.03.003.

Ghamarian, A., H. R. Zarei, M. A. Farsi, and N. Ariaeifar. 2013. "Experimental and Numerical Crashworthiness Investigation of the Empty and Foam-Filled Conical Tube with Shallow Spherical Caps." *Strain* no. 49 (3):199-211. doi: 10.1111/str.12028.

Ghamarian, Ali, and Mohammad Tahaye Abadi. 2011. "Axial crushing analysis of end-capped circular tubes." *Thin-Walled Structures* no. 49 (6):743-752. doi: http://dx.doi.org/10.1016/j.tws.2011.01.006.

Ghamarian, Ali, Hamid Reza Zarei, and Mohammad Taha Abadi. 2011. "Experimental and numerical crashworthiness investigation of empty and foam-filled end-capped conical tubes." *Thin-Walled Structures* no. 49 (10):1312-1319. doi: http://dx.doi.org/10.1016/j.tws.2011.03.005.

Gibson, Lorna J. 2005. "Biomechanics of cellular solids." *Journal of Biomechanics* no. 38 (3):377-399. doi: http://dx.doi.org/10.1016/j.jbiomech.2004.09.027.

Goel, Manmohan Dass. 2015. "Deformation, energy absorption and crushing behavior of single-, double- and multi-wall foam filled square and circular tubes." *Thin-Walled Structures* no. 90 (0):1-11. doi: http://dx.doi.org/10.1016/j.tws.2015.01.004.

Gong, L., and S. Kyriakides. 2005. "Compressive response of open cell foams Part II: Initiation and evolution of crushing." *International Journal of Solids and Structures* no. 42 (5–6):1381-1399. doi: http://dx.doi.org/10.1016/j.ijsolstr.2004.07.024.

Goods, SH, CL Neuschwanger, and LL Whinnery. 1998. Mechanical properties of a structural polyurethane foam and the effect of particulate loading. Paper read at MRS Proceedings.

Guden, M., S. Yüksel, A. Taşdemirci, and M. Tanoğlu. 2007. "Effect of aluminum closed-cell foam filling on the quasi-static axial crush performance of glass fiber reinforced polyester composite and aluminum/composite hybrid tubes." *Composite Structures* no. 81 (4):480-490. doi: http://dx.doi.org/10.1016/j.compstruct.2006.09.005.

Guillow, S. R., G. Lu, and R. H. Grzebieta. 2001. "Quasi-static axial compression of thin-walled circular aluminium tubes." *International Journal of Mechanical Sciences* no. 43 (9):2103-2123. doi: http://dx.doi.org/10.1016/S0020-7403(01)00031-5.

Gupta, N. K., and G. L. Easwara Prasad. 1999. "Quasi-static and dynamic axial compression of glass/polyester composite hemi-spherical shells." *International Journal of Impact Engineering* no. 22 (8):757-774. doi: http://dx.doi.org/10.1016/S0734-743X(99)00027-5.

Gupta, N. K., G. L. Easwara Prasad, and S. K. Gupta. 1999. "Axial compression of metallic spherical shells between rigid plates." *Thin-Walled Structures* no. 34 (1):21-41. doi: http://dx.doi.org/10.1016/S0263-8231(98)00049-4.

Gupta, N. K., N. Mohamed Sheriff, and R. Velmurugan. 2007. "Experimental and numerical investigations into collapse behaviour of thin spherical shells under drop hammer impact." *International Journal of Solids and Structures* no. 44 (10):3136-3155. doi: http://dx.doi.org/10.1016/j.ijsolstr.2006.09.014.

Gupta, N. K., N. Mohamed Sheriff, and R. Velmurugan. 2008a. "Analysis of collapse behaviour of combined geometry metallic shells under axial impact." *International Journal of Impact Engineering* no. 35 (8):731-741. doi: http://dx.doi.org/10.1016/j.ijimpeng.2008.01.005.

Gupta, N. K., N. Mohamed Sheriff, and R. Velmurugan. 2008b. "Experimental and theoretical studies on buckling of thin spherical shells under axial loads." *International Journal of Mechanical Sciences* no. 50 (3):422-432. doi: http://dx.doi.org/10.1016/j.ijmecsci.2007.10.002.

Gupta, N. K., and R. Velmurugan. 1997. "Consideration of internal folding and non-symmetric fold formation in axisymmetric axial collapse of round tubes." *International Journal of Solids and Structures* no. 34 (20):2611-2630. doi: http://dx.doi.org/10.1016/S0020-7683(96)00117-5.

Gupta, N. K., and Venkatesh. 2004. "Experimental and numerical studies of dynamic axial compression of thin walled spherical shells." *International Journal of Impact Engineering* no. 30 (8–9):1225-1240. doi: http://dx.doi.org/10.1016/j.ijimpeng.2004.03.009.

Gupta, N. K., and Venkatesh. 2006. "A study of the influence of diameter and wall thickness of cylindrical tubes on their axial collapse." *Thin-Walled Structures* no. 44 (3):290-300. doi: http://dx.doi.org/10.1016/j.tws.2006.03.005.

Gupta, P. K. 2011. Axial Compression Of Tubular Metallic Shells Having Combined Tube-Frusta Geometry. Paper read at International Conference on Structural Engineering, Construction and Management (ICSECM 2011), at Katubedda, Sri Lanka.

Gupta, P. K., and N. K. Gupta. 2009. "A study of axial compression of metallic hemispherical domes." *Journal of Materials Processing Technology* no. 209 (4):2175-2179. doi: http://dx.doi.org/10.1016/j.jmatprotec.2008.05.004.

Gupta, P. K., and N. K. Gupta. 2013. "A study on axial compression of tubular metallic shells having combined tube–cone geometry." *Thin-Walled Structures* no. 62 (0):85-95. doi: http://dx.doi.org/10.1016/j.tws.2012.07.018.

Guruprasad, S., and Abhijit Mukherjee. 2000. "Layered sacrificial claddings under blast loading Part II — experimental studies." *International Journal of Impact Engineering* no. 24 (9):975-984. doi: http://dx.doi.org/10.1016/S0734-743X(00)00005-1.

Güden, M., and H. Kavi. 2006. "Quasi-static axial compression behavior of constraint hexagonal and square-packed empty and aluminum foam-filled aluminum multi-tubes." *Thin-Walled Structures* no. 44 (7):739-750. doi: http://dx.doi.org/10.1016/j.tws.2006.07.003.

Hall, I. W., M. Guden, and C. J. Yu. 2000. "Crushing of aluminum closed cell foams: density and strain rate effects." *Scripta Materialia* no. 43 (6):515-521. doi: http://dx.doi.org/10.1016/S1359-6462(00)00460-7.

Hallquist, John O. 2007. "LS-DYNA keyword user's manual." *Livermore Software Technology Corporation* no. 970.

Hanssen, A. G., L. Enstock, and M. Langseth. 2002. "Close-range blast loading of aluminium foam panels." *International Journal of Impact Engineering* no. 27 (6):593-618. doi: http://dx.doi.org/10.1016/S0734-743X(01)00155-5.

Hanssen, A. G., M. Langseth, and O. S. Hopperstad. 2000. "Static and dynamic crushing of circular aluminium extrusions with aluminium foam filler." *International Journal of Impact Engineering* no. 24 (5):475-507. doi: http://dx.doi.org/10.1016/S0734-743X(99)00170-0.

Hsu, SS, and N Jones. 2004. "Quasi-static and dynamic axial crushing of thin-walled circular stainless steel, mild steel and aluminium alloy tubes." *International Journal of Crashworthiness* no. 9 (2):195-217.

Hu, Lingling, Fanfan You, and Tongxi Yu. 2013. "Effect of cell-wall angle on the in-plane crushing behaviour of hexagonal honeycombs." *Materials & Design* no. 46 (0):511-523. doi: http://dx.doi.org/10.1016/j.matdes.2012.10.050.

Huang, Jiancheng, and Xinwei Wang. 2009. "Numerical and experimental investigations on the axial crushing response of composite tubes." *Composite Structures* no. 91 (2):222-228. doi: http://dx.doi.org/10.1016/j.compstruct.2009.05.006.

Jackson, Matthew, and Arun Shukla. 2011. "Performance of sandwich composites subjected to sequential impact and air blast loading." *Composites Part B: Engineering* no. 42 (2):155-166. doi: http://dx.doi.org/10.1016/j.compositesb.2010.09.005.

Jensen, Ø, M. Langseth, and O. S. Hopperstad. 2004. "Experimental investigations on the behaviour of short to long square aluminium tubes subjected to axial loading." *International Journal of Impact Engineering* no. 30 (8–9):973-1003. doi: http://dx.doi.org/10.1016/j.ijimpeng.2004.05.002.

Johnson, Gordon R, and William H Cook. 1983. A constitutive model and data for metals subjected to large strains, high strain rates and high temperatures. Paper read at Proceedings of the 7th International Symposium on Ballistics.

Jurisich, Peter L, and Theodore A Achtarides. 1996. Ship having a crushable, energy absorbing hull assembly. Google Patents.

Kazemahvazi, Sohrab, Daniel Tanner, and Dan Zenkert. 2009. "Corrugated all-composite sandwich structures. Part 2: Failure mechanisms and experimental programme." *Composites Science and Technology* no. 69 (7–8):920-925. doi: http://dx.doi.org/10.1016/j.compscitech.2008.11.035.

Kazemahvazi, Sohrab, and Dan Zenkert. 2009. "Corrugated all-composite sandwich structures. Part 1: Modeling." *Composites Science and Technology* no. 69 (7–8):913-919. doi: http://dx.doi.org/10.1016/j.compscitech.2008.11.030.

Kılıçaslan, Cenk. 2014. "Experimental and numerical investigation of the quasi-static and high strain rate crushing behavior of single and multi-layer zig-zag 1050 H14 Al trapezoidal corrugated core sandwich structures."

Kılıçaslan, Cenk, Mustafa Güden, İsmet Kutlay Odacı, and Alper Taşdemirci. 2013. "The impact responses and the finite element modeling of layered trapezoidal corrugated aluminum core and aluminum sheet interlayer sandwich structures." *Materials & Design* no. 46 (0):121-133. doi: http://dx.doi.org/10.1016/j.matdes.2012.09.059.

Kılıçaslan, Cenk, Mustafa Güden, İsmet Kutlay Odacı, and Alper Taşdemirci. 2014. "Experimental and numerical studies on the quasi-static and dynamic crushing responses of multi-layer trapezoidal aluminum corrugated sandwiches." *Thin-Walled Structures* no. 78 (0):70-78. doi: http://dx.doi.org/10.1016/j.tws.2014.01.017.

Kim, A, K Tunvir, GD Jeong, and SS Cheon. 2006. "A multi-cell FE-model for compressive behaviour analysis of heterogeneous Al-alloy foam." *Modelling and Simulation in Materials Science and Engineering* no. 14 (6):933.

Kim, Heung-Soo. 2002. "New extruded multi-cell aluminum profile for maximum crash energy absorption and weight efficiency." *Thin-Walled Structures* no. 40 (4):311-327. doi: http://dx.doi.org/10.1016/S0263-8231(01)00069-6.

Kinkead, A N, A Jennings, J Newell, and J C Leinster. 1994. "Spherical shells in inelastic collision with a rigid wall—tentative analysis and recent quasi-static testing." *The Journal of Strain Analysis for Engineering Design* no. 29 (1):17-41. doi: 10.1243/03093247v291017.

Kooistra, Gregory W., Vikram Deshpande, and Haydn N. G. Wadley. 2005. "Hierarchical Corrugated Core Sandwich Panel Concepts." *Journal of Applied Mechanics* no. 74 (2):259-268. doi: 10.1115/1.2198243.

Kılıçaslan, C., İ K. Odacı, A. Taşdemirci, and M. Güden. 2014. "Experimental Testing and Full and Homogenized Numerical Models of the Low Velocity and Dynamic Deformation of the Trapezoidal Aluminium Corrugated Core Sandwich." *Strain* no. 50 (3):236-249. doi: 10.1111/str.12085.

Langseth, M., and O. S. Hopperstad. 1996. "Static and dynamic axial crushing of square thin-walled aluminium extrusions." *International Journal of Impact Engineering* no. 18 (7–8):949-968. doi: http://dx.doi.org/10.1016/S0734-743X(96)00025-5.

Lee, D.K., and B.J. O'Toole. 2004. Energy absorbing sandwich structures under blast loading. Paper read at 8th International LS-DYNA Users Conference, at Detroit, USA.

Lee, S., F. Barthelat, J. W. Hutchinson, and H. D. Espinosa. 2006. "Dynamic failure of metallic pyramidal truss core materials – Experiments and modeling." *International Journal of Plasticity* no. 22 (11):2118-2145. doi: http://dx.doi.org/10.1016/j.ijplas.2006.02.006.

Lee, W.S., and C.F. Lin. 2002. "Effects of prestrain and strain rate on dynamic deformation characteristics of 304L stainless steel: Part 1—Mechanical behaviour." *Materials Science and Technology* no. 18 (8):869-876. doi: doi:10.1179/026708302225004711.

Lee, Woei-Shyan, and Chi-Feng Lin. 2001. "Impact properties and microstructure evolution of 304L stainless steel." *Materials Science and Engineering: A* no. 308 (1–2):124-135. doi: http://dx.doi.org/10.1016/S0921-5093(00)02024-4.

Li, Wei, Guangyan Huang, Yang Bai, Yongxiang Dong, and Shunshan Feng. 2014. "Dynamic response of spherical sandwich shells with metallic foam core under external air blast loading – Numerical simulation." *Composite Structures* no. 116 (0):612-625. doi: http://dx.doi.org/10.1016/j.compstruct.2014.05.038.

Li, Xin, Zhihua Wang, Feng Zhu, Guiying Wu, and Longmao Zhao. 2014. "Response of aluminium corrugated sandwich panels under air blast loadings: Experiment and numerical simulation." *International Journal of Impact Engineering* no. 65 (0):79-88. doi: http://dx.doi.org/10.1016/j.ijimpeng.2013.11.002.

Li, Zhibin, Jilin Yu, and Liuwei Guo. 2012. "Deformation and energy absorption of aluminum foam-filled tubes subjected to oblique loading." *International Journal of Mechanical Sciences* no. 54 (1):48-56. doi: http://dx.doi.org/10.1016/j.ijmecsci.2011.09.006.

Liang, Cho-Chung, Ming-Fang Yang, and Pin-Wen Wu. 2001. "Optimum design of metallic corrugated core sandwich panels subjected to blast loads." *Ocean Engineering* no. 28 (7):825-861. doi: http://dx.doi.org/10.1016/S0029-8018(00)00034-2.

Liu, X. R., X. G. Tian, T. J. Lu, and B. Liang. 2014. "Sandwich plates with functionally graded metallic foam cores subjected to air blast loading." *International Journal of Mechanical Sciences* no. 84 (0):61-72. doi: http://dx.doi.org/10.1016/j.ijmecsci.2014.03.021.

Liu, Ying, and Xin-Chun Zhang. 2009. "The influence of cell micro-topology on the in-plane dynamic crushing of honeycombs." *International Journal of Impact Engineering* no. 36 (1):98-109. doi: http://dx.doi.org/10.1016/j.ijimpeng.2008.03.001.

LS-DYNA: Keyword User's Manual, Livermore Software Technology Corporation. LSTC.

Lu, Guoxing, and TX Yu. 2003. *Energy absorption of structures and materials*: Elsevier.

Mahdi, E., and A. S. M. Hamouda. 2005. "Many aspects to improve the energy absorption capacity of collapsible energy absorber devices." *Advanced Composite Materials* no. 14 (1):1-23. doi: 10.1163/1568551053297085.

Maker, Zhu. "A Procedure for Springback Analysis Using LS-DYNA."

Marzbanrad, Javad, Amir Abdollahpoor, and Behrooz Mashadi. 2009. "Effects of the triggering of circular aluminum tubes on crashworthiness." *International Journal of Crashworthiness* no. 14 (6):591-599. doi: 10.1080/13588260902896458.

Marzbanrad, Javad, Mehdi Mehdikhanlo, and Ashkan Saeedi Pour. 2009. "An energy absorption comparison of square, circular, and elliptic steel and aluminum tubes under impact loading." *Turkish J. Eng. Env. Sci* no. 33:159-166.

Meng, Q., S. T. S. Al-Hassani, and P. D. Soden. 1983. "Axial crushing of square tubes." *International Journal of Mechanical Sciences* no. 25 (9–10):747-773. doi: http://dx.doi.org/10.1016/0020-7403(83)90080-2.

Mori, L. F., D. T. Queheillalt, H. N. G. Wadley, and H. D. Espinosa. 2009. "Deformation and Failure Modes of I-Core Sandwich Structures Subjected to Underwater Impulsive Loads." *Experimental Mechanics* no. 49 (2):257-275. doi: 10.1007/s11340-008-9166-9.

Naganathan, Prabakaran, Jimin He, and Jim Kirkpatrick. 1999. "The effect of compression of enclosed air on the cushioning properties of corrugated fibreboard." *Packaging Technology and Science* no. 12 (2):81-91.

Nurick, G. N., G. S. Langdon, Y. Chi, and N. Jacob. 2009. "Behaviour of sandwich panels subjected to intense air blast – Part 1: Experiments." *Composite Structures* no. 91 (4):433-441. doi: http://dx.doi.org/10.1016/j.compstruct.2009.04.009.

Odacı, İsmet Kutlay. 2011. "The projectile impact responses of the composite faced aluminum foam and corrugated aluminum sandwich structures: A comparative study."

Palanivelu, Sivakumar, Wim Van Paepegem, Joris Degrieck, Stijn De Pauw, John Vantomme, Jan Wastiels, Dimitrios Kakogiannis, and Danny Van Hemelrijck. 2011. "Low velocity axial impact crushing performance of empty recyclable metal beverage cans." *International Journal of Impact Engineering* no. 38 (7):622-636. doi: http://dx.doi.org/10.1016/j.ijimpeng.2011.02.008.

Palanivelu, Sivakumar, Wim Van Paepegem, Joris Degrieck, Bruno Reymen, Jean-Marie Ndambi, John Vantomme, Dimitrios Kakogiannis, Jan Wastiels, and Danny Van Hemelrijck. 2011. "Close-range blast loading on empty recyclable metal beverage cans for use in sacrificial cladding structure." *Engineering Structures* no. 33 (6):1966-1987. doi: http://dx.doi.org/10.1016/j.engstruct.2011.02.034.

Papadopoulos, Vissarion, and Pavlos Iglesis. 2007. "The effect of non-uniformity of axial loading on the buckling behaviour of shells with random imperfections." *International Journal of Solids and Structures* no. 44 (18–19):6299-6317. doi: http://dx.doi.org/10.1016/j.ijsolstr.2007.02.027.

Papka, S. D., and S. Kyriakides. 1999. "Biaxial crushing of honeycombs: —Part 1: Experiments." *International Journal of Solids and Structures* no. 36 (29):4367-4396. doi: http://dx.doi.org/10.1016/S0020-7683(98)00224-8.

Parsapour, M. 2014. "Experimental and Numerical Studies on the Energy Absorption Characteristics of Simple and Multi-cell Shapes of Quasi-hemisphere Thin-walled Structures." *International Journal of Engineering (1025-2495)* no. 27 (8).

Pingle, SM, NA Fleck, VS Deshpande, and HNG Wadley. 2011. Collapse mechanism maps for a hollow pyramidal lattice. Paper read at Proceedings of the Royal Society of London A: Mathematical, Physical and Engineering Sciences.

Prasad, G. L. Easwara, and N. K. Gupta. 2005. "An experimental study of deformation modes of domes and large-angled frusta at different rates of compression." *International Journal of Impact Engineering* no. 32 (1–4):400-415. doi: http://dx.doi.org/10.1016/j.ijimpeng.2004.12.001.

Radford, D. D., N. A. Fleck, and V. S. Deshpande. 2006. "The response of clamped sandwich beams subjected to shock loading." *International Journal of Impact Engineering* no. 32 (6):968-987. doi: http://dx.doi.org/10.1016/j.ijimpeng.2004.08.007.

Radford, D. D., G. J. McShane, V. S. Deshpande, and N. A. Fleck. 2006. "The response of clamped sandwich plates with metallic foam cores to simulated blast loading." *International Journal of Solids and Structures* no. 43 (7–8):2243-2259. doi: http://dx.doi.org/10.1016/j.ijsolstr.2005.07.006.

Randers-Pehrson, G., and K.A. Bannister. 1997. ARL-TR-1310 : Airblast loading model for DYNA2D and DYNA3D. Army Research Laboratory.

Rathbun, H. J., D. D. Radford, Z. Xue, M. Y. He, J. Yang, V. Deshpande, N. A. Fleck, J. W. Hutchinson, F. W. Zok, and A. G. Evans. 2006. "Performance of metallic honeycomb-core sandwich beams under shock loading." *International Journal of Solids and Structures* no. 43 (6):1746-1763. doi: http://dx.doi.org/10.1016/j.ijsolstr.2005.06.079.

Rezaei Shahreza, Amir, Farshid Dehghani, and Mahmood Salimi. 2012. Experimental and Numerical Investigation on the Formability of Clad Sheets Copper/Stainless Steel 304L in Spinning Process. Paper read at Key Engineering Materials.

Rossi, A., Z. Fawaz, and K. Behdinan. 2005. "Numerical simulation of the axial collapse of thin-walled polygonal section tubes." *Thin-Walled Structures* no. 43 (10):1646-1661. doi: http://dx.doi.org/10.1016/j.tws.2005.03.001.

Ruan, H. H., Z. Y. Gao, and T. X. Yu. 2006. "Crushing of thin-walled spheres and sphere arrays." *International Journal of Mechanical Sciences* no. 48 (2):117-133. doi: http://dx.doi.org/10.1016/j.ijmecsci.2005.08.006.

Rubino, V., V. S. Deshpande, and N. A. Fleck. 2009. "The dynamic response of clamped rectangular Y-frame and corrugated core sandwich plates." *European Journal of Mechanics - A/Solids* no. 28 (1):14-24. doi: http://dx.doi.org/10.1016/j.euromechsol.2008.06.001.

Saleh, M. A., E. Mahdi, A. M. S. Hamouda, and Y. A. Khalid. 2004. "Crushing behaviour of composite hemispherical shells subjected to quasi-static axial compressive load." *Composite Structures* no. 66 (1–4):487-493. doi: http://dx.doi.org/10.1016/j.compstruct.2004.04.073.

Salehghaffari, S., M. Tajdari, M. Panahi, and F. Mokhtarnezhad. 2010. "Attempts to improve energy absorption characteristics of circular metal tubes subjected to axial loading." *Thin-Walled Structures* no. 48 (6):379-390. doi: http://dx.doi.org/10.1016/j.tws.2010.01.012.

Santosa, S. P., T. Wierzbicki, A. G. Hanssen, and M. Langseth. 2000. "Experimental and numerical studies of foam-filled sections." *International Journal of Impact Engineering* no. 24 (5):509-534. doi: Doi 10.1016/S0734-743x(99)00036-6.

Shariati, M., and H. R. Allahbakhsh. 2010. "Numerical and experimental investigations on the buckling of steel semi-spherical shells under various loadings." *Thin-Walled Structures* no. 48 (8):620-628. doi: http://dx.doi.org/10.1016/j.tws.2010.03.002.

Shojaeefard, MohammadHasan, Amir Najibi, Mahdi Anbarloei, and Mohsen Yeganeh. 2014. "Experimental and numerical crashworthiness investigation of combined circular and square sections." *Journal of Mechanical Science and Technology* no. 28 (3):999-1006. doi: 10.1007/s12206-013-1172-x.

Singace, A A, and H El-Sobky. 2001. "Uniaxial crushing of constrained tubes." *Proceedings of the Institution of Mechanical Engineers, Part C: Journal of Mechanical Engineering Science* no. 215 (3):353-364. doi: 10.1243/0954406011520760.

Singace, A. A. 1999. "Axial crushing analysis of tubes deforming in the multi-lobe mode." *International Journal of Mechanical Sciences* no. 41 (7):865-890. doi: http://dx.doi.org/10.1016/S0020-7403(98)00052-6.

Smith, P.D., and J.G. Hetherington. 1994. *Blast and ballistic loading of structures*: Butterworth-Heinemann.

Song, Jie, Yan Chen, and Guoxing Lu. 2013. "Light-weight thin-walled structures with patterned windows under axial crushing." *International Journal of Mechanical Sciences* no. 66 (0):239-248. doi: http://dx.doi.org/10.1016/j.ijmecsci.2012.11.014.

Song, Ming, Shi Rong Ge, and Hai Feng Fang. 2011. "Analysis of Dynamic Response of Mine Rescue Chamber under Axial Impact Load." *Advanced Materials Research* no. 211:576-580.

Song, Yanze, Zhihua Wang, Longmao Zhao, and Jian Luo. 2010. "Dynamic crushing behavior of 3D closed-cell foams based on Voronoi random model." *Materials & Design* no. 31 (9):4281-4289. doi: http://dx.doi.org/10.1016/j.matdes.2010.04.007.

Sotomayor, Oscar E., and Hareesh V. Tippur. 2014. "Role of cell regularity and relative density on elastoplastic compression response of 3-D open-cell foam core sandwich structure generated using Voronoi diagrams." *Acta Materialia* no. 78 (0):301-313. doi: http://dx.doi.org/10.1016/j.actamat.2014.06.051.

Sriram, R., and U.K. Vaidya. 2004. Blast impact on aluminum foam composite sandwich panels. Paper read at 8th International LS-DYNA Users Conference, at Detroit, USA.

Sriram, Rajan, UdayK Vaidya, and Jong-Eun Kim. 2006. "Blast impact response of aluminum foam sandwich composites." *Journal of Materials Science* no. 41 (13):4023-4039. doi: 10.1007/s10853-006-7606-4.

Taber, L. A. 1983. "Compression of Fluid-Filled Spherical Shells by Rigid Indenters." *Journal of Applied Mechanics* no. 50 (4a):717-722. doi: 10.1115/1.3167135.

Tagarielli, V. L., V. S. Deshpande, and N. A. Fleck. 2007. "The dynamic response of composite sandwich beams to transverse impact." *International Journal of Solids and Structures* no. 44 (7–8):2442-2457. doi: http://dx.doi.org/10.1016/j.ijsolstr.2006.07.015.

Tam, L. L., and C. R. Calladine. 1991. "Inertia and strain-rate effects in a simple plate-structure under impact loading." *International Journal of Impact Engineering* no. 11 (3):349-377. doi: http://dx.doi.org/10.1016/0734-743X(91)90044-G.

Tang, Zhiliang, Shutian Liu, and Zonghua Zhang. 2013. "Analysis of energy absorption characteristics of cylindrical multi-cell columns." *Thin-Walled Structures* no. 62 (0):75-84. doi: http://dx.doi.org/10.1016/j.tws.2012.05.019.

Tasdemirci, A., A. K. Turan, and M. Guden. 2012. "The effect of strain rate on the mechanical behavior of Teflon foam." *Polymer Testing* no. 31 (6):723-727. doi: http://dx.doi.org/10.1016/j.polymertesting.2012.05.004.

Tasdemirci, Alper. 2008. "The effect of tube end constraining on the axial crushing behavior of an aluminum tube." *Materials & Design* no. 29 (10):1992-2001. doi: http://dx.doi.org/10.1016/j.matdes.2008.04.011.

Tasdemirci, Alper, Selim Sahin, Ali Kara, and Kivanc Turan. 2015. "Crushing and energy absorption characteristics of combined geometry shells at quasi-static and dynamic strain rates: Experimental and numerical study." *Thin-Walled Structures* no. 86:83-93. doi: http://dx.doi.org/10.1016/j.tws.2014.09.020i.

Taşdemirci, A., Ç Ergönenç, and M. Güden. 2010. "Split Hopkinson pressure bar multiple reloading and modeling of a 316 L stainless steel metallic hollow

sphere structure." *International Journal of Impact Engineering* no. 37 (3):250-259. doi: http://dx.doi.org/10.1016/j.ijimpeng.2009.06.010.

Taşdemirci, A., M. Güden, and Ç. Ergönenç. 2010. Alüminyum metalik köpük sandviç yapıların mayın patlaması yüklerine karşı davranış simülasyonu. Paper read at 5. Savunma Teknolojileri Kongresi, at Ankara-Türkiye.

Taşdemirci, A., M. Güden, A. Kara, K. Turan, and S. Şahin. 2014. Development and optimization of blast-resistant hemi-spherical core sandwich structures. Turkey: The Scientific and Technological Research Council of Turkey (TÜBİTAK).

Tekalur, Srinivasan Arjun, Arun Shukla, and Kunigal Shivakumar. 2008. "Blast resistance of polyurea based layered composite materials." *Composite Structures* no. 84 (3):271-281. doi: http://dx.doi.org/10.1016/j.compstruct.2007.08.008.

Thacker, BH, PC McKeighan, and JE Pepin. 2005. A study of the collapse of spherical shells, part II: model validation. Paper read at 6th European Conference on Structural Dynamics.

Theobald, M. D., and G. N. Nurick. 2010. "Experimental and numerical analysis of tube-core claddings under blast loads." *International Journal of Impact Engineering* no. 37 (3):333-348. doi: http://dx.doi.org/10.1016/j.ijimpeng.2009.10.003.

Thornton, P.H. 1979. "Energy Absorption in Composite Structures." *Journal of Composite Materials* no. 13 (3):247-262. doi: 10.1177/002199837901300308.

Torabi, H, and M Shariati. 2014. "Buckling Analysis of Steel Semi-Spherical Shells with Square Cutout Under Axial Compression." *Strength of Materials* no. 46 (4):531-542.

Torre, L., and J. M. Kenny. 2000. "Impact testing and simulation of composite sandwich structures for civil transportation." *Composite Structures* no. 50 (3):257-267. doi: http://dx.doi.org/10.1016/S0263-8223(00)00101-X.

Updike, D. P. 1972. "On the Large Deformation of a Rigid-Plastic Spherical Shell Compressed by a Rigid Plate." *Journal of Manufacturing Science and Engineering* no. 94 (3):949-955.

Valdevit, L., J. W. Hutchinson, and A. G. Evans. 2004. "Structurally optimized sandwich panels with prismatic cores." *International Journal of Solids and Structures* no. 41 (18–19):5105-5124. doi: http://dx.doi.org/10.1016/j.ijsolstr.2004.04.027.

Vasanthanathan, A., P. Nagaraj, K. M. Kabilash, and M. Sriram. "The influence of stiffeners on axial crushing of glass-fabric-reinforced epoxy composite shells." *Journal of King Saud University - Engineering Sciences* (0). doi: http://dx.doi.org/10.1016/j.jksues.2014.08.001.

Wadley, Haydn, Kumar Dharmasena, Yungchia Chen, Philip Dudt, David Knight, Robert Charette, and Kenneth Kiddy. 2008. "Compressive response of multilayered pyramidal lattices during underwater shock loading." *International Journal of Impact Engineering* no. 35 (9):1102-1114. doi: http://dx.doi.org/10.1016/j.ijimpeng.2007.06.009.

Wang, Ai-Jun, and David L. McDowell. 2003. "Effects of defects on in-plane properties of periodic metal honeycombs." *International Journal of Mechanical Sciences* no. 45 (11):1799-1813. doi: http://dx.doi.org/10.1016/j.ijmecsci.2003.12.007.

Wang, B., and G. Lu. 2002. "Mushrooming of circular tubes under dynamic axial loading." *Thin-Walled Structures* no. 40 (2):167-182. doi: http://dx.doi.org/10.1016/S0263-8231(01)00057-X.

Wang, Dongmei. 2009. "Impact behavior and energy absorption of paper honeycomb sandwich panels." *International Journal of Impact Engineering* no. 36 (1):110-114. doi: http://dx.doi.org/10.1016/j.ijimpeng.2008.03.002.

Wang, E., and A. Shukla. 2012. "Blast Performance of Sandwich Composites with In-Plane Compressive Loading." *Experimental Mechanics* no. 52 (1):49-58. doi: 10.1007/s11340-011-9500-5.

Wang, Erheng, Nate Gardner, and Arun Shukla. 2009. "The blast resistance of sandwich composites with stepwise graded cores." *International Journal of Solids and Structures* no. 46 (18–19):3492-3502. doi: http://dx.doi.org/10.1016/j.ijsolstr.2009.06.004.

Wang, Yingjian. 1991. "Elastic collapse of honeycombs under out-of-plane pressure." *International Journal of Mechanical Sciences* no. 33 (8):637-644. doi: http://dx.doi.org/10.1016/0020-7403(91)90033-Y.

Wang, Zhi-Wei, and Yu-Ping E. 2011. "Energy absorption properties of multi-layered corrugated paperboard in various ambient humidities." *Materials & Design* no. 32 (6):3476-3485. doi: http://dx.doi.org/10.1016/j.matdes.2011.01.059.

Weber, Sebastian, Mauro Martin, and Werner Theisen. 2012. "Impact of heat treatment on the mechanical properties of AISI 304L austenitic stainless steel in high-pressure hydrogen gas." *Journal of Materials Science* no. 47 (16):6095-6107. doi: 10.1007/s10853-012-6526-8.

Wen, H. M. 1997. "Large plastic deformation of spherical shells under impact by blunt-ended missiles." *International Journal of Pressure Vessels and Piping* no. 73 (2):147-152. doi: http://dx.doi.org/10.1016/S0308-0161(97)00043-4.

Wen, H. M. 1998. "Deformation and Perforation of Spherical Shells by Normal Impact of Blunt-Ended Projectiles*." *Mechanics of Structures and Machines* no. 26 (3):239-255. doi: 10.1080/08905459708945429.

Wiernicki, Christopher J, Franz Liem, Gregory D Woods, and ANTHONY J FURIO. 1991. "Structural analysis methods for lightweight metallic corrugated core sandwich panels subjected to blast loads." *Naval Engineers Journal* no. 103 (3):192-202.

Wierzbicki, Tomasz. 1983. "Crushing analysis of metal honeycombs." *International Journal of Impact Engineering* no. 1 (2):157-174. doi: http://dx.doi.org/10.1016/0734-743X(83)90004-0.

Wilbert, A., W. Y. Jang, S. Kyriakides, and J. F. Floccari. 2011. "Buckling and progressive crushing of laterally loaded honeycomb." *International Journal of Solids and Structures* no. 48 (5):803-816. doi: http://dx.doi.org/10.1016/j.ijsolstr.2010.11.014.

Wu, Enboa, and Wu-Shung Jiang. 1997. "Axial crush of metallic honeycombs." *International Journal of Impact Engineering* no. 19 (5–6):439-456. doi: http://dx.doi.org/10.1016/S0734-743X(97)00004-3.

Xu, S., J. H. Beynon, D. Ruan, and T. X. Yu. 2012. "Strength enhancement of aluminium honeycombs caused by entrapped air under dynamic out-of-plane compression." *International Journal of Impact Engineering* no. 47 (0):1-13. doi: http://dx.doi.org/10.1016/j.ijimpeng.2012.02.008.

Xue, Zhenyu, and John W. Hutchinson. 2004. "A comparative study of impulse-resistant metal sandwich plates." *International Journal of Impact Engineering* no. 30 (10):1283-1305. doi: http://dx.doi.org/10.1016/j.ijimpeng.2003.08.007.

Xue, Zhenyu, and John W. Hutchinson. 2006. "Crush dynamics of square honeycomb sandwich cores." *International Journal for Numerical Methods in Engineering* no. 65 (13):2221-2245. doi: 10.1002/nme.1535.

Yan, Libo, Nawawi Chouw, and Krishnan Jayaraman. 2014. "Effect of triggering and polyurethane foam-filler on axial crushing of natural flax/epoxy composite tubes." *Materials & Design* no. 56 (0):528-541. doi: http://dx.doi.org/10.1016/j.matdes.2013.11.068.

Yang, Hui Wei, Bin Qin, Zhi Jun Han, and Guo Yun Lu. 2013. "Numerical Simulation and Experimental Study on Fluid-Filled Hemispherical Shell under Impact." *Applied Mechanics and Materials* no. 364:172-176.

Yasui, Yoshiaki. 2000. "Dynamic axial crushing of multi-layer honeycomb panels and impact tensile behavior of the component members." *International Journal of Impact Engineering* no. 24 (6–7):659-671. doi: http://dx.doi.org/10.1016/S0734-743X(99)00174-8.

Yazici, Murat, Jefferson Wright, Damien Bertin, and Arun Shukla. 2014. "Experimental and numerical study of foam filled corrugated core steel sandwich structures subjected to blast loading." *Composite Structures* no. 110 (0):98-109. doi: http://dx.doi.org/10.1016/j.compstruct.2013.11.016.

Yin, Hanfeng, Guilin Wen, Shujuan Hou, and Kai Chen. 2011. "Crushing analysis and multiobjective crashworthiness optimization of honeycomb-filled single and bitubular polygonal tubes." *Materials & Design* no. 32 (8–9):4449-4460. doi: http://dx.doi.org/10.1016/j.matdes.2011.03.060.

Zarei, Hamidreza, and Matthias Kröger. 2008. "Optimum honeycomb filled crash absorber design." *Materials & Design* no. 29 (1):193-204. doi: http://dx.doi.org/10.1016/j.matdes.2006.10.013.

Zhang, T. G., and T. X. Yu. 1989. "A note on a ‘velocity sensitive’ energy-absorbing structure." *International Journal of Impact Engineering* no. 8 (1):43-51. doi: http://dx.doi.org/10.1016/0734-743X(89)90030-4.

Zhang, X. W., Q. D. Tian, and T. X. Yu. 2009. "Axial crushing of circular tubes with buckling initiators." *Thin-Walled Structures* no. 47 (6–7):788-797. doi: http://dx.doi.org/10.1016/j.tws.2009.01.002.

Zhang, Xin-Chun, Ying Liu, Bin Wang, and Zi-Mao Zhang. 2010. "Effects of defects on the in-plane dynamic crushing of metal honeycombs." *International Journal of Mechanical Sciences* no. 52 (10):1290-1298. doi: http://dx.doi.org/10.1016/j.ijmecsci.2010.06.004.

Zhang, Xiong, and Hui Zhang. 2014. "Axial crushing of circular multi-cell columns." *International Journal of Impact Engineering* no. 65 (0):110-125. doi: http://dx.doi.org/10.1016/j.ijimpeng.2013.12.002.

Zhu, F., and G. Lu. 2007. "A Review of Blast and Impact of Metallic and Sandwich Structures." *Electronic Journal of Structural Engineering* (Special Issue : Loading on Structures):92-101.

Zhu, F.; Lu, G. . 2007. "A review of blast and impact of metallic and sandwich structures." *Electronic Journal of Structural Engineering* (Special Issue: Loading on Structures):92-101.

Zhu, Feng, Liqiang Dong, Honglei Ma, Cliff C. Chou, and King H. Yang. 2014. "Parameterized optimal design of a novel cellular energy absorber." *International Journal of Mechanical Sciences* no. 86 (0):60-68. doi: http://dx.doi.org/10.1016/j.ijmecsci.2013.09.021.

Zhu, Feng, Zhihua Wang, Guoxing Lu, and Longmao Zhao. 2009. "Analytical investigation and optimal design of sandwich panels subjected to shock loading." *Materials & Design* no. 30 (1):91-100. doi: http://dx.doi.org/10.1016/j.matdes.2008.04.027.

Zhu, Feng, Longmao Zhao, Guoxing Lu, and Emad Gad. 2009. "A numerical simulation of the blast impact of square metallic sandwich panels." *International Journal of Impact Engineering* no. 36 (5):687-699. doi: http://dx.doi.org/10.1016/j.ijimpeng.2008.12.004.

Zhu, Feng, Longmao Zhao, Guoxing Lu, and Zhihua Wang. 2008. "Deformation and failure of blast-loaded metallic sandwich panels—Experimental investigations." *International Journal of Impact Engineering* no. 35 (8):937-951. doi: http://dx.doi.org/10.1016/j.ijimpeng.2007.11.003.

VITA

Ali Kara was born in Karşıyaka/İzmir/TURKEY in November 20, 1985. After graduation from Department of Mechanical Engineering – Celal Bayar University, he attended to İzmir Institute of Technology for his M.Sc. and Ph.D. studies. He worked as a research assistant in the Dynamic Testing and Modeling Laboratory of Mechanical Engineering Department during his Ph.D. studies.

Education

- ***Ph.D.*** in English, 2010, Mechanical Engineering, İzmir Institute of Technology.
- ***M.Sc.*** in English, 2007, Mechanical Engineering, İzmir Institute of Technology.
- ***B.Sc.*** in Turkish, 2004, Business Administration, Anadolu University.
- ***B.Sc.*** in Turkish, 2002, Mechanical Engineering, Celal Bayar University.

Publications

- A. Taşdemirci, A. Kara, "The Effect of Perforations on the Stress Wave Propagation Characteristics of Multilayered Materials", Journal of Thermoplastic Composite Materials, Accepted for publication.
- A. Taşdemirci, A. Kara, A.K. Turan, S. Şahin, "Dynamic Crushing and Energy Absorption of Sandwich Structures with Combined Geometry Shell Cores", Thin-Walled Structures, vol. 91, pp. 116-128, 2015.
- A. Taşdemirci, S. Şahin, A. Kara, A.K. Turan, "Crushing and Energy Absorption Characteristics of Combined Geometry Shells at Quasi-Static and Dynamic Strain Rates: Experimental and Numerical Study", Thin-Walled Structures, vol. 86, pp. 83-93, 2015.
- A. Kara, A. Taşdemirci, M. Güden, "Modeling Quasi-Static and High Strain Rate Deformation and Failure Behavior of a (± 45) Symmetric E-glass/Polyester Composite under Compressive Loading", Materials and Design, vol. 49, pp. 566-574, 2013.